Small Molecule Reactivity of Trisphosphine-supported Iron and Cobalt Complexes

Thesis by

Meaghan M. Deegan

In Partial Fulfillment of the Requirements for
the degree of
Doctor of Philosophy

CALIFORNIA INSTITUTE OF TECHNOLOGY
Pasadena, California

2020
(Defended September 4, 2019)

Meaghan M. Deegan
ORCID: 0000-0002-7633-2074

ACKNOWLEDGEMENTS

While the pursuit of a PhD is in many respects an intensely individual endeavor, it goes almost without saying that none of the research described in this thesis would have been possible without the support of many individuals. The few words I can provide here will certainly be insufficient to express appropriate gratitude to all of the people who positively influenced my time in graduate school.

First, my advisor, Jonas Peters, is thanked for his persistent support and guidance throughout my five years in his research group. During my time at Caltech, I have grown to appreciate the freedom Jonas has given me to pursue projects and ideas that have sparked my interest, and have allowed me to grow as a scientist. The frustrations of graduate school often make it challenging to appreciate the opportunity to pursue scientific endeavors with little restraint on a day-to-day basis. As I am halfway out the door I can begin to acknowledge that my time at Caltech in Jonas's research group has truly been a privilege, and I sincerely thank him for the time I have had working in his research group.

The remaining members of my thesis committee, Theo Agapie, Greg Fu, and Sarah Reisman, are acknowledged for their thoughtful insight and support provided in each of our committee meetings.

My interest in pursuing synthetic inorganic/organometallic chemistry research was sparked through my undergraduate experiences in chemistry. I thank David Glueck and Russell Hughes for their enthusiasm for working with undergraduate students, both inside the classroom and the research laboratory.

The expertise of the scientific staff at Caltech is inarguably one of the institute's greatest assets. The work carried out in this thesis would have been impossible without countless hours spent in both the X-ray and NMR facilities. Mike Takase, Larry Henling, and David VanderVelde are thanked both for maintaining these exceptional facilities and for their generous experimental assistance. Larry is especially thanked for truly going above and beyond what can reasonably be expected of him to wrangle useful structural information out of barely crystalline rubbish, often in the middle of the night.

I have been fortunate to work with and learn a great deal from a number of exceptional students and postdocs during my time in the Peters group. First, I would like to thank Sid

Creutz for his patience while mentoring me when I was a young, enthusiastic, and largely clueless first year graduate student. In addition to Sid's helpful guidance, my early scientific development in the Peters group was influenced by a number of senior students and postdocs. Jon Rittle, Gaël Ung, and TP Lin, in particular, are thanked for their thoughtful discussions. My year-mates, Nina Gu and Javier Fajardo, are thanked for their solidarity during our time in the group. The scientific rigor of their research efforts and intense work ethic set a high standard I aspired to match. More importantly, their kind companionship made my time in graduate school more pleasant. Javier was also one of my office-mates during much of my time in the group. I acknowledge him and the remainder of my desk neighbors—Sid, Joe Ahn, Christian Johansen, and more briefly Pablo Garrido-Barros, Koichi Nagata, and Nick Watkins—for our generally enjoyable time shared in the best bay in the office. I thank Kareem Hannoun for his collaboration both on DFT and on Tuesday Ernie's (most recently along with Christian, Nina "extra jalapeños" Gu, and, of course, Ernie). Miles Johnson and Kumiko Yamamoto are thanked for their friendship and for encouraging me to occasionally leave lab; I enjoyed every one of our occasional hiking and food excursions. Teddy Donnell is acknowledged for his generosity and the positive spirit he brought to our group daily.

Women at Caltech and in our research group continue to be far too few in number. Fortunately, the women I have overlapped with during my time in our group have had a disproportionate influence on my time at Caltech. I would especially like to thank Trixia Buscagan and Shabnam Hematian for their encouragement and positivity in support of younger women in our group. I additionally acknowledge the rest of the women I overlapped with in our group Nina Gu, Hsiang-Yun Chen, Gerri Roberts, Kumiko Yamamoto, Tanvi Ratani, Bridget Connor, and Pat Nance and wish them the best of luck in their future scientific plights.

In the now nine years since I first moved away from my family, my closest college friends continue to provide me with incredible friendship that I cannot take for granted, even today as we are scattered across the country. To my Dartmouth family—Marissa Allen, Xavier Curry, Alex Leach, Ryan Smith, Ian Stewart, and Cami Van Putten—I say thanks. I look forward to living closer to several of you in the immediate future and, more distantly, to what lies ahead for each of us.

Finally, I must thank my family for their infinite support. First and foremost, I must acknowledge my mom, who unwaveringly remains the strong person I can only aspire to one day become. Additional thanks are owed to my siblings, Erin and Dan, as well as many cousins, aunts, and uncles that constitute my familial support network. I especially need to thank the individuals who are no longer able to receive them—my grandparents and dad. The work described in this thesis is dedicated to their memory.

ABSTRACT

Novel reactivity patterns in the activation of CO, N_2, and H_2 by phosphine-supported Fe and Co complexes are developed through a series of synthetic studies. First, we explore hydride systems that access CO and N_2 reductive functionalization from highly reduced Fe-hydride precursors. One of the major challenges associated with developing molecular systems that are able to mediate Fischer–Tropsch chemistry is the design of systems that promote the formation of C–H bonds from H_2 and CO while also facilitating the release of the resulting CO-derived organic products. To this end, we describe the synthesis of reduced Fe-hydride/carbonyl complexes that enable an electrophile-promoted hydride migration process, resulting in the reduction of coordinated CO to a siloxymethyl ($L_nFe\text{-}CH_2OSiMe_3$) group. Intramolecular hydride-to-CO migrations are extremely rare, and to our knowledge the system described herein is the first example where such a process can be accessed from a thermally stable M(CO)(H) precursor. Further addition of H_2 to $L_nFe\text{-}CH_2OSiMe_3$ releases CH_3OSiMe_3, demonstrating net four-electron reduction of CO to CH_3OSiMe_3 at a single Fe site.

Relatedly, one of the emerging challenges associated with developing robust synthetic nitrogen fixation catalysts is the competitive formation of hydride species that can play a role in catalyst deactivation or lead to undesired hydrogen evolution reactivity (HER). Thus, synthetic systems where metal hydrides can migrate directly to coordinated N_2 in reductive N–H bond-forming steps are desirable to enable productive M-H incorporation into reduced N_2-derived products. Relevant examples of this type of reactivity in synthetic model systems are limited. We describe the migration of an iron hydride (Fe-H) to N_α of a disilylhydrazido(2-) ligand ($Fe{=}NNR_2$) derived from N_2 *via* double-silylation in a preceding step. This is an uncommon reactivity pattern in general; well-characterized examples of hydride/alkyl migrations to metal heteroatom bonds (*e.g.*, $(R)M{=}NR' \rightarrow M\text{–}N(R)R'$) are very rare. Mechanistic data establish the Fe-to-N_α hydride migration to be intramolecular. The resulting disilylhydrazido(1-) intermediate can be isolated by trapping with CN^tBu, and the disilylhydrazine product can then be liberated upon treatment with an additional acid equivalent.

We next explored a system to extend CO functionalization reactivity to late metals beyond group 8. We describe the synthesis of a series of $L_3Co(CO)$ complexes supported by a trisphosphine ligand framework, with the most reduced of these complexes being amenable to O-functionalization. Despite efforts toward extending multiple bonding motifs to late metal systems, examples of late transition metal carbynes remain scarce. This transformation provides access to the second reported example of a terminal Co-carbyne complex, in this case stabilized in a pseudotetrahedral geometry (*i.e.*, $L_3Co{\equiv}C\text{-}OSiR_3$). Its geometry makes its electronic structure suitable for comparison to structurally-related examples of terminal Co-imido and oxo species.

Next, an unusual pair of stabilized non-classical $Co\text{-}H_2$ adducts can be generated as a neutral radical and in a reduced, anionic state. This redox pair was targeted as a prospective system for accessing new reactivity patterns in the chemistry of σ-adducts. Specifically, we describe the propensity for these systems to access H-atom and hydride transfer reactivity, where the established reactivity of non-classical H_2 adducts is almost exclusively limited to their deprotonation or oxidative addition to dihydrides. We consider in some detail limiting kinetic and thermodynamic considerations for accessing these novel reactions.

Finally, this volume concludes with the synthetic pursuit of a terminal Fe-carbide complex. As a key intermediate in Fischer-Tropsch chemistry and the simplest but often elusive organometallic fragment, the terminal transition metal carbide, remains a compelling synthetic target, especially for first row metal systems. Herein, we describe parallel approaches explored toward the generation of a terminal Fe-carbide complex. To this end, we detail the synthesis of Fe-thiocarbonyl complexes with two different trisphosphine supporting ligands. One of these systems supports S-functionalization reactivity to generate terminal Fe-thiocarbyne complexes that are stable across three formal oxidation states. The second system supports C-S bond cleavage chemistry through a surprising pathway that circumvents the intermediacy of a terminal Fe-carbide complex.

PUBLISHED CONTENT AND CONTRIBUTIONS

This dissertation contains material adapted with permission from the following publications:

Chapter 2: Deegan, M. M.; Peters, J. C. CO Reduction to CH_3OSiMe_3: Electrophile-Promoted Hydride Migration at a Single Fe Site. *J. Am. Chem. Soc.* **2017**, *139*, 2561-2564. [doi: 10.1021/jacs.6b12444]

Chapter 3: Deegan, M. M.; Peters, J. C. Electrophile-promoted Fe-to-N_2 hydride migration in highly reduced Fe(N_2)(H) complexes. *Chem. Sci.* **2018**, *9*, 6264-6270. [doi: 10.1039/C8SC02380H]

Chapter 4: Deegan, M. M.; Peters, J. C. O-Functionalization of a cobalt carbonyl generates a terminal cobalt carbyne. *Chem. Commun.* **2019**, *55*, 9531-9534. [doi: 10.1039/C9CC04032C]

For all publications, M. M. D. designed and conducted all experiments. The published manuscripts were prepared collaboratively by M. M. D. and J. C. P.

TABLE OF CONTENTS

DETAILED TABLE OF CONTENTS

LIST OF ILLUSTRATIONS AND TABLES

Chapter 6

Appendix A

Chapter 1

INTRODUCTION

1.1 Opening Remarks

A unifying motivation behind the chemistry described in this thesis is an interest in developing novel transition metal mediated avenues for transforming strong chemical bonds. The primary emphasis is the study of late, first row transition metal systems that mediate transformations of small molecules, primarily CO and closely related species (Chapters 2[1], 4[2], and 6), with individual chapters detailing transformations of N_2 (Chapter 3[3]) and H_2 (Chapter 5) in structurally related systems. Classically, studies of molecular transition metal-based systems that mediate derivatization of these substrates were largely confined to the early-to-mid transition elements and/or 2nd and 3rd row metals. In recent decades, interest in the development of mid-to-late first row transition metal systems that support transformations of these challenging substrates has grown. This growth was driven, in part, by interest in modeling the chemistry of both biological metallocofactors and industrially relevant heterogeneous catalysts that often employ earth abundant metals such as Fe. This chapter provides a brief introduction to systems that mediate conversions of CO, N_2, and H_2 and motivates our interest in studying late, first row transition metal systems in this context.

1.2 Industrial and Biological Activation of N_2 and CO

1.2.1 Nitrogenase Enzymes

While gaseous dinitrogen (N_2) constitutes 78% of Earth's atmosphere, in its elemental form, the strong, nonpolar N-N triple bond (226 kcal/mol) makes N_2 unreactive to nearly all natural and synthetic systems.[4] Thus, while N_2 itself is chemically inert toward biological systems and therefore a suitable carrier gas for life, it cannot directly provide the requisite N-atom equivalents for construction of essential biomolecules. As such, the evolution of a system with the ability to fix elemental nitrogen (N_2) into bioavailable forms and turn over the global nitrogen cycle played a monumental role in the development of life as we know it. The evolved systems, biological nitrogenase enzymes, long possessed the unique ability to mediate the challenging reduction of N_2 from its elemental form to NH_3 (Figure 1.1A).[5]

As an introduction to the specific model reactivity explored in this thesis, two relevant aspects of nitrogenase chemistry should be emphasized. First, while relatively little is known about the intimate mechanistic details of N_2 conversion at the FeMo-cofactor, one comparatively well-understood aspect of nitrogenase chemistry is the buildup of Fe(H) precursors prior to N_2 binding and fixation. This is outlined in the Lowe-Thorneley kinetic model that was first developed through kinetic investigations of nitrogenase activity (Figure 1.1B).[5b] More recent spectroscopic work, including extensive pulsed EPR studies from Hoffman, Seefeldt, and Dean, have allowed for more detailed characterization of reaction intermediates generated prior to N_2 binding.[6,7] These studies have also demonstrated the viability of H_2 reductive elimination[8,9] from the key E4(4H) state, which is proposed to control the limiting reaction stoichiometry for these systems.[10] The inability to directly study reaction intermediates generated following initial N_2 binding remains a central challenge in this field; this currently limits the intimate mechanistic understanding of chemistry mediated by this complex metallocofactor.[11]

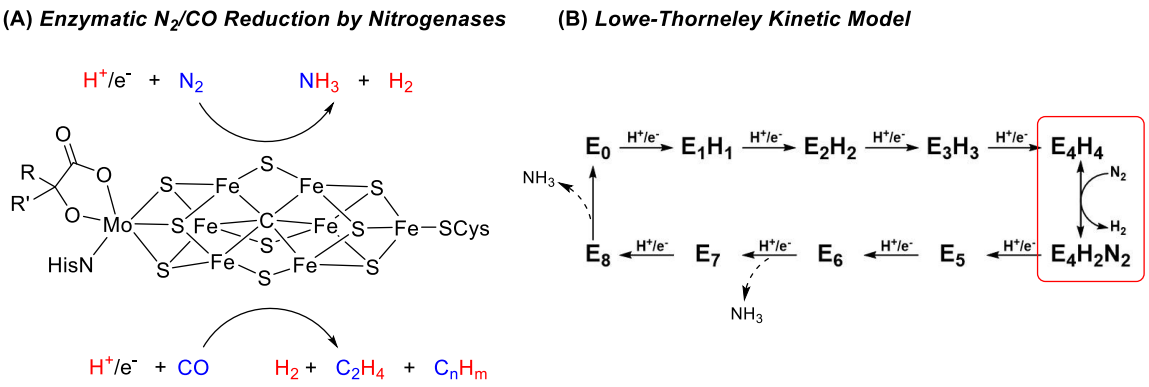

Figure 1.1. (**A**) Structural depiction of the nitrogenase FeMo-cofactor and its overall reactivity toward N_2 and CO reduction. (**B**) Lowe-Thorneley kinetic model for N_2 binding and fixation.

A second intriguing feature of these enzymatic systems is their chemical promiscuity, where they have been shown to promote the proton-coupled reduction of a number of small molecule substrates in addition to their native substrate N_2. Arguably the most remarkable transformation mediated by nitrogenase enzymes is the deoxygenative reductive coupling of CO to C_n products, which was initially observed only for the VFe variant of this enzyme.[12] Follow up studies by Ribbe and coworkers have established that the MoFe enzyme is a catalyst for this transformation,[13,14] and that the protein environment

is not a prerequisite for accessing this challenging reactivity, as the extracted cofactor is also a competent catalyst for C-C reductive coupling under a variety of conditions.[15]

1.2.2 Industrial N_2 and CO Conversion

Early in the 20th century, growing agricultural demand for NH_3 incentivized the development of an efficient synthetic approach to NH_3 synthesis to augment existing biological nitrogen fixing processes. This ultimately gave rise to the Haber-Bosch process, through which N_2 is hydrogenated to NH_3 over a heterogeneous Fe catalyst at elevated temperatures and pressures.[4] Shortly thereafter, economic forces drove the development of the conceptually related Fischer-Tropsch process, in which the hydrogenation of CO is mediated by Fe or Co heterogeneous catalysts to yield liquid hydrocarbon products.[16] Effectively, this process provides an economically viable pathway for the conversion of gaseous or solid hydrocarbon fuels to more valuable liquid hydrocarbons through a CO intermediate. Both of these processes are still operative today, with the ability to produce synthetic ammonia of ever-increasing importance for modern agriculture[17] and our global addiction to liquid fossil fuels driving improvements to the Fischer-Tropsch process.[18]

Figure 1.2. Summary of industrial processes for the hydrogenation of (**A**) N_2 and (**B**) CO to reduced products

For both of these systems, an additional parallel can be drawn between their mechanisms, which have been elucidated through detailed studies. In both the Haber-Bosch[19] and Fischer-Tropsch[16] processes, complete scission of the strong N≡N and C≡O bonds at the catalyst surface initiates reduction of these species. Surface hydrides generated by activation of H_2 combine with surface nitrides or carbides to generate C-H and N-H bonds as these substrates are reduced, ultimately toward the release of their terminal products.

1.3 Why Molecular Model Chemistry?

The chemistry detailed in this thesis bears, at best, a passing resemblance to the processes outlined in the above sections. The advantage well-defined molecular systems

provide when compared to enzymatic and heterogeneous systems is exquisite control over structure and, often, more practical methods for detailed spectroscopic and mechanistic studies. This allows for an understanding of their reactivity on an atomic level, which can be challenging, if not impossible, in studies of biological or heterogeneous catalyst systems. Ideally, these advantages in model systems can be applied to improve conceptually related processes in real systems. To this end, the reactivity targeted in my dissertation aims primarily to access unusual structure types and develop novel reactivity on late first row transition metal platforms.

1.4 Transition Metal Hydrides in Small Molecule Transformations

As outlined above, for both biological and industrial systems that mediate the reduction of CO and N_2, Fe-H intermediates appear to play a critical role. Despite this, well-defined molecular systems where CO and N_2 reduction can be accessed by leveraging transition metal hydride precursors are limited, especially where only Fe-based systems are considered.[20,21] This section introduces in some detail existing molecular systems where metal hydrides are involved in N_2 and CO reductions and underscores existing limitations in this chemistry.

1.4.1 Transition Metal Hydrides in Molecular CO Reduction Chemistry

The most obvious and simple pathway for the reduction of CO by M-hydride precursors is *via* migratory insertion to generate a formyl complex. While this step is ubiquitous for the generation of M-acyls from M-alkyl precursors, migratory insertion steps for M-H are typically thermodynamically disfavored.[22] As a matter of fact, to our knowledge, a single system is known that is able to access a reversible migratory insertion process from a hydride precursor, in this case generating an η^2-formyl adduct of Th upon CO addition.[23] In general, for late transition metal systems applied in reductive CO chemistry, disfavored migratory insertion steps are believed to be a key limitation.

Early transition metal hydride systems that are able to access well-defined CO reduction reactivity been described, with spontaneous C-H bond forming steps driven in these cases by the formation of strong M-O bonds. In an early example developed by Bercaw and coworkers, zirconocene dihydride systems were explored for their ability to promote C-H bond formation and C-C coupling reactivity (Scheme 1.1A).[24] Wolczanski and coworkers developed related transformations for bimetallic Ta_2 systems, in which they

demonstrated the accessibility of C-H bond formation, C≡O cleavage, and C-C coupling reactivity upon CO addition to [(^{t}Bu$_3$SiO)$_2$Ta(H)$_2$]$_2$ (Scheme 1.1B).[25] Though remarkable in their own right, the prerequisite formation of strong M-O bonds in these systems is an inherent limitation preventing catalysis for early transition metal systems where these reactivity patterns are readily accessed.[26]

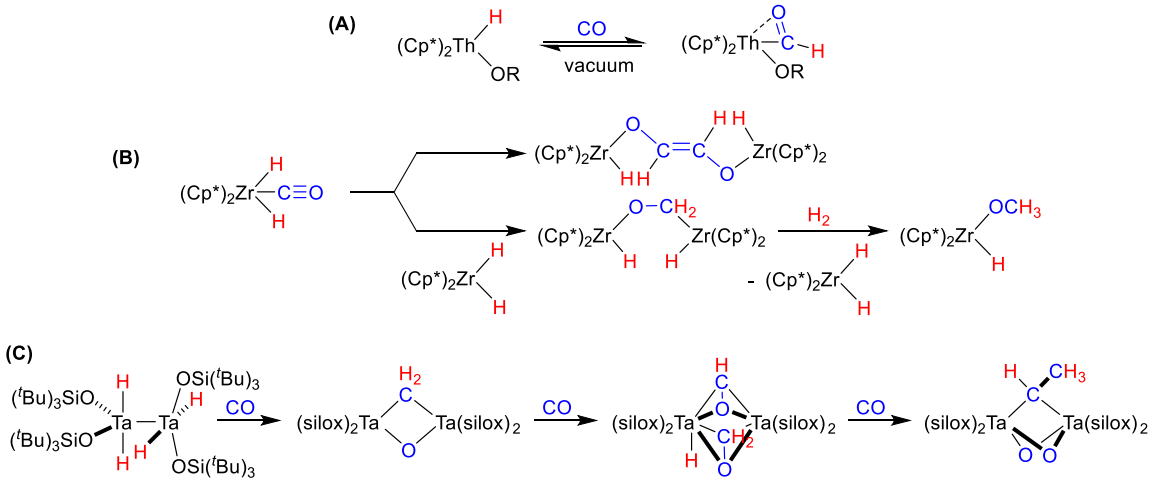

Scheme 1.1. A) Reversible CO migratory insertion into a Th-H complex. Reactivity of Zr (**B**) and Ta (**C**) systems that mediate the reduction of CO from metal hydride precursors.

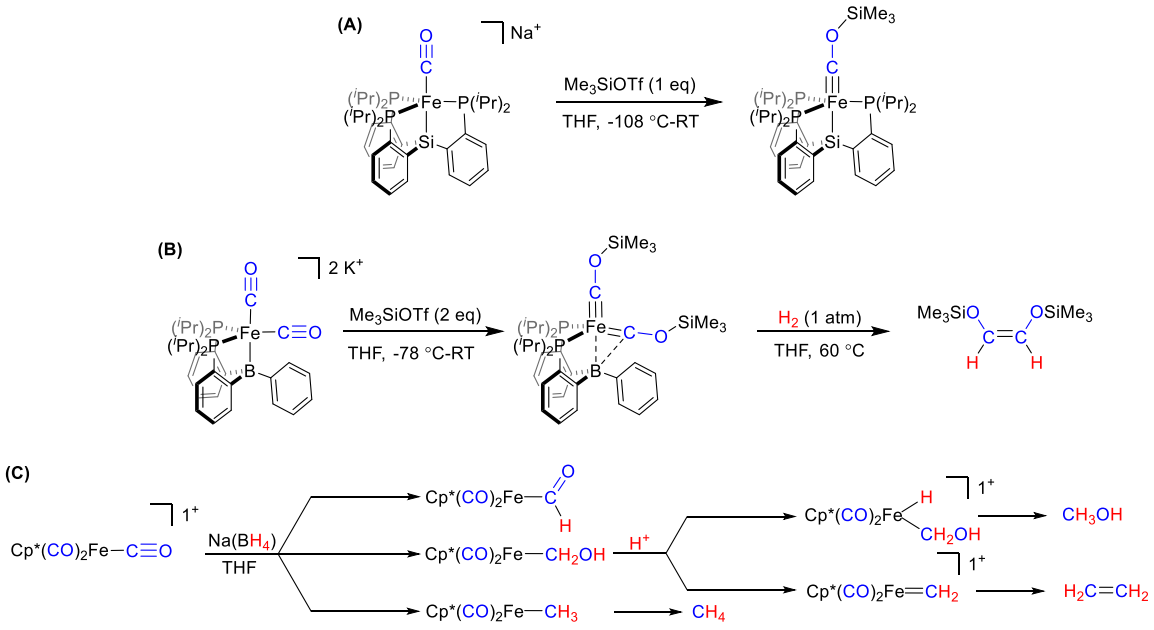

Scheme 1.2. Representative examples of Fe-mediated transformations of CO including (**A**) O-functionalization, (**B**) C-C coupling, and (**C**) main group hydride reactivity.

For Fe-based systems, aspects of CO reductive functionalization have been modeled and include O-functionalization[27] and C-C coupling reactivity (Scheme

1.2A,B).[28,29] Direct migratory insertion reactivity from late metal hydride precursors, however is not observed and C-H bond forming chemistry typically requires the addition of exogenous hydride donors. A representative series of transformations have been described for [Cp*Fe(CO)$_3$][PF$_6$], through which the addition of hydride and proton equivalents can provide access to diverse C-H bond forming steps, including with C-O bond cleavage and C-C coupling steps (Scheme 1.2C).[30] Alternative approaches to accessing C-H bond forming reactions by promoting migratory insertion reactivity or using weak hydride donors continue to be of interest. To this end, Lewis acid coordination at O has been shown to activate metal-bound carbonyls toward C-H bond forming chemistry, albeit without evidence for direct insertion reactivity.[31,32]

1.4.2 Transition Metal Hydrides in Molecular N_2 Reduction Chemistry

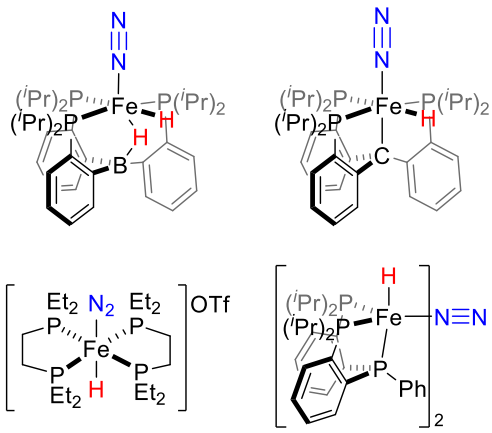

Figure 1.3 Hydride complexes proposed to play a role in limiting catalytic activity and/or selectivity in Fe systems that catalyze N_2 fixation.

In recent decades, molecular chemistry modeling aspects of N_2 fixation by well-defined Fe complexes has been extensively developed,[33,34] including the first molecular Fe catalysts for the reduction of N_2 to NH_3.[35] Like the industrial and biological systems that mediate the reduction of N_2, a role for hydride species also features prominently in molecular Fe systems that catalyze N_2 conversion. In these systems, hydrides are proposed to play a role in promoting catalyst decomposition, sequestering active catalyst material in off-path states, and catalyzing competitive and unproductive hydrogen evolution reactivity (Figure 1.3).[36,37] These observations have led to the demonization of metal hydrides in molecular systems where catalytic N_2 fixation is targeted. A single system has been described that accesses productive N-H bond forming chemistry from a metal hydride

precursor is an unusual $(Cp')_3Ti_3(H)_7$ cluster.[38,39] This trinuclear cluster promotes the complete cleavage of two equivalents of N_2 concurrent with the formation of three new N-H bonds, generating a new trinuclear cluster with each of the symmetric Ti sites bridged by two μ_2-imido and one μ_3-nitrido ligands (Scheme 1.3). Given the obvious distance between these Ti_3 clusters and Fe systems that catalyze N_2 fixation, the development of Fe-based models that are able to access productive N-H bond forming chemistry a compelling stoichiometric target.

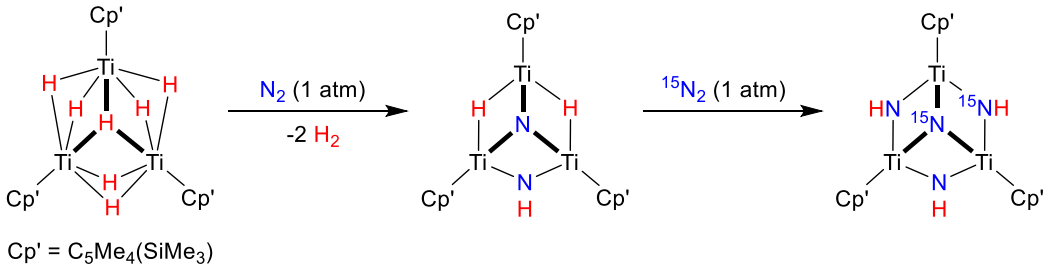

Scheme 1.3 Activation of N_2 by $(Cp')_3Ti_3(H)_7$ clusters.

1.5 Reactivity Profiles of Transition Metal Dihydrogen Adducts

In the above sections, we describe in some detail the chemistry of transition metal hydride complexes and the relevance to the reduction of small molecules. As an extension of the chemistry of dihydrides, studies of their isomeric dihydrogen complexes remain an area of fundamental interest, especially for late, first row transition metal systems. The discovery of Kubas's seminal complex[40] initiated studies in this field and sparked the development of additional systems that stabilize H_2 σ-adducts over their dihydride tautomers. Studies of these σ-adducts largely provide the foundation for our understanding of the bonding and resultant reactivity in H_2 adducts, specifically their ability to serve strictly as acids.[41] This contrasts sharply with the reactivity accessed for transition metal hydrides, where their reactivity patterns are essentially dictated by the hydride-bound transition metal and additional supporting ligands rather than reactivity inherent to "hydrides".[42]

The development of late first row transition metal systems (*i.e.*, Co, Ni) that stabilize non-classical H_2 adducts has only recently gained significant momentum. Over roughly the last decade, several notable examples of first row transition metal H_2 adducts have been discovered; these include previously unknown half-integer spin,[43] anionic,[44] and formally d^{10} dihydrogen adducts[45] (Figure 1.4A,B). It stands to reason that, from a

reactivity standpoint, the distinguishing features of these species might give rise to reactivity that has not previously been explored for σ-adducts. Despite this, reactivity studies for these systems remain underdeveloped. The unique case where the reactivity of one of these species has been examined in detail exhibited the propensity for a radical H_2 adduct to serve as a net H-atom donor (Figure 1.4C).[43 d,e]

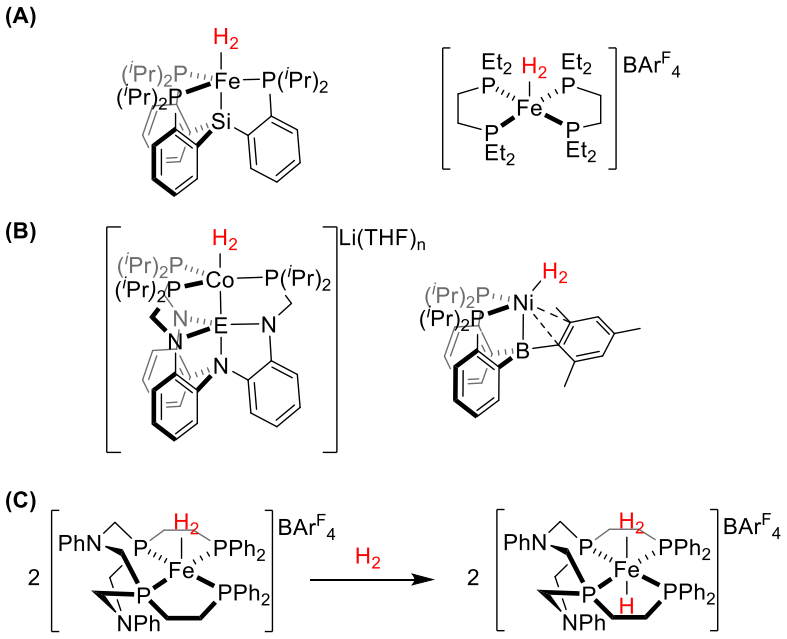

Figure 1.4 Unusual examples of first row transition metal dihydrogen adducts including (**A**) representative examples of doublet species, as well as (**B**) anionic (left) and formally d^{10} dihydrogen adducts. (**C**) Novel reactivity of an $S = ½$ σ-adduct precursor toward net H-atom transfer.

1.6 Chapter Summaries

The above sections contextualize the chemistry detailed in this thesis by introducing relevant enzymatic and industrial processes and highlighting the state-of-the-art in relevant molecular model chemistry. The following two chapters are primarily concerned with the chemistry of highly-reduced $[Fe(CO)(H)_n]^{m-}$ and $[Fe(N_2)(H)_n]^{m-}$ complexes, more specifically the reactivity of these species toward silyl electrophiles and their propensity for accessing hydride migration steps to generate new C-H and N-H bonds. In Chapter 2, the synthesis of a series of Fe carbonyl/hydride complexes supported by a trisphosphine ligand is described. The most reduced of these complexes is amenable to O-functionalization reactivity, which triggers intramolecular hydride migration to form two new C-H bonds and generate a CO-derived $Fe(CH_2OSiMe_3)$ species; labeling studies

confirm that the key C-H bond forming steps are intramolecular. Treating this complex with H_2 or $PhSiH_3$ liberates organic products derived from CO, namely CH_3OSiMe_3 and $PhSiH_2CH_2OSiMe_3$, where CO has undergone net four-electron reduction.

Building on this discovery in CO functionalization chemistry, Chapter 3 extends electrophile-promoted hydride migration reactivity to the transformation of Fe-bound N_2. In this case, the synthesis of a series of dinitrogen/hydride complexes supported by the same trisphosphine ligand is described. The most reduced of these complexes reacts with silyl chloride electrophiles; in this case, monofunctionalization of the most reduced complex yields a terminal diazenido complex that retains both of its hydride ligands. Difunctionalization of the same reduced precursor promotes hydride migration and the formation of a new N-H bond to generate a hydrazido(1-) species that can be stabilized upon trapping with an isocyanide ligand. The intermediate hydrazido(2-) species is stable at low temperature, which allows for detailed kinetic study of the unusual N-H bond forming step and the determination of Eyring parameters for this transformation.

In Chapter 4, the synthesis of a series of Co(CO) complexes supported by a distinct trisphosphine ligand framework is described. The most activated of the Co-bound carbonyl ligands is amenable to O-functionalization with silyl-triflate electrophiles to generate a terminal cobalt carbyne. While this type of reactivity had been described for the synthesis of metal carbyne complexes of the mid transition elements, this is the first case where this reactivity could be demonstrated beyond the group 8 elements. The cobalt carbyne complex generated upon O-functionalization is a quite unusual example of a late transition metal carbyne. In this context, we consider the electronic structure of this species and compare its electronic structure to related imido and oxo complexes.

In Chapter 5, the reactivity of a unique redox pair of a neutral radical and anionic $Co(H_2)$ adducts is described. Like certain transition metal hydride radicals, the doublet dihydrogen adduct serves as a precursor to net H-atom transfer reactivity. Moving to the one-electron reduced anionic H_2 complex, the exceptional thermodynamic hydricity of this species is demonstrated, and it is observed to be competent for hydride transfer to BEt_3 to generate an equivalent of $KHBEt_3$; this is a unique case where a dihydrogen complex has been shown to serve as a hydride donor. Given the unusual nature of these reactions, thermodynamic and kinetic considerations for these transformations are discussed,

particularly with respect to preferred pathways for accessing the H-atom and hydride transfer for these and closely related systems.

For the final chapter of this thesis, we outline our synthetic efforts targeting the synthesis of a terminal Fe-carbide complex derived from thiocarbonyl cleavage chemistry. Over the course of this chapter, we describe the synthesis of a number of Fe-thiocarbonyl complexes supported by trisphosphine ligand frameworks. For one of these systems, S-functionalization allows for the generation of a series of three thiocarbyne complexes. In this chapter we also describe an unusual C-S bond cleavage reaction that, in this case, circumvents the generation of a terminal Fe-carbide. This chapter touches on additional and ultimately unsuccessful approaches we have explored to the generation of CS-derived carbide complexes on these platforms.

1.7 Notes and References

(1) Deegan, M. M.; Peters, J. C. *J. Am. Chem. Soc.* **2017**, *139*, 2561-2564.

(2) Deegan, M. M.; Peters, J. C. *Chem. Commun.* **2019**, *55*, 9531-9534.

(3) Deegan, M. M.; Peters, J. C. *Chem. Sci.* **2018**, *9*, 6264-6270.

(4) (a) Smil, V. *Enriching the Earth*; MIT Press: Cambridge, 2001. (b) Chen, J. G.; Crooks, R. M.; Seefeldt, L. C.; Bren, K. L.; Bullock, R. M.; Darensbourg, M. Y.; Holland, P. L.; Hoffman, B.; Janik, M. J.; Jones, A. K.; Lancaster, K. M.; Lymar, S. V.; Pfromm, P.; Schneider, W. F.; Schrock, R. R. *Science* **2018**, *360*, eaar6611.

(5) For reviews of nitrogenase chemistry, see: (a) Howard, J. B.; Rees, D. C. *Chem. Rev.* **1996**, *96*, 2965-2982; (b) Burgess, B. K.; Lowe, D. J. *Chem. Rev.* **1996**, *96*, 2983-3012; (c) Hoffman, B. M.; Lukoyanov, D.; Yang, Z.-Y.; Dean, D. R.; Seefeldt, L. C. *Chem. Rev.* **2014**, *114*, 4041-4062.

(6) (a) Hoeke, V.; Tociu, L.; Case, D. A.; Seefeldt, L. C.; Raugei, S.; Hoffman, B. M. *J. Am. Chem. Soc.* **2019**, *141*, 11984-11996. (b) Lukoyanov, D. A.; Khadka, N.; Yang, Z.-Y.; Dean, D. R.; Seefeldt, L. C.; Hoffman, B. M. *Inorg. Chem.* **2018**, *57*, 6847-6852. (c) Lukoyanov, D.; Yang, Z.-Y.; Duval, S.; Danyal, K.; Dean, D. R.; Seefeldt, L. C.; Hoffman, B. M. *Inorg. Chem.* **2014**, *53*, 3688-3693.

(7) Morrison, C. N.; Spatzal, T.; Rees, D. C. *J. Am. Chem. Soc.* **2017**, *139*, 10856-10862.

(8) (a) Lukoyanov, D.; Khadka, N.; Yang, Z.-Y.; Dean, D. R.; Seefeldt, L. C.; Hoffman, B. M. *J. Am. Chem. Soc.* **2016**, *138*, 10674-10683. (b) Lukoyanov, D.; Khadka, N.; Dean, D. R.; Raugei, S.; Seefeldt, L. C.; Hoffman, B. M. *Inorg. Chem.* **2017**, *56*, 2233-2240. (c)

Lukoyanov, D.; Yang, Z.-Y.; Khadka, N.; Dean, D. R.; Seefeldt, L. C.; Hoffman, B. M. *J. Am. Chem. Soc.* **2015**, *137*, 3610-3615.

(9) Hoffman, B. M.; Lukoyanov, D.; Dean, D. R.; Seefeldt, L. C. *Acc. Chem. Res.* **2013**, *46*, 587-595.

(10) (a) Simpson, F. B.; Burris, R. H. *Science* **1984**, *224*, 1095−1097. (b) Schubert, K. R.; Evans, H. J. *Proc. Natl. Acad. Sci. U. S. A.* **1976**, *73*, 1207−1211.

(11) (a) Sippel, D.; Rohde, M.; Netzer, J.; Trncik, C.; Gies, J.; Grunau, K.; Djurdjevic, I.; Decamps, L.; Andrade, S. L. A.; Einsle, O. *Science* **2018**, *359*, 1484-1489. (b) Benediktsson, B.; Thorhallsson, A. T.; Bjornsson, R. *Chem. Commun.* **2018**, *54*, 7310-7313. (c) Rohde, M.; Sippel, D.; Trncik, C.; Andrade, S. L. A.; Einsle, O. *Biochemistry* **2018**, *57*, 5497-5504.

(12) (a) Lee, C. C.; Hu, Y.; Ribbe, M. W. *Science* **2010**, *329*, 642. (b) Lee, C. C.; Fay, A. W.; Weng, T.-C.; Krest, C. M.; Hedman, B.; Hodgson, K. O.; Hu, Y.; Ribbe, M. W. *Proc. Natl. Acad. Sci.* **2016**, *112*, 13845-13849.

(13) (a) Hu, Y.; Lee, C. C.; Ribbe, M. W. *Science* **2011**, *333*, 753-755. (b) Yang, Z. Y.; Dean, D. R.; Seefeldt, L. C. *J. Biol. Chem.* **2011**, *286*, 19417-19421. (c) Lee, C. C.; Tanifuji, K.; Newcomb, M.; Liedtke, J.; Hu, Y.; Ribbe, M. W. *ChemBioChem* **2018**, *19*, 649-653.

(14) Spatzal, T.; Perez, K. A.; Einsle, O.; Howard, J. B.; Rees, D. C. *Science* **2014**, *345*, 1620-1623.

(15) (a) Lee, C. C.; Hu, Y.; Ribbe, M. W. *Angew. Chem. Int. Ed.* **2012**, *51*, 1947-1949. (b) Lee, C. C.; Hu, Y.; Ribbe, M. W. *Angew. Chem. Int. Ed.* **2015**, *54*, 1219-1222.

(16) Rofer-DePoorter, C. K. *Chem. Rev.* **1981**, *81*, 447-474.

(17) Erisman, J. W.; Sutton, M. A.; Galloway, J.; Klimont, Z.; Winiwarter, W. *Nat. Geosci.* **1**, 636-639.

(18) Casci, J. L.; Lok, C. M.; Shannon, M. D. *Catal. Today* **2009**, *145*, 38-44.

(19) (a) Ertl, G. *J. Vac. Sci. Technol., A* **1983**, *1*, 1247-1253. (b) Ertl, G. *Angew. Chem., Int. Ed.* **2008**, *47*, 3524-3535.

(20) For a recent review of M-N_2/H_n chemistry, see: Shima, T.; Hou, Z. *Top. Organomet. Chem.* **2017**, *60*, 23-43.

(21) For a review of Fischer-Tropsch model chemistry, see: West, N. M.; Miller, A. J. M.; Labinger, J. A.; Bercaw, J. E. *Coord. Chem. Rev.* **2011**, *255*, 881.

(22) (a) Berke, H.; Hoffman, R. *J. Am. Chem. Soc.* **1978**, *100*, 7224. (b) Ziegler, T.; Versluis, L.; Tschinke, V. *J. Am. Chem. Soc.* **1986**, *108*, 612.

(23) Fagan, P. J.; Moloy, K. G.; Marks, T. J. *J. Am. Chem. Soc.* **1981**, *103*, 6959.

(24) (a) Manriquez, J. M.; McAlister, D. R.; Sanner, R. D.; Bercaw, J. E. *J. Am. Chem. Soc.* **1976**, *98*, 6733-6735. (b) Wolczanski, P. T.; Bercaw, J. E. *Acc. Chem. Res.* **1980**, *13*, 121-127.

(25) (a) LaPointe, R. E.; Wolczanski, P. T.; Mitchell, J. F. *J. Am. Chem. Soc.* **1986**, *108*, 6382-6384. (b) Toreki, R.; LaPointe, R. E.; Wolczanski, P. T. *J. Am. Chem. Soc.* **1987**, *109*, 7558-7560.

(26) For an additional, more recent systems that demonstrates C-O bond cleavage and C-C coupling reactivity, see: (a) Buss, J. A.; Agapie, T. *Nature* **2016**, *529*, 72-75. (b) Buss, J. A.; Agapie, T. *J. Am. Chem. Soc.* **2016**, *138*, 16466-16477.

(27) Lee, Y.; Peters, J. C. *J. Am. Chem. Soc.* **2011**, *133*, 4438-4446.

(28) Suess, D. L. M.; Peters, J. C. *J. Am. Chem. Soc.* **2013**, *135*, 12580-12583.

(29) For related transformations in group 5 systems, see: (a) Bianconi, P. A.; Williams, I. D.; Engeler, M. P.; Lippard, S. J. *J. Am. Chem. Soc.* **1986**, *108*, 311-313. (b) Bianconi, P. A.; Vrtis, R. N.; Rao, C. P.; Williams, I. D.; Engeler, M. P.; Lippard, S. J. *Organometallics* **1987**, *6*, 1968-1977. (c) Protasiewicz, J. D.; Lippard, S. J. *J. Am. Chem. Soc.* **1991**, *113*, 6564-6570. (d) Carnahan, E. M.; Protasiewicz, J. D.; Lippard, S. J. *Acc. Chem. Res.* **1993**, *26*, 90-97.

(30) (a) Lapinte, C.; Catheline, D.; Astruc, D. *Organometallics* **1988**, *7*, 1683-1691. (b) Cutler, A. R.; Hanna, P. K.; Vites, J. C. *Chem. Rev.* **1988**, *88*, 1363-1403.

(31) (a) Miller, A. J. M.; Labinger, J. A.; Bercaw, J. E. *J. Am. Chem. Soc.* **2008**, *130*, 11874-11875. (b) Miller, A. J. M.; Labinger, J. A.; Bercaw, J. E. *J. Am. Chem. Soc.* **2010**, *132*, 3301-3303.

(32) (a) Labinger, J. A.; Miller, J. S. *J. Am. Chem. Soc.* **1982**, *104*, 6856-6858. (b) Grimmett, D. L.; Labinger, J. A.; Bonfiglio, J. N.; Masuo, S. T.; Shearin, E.; Miller, J. S. *J. Am. Chem. Soc.* **1982**, *104*, 6858-6859.

(33) For examples from our group, see: (a) Betley, T. A.; Peters, J. C. *J. Am. Chem. Soc.* **2003**, *125*, 10782-10783. (b) Lee, Y.; Mankad, N. P.; Peters, J. C. *Nature Chem.* **2010**, *2*, 558-565. (c) Moret, M.-E.; Peters, J. C. *Angew. Chem. Int. Ed.* **2011**, *50*, 2063-2067. (d) Moret, M.-E.; Peters, J. C. *J. Am. Chem. Soc.* **2011**, *133*, 18118-18121. (e) Anderson, J. S.; Moret, M.-E.; Peters, J. C. *J. Am. Chem. Soc.* **2013**, *135*, 534-537. (f) Anderson, J. S.; Cutsail III, G. E.; Rittle, J.; Connor, B. A.; Gunderson, W. A.; Zhang, L.; Hoffman, B. M.; Peters. J. C. *J. Am. Chem. Soc.* **2015**, *137*, 7803-7809. (g) Rittle, J.; Peters, J. C. *J. Am. Chem. Soc.* **2016**, *138*, 4243-4248. (h) Thompson, N. B.; Green, M. T.; Peters, J. C. *J. Am.*

Chem. Soc. **2017**, *139*, 15312-15315. (i) Nesbit, M. A.; Oyala, P. H.; Peters, J. C. *J. Am. Chem. Soc.* **2019**, *141*, 8116-8127.

(34) For additional examples, see: (a) Rodriguez, M. M.; Bill, E.; Brennessel, W. W.; Holland, P. L. *Science* **2011**, *334*, 780-783. (b) Grubel, K.; Brennessel, W. W.; Mercado, B. Q.; Holland, P. L. *J. Am. Chem. Soc.* **2014**, *136*, 16807-16816. (c) MacLeod, K. C.; McWilliams, S. F.; Mercado, B. Q.; Holland, P. L. *Chem. Sci.* **2016**, *7*, 5736-5746. (d) McWilliams, S. F.; Holland, P. L. *Acc. Chem. Res.* **2015**, *48*, 2059-2065.

(35) Anderson, J. S.; Rittle, J.; Peters, J. C. *Nature* **2013**, *501*, 84-87.

(36) (a) Creutz, S. E.; Peters, J. C. *J. Am. Chem. Soc.* **2014**, *136*, 1105-1115. (b) Del Castillo, T. J.; Thompson, N. B.; Peters, J. C. *J. Am. Chem. Soc.* **2016**, *138*, 5341-5350. (c) Buscagan, T. M.; Oyala, P. H.; Peters, J. C. *Angew. Chem. Int. Ed.* **2017**, *56*, 6921-6926. (d) Schild, D. J.; Peters, J. C. *ACS Catal.* **2019**, *9*, 4286-4295.

(37) For additional Fe-based N_2 fixation catalysts, see: (a) Ung, G.; Peters, J. C. *Angew. Chem. Int. Ed.* **2015**, *54*, 532-535. (b) Kuriyama, S.; Arashiba, K.; Nakajima, K.; Matsuo, Y.; Tanaka, H.; Ishii, K.; Yoshizawa, K.; Nishibayashi, Y. *Nat. Comm.* **2016**, *7*, 12181. (c) Hill, P. J.; Doyle, L. R.; Crawford, A. D.; Myers, W. K.; Ashley, A. E. *J. Am. Chem. Soc.* **2016**, *138*, 13521-13524.

(38) Shima, T.; Hu, S.; Luo, G.; Kang, X.; Hou, Z. *Science* **2013**, *340*, 1549-1552.

(39) Conceptually related chemistry has been described for the reduction of N_2 upon the addition of H_2 (or silanes) to N_2 and N_2-derived species. For select examples, see: (a) Fryzuk, M. D.; Love, J. B.; Rettig, S. J.; Young, V. G. *Science* **1997**, *275*, 1445-1447. (b) Pool, J. A.; Lobovsky, E.; Chirik, P. J. *Nature* **2004**, *427*, 527-530. (c) Fryzuk, M. D. *Acc. Chem. Res.* **2009**, *42*, 127-133. (d) Wang, B.; Luo, G.; Nishiura, M.; Hu, S.; Shima, T.; Luo, Y.; Hou, Z. *J. Am. Chem. Soc.* **2017**, *139*, 1818-1821. (e) Suess, D. L. M.; Peters, J. C. *J. Am. Chem. Soc.* **2013**, *135*, 4938-4941. (f) Liao, Q.; Cavaillé, A.; Saffon-Merceron, N.; Mézailles, N. *Angew. Chem. Int. Ed.* **2016**, *55*, 11212-11216.

(40) Kubas, G. J.; Ryan, R. R.; Swanson, B. I.; Vergamini, P. J.; Wasserman, H. J. *J. Am. Chem. Soc.* **1984**, *106*, 451-452.

(41) For reviews, see: (a) Kubas, G. J. Metal Dihydrogen and σ-bond Complexes; Kluwer/ Plenum: New York, 2001. (b) Kubas, G. J. *Chem. Rev.* **2007**, *107*, 4152-4205. (c) Crabtree, R. H. *Chem. Rev.* **2016**, *116*, 8750-8769. (d) Jessop, P. G.; Morris, R. H. *Coord. Chem. Rev.* **1992**, *121*, 155-284.

(42) For reviews of various modes of reactivity for transition metal hydrides, see: (a) Morris, R. H. *Chem. Rev.* **2016**, *116*, 8588-8654. (b) Hu, Y.; Shaw, A. P.; Estes, D. P.; Norton, J. R. *Chem. Rev.* **2016**, *116*, 8427-8462. (c) Eisenberg, D. C.; Norton, J. R. *Isr. J. Chem.* **1991**, *31*, 55-66. (d) Wiedner, E. S.; Chambers, M. B.; Pitman, C. L.; Bullock, R. M.; Miller, A. J. M.; Appel, A. M. *Chem. Rev.* **2016**, *116*, 8655-8692.

(43) (a) Lee, Y.; Kinney, R. A.; Hoffman, B. M.; Peters, J. C. *J. Am. Chem. Soc.* **2011**, *133*, 16366-16369. (b) Suess, D. L. M.; Tsay, C.; Peters, J. C. *J. Am. Chem. Soc.* **2012**, *134,* 14158-14164. (c) Gunderson, W. A.; Suess, D. L. M.; Fong, H.; Wang, X.; Hoffman, C. M.; Cutsail III, G. E.; Peters, J. C.; Hoffman, B. M. *J. Am. Chem. Soc.* **2014**, *136*, 14998-15009. (d) Doyle, L. R.; Scott, D. J.; Hill, P. J.; Fraser, D.; Myers, W.; White, A. J. P.; Green, J.; Ashley, A. E. *Chem. Sci.* **2018**, *9*, 7362-7369. (e) Prokopchuk, D. E.; Chambers, G. M.; Walter, E. D.; Mock, M. T.; Bullock, R. M. *J. Am. Chem. Soc.* **2019**, *141*, 1871-1876.

(44) Vollmer, M. V.; Xie, J.; Lu, C. C. *J. Am. Chem. Soc.* **2017**, *139*, 6570-6573.

(45) (a) Harman, W. H.; Lin, T.-P.; Peters, J. C. *Angew. Chem. Int. Ed.* **2014**, *53*, 1081-1086. (b) Cammarota, R. C.; Lu, C.C. *J. Am. Chem. Soc*. **2015**, *137*, 12486–12489. (c) Cammarota, R. C.; Xie, J.; Burgess, S. A.; Vollmer, M. V.; Vogiatzis, K. D.; Yem J.; Linehan, J. C.; Appel, A. M.; Hoffmann, C.; Wang, X.; Young, V. G.; Lu, C. C. *Chem. Sci.* **2019**, *10*, 7029-7042.

Chapter 2

CO REDUCTION TO CH_3OSiMe_3: ELECTROPHILE-PROMOTED HYDRIDE MIGRATION AT A SINGLE IRON SITE

2.1 Introduction

In the industrial Fischer-Tropsch (FT) process, pressurized mixtures of CO and H_2 are heated over a heterogeneous transition metal catalyst, most commonly Fe or Co, to yield a mixture of liquid organic products.[1] Interestingly, it was recently demonstrated that nitrogenase enzymes also facilitate some degree of FT reactivity, with H equivalents provided as protons and electrons.[2] Well-defined model complexes can be used to explore viable pathways for mechanistically relevant CO reductions under controlled reaction conditions. In particular, Fe-mediated model systems are of interest owing to iron's role in both industrial and (presumably) biological FT systems.

One of the major challenges associated with molecular CO reduction reactivity is early stage C-H bond formation from H_2.[3] Migratory insertion of CO into M-H bonds is generally presumed to be thermodynamically unfavorable.[4,5] For early transition metal systems, C-H bond formation is concomitant with strong M-O bond formation.[6] Mid-to-late transition metal systems are thought to lack this driving force, and C-H bond forming steps have instead been established using strong hydride donors that are not generated from H_2.[7,8] Recently, it has been demonstrated that weaker, H_2-derived hydride sources can be used to facilitate C-H bond formation from H_2 in Lewis acid-activated Re-CO complexes.[9,10] C-H bond formation in this latter case is driven by the formation of strong B-O bonds.

Our group has previously studied reduced Fe-CO complexes that react with silyl electrophiles at oxygen to generate carbyne products (*e.g.*, $Fe\text{-}CO^- + SiMe_3^+ \rightarrow Fe{\equiv}C\text{-}OSiMe_3$).[11] We wondered whether related O-functionalization at reduced $Fe(CO)(H)_n$ species might promote concomitant hydride migration to carbon. Herein, we describe the synthesis of a series of reduced $Fe(CO)(H)_n$ complexes. One of these complexes serves as a key intermediate from which functionalization of the coordinated CO promotes the migration of two hydride equivalents to carbon.

2.2 Results and Discussion

2.2.1 Synthesis of $[Fe(CO)(H)_n]^{m-}$ Complexes

In this study we employ the P_3^BFe-system[12] ($P_3^B = B(o\text{-}^iPr_2PC_6H_4)_3$)[13], for which its monocarbonyl complex, P_3^BFe-CO, was previously shown to activate H_2 to generate $P_3^B(\mu\text{-}H)Fe(H)(CO)$, **2.1**.[14] Two-electron reduction of **2.1** can be readily accomplished with excess potassium metal in THF, leading to a distinct color change from yellow to dark red-brown. NMR spectroscopy reveals that a new diamagnetic species, **2.2**, is cleanly generated, with hydridic resonances observed in the ^1H NMR spectrum at -19.12 ppm (B-*H*-Fe, br, 1H) and -20.76 ppm (Fe-*H*, t, $^2J_{HP}$ = 65 Hz, 1H). The ^{31}P NMR spectrum has two resonances at 102.3 and -1.5 ppm (2:1 integration), indicating that one of the phosphine arms has dechelated from the Fe center, while the thin film IR spectrum of **2.2** indicates a highly activated CO ligand with a stretch at 1575 cm^{-1}. Structural characterization of dianionic **2.2** confirms that the product has two coordinated phosphine ligands and the CO ligand in an approximate trigonal geometry (average ∑(trigonal plane) = 359.52),[15] with the axial sites presumably occupied by the hydride and borohydride ligands that are not crystallographically observed (Figure 1). Among Fe-CO complexes, **2.2** has an unusually short Fe-C distance (1.70 Å; average) with corresponding elongation of the C-O bond (1.24 Å; average), consistent with significant contribution of carbyne character in this species. For relevant comparison, P_3^BFe-CO (ν(CO) = 1857 cm^{-1}) has an Fe-C distance of 1.75 Å and a C-O distance of 1.17 Å,[12] while the carbyne complex $P_3^{Si}Fe{\equiv}C\text{-}OSiMe_3$ has an Fe-C distance of 1.67 Å and a C-O distance of 1.28 Å.[11a]

A number of structurally unusual reduced hydride species are readily available from **2.2**. For example, complex **2.2** can be protonated selectively by water *via* addition of wet N_2 (produced by bubbling N_2 through water) yielding the anionic trihydride complex $[P_3^B(\mu\text{-}H)Fe(H)_2(CO)][K(THF)_n]$, **2.3**. NMR spectroscopy reveals inequivalent ^{31}P NMR resonances at 106.7 and -9.6 ppm (2:1 integration) and three hydridic resonances in the ^1H NMR spectrum at -8.40 ppm (Fe-*H*, td, $^2J_{HP}$ = 66 Hz, $^2J_{HH}$ = 16 Hz, 1H), -14.69 ppm (B-*H*-Fe, br, 1H), and -20.53 ppm (Fe-*H*, t, $^2J_{HP}$ = 48 Hz, 1H). An IR stretch is observed for Fe-ligated CO at 1787 cm^{-1}. The coordinated phosphine ligands are located *trans* to one

another in the solid state, with one of the terminal hydride ligands *trans* to the terminal CO (Figure 1).[16]

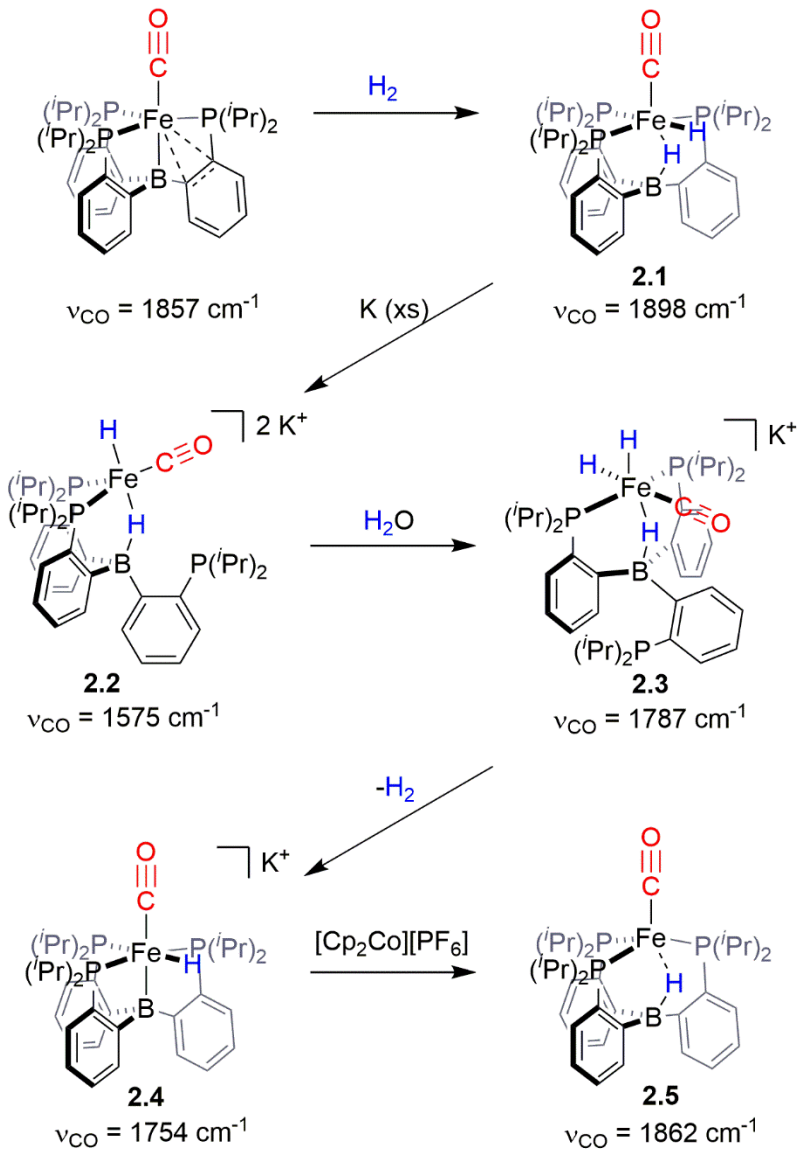

Scheme 2.1. Synthesis of $P_3^BFe(CO)(H)_n$ complexes.

The trihydride complex **2.3** is unstable to the loss of H_2 in solution, with clean, irreversible conversion to the anionic and diamagnetic monohydride complex $[P_3^BFe(H)(CO)][K(THF)_n]$, **2.4**, observed over 2 d (ν(CO) = 1754 cm^{-1}; see SI for NMR details). In the solid state, **2.4** adopts an approximately octahedral geometry, with the hydride ligand located in the difference map as a terminal Fe-H (Figure 1). Oxidation of **2.4** using $[Cp_2Co][PF_6]$ generates the doublet product $(P_3^B\text{-}H)Fe(CO)$, **2.5**, featuring a broad, axial EPR signal at 77 K. The IR spectrum of **2.5** shows an intense CO stretch at

1862 cm^{-1} and a broad hydride stretch at 2588 cm^{-1}, consistent with a boron-coordinated hydride, as revealed in its solid-state structure (Figure 1).

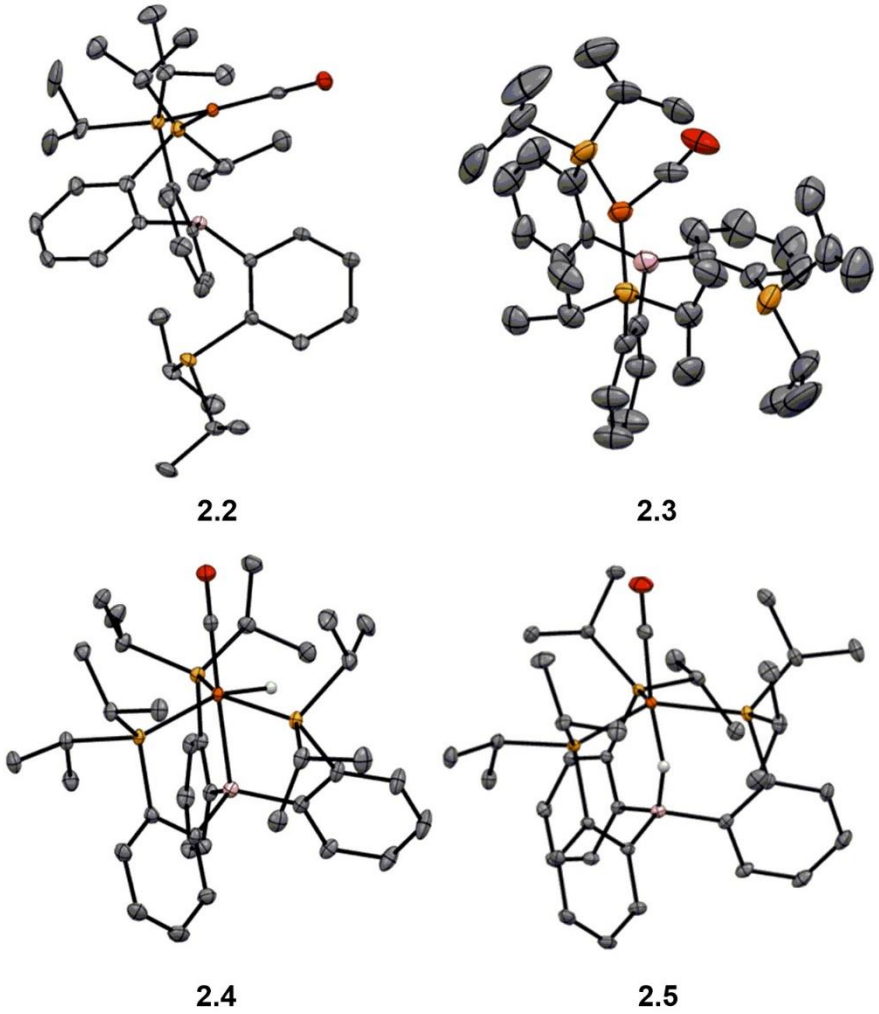

Figure 2.1 Crystal structures of $Fe(CO)(H)_n$ complexes **2.2**-**2.5**. Displacement ellipsoids shown at 50% probability; hydrogen atoms (except for hydride ligands located in the difference map), solvent molecules, counter cations, and disorder of **2.3** omitted for clarity.

2.2.2 O-Functionalization Reactivity with Silyl-Electrophiles

With these complexes in hand, we next canvassed their reactivity with electrophiles. Accordingly, *in situ* generation of a THF solution of dianion **2.2** followed by treatment with at least two equivalents of Me_3SiOTf at low temperature generates a new paramagnetic species, $P_3^BFe\text{-}CH_2OSiMe_3$, **2.6**, as the major product (Scheme 2.2).[17] Mössbauer spectroscopy indicates that **2.6** is generated in ~80% chemical yield and its parameters (δ = 0.49 mm/s; ΔE_Q = 2.05 mm/s) are consistent with an S = 3/2 P_3^BFe

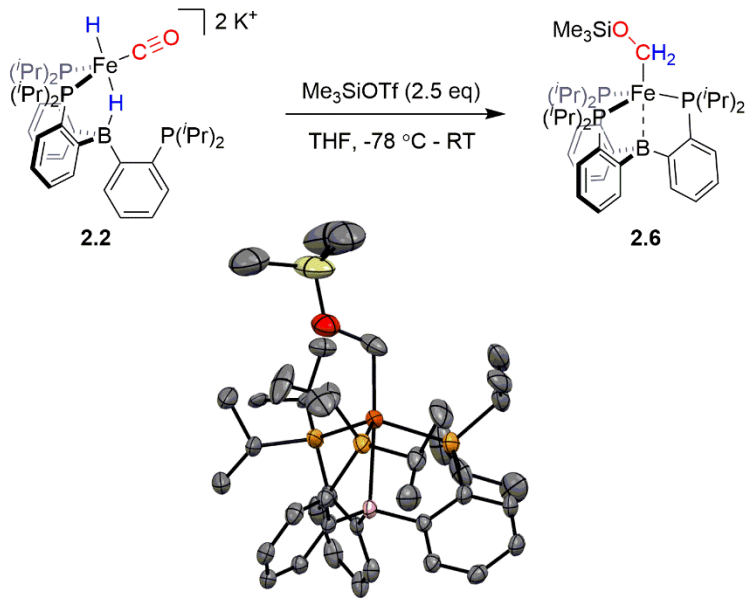

Scheme 2.2. Reaction of **2.2** with 2.5 equiv of Me_3SiOTf and the crystal structure of the reaction product **2.6**. Ellipsoids are shown at 50% probability; solvent and disorder are omitted for clarity.

species.[18] For representative comparison, the previously reported complex P_3^BFe-Me has the following parameters: δ = 0.50 mm/s, ΔE_Q = 1.84 mm/s.[19] Structure determination of **2.6** by XRD analysis confirms its assignment and clearly establishes that the carbonyl ligand has been O-functionalized by the silyl electrophile, with both hydride equivalents having migrated to the carbonyl carbon; one equivalent of electrophile (Me_3Si^+) presumably serves as a one-electron oxidant. Despite repeated attempts, we have been unable to isolate complex **2.6** in analytically pure form owing to its high hydrocarbon solubility. Persistent S = 1/2 Fe-containing impurities that are similarly soluble, including **2.5** as an oxidation side-product, are consistently present in preparative scale, worked-up reactions.[20]

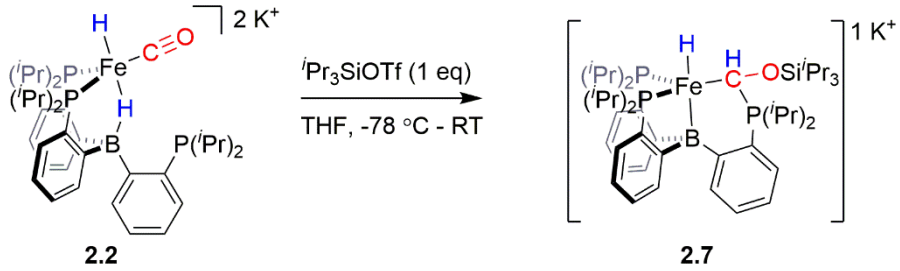

Scheme 2.3 Generation of **2.7** from the reaction of **2.2** with $^iPr_3SiOTf$.

Given the unusual C-H bond forming steps achieved in the conversion from **2.2** to **2.6**, we next targeted the product of CO monofunctionalization. The reaction of the dianionic precursor **2.2** with a bulkier electrophile, $^{i}Pr_3SiOTf$, yielded a single major diamagnetic product **2.7** (Scheme 2.3). Interestingly, only one hydridic resonance is retained in **2.7**, with the growth of an unusual resonance at -0.55 in the ^{1}H NMR spectrum. Isotopic labeling experiments confirm that this signal is derived from one of the original hydride ligands and shows strong coupling to the CO-derived C-atom (127 Hz), consistent with the formation of a new C-H bond in **2.7**. An additional interaction between the CO-derived C and the third phosphine arm of the supporting ligand is proposed based on analysis of the ^{13}C and ^{31}P NMR spectra; attempts to confirm this assignment using structural methods have been unsuccessful.[21] Notably, oxidation of complex **2.7** does not promote the formation of a second C-H bond to generate **2.6**; we speculate that the formation of the P-C bond in **2.7** precludes this reactivity and, therefore, does not serve as an intermediate in the conversion of **2.2** to **2.6**.

2.2.3 Release of CO-Derived Organic Products

We next surveyed conditions for the release of the CO-derived organic fragment.[22] For related P_3^BFe-Me, treatment with acid results in methane release.[19] For complex **2.6**, treatment with acid ($[H(OEt_2)_2][BAr^F]$, [LutH][Cl] and H_2O, for example) invariably results in unproductive decomposition to regenerate $P_3^B(\mu\text{-H})Fe(H)(CO)$, **2.1**, as the major product, presumably *via* acidic cleavage of the Si-O bond.[23] We therefore canvassed the reactivity of **2.6** towards hydrogen and silanes (Scheme 2.4). Treatment of **2.6** with an atmosphere of H_2 at RT results in the release of CH_3OSiMe_3 over 24 h in moderate yields (50%, average of three runs; assumes **2.6** present at 80% purity initially based on Mössbauer analysis; vide supra). Product release can also be affected by the addition of

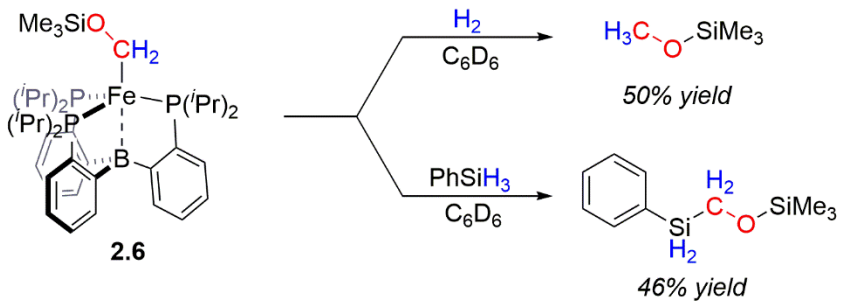

Scheme 2.4. Reactivity of **2.6** with H_2 or $PhSiH_3$ to release CO-derived products.

excess $PhSiH_3$ (5 equiv), with C-Si bond formation in this case and similar yields of the CO-derived product, $PhSiH_2CH_2OSiMe_3$ (46%, average of three runs; again assumes **2.6** present at 80% purity initially). The Fe-containing products of these reactions have not yet been identified; spectroscopic analysis indicates complex mixtures of P_3^BFe-containing products.[24]

To track the origin of the H equivalents delivered to the terminal organic product, CH_3OSiMe_3, upon H_2 addition we undertook a series of labeling studies. These experiments are particularly valuable given our inability to isolate **2.6** in analytically pure form. Use of the dianionic complex **2.2** as a precursor to the alkyl complex **2.6** resulted in full H incorporation into the free organic product, CH_3OSiMe_3 as determined by ^1H NMR spectroscopy (Scheme 2.5A). Likewise, using the ^2H-labeled analog **2.2-D2** to generate **2.6-D2**, followed by treatment with D_2, resulted in (nearly) complete incorporation of deuterium in the released product CD_3OSiMe_3 (Scheme 2.5B; ~5% $CD_2HOSiMe_3$ was also detected). These results suggest that the three H equivalents delivered to the CO C-atom are derived from the hydride ligands and/or the added H_2 gas; scrambling into the alkyl phosphine substituents or incorporation of H-equivalents from solvent, is therefore not kinetically relevant. Interestingly, when **2.6-D2** was treated with an atmosphere of H_2, the partially-deuterated organic products CDH_2OSiMe_3 and $CD_2HOSiMe_3$ were obtained in a 5:1 ratio (Scheme 2.5C). Similarly, when **2.6** was treated with D_2 a mixture of products was observed, with $CD_2HOSiMe_3$ and CDH_2OSiMe_3 obtained in a 3:1 ratio, and ~5% CH_3OSiMe_3 also detected (Scheme 2.5D). These results are suggestive of a facile exchange

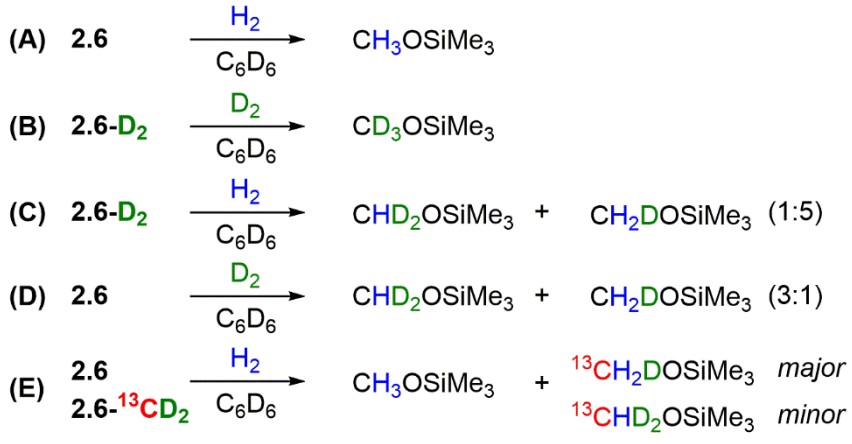

Scheme 2.5. Summary of isotopic labeling experiments.

process between the alkyl C-H bonds and the added H_2 or D_2 prior to product release. One scenario by which such an exchange could occur involves reversible alpha elimination from **2.6-D₂** to generate a carbene-deuteride intermediate (*i.e.*, $P_3^BFe\text{-}CD_2OSiMe_3 \rightleftharpoons P_3^B(\mu\text{-}D)Fe{=}C(D)(OSiMe_3)$) that then reacts with H_2.[25]

To probe the possibility of intermolecular C-H bond forming steps we undertook a crossover experiment wherein the dianionic complex **2.2** was synthesized as a 50:50 mixture of its $[P_3^B(\mu\text{-}D)Fe(D)(^{13}CO)]^{2-}$ and $[P_3^B(\mu\text{-}H)Fe(H)(^{12}CO)]^{2-}$ variants. Standard functionalization of this labeled mixture to generate the corresponding alkyl complexes **2.6**, and product release *via* the addition of H_2, showed deuterium incorporation exclusively in the ^{13}C-labeled complex (Scheme 2.5E). This result is fully consistent with an intramolecular pathway for the initial C-H bond-forming steps to generate the alkyl complex **2.6**, and also the subsequent C-H bond formation from H_2 to promote the release of the organic product.

2.3 Conclusions

To conclude, using a mononuclear iron system we have explored a silyl electrophile promoted hydride-to-CO migration process that allows for the net 4-electron reduction of CO, releasing CH_3OSiMe_3 upon hydrogenolysis. Use of the bifunctional tris(phosphine)borane ligand, P_3^B, is key to the hydride migration step as it helps to stabilize the unusual bis(phosphine)-dihydride-carbonyl precursor, **2**, *via* a bridging interaction of one of the hydride ligands with the borane. Isotopic labeling studies establish that the C-H bond forming steps are unimolecular. Intramolecular hydride-to-CO migrations are extremely rare; to our knowledge the iron system described herein is the first thermally stable M(CO)(H) complex to exhibit such reactivity. Future studies will be aimed at expanding the scope of this reactivity, for example by replacing the silyl electrophile Me_3Si^+ with H^+ as a route to CH_3OH generation.

2.4 Experimental Details

2.4.1 General Considerations

All manipulations were carried out using standard Schlenk or glovebox techniques under an N_2 atmosphere. Solvents were deoxygenated and dried by thoroughly sparging

with N_2 followed by passage through an activated alumina column in a solvent purification system by SG Water, USA LLC. THF was dried further by stirring over Na/K (>2 h) and was filtered through Celite prior to use. Deuterated solvents were purchased from Cambridge Isotope Laboratories, Inc., degassed, and dried over activated 3 Å molecular sieves before use. Reagents were purchased from commercial vendors and used without further purification unless otherwise noted. $P_3^B(\mu\text{-H})Fe(H)(CO)$ **2.1** was prepared according to a literature procedure.[14] Labeled analogs of **2.1** (**2.1-D_2**, **2.1-^{13}CO**, and **2.1-D_2/^{13}CO**) were prepared analogously using ^{13}CO and D_2 gases.

2.4.2 Physical Methods

NMR spectra (^1H, ^{13}C, ^{31}P, ^{11}B, and ^{29}Si) were collected at room temperature (25 °C unless specified) on Varian 300, 400, or 500 MHz spectrometers. ^1H, ^{13}C, and ^{29}Si chemical shifts are reported in ppm, relative to tetramethylsilane using residual proton and ^{13}C resonances from solvent as internal standards. ^{31}P chemical shifts are reported in ppm relative to 85% aqueous H_3PO_4 and ^{11}B spectra were referenced to $BF_3 \bullet Et_2O$. Thin film IR spectra were obtained using a Bruker Alpha Platinum ATR spectrometer with OPUS software in a glovebox under an N_2 atmosphere. UV-vis measurements were collected using a Cary 50 instrument with Cary WinUV software. X-band EPR spectra were obtained on a Bruker EMX spectrometer on solutions prepared as frozen glasses in 2-MeTHF. Spectra were simulated using the EasySpin suite of programs with MatLab. Mössbauer spectra were recorded on a spectrometer from SEE Co. (Edina, MN) operating in the constant acceleration mode in a transmission geometry. The sample was kept in an SVT-400 cryostat from Janis (Wilmington, MA). The quoted isomer shifts are relative to the centroid of the spectrum of a metallic foil of α-Fe at room temperature. Solution samples were prepared by freezing solutions in a Delrin cup in a glovebox with rapid transfer of frozen samples to a liquid nitrogen bath before mounting in the cryostat. Samples were collected with no applied magnetic field unless otherwise specified. Data analysis was performed using the program WMOSS (www.wmoss.org) and quadrupole doublets were fit to Lorentzian lineshapes.

X-Ray diffraction and combustion analysis measurements were carried out in the Beckman Institute Crystallography Facility. XRD measurements were collected using a dual source Bruker D8 Venture, four-circle diffractometer with a PHOTON CMOS

detector. Structures were solved using SHELXT and refined against F^2 on all data by full-matrix least squares with SHELXL. The crystals were mounted on a glass fiber under Paratone N oil. See below for any special refinement details for individual data sets. Combustion analysis measurements were collected using a PerkinElmer 2400 Series II CHN Elemental Analyzer by facility staff.

2.4.3 Synthetic Details

2.4.3.1 $[P_3^B(\mu\text{-H})Fe(H)(CO)][K_2(THF)_n]$ 2.2

A bright yellow THF solution of $P_3^B(\mu\text{-H})Fe(H)(CO)$ **2.1** (18.2 mg, 26.9 μmol) was stirred over an excess of K metal for 2 h becoming very dark red-brown. The solution was decanted away from the K and the solvent was removed. The resulting dark residue was washed with pentane and extracted with THF. The solvent was removed and triturated with Et_2O, yielding the product as a dark powder (17.1 mg). X-Ray quality crystals were grown by vapor diffusion of pentane into a THF/benzene (2:1) solution of the complex. Additional characterization and reactivity studies were carried out with *in situ* generation of this complex (>90% yield by NMR versus PPh_3 internal standard; Mössbauer spectroscopy) because of its facile oxidation. The compound was observed to be stable in sealed solutions over time (J. Young tube; monitored by NMR), but decomposed when attempts were made to store the complex in the glovebox under a nominally inert atmosphere as a solid, even at low temperatures (-35 °C). $^{31}P\{^1H\}$ NMR (THF/C_6D_6; 162 MHz): δ 102.3 (2P), -1.5 (1P). ^1H NMR (THF-d_8; 400 MHz): δ 7.85-7.75 (overlapping m, 3H), 7.25-7.4 (overlapping m, 3H), 7.00-6.75 (overlapping m, 6H), 2.48 (^{i}Pr C*H*, br, 2H) 2.43 (^{i}Pr C*H*, br, 2H), 1.90 (^{i}Pr C*H*, septd, J = 7, 2.3 Hz, 2H) 1.45-0.8 (^{i}Pr CH_3, 36H), -19.12 (B-*H*-Fe, br, 1H), -20.76 (Fe-*H*, t, J = 65 Hz, 1H). $^{11}B\{^1H\}$ NMR (THF-d_8; 128 MHz): δ 2.0. $^{13}C\{^1H\}$ NMR (THF/C_6D_6; 101 MHz; ^{13}CO-labeled): δ 230.7 (br). IR of $[P_3^B(\mu\text{-H})Fe(H)(^{12}CO)][K_2(THF)_n]$ (thin film, cm^{-1}) : ν_{CO} = 1575; $\nu_{Fe\text{-}H}$ = 1760, 1824. IR of $[P_3^B(\mu\text{-H})Fe(H)(^{13}CO)][K_2(THF)_n]$ (thin film, cm^{-1}) : ν_{CO} = 1538. Mössbauer (80 K; frozen THF solution, mm/s): $\delta = 0.09$; $\Delta E_Q = 2.39$.

2.4.3.2 $[P_3^B(\mu\text{-H})Fe(H)_2(CO)][K(THF)_n]$ 2.3

A solution of dianionic **2.2** in THF was generated *in situ* and transferred to a J. Young NMR tube. Concurrently, a stream of wet, O_2-free N_2 was prepared by bubbling N_2

through water over several hours. The headspace of the reaction vessel was evacuated and backfilled with wet N_2 and thoroughly mixed. This process was repeated iteratively (~5x) until the reaction underwent a dramatic color change from very dark red-brown to yellow-orange. This resulted in quantitative conversion to the trihydride complex **2.3** as judged by NMR spectroscopy (versus PPh_3 internal standard). Clean isolation of this species was complicated by its tendency to reductively eliminate H_2, yielding **2.4**. X-Ray quality crystals could be grown by slow evaporation of an Et_2O solution of the complex in a sealed vessel containing HMDSO. $^{31}P\{^1H\}$ NMR (THF-d_8; 162 MHz): δ 106.72 (m, 2P), -9.64 (1P). ^1H NMR (THF-d_8; 400 MHz): 7.31 (Ar C-*H*, 2H), 7.26 (Ar C-*H*, 2H), 7.17 (Ar C-*H*, d, *J* = 7.4 Hz, 1H), 6.79 (Ar C-*H*, overlapping, 5H), 6.64 (Ar C-*H*, t, *J* = 7.3 Hz, 1H), 6.51 (Ar C-*H*, br, 1H), 2.53 (PC-*H*, br, 4H), 1.58 (PC-*H*, br, 2H), 1.31 (C*H*$_3$, dd, *J* = 12, 6.7 Hz, 6H), 1.13 (C*H*$_3$, dq, *J* = 27, 6.6 Hz, 12H), 0.96 (C*H*$_3$, dd, *J* = 12, 6.8 Hz, 6H), 0.67 (C*H*$_3$, ddd, *J* = 19.4, 12.5, 6.9 Hz, 12H), -8.40 (Fe-*H*, td, *J* = 66, 16 Hz, 1H), -14.69 (Fe-*H*-B, br, 1H), -20.53 (t, *J* = 48 Hz, 1H). ^{11}B NMR (THF; 128 MHz): δ -4.15. $^{13}C\{^1H\}$ NMR (THF; 101 Mz; ^{13}CO-labeled): 225.3 (m). IR of $[P_3^B(\mu\text{-H})Fe(H)_2(^{12}CO)][K(THF)_n]$ (thin film, cm^{-1}): ν_{CO} = 1787; $\nu_{Fe\text{-}H}$ = 1826, 1862. IR of $[P_3^B(\mu\text{-H})Fe(H)_2(^{13}CO)][K(THF)_n]$ (thin film, cm^{-1}): ν_{CO} = 1748.

2.4.3.3 $[P_3^BFe(H)(CO)][K(THF)_n]$ 2.4

A solution of **2.2** was generated *in situ* from **2.1** (74 mg, 0.109 mmol) and transferred to a Schlenk tube. From this mixture, **2.3** was generated (*vide supra*), the solution was frozen, the headspace was evacuated and the mixture was stirred at room temperature for 36 h, resulting in the conversion of **2.3** to **2.4** with loss of H_2. The solution was filtered through Celite, the solvent was removed *in vacuo*, and the residue was extracted with THF. The solvent was again removed and the residue was washed with benzene and then extracted with THF, yielding the product as an orange-yellow powder after the THF was removed (82.5 mg, 81% yield). X-Ray quality crystals were grown by vapor diffusion of pentane into a THF/benzene solution of the complex. $^{31}P\{^1H\}$ NMR (THF-d_8; 162 MHz): δ 90.7. ^1H NMR (THF-d_8; 400 MHz): δ 7.25 (d, *J* = 7.4 Hz, 3H), 7.01 (d, *J* = 7.3 Hz, 3H), 6.68 (t, *J* = 7.1 Hz, 3H), 6.51 (t, *J* = 7.1 Hz, 3H), 2.15 (br, 3H), 2.27 (br, 6H), 0.99 (br, 18H), 0.81 (br, 18H) -13.93 (qd, *J* = 47, 7.2 Hz, 1H). $^{11}B\{^1H\}$ NMR (THF-d_8; 128 MHz): δ 12.9. $^{13}C\{^1H\}$ NMR (THF-d_8; 101 MHz; ^{13}CO-labeled): δ 222.2

(m). UV/Vis (THF, nm {M^{-1} cm^{-1}}): 407 {sh}, 344 {8500}. IR of [P_3^BFe(H)(^{12}CO)][K(THF)$_n$] (thin film, cm^{-1}): ν_{CO} = 1754. IR of [P_3^BFe(H)(^{13}CO)][K(THF)$_n$] (thin film, cm^{-1}): ν_{CO} = 1705. Mössbauer (80 K; 2-MeTHF/C_6H_6 solution, mm/s): δ = 0.03; ΔE_Q = 1.28.

2.4.3.4 (P_3^B-H)Fe(CO) 2.5

2.4 (64.9 mg, .076 mmol) was dissolved in THF (4 mL) and cooled to -78 °C. The solution was added to a similarly chilled THF (2 mL) suspension of [Cp_2Co][PF_6] (30.3 mg, .0901 mmol). The mixture was stirred at -78 °C for 5 min, turning red-brown, then at room temperature for an additional 30 min. The solution was filtered, the solvent was removed *in vacuo,* and the resulting brown powder was triturated with Et_2O (5 mL). The product was washed with pentane (3 mL) and then extracted with benzene (5 mL). Lyophilization yielded the product as a brown powder (38.9 mg, 78%). X-Ray quality crystals were grown by slow evaporation of an Et_2O solution of the complex. ^{1}H NMR (C_6D_6; 300 MHz): 13.9, 8.9, 7.4, 5.6, 4.2, 1.3, -0.2. UV/Vis (THF, nm {M^{-1} cm^{-1}}): 865 {300}, 575 {sh}, 495 {800}. Solution magnetic moment (Evans Method; 25 °C): 1.9μ_B. IR of (P_3^B-H)Fe(CO) (thin film, cm^{-1}): ν_{CO} = 1862 cm^{-1}; $\nu_{B\text{-}H}$ = 2588 cm^{-1}. Anal. Calcd for $C_{37}H_{55}BFeOP_3$: C, 65.80; H, 8.21; N, 0.00. Found: C, 65.45; H, 8.53; N, <0.02. Mössbauer (80 K, frozen benzene solution, 50 mT, mm/s): δ = 0.22; ΔE_Q = 0.43.

2.4.3.5 P_3^BFe(CH_2OTMS) 2.6

A THF solution of the dianionic complex **2.2** was generated *in situ* from **2.1** (20.3 mg) and cooled to -78 °C. A slight excess of Me_3SiOTf (16 μL; 2.5 equiv) was added. The reaction mixture was stirred at -78 °C for 15 min then at room temperature for 15 min. The solvent was removed *in vacuo* and the product was extracted with pentane and filtered through Celite. The solvent was removed and the residue was dissolved in benzene and lyophilized to yield the product mixture as a dark orange/brown powder (19.5 mg; ~80% **2.6** as determined by Mössbauer spectroscopy). All reactivity studies and characterization were carried out using this product mixture, which has doublet impurities including **2.5**. X-Ray quality crystals were grown by cooling a saturated Et_2O/MeCN solution at -30 °C. ^{1}H NMR (C_6D_6; 400 MHz): δ 59.5, 30.1, 21.7, 17.6, 7.8, 5.8, 4.8, -3.1, -3.3, -4.4, -15.2.

Solution magnetic moment (Evans Method; 25 °C; ~80% **6**, 20% low-spin (1/2) impurity): 3.44μ_B. Mössbauer (80 K, frozen benzene solution, mm/s): δ = 0.49; ΔE_Q = 2.05.

2.4.3.6 Reaction of 2.6 with H_2

A solution of **2.6** (10-20 mg) was prepared in C_6D_6. In a J. Young NMR tube, the solution was frozen and the headspace was evacuated and backfilled with H_2. The solution was mixed at room temperature until full conversion of the starting material was observed by NMR spectroscopy (~24 h). From these mixtures, the volatiles were vacuum transferred into a second J. Young NMR tube containing a stock solution of ferrocene as an internal standard and the yield of CH_3OSiMe_3 was determined (55%, 50%, 46%; 50% average; assumes starting material **2.6** is 80% clean). The identity of the product was confirmed by comparison to an authentic sample.

2.4.3.7 Reaction of 2.6 with $PhSiH_3$

A solution of **2.6** (10-20 mg) was prepared in C_6D_6. This solution was added to a J. Young NMR tube with excess $PhSiH_3$ (5 equiv) and a stock solution of ferrocene as an NMR standard. The resulting solution was mixed at room temperature until full conversion of the starting material was observed and the yield of $PhSiH_2CH_2OSiMe_3$ was determined by integration versus a ferrocene internal standard (36%, 45%, 58%; 47% average; assumes starting material **2.6** is 80% clean). Vacuum transfer of this compound was not found to be reliable for quantification. The product of this reaction was assigned on the basis of NMR spectroscopy with comparison to a similar species reported by Hill and coworkers (*Angew. Chem. Int. Ed.* **2015**, *54*, 10009.). ^{1}H NMR (C_6D_6; 400 MHz): δ 4.57 (SiH_2, t, J = 3 Hz, 2H), 3.56 (CH_2, t, J = 3 Hz, 2H), 0.05 (Si(CH_3)$_3$, s, 9H). Aromatic C-H resonances in the ^{1}H NMR overlap with $PhSiH_3$ resonances, which is present in excess. ^{13}C{^{1}H} NMR (C_6D_6; 101 MHz; ^{13}C-labeled): δ 50.42 (Si-CH_2O).

2.4.3.8 Rate comparison for the reaction of 2.6 with H_2/D_2

A stock solution of **2.6** was prepared in C_6D_6 and equal volumes of the solution were added to two separate J. Young NMR tubes. The tubes were degassed by two freeze-pump-thaw cycles, frozen, and the headspace was backfilled with either an atmosphere of H_2 or an atmosphere of D_2. The solutions were thawed and mixed at room temperature, proceeding partially to completion as observed by NMR spectroscopy. In either case, the

resulting solution was frozen, the headspace was evacuated, and the volatiles were vacuum transferred into a second J. Young NMR tube containing a stock solution of Fc as an internal standard (50 μL; 0.1 M in C_6D_6). Comparison of the relative product yields gives a small, normal KIE value of 1.25 (average; individual runs: 1.16, 1.35).

2.5 Notes and References

(1) (a) Rofer-DePoorter, C. K. *Chem. Rev.* **1981**, *81*, 447. (b) Maitlis, P. M.; Zanotti, V. *Chem Commun.* **2009**, 1619.

(2) (a) Lee, C. C.; Hu, Y.; Ribbe, M. W. *Science* **2010**, *329*, 642. (b) Hu, Y.; Lee, C. C.; Ribbe, M. W. *Science* **2011**, *333*, 753.

(3) For a recent review of molecular FT model chemistry see: West, N. M.; Miller, A. J. M.; Labinger, J. A.; Bercaw, J. E. *Coord. Chem. Rev.* **2011**, *255*, 881.

(4) (a) Berke, H.; Hoffmann, R. *J. Am. Chem. Soc.* **1978**, *100*, 7224. (b) Ziegler, T.; Versluis, L.; Tschinke, V. *J. Am. Chem. Soc.* **1986**, *108*, 612.

(5) There is a single reported example of reversible CO migratory insertion into a metal-hydride (Th-H) bond. Th-O bond formation helps to drive the insertion. See: Fagan, P. J.; Moloy, K. G.; Marks, T. J. *J. Am. Chem. Soc.* **1981**, *103*, 6959.

(6) Select examples: (a) Wolczanski, P. T.; Bercaw, J. E. *Acc. Chem. Res.* **1980**, *13*, 121. (b) Toreki, R.; LaPointe, R. E.; Wolczanski, P. T. *J. Am. Chem. Soc.* **1987**, *109*, 7558.
(7) For a review of CO reduction reactivity supported by the Fp fragment (Fp = (η5-C5H5)Fe(CO)2) see: Cutler, A. R.; Hanna, P. K.; Vites, J. C. *Chem. Rev.* **1988**, *88*, 1363. For additional examples see Ref. 3.

(8) For exceptions see: (a) Wayland, B. B.; Woods, B. A. *J. Chem Soc., Chem. Commun.* **1981**, 700. (b) Wayland, B. B.; Woods, B. A.; Pierce, R. *J. Am. Chem. Soc*. **1982**, *104*, 302. (c) Paonessa, R. S.; Thomas, N. C.; Halpern, J. *J. Am. Chem. Soc.* **1985**, *107*, 4333. (d) Grimmett, D. L.; Labinger, J. A.; Bonfiglio, J. N.; Masuo, S. T.; Shearin, E.; Miller, J. S. *J. Am. Chem. Soc.* **1982**, *104*, 6858. (e) Lambic, N. S.; Lilly, C. P.; Sommer, R. D.; Ison, E. A. *Organometallics* **2016**, *35*, 3060.

(9) Lewis acid-promoted migratory insertion reactions are well-established for the formation of metal-acyl complexes and the stabilization of metal-acyl or metal-formyl complexes. Select examples: (a) Butts, S. B.; Holt, E. M.; Strauss, S. H.; Alcock, N. W.; Stimson, R. E.; Shriver, D. F. *J. Am. Chem. Soc.* **1979**, *101*, 5864. (b) Anderson, G. D. W.; Boys, O. J.; Cowley, A. R.; Green, J. C.; Green, M. L. H.; Llewellyn, S. A.; von Beckh, C. M.; Pascu, S. I.; Vei, I. C. *J. Organomet. Chem.* **2004**, *689*, 4407. (c) Elowe, P. R.; West, N. M.; Labinger, J. A.; Bercaw, J. E. *Organometallics* **2009**, *28*, 6218.

(10) (a) Miller, A. J. M.; Labinger, J. A.; Bercaw, J. E. *J. Am. Chem. Soc.* **2008**, *130*, 11874. (b) Miller, A. J. M.; Labinger, J. A.; Bercaw, J. E. *J. Am. Chem. Soc.* **2010**, *132*, 3301.

(11) (a) Lee, Y.; Peters, J. C. *J. Am. Chem. Soc.* **2011**, *133*, 4438. (b) Suess, D. L. M.; Peters, J. C. *J. Am. Chem. Soc.* **2013**, *135*, 12580.

(12) Moret, M.-E.; Peters, J. C. *Angew. Chem. Int. Ed.* **2011**, *50*, 2063.

(13) Bontemps, S.; Bouhadir, G.; Dyer, P. W.; Miqueu, K.; Bourissou, D. *Inorg. Chem.* **2007**, *46*, 5149.

(14) Fong, H.; Moret, M.-E.; Lee, Y.; Peters, J. C. *Organometallics* **2013**, *32*, 3053.

(15) The dianionic dihydride complex **2** crystallizes as a cluster with four crystallographically distinct iron centers and eight associated potassium countercations (See SI).

(16) Analysis of the detailed bond metrics of this complex is complicated by the presence of a constitutional disorder, with the trihydride complex **3** cocrystallizing with a ~10% impurity of the monoanionic hydride complex **4**.

(17) When one equivalent of silyl electrophile is used a new diamagnetic product is observed as the major species (see SI). This new complex does not appear to be an intermediate in the formation of **6**.

(18) For a discussion of the trend observed relating spin-state and isomer shift in P3B-supported Fe complexes see: Del Castillo, T. J.; Thompson, N. B.; Peters, J. C. *J. Am. Chem. Soc.* **2016**, *138*, 5341.

(19) Anderson, J. S.; Moret, M.-E.; Peters, J. C. *J. Am. Chem. Soc.* **2013**, *135*, 534.

(20) The product mixture generated in the conversion of **2** to **6** is highly soluble in nonpolar solvents (*e.g.,* alkanes, hexamethyldisiloxane, tetramethylsilane), even at low temperature. While the mixtures show some insolubility in polar solvents (*e.g.,* MeCN), reaction impurities and **6** exhibit similar solubility properties, precluding further purification of **6**.

(21) A conceptually-related phosphine-trapped product has been reported. Fryzuk, M. D.; Mylvaganam, M.; Zaworotko, M. J.; MacGillivray, L. R. *Organometallics* **1996**, *15*, 1134.

(22) Note: Owing to our inability to obtain analytically pure **6**, reactions were by necessity carried-out in the presence of remaining iron impurities.

(23) Treatment of **6** with MeOTf or H-atom sources (*e.g.,* TEMPO-H, Bu3Sn-H) similarly leads to unproductive decomposition of **6**. Me3SiOTf did not react with **6** under conditions we have explored.

(24) The addition of PMe_3 to these reactions leads to more tractable product mixtures, although the major species has not yet been identified (see SI).

(25) A normal KIE (1.25) is observed for the reaction of **6** with H2/D2.

Chapter 3

ELECTROPHILE-PROMOTED IRON-TO-N_2 HYDRIDE MIGRATION IN HIGHLY REDUCED Fe(N_2)(H) COMPLEXES

3.1 Introduction

The Haber-Bosch process has been used since early in the last century for the industrial conversion of dinitrogen (N_2) and dihydrogen (H_2) to the bio-available N-atom source ammonia (NH_3). This energy intensive process accounts for some 1-2% of annual global energy consumption, with high associated CO_2 emissions.[1] Attractive alternatives to this process that operate under mild temperature and pressure conditions have long been sought, motivated by biological nitrogenase enzymes that facilitate the proton-coupled reduction of N_2 under ambient temperature and pressure conditions.[2,3]

Despite extensive study of the enzymatic system, the detailed mechanism of biological N_2 fixation is not reliably known. Based on kinetic and pulsed EPR studies, it has been hypothesized that the build-up of a reduced hydride cluster state, generated by alternate addition of protons and electrons, precedes N_2 binding and fixation.[4] Given inherent challenges associated with direct study of the complex biological system, molecular model chemistry provides a means to develop and constrain mechanistic possibilities concerning reactivity patterns germane to N_2-to-NH_3 conversion.[5]

In recent years, Fe-based synthetic systems have garnered significant attention, including the development of Fe-based molecular catalysts that facilitate proton-coupled N_2 reduction to ammonia.[6] As has been proposed for the biological cofactor, hydride species appear to play a significant role during catalysis for a number of these iron systems (Figure 3.1). In initial reports, the generation of Fe-H species under turnover relevant conditions was hypothesized to play a role in catalyst deactivation;[6a,b] more recent studies show that Fe-H species can be observed as off-path resting states and, as such, can serve as competent pre-catalysts for N_2 fixation.[7,6d,f] Of particular relevance are *in situ* spectroscopic studies on the P_3^BFe (P_3^B = B(*o*-^{i}Pr$_2$PC$_6$H$_4$)$_3$) system from our lab, which allowed for the observation of a hydride resting state, P_3^B(μ-H)Fe(H)(N_2) **3.1**, under catalytic conditions for a specific acid/reductant combination.[8] In examples where hydride

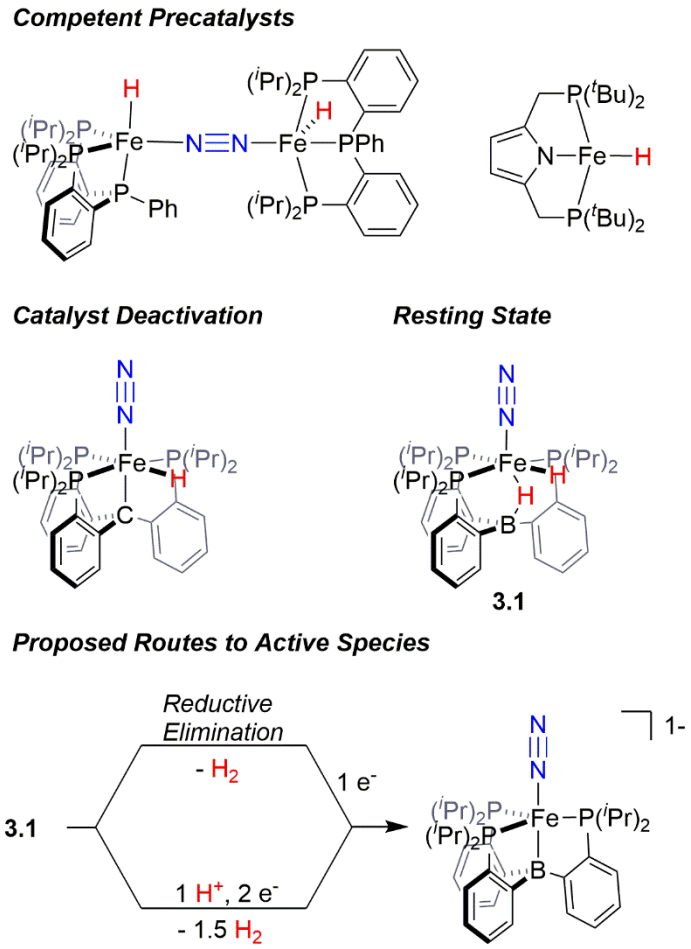

Figure 3.1. Fe-H species relevant to catalytic N_2 fixation by molecular Fe complexes and proposed routes for the generation of an on path Fe-N_2 intermediate from dihydride resting state **1**.[6b,d,f,8]

species have been shown to be amenable to productive N_2 fixation, it has generally been suggested that unproductive H_2 evolution pathways are accessible, and precede the generation of a catalytically active, hydride-free species.[9]

An alternative possibility can be considered where Fe-H intermediates are able to undergo Fe-to-N migration steps, and therefore be incorporated into productive overall schemes for N_2 fixation. While such a scenario has been suggested to occur within the iron-molybdenum cofactor during catalysis,[2c] relevant N_2 model chemistry demonstrating such a reactivity pattern is limited to a fascinating set of Ti_nH_m clusters, which have been shown to promote N_2-cleavage with N-H bond formation (Scheme 3.1A).[10] Conceptually related

reactivity has also been reported for a number of multimetallic systems, where bridged N_2 ligands are reactive towards a variety of E-H substrates (Scheme 3.1B).[11,12,13]

Recently, we demonstrated that a P_3^BFe system supports a series of highly reduced hydride complexes with CO as a co-ligand.[14] These species are able to undergo facile O-functionalization that promotes the rapid intramolecular formation of two new C-H bonds from an $Fe(H)_2$ precursor (Scheme 3.1C). Thus, we wondered whether related N_2 complexes might also be supported by this platform. If so, they would be of interest as

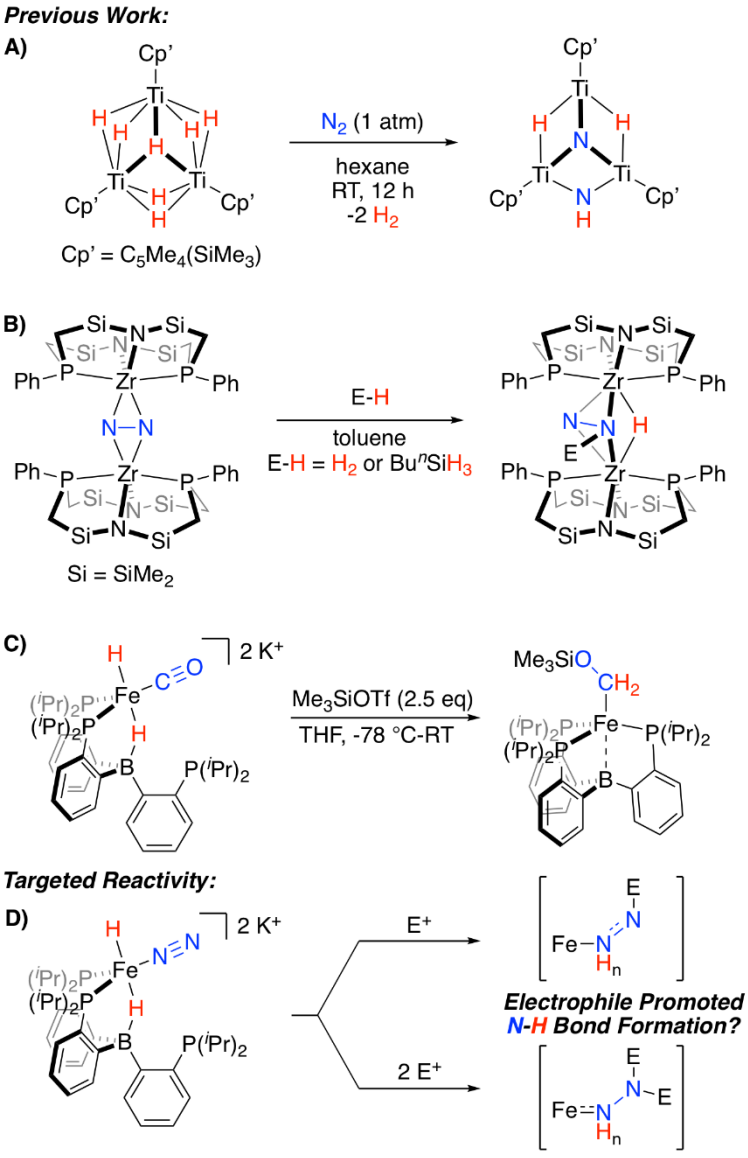

Scheme 3.1. Representative stoichiometric reactions exhibiting relevant reactivity patterns for N_2 (**A** and **B**)[10,11a] or CO (**C**)[14] functionalization, and the targeted Fe-H incorporation for N_2 fixation (**D**).

targets for exploring electrophile-promoted Fe-H migration, to generate new N-H bond(s), as a new reactivity pattern (Scheme 3.1D).

Herein we describe the synthesis and characterization of a series of $[P_3^BFe(N_2)(H)_n]^{m-}$ complexes. One of these species, in a highly reduced state, is reactive toward β-functionalization with silyl electrophiles; intramolecular Fe-to-N_α hydride migration is observed upon difunctionalization. The N-H bond-forming step proceeds slowly in solution at low temperature and is thereby amenable to a detailed kinetic analysis with the determination of associated activation parameters. Trapping of the product with an exogenous CN^{t}Bu ligand allows for its isolation as a hydrazido(1-) species, with N_2-derived disilylhydrazine products liberated upon protonolysis of this complex. Overall, this reactivity demonstrates a plausible series of steps through which an Fe-H equivalent can be incorporated as part of a productive N_2 fixing scheme, in contrast to unproductive H_2 evolution. The utility of silyl, as opposed to proton, electrophiles is highlighted by the ability to kinetically stabilize and characterize extremely reactive species along the reaction pathway.

3.2 Results and Discussion

3.2.1 Synthesis of $Fe(N_2)(H)_n$ Complexes

We initially targeted $[Fe(N_2)(H)_n]^{m-}$ complexes analogous to the previously reported $[Fe(CO)(H)_n]^{m-}$ species supported by the P_3^B ligand platform.[14] Thus, reduction of $P_3^B(\mu\text{-H})Fe(H)(N_2)$ **3.1**[8,15] with an excess of KC_8 at -78 °C led to the formation of the dianionic complex $[P_3^B(\mu\text{-H})Fe(H)(N_2)][K_2(S)_n]$ **3.2** (Scheme 3.2). The ^{31}P NMR spectrum of this species shows one of the phosphine arms dechelated from the Fe center (δ = 92.6 (2P), -1.5 (1P)), with both of the hydride resonances apparent in the ^{1}H NMR spectrum at -18.19 (Fe-*H*-B) and -20.78 (Fe-*H*) ppm. The IR spectrum of dianionic **3.2** exhibits a highly activated N_2 ligand (ν_{NN} = 1746 cm^{-1}), with a 325 cm^{-1} increase in N_2 activation compared to the neutral precursor **3.1** (ν_{NN} = 2071 cm^{-1}). Crystallographic characterization of this species confirmed its assignment, with hydride ligands occupying axial sites of an approximate trigonal bipyramid (Figure 3.2). Strong π-backbonding to the phosphine and

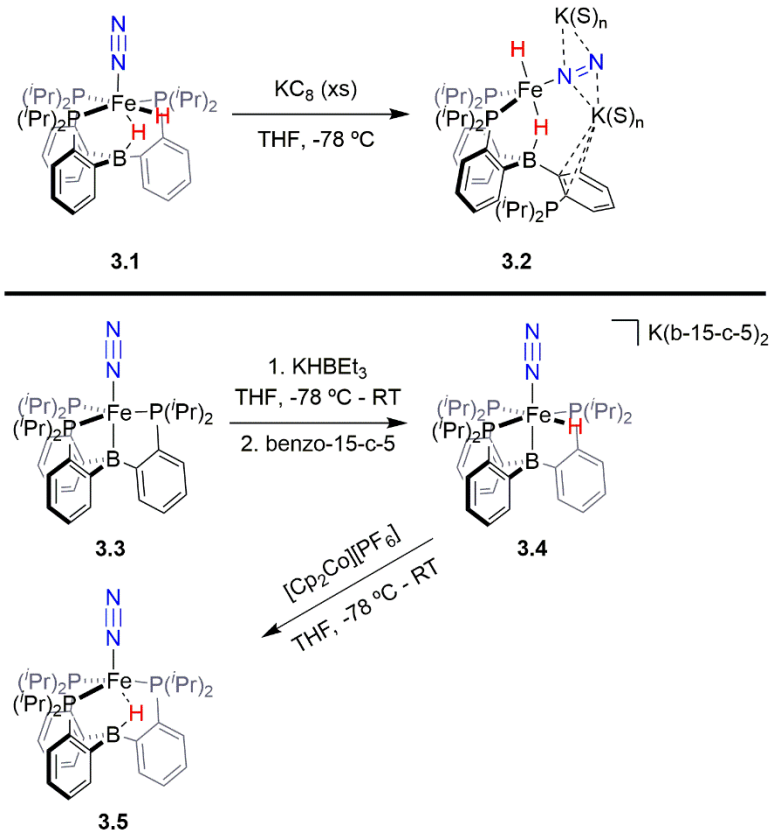

Scheme 3.2. Synthesis of $[Fe(N_2)(H)_n]^{m-}$ complexes **3.2**, **3.4**, and **3.5**.

N_2 ligands is apparent, with quite short Fe-P (2.15 Å, average) and Fe-N (1.743(2) Å) distances, and an elongated N-N distance (1.169(3) Å) where compared to **3.1** (1.128(4) Å). Taken together, the spectroscopic and structural data suggest an N-N bond order that can be described as lying between a double and triple bond. The extreme sensitivity of the dianionic complex **3.2** precluded prolonged handling and storage of this species, so its spectroscopic characterization and further reactivity studies were carried out on samples that were generated *in situ*.[16]

We also found that the monoanionic hydride complex $[P_3^BFe(H)(N_2)][K(benzo\text{-}15\text{-}crown\text{-}5)_2]$ **3.4** could be generated by the addition of a solution of $KHBEt_3$ to a THF solution of $P_3^BFe(N_2)$ **3.3** at -78 °C.[17] The product was readily isolated as a crystalline orange material following workup as its benzo-15-crown-5 encapsulated K salt (Scheme 3.2). This species exhibits a sharp N_2 stretch (1956 cm^{-1}) that is 51 cm^{-1} higher than the hydride-free anion $[P_3^BFe(N_2)][Na(12\text{-}crown\text{-}4)_2]$ (1905 cm^{-1}).[17] The hydride of **3.4** could be identified by ^1H NMR spectroscopy *via* a quartet resonance at -12.59 ppm, with equal

coupling to each of the three coordinated phosphine ligands. This hydride was crystallographically located as a terminal ligand in the plane of the three Fe-ligated phosphines (Figure 3.2). In solution, **3.4** exhibits three-fold symmetry at room temperature, reflected by a single ^{31}P NMR resonance (δ = 77.1); the asymmetry observed in the solid state is borne out in solution upon cooling of **3.4** to lower temperatures (At -80 °C: δ = 95.5, 79.3, 59.7; see SI). Similar solution state behavior has been observed for the analogous CO complex **3.4-CO** and we presume that in both cases this may be attributed to rapid equilibration of the hydride position through a borohydride intermediate.[14,18,19]

We next explored conditions to access the neutral hydride complex (P_3^B-H)Fe(N_2) **3.5**, where the analogous CO complex has been reported.[14] One electron oxidation of the anionic hydride complex **3.4** with [Cp_2Co][PF_6] at -78 °C in THF provides access to a new doublet species with a broad, axial EPR signal, consistent with the formation of **3.5**. The IR spectrum of the product shows B-H and N-N stretches observed at 2590 cm^{-1} and 2011 cm^{-1}, respectively; this N_2 stretch is identical to its neutral hydride-free counterpart **3.3**, though is distinguished by its greater intensity and the presence of the unique B-H stretch.[20] The Mössbauer spectrum of **3.5** exhibits an asymmetric quadrupole doublet with an isomer shift (δ = 0.42) and quadrupole splitting (ΔE_Q = 0.93) consistent with typical doublet species on this scaffold. This is clearly distinct from the hydride-free N_2 complex, which has a Mössbauer spectrum with a higher isomer shift (δ = 0.56) and much wider quadrupole

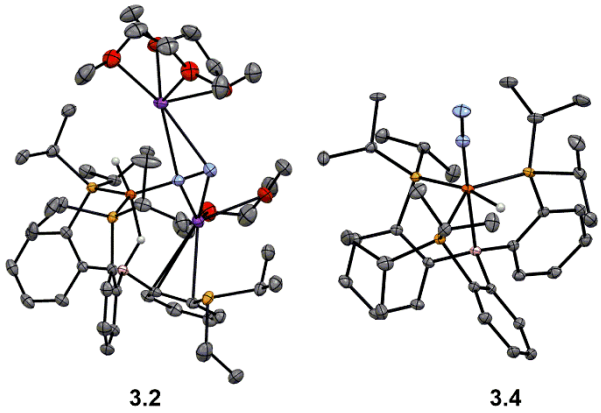

Figure 3.2. Crystal structures of the dianioic complex **3.2** (left) and the anionic complex **3.4** (right). Displacement ellipsoids shown at 50% probability; C-bound H atoms, disorder of ^{i}Pr groups, and the crown encapsulated potassium countercation in **3.4** have been omitted for clarity.

splitting (ΔE_Q = 3.34).[8] Attempts to structurally characterize either of these complexes have been unsuccessful.

Bond metrics for a series of structurally related P_3^E-supported (E = B, Si) Fe-N_2 complexes are shown in Table 3.1 for direct comparison. For complex **3.4**, relevant metrics compare quite well to the related, formally Fe(0)-N_2 complex [P_3^{Si}Fe(N_2)][Na(12-crown-4)$_2$] (Table 3.1).[21] Direct comparison of bond metrics and the degree of N_2 activation with dianionic **3.4** is complicated by structural differences and interactions with K countercations, where **3.4**, like its analogous CO complex, was found to be unstable in the presence of encapsulating reagents (*e.g.,* benzo-15-crown-5). As might be expected, there appears to be a substantially greater degree of N_2 activation and associated π-backdonation in **3.4** than for any of the other crystallographically characterized N_2 complexes supported by these ligand frameworks.

Table 3.1. N-N stretching frequencies, formal oxidation states (FOS), and bond metrics for relevant Fe-N_2 complexes supported by tetradentate P_3^E scaffolds (E = B, Si).

Complex	ν(NN) (cm^{-1})	FOS	N-N (Å)	Fe-N (Å)	Fe-P (ave, Å)	Fe-E (Å)	Reference
P_3^B(μ-H)Fe(H)(N_2) 3.1	2071	+2	1.128(4)	1.801(3)	2.283	2.602(3)	15
[P_3^{Si}Fe(N_2)][BAr^F_4]	2143	+2	1.091(3)	1.914(2)	2.390	2.298(7)	21
P_3^{Si}Fe(N_2)	2003	+1	1.1245(2)	1.8191(1)	2.285	2.2713(2)	21
[P_3^B(μ-H)Fe(H)(N_2)][$K_2(S)_n$] 3.2	1746	0	1.169(3)	1.743(2)	2.148	2.749(3)	This work
[P_3^BFe(H)(N_2)][K(b-15-c-5)$_2$] 3.4	1956	0	1.132(2)	1.800(1)	2.205	2.289(1)	This work
[P_3^{Si}Fe(N_2)][Na(12-c-4)$_2$]	1920	0	1.132(2)	1.795(3)	2.196	2.236(1)	21
[P_3^BFe(N_2)][Na(12-c-4)$_2$]	1905	-1	1.144(3)	1.781(2)	2.251	2.293(3)	17

3.2.2 Functionalization with Silyl Electrophiles

Exploring the N_2 functionalization of these reduced hydride complexes, we found that the functionalization of the anionic hydride complex **3.4** with an equivalent of TMSOTf leads, to the generation of a new species that is observable at low temperatures. Based on its polynuclear NMR spectra, the major diamagnetic product of this transformation is tentatively assigned as P_3^BFe(H)(NNSiMe$_3$) **3.6**, with a broad hydride resonance observed in its ^{1}H NMR spectrum (~ -11.5 ppm; -20 °C, THF-d_8). Upon

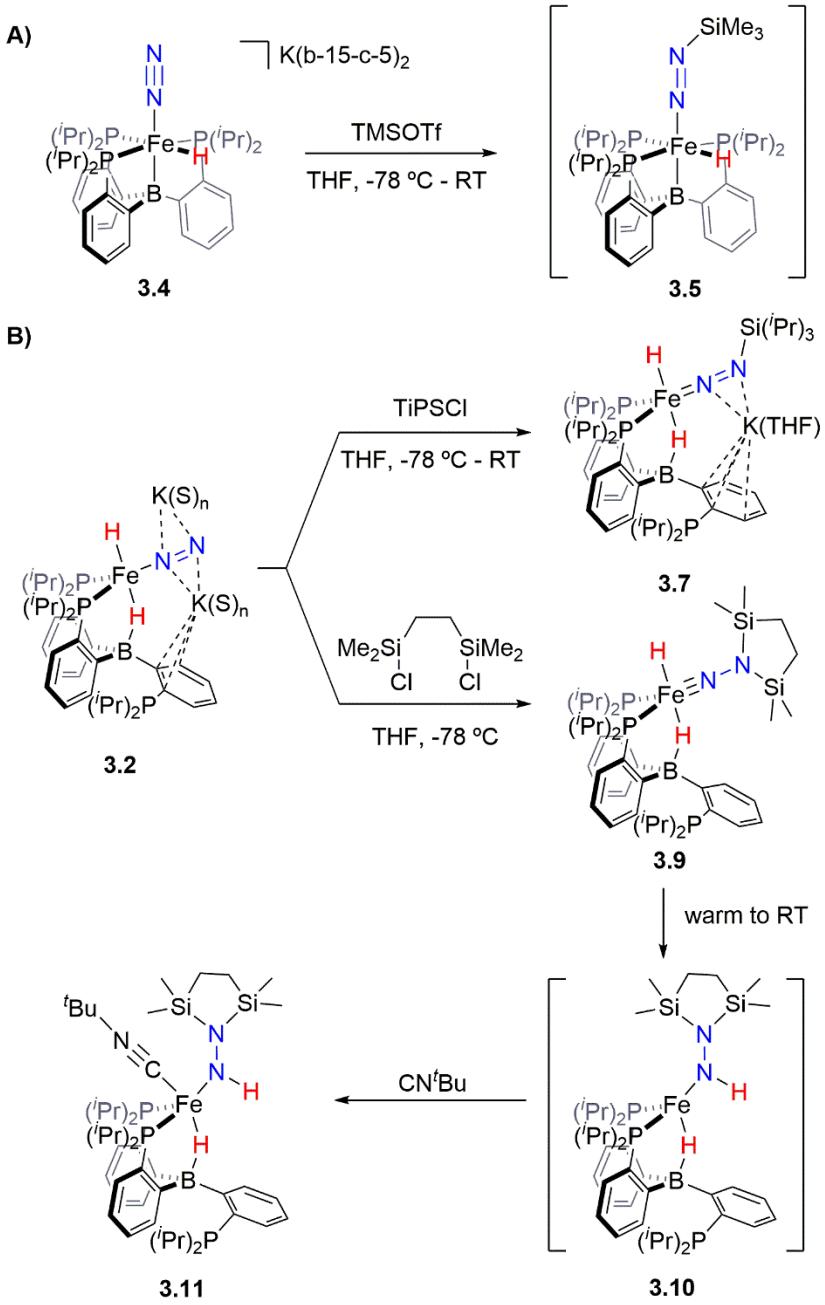

Scheme 3.3. Silyl functionalization reactivity of $P_3^BFe(H)(N_2)$ **3.4** (**A**) and functionalization of dianionic $[P_3^B(\mu\text{-}H)Fe(H)(N_2)][K_2(S)_n]$ **3.2** (**B**) with silyl electrophiles and subsequent hydride migration to generate intermediate **3.10**, trapped as **3.11**.

warming, this compound decays to a mixture of species over time, including $P_3^BFe(NNSiMe_3)$,[22] $(P_3^B\text{-}H)Fe(N_2)$ **3.5**, $P_3^BFe(N_2)$,[17] and $P_3^BFe(OTf)$[23] (Scheme 3.3A).

To access tractable functionalization reactivity, the dianionic dihydride complex **3.2** was treated with TiPSCl to generate the thermally stable, anionic silyl diazenido

complex, [P_3^B(μ-H)Fe(H)(NNSi^{i}Pr$_3$)][K(THF)] **3.7** (Scheme 3.3). In the transformation from dianionic **3.2** to monoanionic **3.7**, the phosphine asymmetry is retained, with one of the phosphines dechelated, as observed in the ^{31}P NMR spectrum (90.6 (br, 2P), -1.0 (1P)). Further, the hydride and borohydride ligands are readily observed in the ^{1}H NMR spectrum at -9.71 (t) and -11.10 ppm respectively, along with activated N-N stretches in the IR spectrum (1541, 1588 cm^{-1}), consistent with the formation of an anionic silyl diazenido complex. This was confirmed by XRD analysis (Figure 3.3). Complex **3.7** is structurally comparable to the previously reported anionic silyl diazenido complex [P_3^BFe(NNSiMe$_3$)][Na(THF)] **3.8**, in which one of the phosphine ligands is similarly dechelated from the Fe center (Figure 3.4A).[22] Both **3.7** and **3.8** have tightly interacting countercations bridging the terminal silyl diazenido ligand and the phenylene linker of the dechelated phosphine arm. In **3.7** the hydride and borohydride ligands occupy the axial sites of an approximate trigonal bipyramidal structure, whereas the Fe center in **3.8** is ligated by an additional η^2 interaction with the phenylene linker. Complex **3.7** has a similar overall geometry to the dianionic precursor **3.2**, featuring hydride and borohydride ligands that are unperturbed upon N_2-silylation. Nevertheless, the relevant bond metrics for the Fe-coordinated ligands in the anionic silyldiazenido complexes **3.7** and **3.8** compare favorably (Table 3.2).

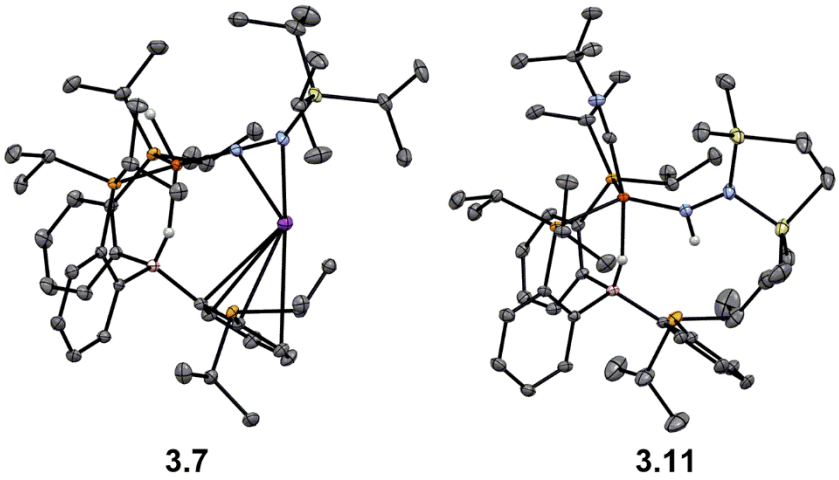

Figure 3.3. Crystal structures of the silyl diazenido complex **3.7** (left) and the disilylhydrazido(1-) complex **3.11** (right). Displacement ellipsoids shown at 50% probability; C-bound H atoms, solvent molecules, and disorder of ^{i}Pr groups in **3.7** have been omitted for clarity.

Treatment of **3.2** with the disilylating reagent 1,2-bis(chlorodimethylsilyl)ethane (Si_2) at -78 °C resulted in the formation of a new species. This reaction could be monitored at low temperatures (<-20 °C), allowing for the observation of a diamagnetic intermediate, with both hydride resonances retained in the ^{1}H NMR spectrum at -16.74 (br) and -17.51 (t) ppm. The asymmetry in this species is also evident by ^{31}P NMR spectroscopy (-80 °C; δ = 106.6, 95.1, -10.2), consistent with its tentative assignment as the five-coordinate disilylhydrazido(2-) species **3.9** (Scheme 3.3). Upon warming the reaction mixture further, decay of this intermediate was observed concurrent with the appearance of a new set of paramagnetically shifted ^{1}H NMR resonances. A ^{1}H NMR spectrum reflecting a mixture of paramagnetic species was obtained after several minutes at room temperature.

We hypothesized the initially generated paramagnetic intermediate to be the product of N-H bond formation *via* alpha-hydride migration to generate the hydrazido(1-) complex **3.10** (Scheme 3.3). Such a formulation would be consistent with IR spectra of the reaction mixture; no diagnostic N-N multiple 3 stretch is observed, whereas an N-H vibration is located at 3263 cm^{-1}; the latter is absent in the spectrum of the deuterium labeled analog **3.10-D$_2$**.[24]

To generate an isolable analog of the disilylhydrazido(1-) complex, we explored the addition of coordinating exogenous ligands to **3.10** (*e.g.,* CO, PMe_3) to trap it. We found that addition of an excess of CN^{t}Bu resulted in the formation of a comparatively stable, diamagnetic complex P_3^B(μ-H)Fe(NHNSi_2)(CN^{t}Bu) **3.11** (Scheme 3.3). This species was assigned initially through the use of multinuclear NMR spectroscopy, with the hydride resonating at -12.59 ppm and the N-H at 7.84 ppm; the latter exhibits weak coupling to Si in the ^{29}Si-HMBC spectrum (see SI); these assignments could be confirmed by comparison to the D_2-labeled analog **3.11-D$_2$**. By IR spectroscopy, an intense vibration associated with the isocyanide C-N stretch is observed at 1997 cm^{-1}, with the N-H and B-H-Fe vibrations assigned at 3197 and 2070 (br) cm^{-1}, respectively, shifting to 2377 and 1515 (br) cm^{-1} in the labeled analog **3.11-D$_2$**. The ^{31}P NMR spectrum reflects asymmetry with one phosphine ligand dechelated from the Fe center (δ = 88.9, 82.7, -2.1).

Confirmation of the proposed assignment for **3.11** was enabled by XRD analysis, with the disilylhydrazido(1-) ligand located in the plane of the coordinated phosphine

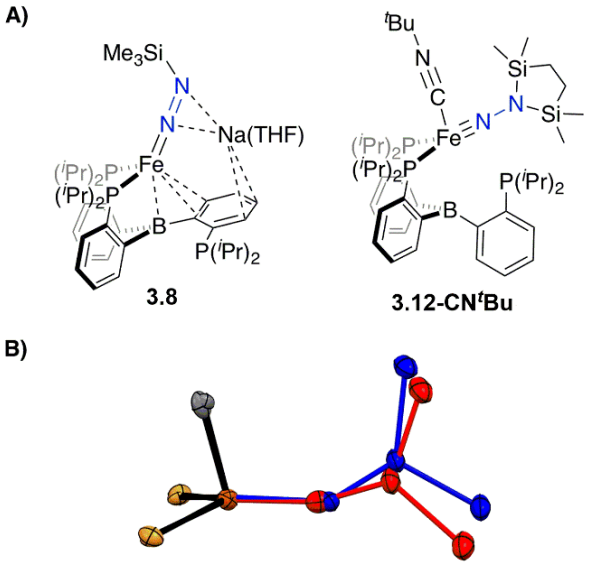

Figure 3.4 (A) Depictions of previously reported silyl-functionalized N_2 complexes **3.8** and **3.12-CN^{t}Bu**. **(B)** Overlay of the core structures of the hydrazido(1-) complex **3.11** (blue) and the previously reported hydrazido(2-) complex **3.12-CN^{t}Bu** (red).[22]

ligands and the CN^{t}Bu ligand *trans* to the coordinated borohydride moiety (Figure 3.3). The overall geometry of this complex is similar to a previously reported, CN^{t}Bu-trapped disilylhydrazido(2-) complex, **3.12-CN^{t}Bu** (Figure 3.4A).[22] Examination of an overlay of these structures (Figure 3.4B) highlights the key differences distinguishing the hydrazido(1-) and hydrazido(2-) ligands in **3.11** and **3.12-CN^{t}Bu**, respectively; they otherwise have remarkably similar structures. Upon formation of the new N_α-H bond in **3.11**, multiple bond character of both the Fe-N and N-N bonds is predicted to decrease with associated bending of the Fe-N-N angle. This is readily observed in the crystallographic bond metrics for these species; hydrazido(1-) **3.11** exhibits substantial elongation of the Fe-N distance (1.824(2) vs. 1.640(2)) and the N-N distance (1.404(2) vs. 1.351(3)) as well as increased bending in the Fe-N-N angle (145.8(1) vs. 162.7(2)) (Table 3.2) when compared with the hydrazido(2-) complex **3.12-CN^{t}Bu**.

Table 3.2. Relevant bond metrics for β-N silyl-functionalized Fe complexes.

Complex	N-N (Å)	Fe-N (Å)	Fe-P (ave, Å)	Fe-B (Å)	Fe-N-N (°)	Reference
[P_3^B(μ-H)Fe(H)(NNSi^{i}Pr$_3$)][K(THF)] 3.7	1.249(2)	1.672(1)	2.219	2.791(1)	169.31(9)	This work
[P_3^BFe(NNSiMe$_3$)][Na(THF)] 3.8	1.259(4)	1.673(3)	2.229	2.319(4)	169.8(2)	22
P_3^B(μ-H)Fe(NHNSi$_2$)(CN^{t}Bu) 3.11	1.404(2)	1.824(2)	2.231	2.885(2)	145.8(1)	This work
P_3^BFe(NNSi$_2$)(CN^{t}Bu) 3.12-CN^{t}Bu	1.351(3)	1.640(2)	2.247	2.863(3)	162.7(2)	22

3.2.3 N-H Bond Formation

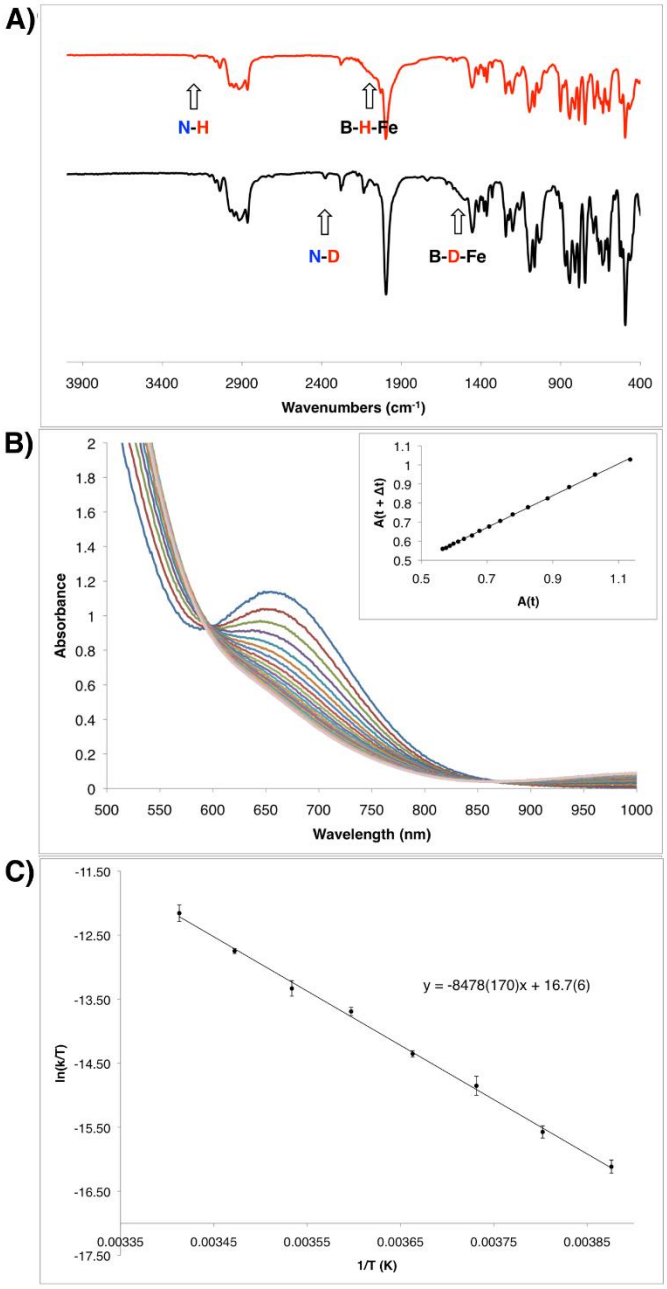

Figure 3.5 (A) IR spectra of the hydrazido(1-) complexes **3.11** (top) and **3.11-D_2** (bottom). **(B)** Transformation of the intermediate hydrazido(2-) complex **3.9** to the hydrazido(1-) complex **3.10** observed by UV-Visible spectroscopy in 6 minute intervals at 10 °C. Inset shows the corresponding linear plot of A(t) vs. A(t + Δt), which is consistent with a first order decay process (R^2 = 0.9996). Rate constant: 4.98 x 10^{-4} s^{-1}. **(C)** Eyring plot for the decay from **3.9** to **3.10** measured in 5 degree increments from -15 °C to 20 °C. Measurements were made in duplicate at each temperature. Eyring parameters: $\Delta H^{\ddagger}$ = 16.8(3) kcal/mol; $\Delta S^{\ddagger}$ = -14(1) e.u.; $\Delta G^{\ddagger}$ = 20.9 kcal/mol (at 20 °C).

Given the unusual nature of the N-H bond-forming step from **3.9** to **3.10** (and **3.11**), we were interested in further understanding its mechanism. As discussed above, selective D-incorporation into the N-D bond for the labeled complex **3.11-D$_2$** confirmed that the newly formed N-H(D) bond is derived from one of the original hydride/deuteride ligands (Figure 3.5A). Further, this transformation does not appear to proceed through the loss of free H_2 prior to the N-H bond-forming step. Consistent with this supposition, the complexes **3.12** and **3.12-CN^{t}Bu** do not undergo productive reactivity with free H_2,[25] and the transformation from **3.9** to **3.11** can be carried out under an atmosphere of D_2 without the generation of the D-labeled Fe product **3.11-D$_2$**. The kinetics of this transformation can conveniently be monitored by UV-visible spectroscopy; the process is first order in Fe, with a kinetic isotope effect of 1.39 (measured at 10 °C; Figure 3.5B).

Combined, these observations are consistent with an intramolecular hydride migration step as the operative mechanism for N-H bond formation. This type of reaction is highly unusual, even when expanded to include the migration of any R group (R = alkyl, aryl, or hydride) to any multiply bonded heteroatom (M=E; E = O, NR, etc.). Well-studied examples of this reactivity pattern are scarce, with early detailed studies from the Mayer group reporting the migration of a variety of R groups (R = alkyl, aryl, H) to electrophilic Re(=O).[26] Perhaps more closely related to the present system, Wolczanski, Cundari, and coworkers very recently reported a four-coordinate Fe(IV) imido complex that formally inserts into an Fe-R bond (R = ^{neo}Pe, 1-nor) to generate a new, three-coordinate Fe(II) amido complex (Scheme 3.4).[27]

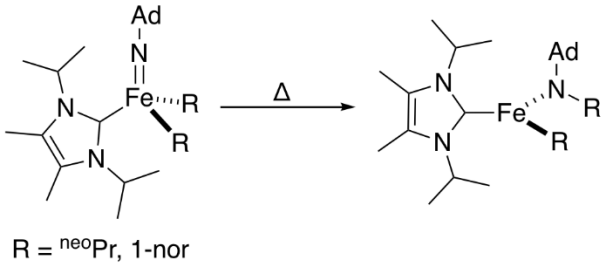

Scheme 3.4 Reported Fe-imido to Fe-amido transformation proceeding through the migration of a bulky alkyl group.[27]

The observed transformation of **3.9** to **3.10** that leads to the generation of an N-H bond could be monitored over a 35 °C temperature range[28](-15 °C up to 20 °C), enabling an Eyring analysis to obtain the following pertinent transition state parameters: $\Delta H^{\ddagger}$ =

16.8(3) kcal/mol; $\Delta S^{\ddagger}$ = -14(1) e.u.; $\Delta G^{\ddagger}$ = 20.9 kcal/mol (at 20 °C) (Figure 3.5C). The negative entropy of activation observed is unexpected for an intramolecular process that is first order in Fe when compared with previous observations. In the related Fe study by Wolzcanski and coworkers (Scheme 3.4), small, positive activation entropies ($\Delta S^{\ddagger}$) were determined, with values of 6.5(1) e.u. (R = ^{neo}Pe) and 1.3(1) e.u. (R = 1-nor); these values were close to those predicted computationally.[27,29] We suspect that, for our present system, some sort of ordering of the flexible phosphine-borane ligand may be present in the transition state, leading to a negative entropy of activation for example *via* the interaction of the otherwise free phosphine arm.

3.2.4 Release of N-Fixed Products

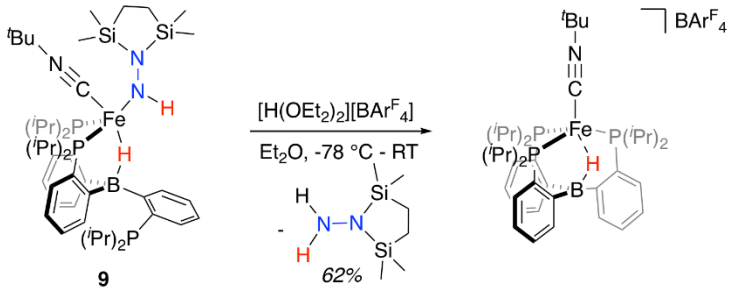

Scheme 3.5 Release of disilylhydrazine upon treatment with stoichiometric acid (BAr^F_4 = $B(C_8H_3F_6)_4$).

With the isolable hydrazido(1-) complex **3.11-CN^{t}Bu** in hand, we explored conditions for the release of reduced, N_2-derived products. Initially, we explored possible conditions for the reductive elimination of the final N-H bond to liberate disilylhydrazine. In these attempts, which included both thermal and photochemical reaction conditions, N-fixed products could be detected in low yields in certain cases, but invariably these reactions yielded mixtures of ill-defined Fe-containing products. Direct treatment of **3.11-CN^{t}Bu** instead with a stoichiometric equivalent of $[H(OEt_2)_2][BAr^F_4]$ (BAr^F_4 = $B(C_8H_3F_6)_4$) at low temperature, followed by warming the solution, proved more tractable (Scheme 3.5); liberated disilylhydrazine products could be detected (62%) in the absence of detectable NH_3. The major Fe-containing product, cationic $[P_3^B(\mu\text{-}H)Fe(CN^tBu)][B(C_8H_3F_6)_4]$, could be isolated in similar yields.

3.3 Conclusions

We have described the synthesis and characterization of a series of unusual $Fe(N_2)(H)_n$ complexes, one of which undergoes β-N-functionalization with silyl electrophiles to generate silyldiazenido and disilylhydrazido(2-) species featuring hydride and borohydride ligands. Of most interest, the disilylhydrazido(2-) complex is observed to undergo a highly unusual Fe-to-N_α hydride migration step to generate a dislylhydrazido(1-) complex that is isolable upon trapping with an exogenous CN^{t}Bu ligand. The hydride migration step is shown to be intramolecular and proceeds over a temperature range that enables activation parameters to be measured. The ability to generate an N-H bond at N_α of an $Fe(H)(N_2)$ species, triggered by electrophilic derivatization of the N_β position, opens up interesting opportunities to generate new N_2-derived products from Fe-mediated processes. That disilylhydrazine can be liberated in the present system provides a promising starting point in this context.

3.4 Experimental Section

3.4.1 General Considerations

All manipulations were carried out using standard Schlenk or glovebox techniques under an N_2 atmosphere. Solvents were deoxygenated and dried by thoroughly sparging with N_2 followed by passage through an activated alumina column in a solvent purification system by SG Water, USA LLC. Ethereal solvents (THF, Et_2O, DME) were dried further by stirring over Na/K alloy (>2 h) and were filtered through Celite prior to use. Deuterated benzene was purchased from Cambridge Isotope Laboratories, Inc., and dried by refluxing over Ca-H then distilled and stored over Na. Deuterated THF was purchased from Cambridge Isotope Laboratories and dried over Na/K alloy and was filtered through Celite prior to use. Reagents were purchased from commercial vendors and used without further purification unless otherwise noted. $P_3^BFe(N_2)$ **3.3** and $P_3^B(\mu\text{-}H)Fe(H)(N_2)$ **3.1** were prepared according to literature procedures.[15,17]

3.4.2 Physical Methods

NMR spectra (^1H, ^{13}C, ^{31}P, ^{11}B, and ^{29}Si) were collected at room temperature (25 °C unless specified) on Varian 300, 400, or 500 MHz spectrometers. ^1H, ^{13}C, and ^{29}Si chemical shifts are reported in ppm, relative to tetramethylsilane using residual proton and

^{13}C resonances from solvent as internal standards. ^{29}Si NMR chemical shifts were determined from ^{29}Si-HMBC two-dimensional spectra. ^{31}P chemical shifts are reported in ppm relative to 85% aqueous H_3PO_4 and ^{11}B spectra were referenced to $BF_3 \bullet Et_2O$. Thin film IR spectra were obtained using a Bruker Alpha Platinum ATR spectrometer with OPUS software in a glovebox under an N_2 atmosphere. UV-Vis measurements were collected using a Cary 50 instrument with Cary WinUV software. X-band EPR spectra were obtained on a Bruker EMX spectrometer on solutions prepared as frozen glasses in 2-MeTHF. Mössbauer spectra were recorded on a spectrometer from SEE Co. (Edina, MN) operating in the constant acceleration mode in a transmission geometry. The sample was kept in an SVT-400 cryostat from Janis (Wilmington, MA). The quoted isomer shifts are relative to the centroid of the spectrum of a metallic foil of α-Fe at room temperature. Solution samples were prepared by freezing solutions in a Delrin cup in a glovebox with rapid transfer of frozen samples to a liquid nitrogen bath before mounting in the cryostat. Samples were collected with no applied magnetic field unless otherwise specified. Data analysis was performed using the program WMOSS (www.wmoss.org) and quadrupole doublets were fit to Lorentzian lineshapes.

X-Ray diffraction and combustion analysis measurements were carried out in the Beckman Institute Crystallography Facility. XRD measurements were collected using a dual source Bruker D8 Venture, four-circle diffractometer with a PHOTON CMOS detector or a Brüker Apex II diffractometer with an APEX II CCD detector. Structures were solved using SHELXT and refined against F2 on all data by full-matrix least squares with SHELXL. The crystals were mounted on a glass fiber under Paratone N oil. See below for any special refinement details for individual data sets. Combustion analysis measurements were collected using a PerkinElmer 2400 Series II CHN Elemental Analyzer by facility staff.

3.4.3 Synthetic Details

3.4.3.1 $[P_3^B(\mu\text{-}H)Fe(H)(N_2)][K_2(THF)_x]$ 3.2

A yellow-orange THF solution (~20 mM) of $P_3^B(\mu\text{-}H)Fe(H)(N_2)$ **3.1** was cooled to -78 °C. To this solution, an excess of KC_8 was added with the mixture turning very dark brown/black upon the addition of reductant. After stirring for 3 min at -78 °C, the

suspension was filtered through a prechilled Celite pipette filter to remove excess KC_8 and graphite. Characterization of this complex and studies of its reactivity were done using material that was generated *in situ* according to this procedure because of the extreme air and moisture sensitivity of this complex as well as its apparent thermal instability (solutions of the complex were observed to completely decompose over the course of hours at room temperature in a sealed J. Young NMR tube under a nominally inert atmosphere). To generate X-Ray quality crystals of this complex, the THF was removed in vacuo and the residue was redissolved in a 2:1 mixture of dimethoxyethane and toluene and layered with pentane at -35 °C. $^{31}P\{^1H\}$ NMR (THF-d_8; 162 MHz): δ 92.6 (d, J = 59 Hz, 2P) -1.5 (s, 1P). ^1H NMR (THF/THF-d_8; 400 MHz): δ 7.67 (Ar C-*H*, br, 1H), 7.53 (Ar C-H, d, J = 6.5 Hz, 2H), 7.26 (Ar C-*H*, 1H), 7.02 (Ar C-*H*, d, J = 6.3 Hz, 2H), 6.88 (Ar C-*H*, m, 2H), 6.57 (Ar C-*H*, m, 4H), 2.21 (PC-*H*, overlapping, br, 6H), 1.15 (CH_3, m, 12H), 0.91 (CH_3, dd, J = 11, 7 Hz, 6H), 0.79 (CH_3, q, J = 6 Hz, 6H), 0.70 (CH_3, dd, J = 12, 7 Hz, 6H), 0.61 (CH_3, q, J = 6 Hz, 6H), -18.19 (Fe-*H*-B, br, 1H), -20.78 (Fe-*H*, td, J = 64.8, 8.5 Hz, 1H). $^{11}B\{^1H\}$ NMR (THF/THF-d_8; 128 MHz): δ 1.72 (br). IR of $[P_3^B(\mu\text{-}H)Fe(H)(N_2)][K_2(THF)_x]$ (thin film, cm^{-1}) : ν_{NN} = 1746 cm^{-1}. Mössbauer (80 K; frozen THF solution, mm/s): δ = 0.25; ΔE_Q = 2.28. The extreme sensitivity and thermal instability of this complex precluded obtaining satisfactory EA of this complex

3.4.3.2 $[P_3^BFe(H)(N_2)][K(benzo\text{-}15\text{-}crown\text{-}5)_2]$ 3.4

A stirring THF solution of $P_3^BFe(N_2)$ **3.3** (293 mg, 0.434 mmol) was cooled to -78 °C. To this solution, a slight excess of $KHBEt_3$ (1.0 M in THF, 520 μL, 0.521 mmol, 1.2 equiv) was added and the mixture was stirred at -78 °C for 3 h and then warmed to room temperature and stirred for an additional 30 min. A THF solution of benzo-15-crown-5 (0.955 mmol, 2.2 equiv) was added and the mixture was stirred for an additional 15 min. The solvent was removed *in vacuo* and the resulting orange solid was redissolved in a minimal amount of THF and layered with pentane at -35 °C overnight. The mother liquor was decanted and the material was washed with additional pentane (5 mL), yielding the product as an orange, crystalline solid (472 mg, 87%). Crystalline material suitable for XRD analysis was prepared similarly. $^{31}P\{^1H\}$ NMR (THF-d_8; 162 MHz): δ 77.1. $^{31}P\{^1H\}$ NMR (THF-d_8; 202 MHz, -80 °C): δ 95.5 (d, 1P), 79.3 (s, 1P), 59.7 (d, 1P). ^1H NMR (THF-

d$_8$; 400 MHz): δ 7.10 (Ar C-*H*, br, 3H), 7.05 (Ar C-*H*, br, 3H), 6.62 (Ar C-*H*, br, 3H), 6.50 (Ar C-*H*, br, 3H), 2.31 (PC-*H*, br, 6H), 1.08 (C*H*$_3$, br, 18H), 0.87 (C*H*$_3$, br, 18H), -12.59 (Fe-H, q, *J* = 46 Hz, 1H). ^{11}B{^{1}H} NMR (THF-*d*$_8$; 128 MHz): δ 5.8. IR of [P$_3^B$Fe(H)(N$_2$)][K(benzo-15-crown-5)$_2$] (thin film, cm^{-1}) : ν_{N2} = 1956 cm^{-1};(ν_{Fe-H} overlaps with the intense N$_2$ stretch). Mössbauer (80 K; frozen THF solution, mm/s): δ = 0.20; ΔE_Q = 0.84. Attempts to obtain satisfactory EA invariably gave slightly low values for N, which may be due to some lability. Anal. Calcd. for $C_{64}H_{95}BFeKN_2O_{10}P_3$: C 61.44; H 7.65; N 2.24. Found: C 61.28; H 8.03; N 1.66.

3.4.3.3 [P$_3^B$(*μ*-H)Fe(H)(NNSi^{i}Pr$_3$)][K(THF)] 3.7

A THF solution of [P$_3^B$(*μ*-H)Fe(H)(N$_2$)][K$_2$(THF)$_n$] **3.2** was generated from **3.1** (103.8 mg, 0.153 mmol) *in situ* at -78 °C. A prechilled Et$_2$O solution of the silylating reagent ^{i}Pr$_3$SiCl (26.6 mg, 0.138 mmol, 0.9 equiv) was added and the mixture was stirred at -78 °C for 15 min then warmed to room temperature and stirred for an additional 15 min. The solvent was removed *in vacuo* from the resultant brown solution, the residue was triturated with pentane and then extracted into pentane. The solvent was again removed and the brown residue was redissolved in benzene and lyophilized, yielding the product as a brown powder (101.9; 78% yield). Single crystals suitable for X-ray diffraction were grown by dissolving this powder in a 1:1 Et$_2$O/pentane mixture and allowing the solvent to evaporate slowly in a vessel containing MeCy at -35 °C. ^{31}P{^{1}H} NMR (C$_6$D$_6$; 162 MHz): δ 90.6 (br, 2P), -1.0 (1P). ^{1}H NMR (C$_6$D$_6$; 400 MHz): δ 7.91 (Ar C-*H*, br s, 1H), 7.86 (Ar C-*H*, d, *J* = 7.5 Hz, 2H), 7.51 (Ar C-*H*, d, *J* = 7.5 Hz, 1H), 7.2-7.1 (Ar C-*H*, multiple resonances overlapping C$_6$H$_6$, 4H), 6.99 (Ar C-*H*, t, *J* = 7.5 Hz, 2H), 6.91 (Ar C-*H*, t, *J* = 7 Hz, 2H), 2.40 (^{i}Pr C-*H*, m, 2H), 1.95 (^{i}Pr C-*H*, m 2H), 1.87 (^{i}Pr C-*H*, br, 2H), 1.42 (^{i}Pr-C*H*$_3$, dd, *J* = 12, 6.5 Hz, 6H), 1.23 (^{i}Pr-C*H*$_3$, s, 18H), 1.25-1.1 (^{i}Pr-C*H*$_3$, overlapping m, 21H) 1.03 (^{i}Pr-C*H*, s, 3H), 0.97 (^{i}Pr-C*H*$_3$, q, *J* = 7 Hz, 9H), -9.71 (Fe-*H*, t, *J* = 84 Hz, 1H), -11.08 (B-*H*-Fe, br s, 1H). ^{11}B{^{1}H} NMR (C$_6$D$_6$; 128 MHz): δ 2.1 (br). ^{29}Si NMR (C$_6$D$_6$; 79 MHz): δ -5.6. IR of [P$_3^B$(*μ*-H)Fe(H)(NSi^{i}Pr$_3$)][K(THF)] (thin film, cm^{-1}) : ν_{NN} = 1537, 1577; ν_{Fe-H} = 1757, 1816; ν_{B-H-Fe} = 2078 (br). Anal. Calcd. for $C_{49}H_{84}BFeKN_2OP_3Si$: C 62.35; H 8.97; N 2.97. Found: C 61.92; H 9.10; N 2.77.

3.4.3.4 $P_3^B(\mu\text{-H})Fe(H)(NNSi_2)$ 3.9

A THF solution of $[P_3^B(\mu\text{-H})Fe(H)(N_2)][K_2(THF)_n]$ was generated *in situ* at -78 °C. A prechilled Et_2O solution of the disilylating reagent Si_2Cl_2 (Si_2 = $Me_2Si(CH_2CH_2)SiMe_2$; 0.9 equiv) was added to a stirred solution of the dianionic Fe complex and stirred at -78 °C for five minutes changing from dark brown to green in color, indicating conversion to the disilylhydrazido(2-) complex **7**. This species could be generated *in situ* and characterized in solution at low temperature. Attempts to crystallographically characterize this species in the solid state were unsuccessful, likely due its high solubility in nonpolar solvents and thermal instability. Variable temperature NMR spectra for this complex are shown below. ^{31}P NMR (THF/THF-d_8; 202.4 MHz; -40 °C): δ 100.5 (br, 2P), -8.0 (s, 1P). ^{1}H NMR (THF/THF-d_8; 500 MHz; -40 °C): 7.43 (Ar C*H*, br, 2H), 7.34 (Ar C*H*, d, *J* = 7 Hz, 1H), 6.96 (Ar C*H*, t, *J* = 7 Hz, 1H), 6.89 (Ar C*H*, t, *J* = 7, 2H), 6.82 (Ar C*H*, t, *J* = 7.5, 2H), 6.78 (Ar C*H*, t, *J* = 7.5, 1H), 6.66 (Ar *CH*, d, *J* = 7.5 Hz, 2H), 6.29 (Ar C*H*, d, *J* = 7 Hz, 1H), 2.86 (^{i}Pr C*H*, br, 4H), 2.46 (^{i}Pr C*H*, br, 2H), 1.48 (^{i}Pr-C*H*$_3$, dd, *J* = 13.5, 7 Hz, 6H), 1.34 (^{i}Pr-C*H*$_3$, br, 6H), 1.17 (^{i}Pr-C*H*$_3$, br, 6H), 0.98 (^{i}Pr-C*H*$_3$, dd, *J* = 11, 7 Hz, 6H), 0.69 (^{i}Pr-C*H*$_3$, br, 9H), 0.67 (Si-C*H*$_2$, s, 4H), 0.38 (Si-C*H*$_3$, s, 6H), 0.21 (Si-C*H*$_3$, s, 6H), -16.58 (B-*H*-Fe, br, 1H), -17.32 (Fe-*H*, t, *J* = 91 Hz, 1H). Three of the phosphine isopropyl methyl resonances are not accounted for in this assignment; these may be located under the solvent resonances. UV-vis (THF, nm {M^{-1} cm^{-1}}, -80 °C): 660 {240}.

3.4.3.5 $P_3^B(\mu\text{-H})Fe(NHNSi_2)(CN^tBu)$ 3.11

A THF solution of $[P_3^B(\mu\text{-H})Fe(H)(N_2)][K_2(THF)_n]$ **3.2** was generated *in situ* from **3.1** (88.2 mg, .130 mmol) at -78 °C. A prechilled Et_2O solution of the disilylating reagent Si_2Cl_2 (Si_2 = $Me_2Si(CH_2CH_2)SiMe_2$; 25.3 mg, 0.117 mmol, 0.9 equiv) was added to a stirred solution of the dianionic Fe complex and stirred at -78 °C for five minutes. Neat ^{t}BuNC (5 equiv, 74 μL, 0.652 mmol) was added via syringe and the mixture was warmed to room temperature and stirred for an additional hour. The solvent was removed *in vacuo*, and the deep red residue was extracted into pentane and filtered through Celite. The solvent was again removed and the residue was redissolved in a minimum of pentane and crystallized overnight via solvent evaporation in a vessel containing methylcyclohexane. X-Ray quality crystals were prepared according to this procedure. To complete

purification, the crystalline material was cooled to -78 °C and washed with prechilled pentane. After warming to room temperature, the crystals were extracted into benzene and lyophilized, yielding the product as a fine red powder (79.7 mg; 75%). $^{31}P\{^{1}H\}$ NMR (C_6D_6; 162 MHz): δ 88.9 (d, *J* = 19 Hz, 1P), 82.7 (d, *J* = 19 Hz, 1P), -2.1 (s, 1P). ^{1}H NMR (C_6D_6; 400 MHz): δ 7.84 (N*H*, s, 1H), 7.73 (Ar C*H*, br, 1H), 7.55 (Ar C*H*, t, *J* = 8.5 Hz, 2H), 7.44 (Ar C*H*, dt, *J* = 6, 3 Hz, 1H), 7.38 (Ar C*H*, t, *J* = 7 Hz, 1H), 7.21 (Ar C*H*, m, overlapping benzene, 1H), 7.13 (Ar C*H*, m, overlapping benzene, 3H), 7.02 (Ar C*H*, t, *J* = 7 Hz, 1H), 6.95 (Ar C*H*, br, 2H), 2.77 (^{i}Pr C*H*, sept, *J* = 7.5 Hz, 2H), 2.50 (^{i}Pr C*H*, m, 1H), 2.19 (^{i}Pr C*H*, br, 2H), 1.99 (^{i}Pr C*H*, sept, *J* = 7.5 Hz, 1H), 1.55 (^{i}Pr C*H*$_3$, dd, *J* = 13, 7 Hz, 3H), 1.60-0.90 (^{i}Pr C*H*$_3$, overlapping m, 36H), 1.31 (CN^{t}Bu, s, overlapping, 9H), 0.68 (Si C*H*$_2$, d, *J* = 3.5 Hz, 4H), 0.34 (Si C*H*$_3$, s, 6H), -0.08 (C*H*$_3$, s, 6H), -10.42 (B-H-Fe, br, 1H). $^{11}B\{^{1}H\}$ NMR (C_6D_6; 128 MHz): δ 7.9. IR of P_3^B(μ-H)Fe(NHN(Si$_2$))(CN^{t}Bu) (thin film, cm^{-1}): ν_{CN} = 1997; $\nu_{N\text{-}H}$ = 3197; $\nu_{B\text{-}H\text{-}Fe}$ = 2090 (br). IR of P_3^B(μ-D)Fe(NDN(Si$_2$))(CN^{t}Bu) (thin film, cm^{-1}): $\nu_{N\text{-}D}$ = 2377; $\nu_{B\text{-}D\text{-}Fe}$ = 1510 (br). Anal. Calcd. for $C_{47}H_{81}BFeN_3P_3Si_2$: C 62.45; H 9.03; N 4.65. Found: C 63.06; H 9.44; N 4.22.

3.4.3.6 [(P_3^B-H)Fe(CN^{t}Bu)][B($C_8H_3F_6$)$_4$]

A solution of P_3^B(μ-H)Fe(NHNSi$_2$)(CN^{t}Bu) **9** (28.5 mg, 0.0315 mmol, 1 equiv) in Et$_2$O (2 mL) was cooled to -78 °C. To this solution, a prechilled solution of [H(OEt$_2$)$_2$][B($C_8H_3F_6$)$_4$] (28.7 mg, 0.0284 mmol, 0.9 equiv) in Et$_2$O (2 mL) was added. The mixture was allowed to stir at -78 °C for 30 min then warmed to room temperature and stirred for an additional 30 min. The solvent was removed *in vacuo*, and the remaining purple foam was washed with pentane and then extracted into Et$_2$O. Isolation of the product as a crystalline purple solid was carried out by layering a concentrated Et$_2$O solution with pentane at -35 °C (35.1 mg, 77%). Crystals suitable for XRD analysis could be obtained in this fashion. ^{19}F NMR (THF-*d*$_8$; 376 MHz): δ -61.5. ^{1}H NMR (THF-*d*$_8$; 400 MHz): δ 28.7 (br), 11.7, 9.8, 7.8, 7.5, 5.3, 5.0, -0.5, -6.3. IR spectrum (thin film, cm^{-1}): $\nu_{B\text{-}H}$ = 2483; ν_{CN} = 2115.

3.4.3.7 Quantification of NH$_2$NSi$_2$

A solution of P_3^B(μ-H)Fe(NHNSi$_2$)(CN^{t}Bu) **9** (25.3 mg, 0.028 mmol, 1 equiv) was dissolved in Et$_2$O (2 mL) and cooled to -78 °C. Similarly a solution of

$[H(OEt_2)_2][B(C_8H_3F_6)_4]$ (28.3 mg, 0.028 mmol, 1 equiv) in Et_2O (2 mL) was cooled to -78 °C. The acid solution was added to the solution of **9** and the mixture was allowed to stir at low temperature for 10 min then at room temperature for an additional 30 min. After stirring was complete, the solutions were exposed to air and an aqueous solution of HCl was added (2 mL, 1 M in THF). After 24 h of stirring at room temperature, hydrazine could be detected according to the standard colorimetric method[30] using a reported calibration curve[31] (Yields of four runs: 57%, 61%, 62%, 66%). No NH_3 was detected in these reaction mixtures using the indophenol method.[32]

3.5 Notes and References

(1) Smil, V. Enriching the Earth. Boston: MIT Press; 2001.

(2) Reviews: (a) Howard, J. B.; Rees, D. C. *Chem. Rev.* **1996**, *96*, 2965-2982. (b) Burgess, B. K.; Lowe, D. J. *Chem. Rev.* **1996**, *96*, 2983-3012. (c) Hoffman, B. M.; Lukoyanov, D.; Yang, Z.-Y.; Dean, D. R.; Seefeldt, L. C. *Chem. Rev.* **2014**, *114*, 4041-4062.

(3) Representative experimental studies: (a) Yoo, S. J.; Angove, H. C.; Papaefthymiou, V.; Burgess, B. K.; Münck, E. *J. Am. Chem. Soc.* **2000**, *122*, 4926-4936. (b) Einsle, O.; Tezcan, F. A.; Andrade, S. L. A.; Schmid, B.; Yoshida, M.; Howard, J. B.; Rees, D. C. *Science* **2002**, *297*, 1696-1700. (c) Spatzal, T.; Aksoyoglu, M.; Zhang, L.; Andrade, S. L. A.; Schleicher, E.; Weber, S.; Rees, D. C.; Einsle, O. *Science* **2011**, *334*, 940. (d) Hoffman, B. M.; Lukoyanov, D.; Dean, D. R.; Seefeldt, L. C. *Acc. Chem. Res.* **2013**, *46*, 587-595. (e) Kowalska, J.; DeBeer, S. *Biochim. Biophys. Acta Mol. Cell Res.* **2015**, *1853*, 1406-1415.

(4) (a) Lowe, D. J.; Thornley, R. N. F. *Biochem. J.* **1984**, *224*, 877-886. (b) Lukoyanov, D.; Khadka, N.; Yang, Z.-Y.; Dean, D. R.; Seefeldt, L. C.; Hoffman, B. M. *J. Am. Chem. Soc.* **2016**, *138*, 10674-10683. (c) Lukoyanov, D.; Khadka, N.; Yang, Z.-Y.; Dean, D. R.; Seefeldt, L. C.; Hoffman, B. M. *J. Am. Chem. Soc.* **2016**, *138*, 1320-1327. (d) Morrison, C. N.; Spatzal, T.; Rees, D. C. *J. Am. Chem. Soc.* **2017**, *139*, 10856-10862.

(5) For representative reviews, see: (a) Chatt, J.; Dilworth, J. R.; Richards, R. L. *Chem. Rev.* **1978**, *78*, 589-625. (b) Schrock, R. R. *Acc. Chem. Res.* **2005**, *38*, 955-962. (c) Nishibayashi, Y. *Inorg. Chem.* **2015**, *54*, 9234-9247. (d) MacLeod, K. C.; Holland, P. L. *Nat. Chem.* **2013**, *5*, 559-565. (e) Stucke, N.; Flöser, B. M.; Weyrich, T.; Tuczek, F. *Eur. J. Inorg. Chem.* **2018**, *2018*, 1337-1355. (f) Roux, Y.; Duboc, C.; Gennari, M.; *ChemPhysChem* **2017**, *18*, 2606-2617.

(6) (a) Anderson, J. S.; Rittle, J.; Peters, J. C. *Nature* **2013**, *501*, 84-87. (b) Creutz, S. E. Peters, J. C. *J. Am. Chem. Soc.* **2014**, *136*, 1105-1115. (c) Ung, G.; Peters, J. C. *Angew. Chem. Int. Ed.* **2015**, *54*, 532-535. (d) Shogo, K.; Arashiba, K.; Nakajima, K.; Matsuo, Y.; Tanaka, H.; Ishii, K.; Yoshizawa, K.; Nishibayashi, Y. *Nat. Commun.* **2016**, *7*, 12181. (e) Hill, P. J.; Doyle, L. R.; Crawford, A. D.; Myers, W. K.; Ashley, A. E. *J. Am. Chem. Soc.*

2016, *138*, 13521-13524. (f) Buscagan, T. M.; Oyala, P. H.; Peters, J. C. *Angew. Chem. Int. Ed.* **2017**, *56*, 6921-6926.

(7) For a review of H_2 reductive elimination preceding N_2 binding and activation: Ballmann, J.; Munhá, R. F.; Fryzuk, M. D. *Chem. Commun.* **2010**, *46*, 1013-1025.

(8) Del Castillo, T. J.; Thompson, N. B.; Peters, J. C. *J. Am. Chem. Soc.* **2016**, *138*, 5341-5350.

(9) For a recent review see: Shima, T.; Hou, Z. *Top. Organomet. Chem.* **2017**, *60*, 23-43.

(10) Shima, T.; Hu, S.; Luo, G.; Kang, X.; Hou, Z. *Science* **2013**, *340*, 1549-1552.

(11) Select examples: (a) Fryzuk, M. D.; Love, J. B.; Rettig, S. J.; Young, V. G. *Science* **1997**, *275*, 1445-1447. (b) Pool, J. A.; Lobovsky, E.; Chirik, P. J. *Nature* **2004**, *427*, 527-530. (c) Fryzuk, M. D. *Acc. Chem. Res.* **2009**, *42*, 127-133. (d) Wang, B.; Luo, G.; Nishiura, M.; Hu, S.; Shima, T.; Luo, Y.; Hou, Z. *J. Am. Chem. Soc.* **2017**, *139*, 1818-1821.

(12) Similar reactivity with E-H substrates has been demonstrated for pre-functionalized, or products of, N_2 cleavage at monometallic centers: (a) Suess, D. L. M.; Peters, J. C. *J. Am. Chem. Soc.* **2013**, *135*, 4938-4941. (b) Liao, Q.; Cavaillé, A.; Saffon-Merceron, N.; Mézailles, N. *Angew. Chem. Int. Ed.* **2016**, *55*, 11212-11216.

(13) The reactivity of Fe-H for the cleavage of N=N bonds has been explored: (a) Smith, J. M.; Lachicotte, R. J.; Holland, P. L. *J. Am. Chem. Soc.* **2003**, *125*, 15752-15753. (b) Sadique, A. R.; Gregory, E. A.; Brennessel, W. W.; Holland, P. L. *J. Am. Chem. Soc.* **2007**, *129*, 8112-8121.

(14) Deegan, M. M.; Peters, J. C. *J. Am. Chem. Soc.* **2017**, *139*, 2561-2564.

(15) Fong, H.; Moret, M.-E.; Lee, Y.; Peters, J. C. *Organometallics* **2013**, *32*, 3053-3062.

(16) A solution of the species that was generated *in situ* from the precursor **1** was observed to completely decompose under an inert atmosphere in a sealed J. Young NMR tube over the course of ~2 hours at room temperature.

(17) Moret, M.-E.; Peters, J. C. *Angew. Chem. Int. Ed.* **2011**, *50*, 2063-2067.

(18) Solution symmetry has been observed in isoelectronic Rh and Ir hydride complexes at room temperature: (a) Kameo, H.; Hashimoto, Y.; Nakazawa, H. *Organometallics* **2012**, *31*, 3155-3162. (b) Kameo, H.; Hashimoto, Y.; Nakazawa, H. *Organometallics* **2012**, *31*, 4251-4258.

(19) Previously reported complexes supported by this ligand scaffold demonstrate that this ligand system can accommodate approximately three-fold symmetric B-H-Fe motifs. See ref. 14 and 15.

(20) The analogous CO complexes $P_3^BFe(CO)$ and $(P_3^B\text{-}H)Fe(CO)$ also have quite similar CO stretching frequencies, which are reported to be 1857 cm^{-1} and 1862 cm^{-1} respectively and the latter having a similar B-H stretch to $(P_3B\text{-}H)Fe(N_2)$ at 2588 cm^{-1}.

(21) Lee, Y.; Mankad, N. P.; Peters, J. C. *Nature Chem.* **2010**, *2*, 558-565.

(22) Moret, M.-E.; Peters, J. C. *J. Am. Chem. Soc.* **2011**, *133*, 18118-18121.

(23) Thompson, N. B.; Green, M. T.; Peters, J. C. *J. Am. Chem. Soc.* **2017**, *139*, 15312-15315.

(24) Attempts to identify the isotopically shifted N-D stretch were unsuccessful, complicated by the very weak intensity of these vibrations and our inability to isolate **8** as an analytically pure compound.

(25) This observation is noted in (Ref. 12a) for **10** and has been reproduced for **10-CN^{t}Bu**.

(26) (a) Brown, S. N.; Mayer, J. M. *J. Am. Chem. Soc.* **1994**, *116*, 2219-2220. (b) Brown, S. N.; Mayer, J. M. *J. Am. Chem. Soc.* **1996**, *118*, 12119-12133. (c) Matano, Y.; Brown, S. N.; Northcutt, T. O.; Mayer, J. M. *Organometallics* **1998**, *17*, 2939-2941. d) Williams, D. S.; Schrock, R. R. *Organometallics* **1993**, *12*, 1148-1160.

(27) (a) Jacobs, B. P.; Wolczanski, P. T.; Jiang, Q.; Cundari, T. R.; MacMillan, S. N. *J. Am. Chem. Soc.* **2017**, *139*, 12145-12148. b) Cundari, T. R.; Jacobs, B. P.; MacMillan, S. N.; Wolczanski, P. T. *Dalton Trans.* **2018**, *47*, 6025-6030.

(28) At higher temperatures, the thermal decay of the product becomes competitive and the transformation of **3.9** to **3.10** no longer exhibits isosbestic behavior.

(29) Direct comparison to the reported values for the Re(=O) complexes reported by Mayer and coworkers is complicated by the coordination of an additional exogenous ligand; however, in the detailed examination of phenyl-to-oxo migration for those complexes, an even larger, negative entropy of activation was found ($\Delta S^{\ddagger}$ = -20.5(25); see Ref. 24b).

(30) G. W. Watt, and J. D. Crisp, *Anal. Chem.*, 1952, **24**, 2006.

(31) J. Fajardo Jr., and J. C. Peters, *J. Am. Chem. Soc.*, 2017, **139**, 16105.

(32) M. W. Weatherburn, *Anal. Chem.*, 1967, **39**, 971.

Chapter 4

O-FUNCTIONALIZATION OF A COBALT CARBONYL GENERATES A TERMINAL COBALT CARBYNE

4.1 Introduction

One area of longstanding interest among synthetic inorganic and organometallic chemists is the study of species with metal-to-ligand multiple bonds (M=E, M≡E),[1] which serve as key intermediates in a variety of important synthetic and biological processes.[2] In recent years, there has been significant effort to extend these bonding motifs to late metal systems; relative to the mid-transition elements in groups 5 through 8, reports of late, and especially first row, metal systems that support strong, metal-ligand multiple bonds are less common, with reports of metal-to-ligand triple bonds (M≡E) almost exclusively limited to metal imidos.[3,4] For Co specifically, isolable examples of oxo[5,6] and carbyne[7,8,9] complexes having been reported only very recently; spectroscopic characterization of a terminal Co≡N species has also been reported.[10] Moving to the heavier group 9 elements, reports of Rh[11] and Ir[12] carbynes are similarly scarce (Figure 1A).

With this in mind, we became interested in targeting a pseudotetrahedral Co-carbyne complex for comparison to structurally-related Co-imido species[4d,13] and a recently reported Co-oxo complex[5] (Figure 1B). A substantial barrier to accessing carbynes beyond group 8 is the lack of synthetic strategies that are easily translated to late metal systems. One intriguing approach to carbyne generation that has seen successful application in groups 5 through 8 is via the reductive functionalization of metal-ligated CO or CN ligands (*i.e.,* $[M\text{-}C{\equiv}O]^{1-} + R^{+} \rightarrow M{\equiv}C\text{-}OR$; $[M\text{-}C{\equiv}N]^{1-} + 2\ R^{+} \rightarrow [M{\equiv}C\text{-}NR_2]^{+}$).[14,15] A challenge in translating this approach to a Co-system is overcoming its comparatively weak π-basicity, a byproduct of its enhanced electronegativity and contracted d-orbitals relative to earlier metal systems where this strategy has been successfully applied. For instance, comparing isostructural $[P_3^{Si}]$Fe(CO) and $[P_3^{Si}]$Co(CO), both with fully-populated orbitals of appropriate symmetry for π-backdonation into the CO ligand, moving from Fe to Co diminishes CO activation by ~50 cm^{-1} (Figure 1C).[15a,16] We postulated that

moving to a sufficiently reducing supporting ligand might afford access to productive CO-functionalization to generate a rare example of a group 9 metal carbyne.

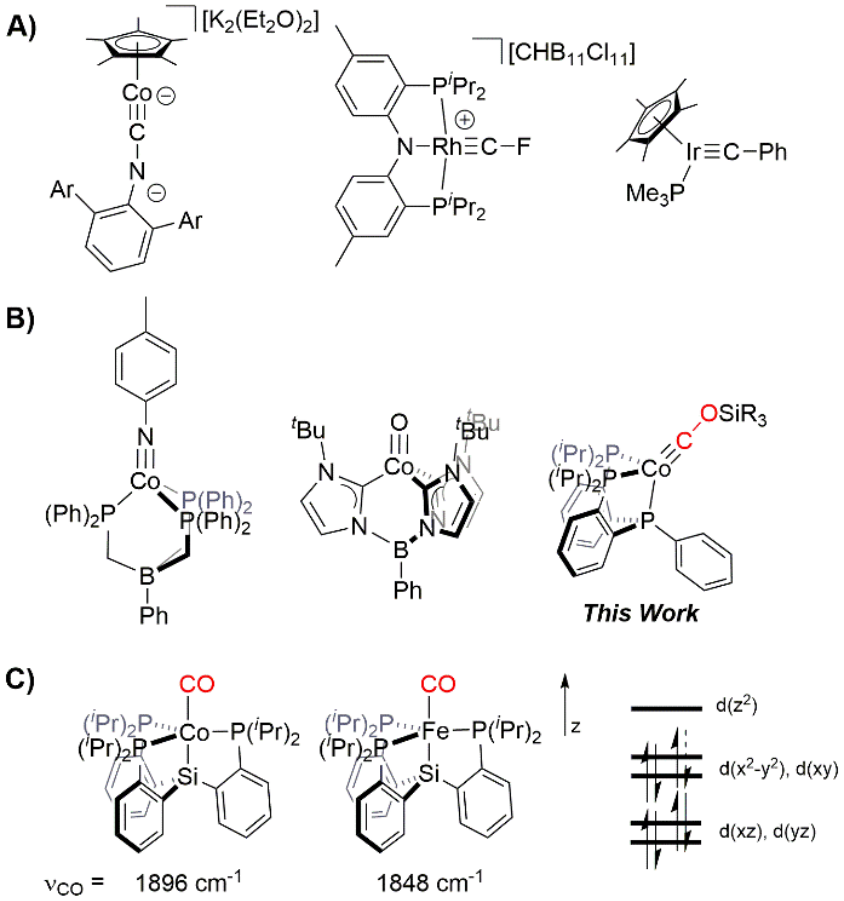

Figure 4.1. A) Examples of isolable terminal carbyne complexes of group 9 metals.[7,11b,12] B) Representative examples of Co complexes stabilized in a pseudotetrahedral coordination environment.[4d,5] C) Comparison of CO activation at isostructural Co^{I} and Fe^{I} complexes.[15a,16] For both species, orbitals of d-parentage are shown to the right; the d(xz), d(yz) are of appropriate symmetry for π-backdonation to CO orbitals and are fully populated. The additional electron for the Co complex is located in the xy plane (indicated by the dashed half-arrow).

4.2 Results and Discussion

4.2.1 Synthesis of Cobalt Carbonyl Complexes

Building upon recent work from our group,[17] we targeted the use of a trisphosphine (P_2^P = PhP(*o*-^{i}Pr$_2$PC$_6$H$_4$)$_2$) ligand. Initial access to the chemistry of [(P_2^P)Co] was provided by *in situ* ligation of $CoBr_2$ with P_2^P in THF, followed by one-electron reduction with Na naphthalenide to yield dark red (P_2^P)CoBr **4.1** (Scheme 1; 71% yield). In solution, the paramagnetically-shifted ^{1}H NMR spectrum and magnetic moment (2.7μ_B; Evans Method)

of **4.1** are consistent with a triplet ground state expected for a pseudotetrahedral Co^{I} complex. The crystal structure of **4.1** reveals a geometry that can be qualitatively described as lying between tetrahedral and trigonal pyramidal. In a quantitative sense, the geometric parameter τ_4, as described by Holland,[18] distinguishes between these limiting geometries, with a calculated τ_4 of 0.49 for **4.1**.

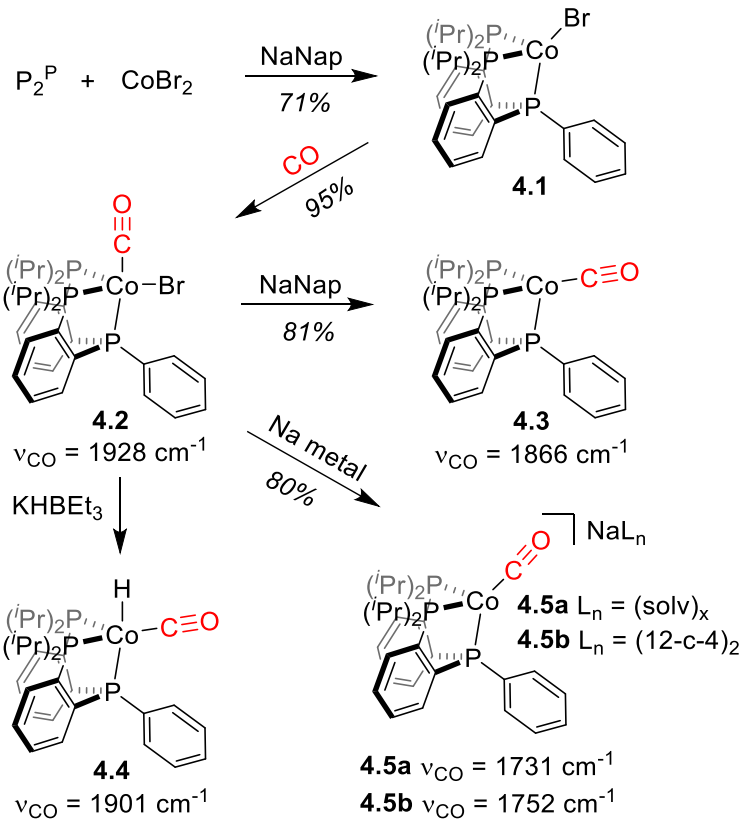

Scheme 4.1. Synthesis of [P_2^PCo] carbonyl complexes (Nap = Naphthalenide; 12-c-4 = 12-crown-4).

Complex **4.1** is a suitable precursor to monocarbonyl chemistry in this system; addition of an atmosphere of CO to a benzene solution of **4.1** resulted in the rapid formation of (P_2^P)CoBr(CO) **4.2** (Scheme 1; 95% yield). Diamagnetic **4.2** is generated as a 6:1 mixture of isomers in solution, as judged by NMR spectroscopy. In the solid state, **4.2** crystallizes with the CO ligand preferentially occupying the axial position of a distorted trigonal bipyramidal structure (τ_5 = 0.63[19]) opposite the central phosphine of the tris(phosphine) ligand.[20] The Co-ligated CO of **4.2** exhibits a diagnostic stretch at 1928 cm^{-1} (^{13}CO: 1884 cm^{-1}).

Reduction of **4.2** by addition of one equivalent of Na naphthalenide produces orange-red, zerovalent $P_2^PCo(CO)$ **4.3** (Scheme 1; 81% yield).[21] Spectroscopic data for this transformation shows a shift in the CO stretch to 1866 cm^{-1} (^{13}CO: 1824 cm^{-1}), and the concomitant appearance of a pseudo-axial EPR signal. In the solid state, **4.3** adopts a distorted trigonal pyramidal geometry (τ_4 = 0.82), with the CO ligand deviating toward coplanarity with Co and the two P^{iPr} ligands; a similarly distorted structure was obtained upon DFT-optimization (τ_4 = 0.87; see SI).[22] To confirm the absence of a hydride ligand in the structure of **4.3**, the hydride complex $P_2^PCo(CO)(H)$ **4.4** was targeted. Treating the $P_2^PCoBr(CO)$ complex **4.1** with an equivalent of $KHBEt_3$ provided clean access to **4.4**. By IR spectroscopy, an intense CO stretch is observed at 1901 cm^{-1}, with the hydride ligand observed in the NMR spectrum of **4.4** (-11.28 ppm, dt, *J* = 70, 50 Hz). Importantly, while the structures of **4.3** and **4.4** are of exceptional quality and, while similar, are crystallographically distinguishable, with the hydride ligand located in the structure of **4.4**.

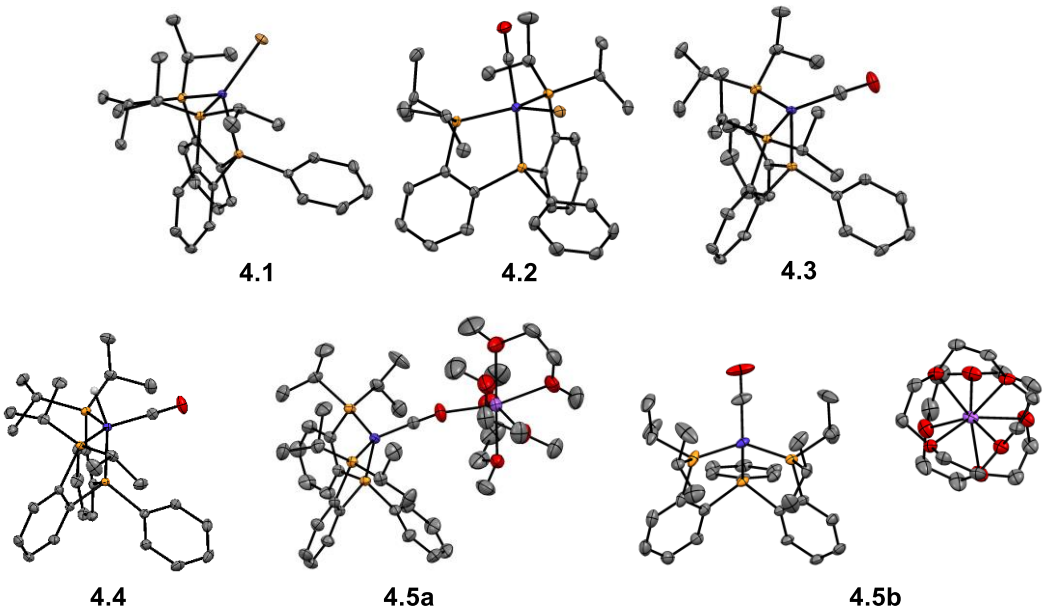

Figure 4.2. Crystal structures of Co complexes with ellipsoids shown at 50% probability. Hydrogen atoms, solvent molecules, and disorder are omitted for clarity.

A further reduction step proved accessible by stirring **4.2** over an excess of Na metal, generating the anionic Co(-1) complex, $[P_2^PCo(CO)][Na(solv)_x]$ **4.5a**; this species could also be isolated as its crown-encapsulated Na salt $[P_2^PCo(CO)][Na(12\text{-crown-}4)_2]$ **4.5b**. To our knowledge, among reported Co complexes, **4.5b** promotes the highest degree

of terminal CO activation, with the CO stretch observed in the IR spectrum of Na-capped **4.5a** at 1731 cm^{-1} (**4.5a-^{13}CO**: ν_{CO} = 1691 cm^{-1}), shifting to 1752 cm^{-1} in the crown-ether encapsulated Na salt **4.5b**. Like **4.1**, both **4.5a** and **4.5b** adopt a geometry lying between tetrahedral and trigonal pyramidal (τ_4 = 0.49), with strong π-backdonation into the ligands apparent from short Co-P distances (**4.5b**: 2.0838(8), 2.1191(8), 2.1304(7) Å vs. **4.3**: 2.1344(6), 2.1769(5), 2.1922(5) Å) and a contracted Co-C distance (**4.5b**: 1.733(3) Å vs. **4.3:** 1.752(2) Å), with corresponding elongation of the C-O bond (**4.5b**: 1.177(4) Å vs. **4.3**: 1.161(3) Å).[23]

4.2.2 O-Functionalization Reactivity

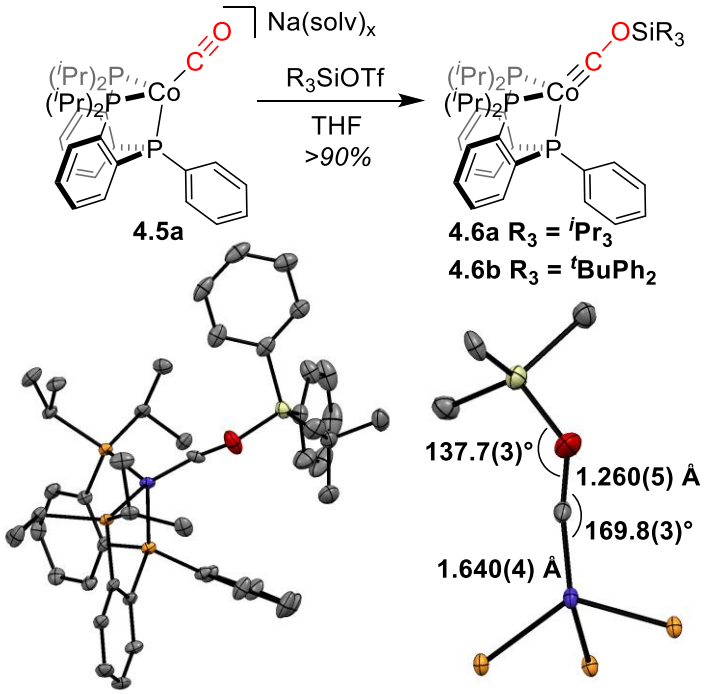

Figure 4.3. Reactivity of **4.5a** with silyl triflate electrophiles to generate carbyne **4.6** (top). The crystal structure of shown **4.6b** is shown with ellipsoids depicted at 50% probability; hydrogen atoms and disorder are omitted for clarity (bottom left). A truncated structure of **4.6b** is depicted highlighting the bonding in the carbyne ligand (bottom right).

Anionic **4.5a** exhibits a degree of CO activation comparable to the reduced Fe species [P_3^{Si}Fe(CO)][Na(THF)$_3$] (Figure 1A; ν(CO) = 1717 cm^{-1}) and, for the Na-capped structure, similar M-C (1.732(8) Å) and C-O (1.188(3) Å) bond distances.[15a] [P_3^{Si}Fe(CO)][Na(THF)$_3$] was successfully used to demonstrate CO-to-carbyne conversion via silylation, setting the stage to explore a related transformation with **4.5a** to afford a

terminal cobalt-carbyne. To our satisfaction, treating **4.5a**[24] with the sterically-hindered silyl-triflate electrophiles $^{i}Pr_3Si$- or $^{t}BuPh_2SiOTf$ promoted the clean generation of a new diamagnetic product (**4.6a** and **4.6b**, respectively) in both cases (>90% yield; Figure 3), void of the terminal Co-CO stretch observed in the IR spectrum of the precursor **4.5a**. In the $^{i}Pr_3SiOTf$ case, the assignment of **4.6a** as the product of O-functionalization of **4.5a** was corroborated by preparation of its ^{13}CO-labeled analog **4.6a-^{13}COSi^{i}Pr$_3$**. The solution IR difference spectrum of **4.6a** and **4.6a-^{13}COSi^{i}Pr$_3$** allowed for the identification of the C-O stretch in the fingerprint region of the spectrum at 1387 cm^{-1} (^{13}CO: 1347 cm^{-1}), higher than typically observed, for example, in silyl ethers (~1250 cm^{-1}), but clearly lower than bona fide C=O double bonds (>1650 cm^{-1}), consistent with the formation of a species that retains little C-O multiple bond character.[25] The ^{13}C NMR carbonyl resonance shifts from 227.2 ppm in **4.5a-^{13}CO** to 229.8 ppm in **4.6a-^{13}COSi^{i}Pr$_3$**.

Solid-state characterization of the $^{t}BuPh_2Si$-functionalized complex **4.6b** confirmed its assignment as a terminal carbyne complex (Figure 3). Substantial contraction in the Co-C bond distance (1.640(4) Å) and a corresponding elongation of the C-O distance (1.260(5) Å) occurs upon O-silylation from **4.5a** to **4.6b**. Slight bending is also observed in the Co-C-O angle (169.8(3)°) of **4.6b**, with substantial bending at the C-O-Si bond (137.7(3)°). Collectively, the structural and spectroscopic observations for complex **4.6** track closely with those made for similar CO-derived carbyne complexes of Fe,[15a,b] as well as other reported examples of Fischer-type carbyne complexes of Fe[15c,d,26] and the single, structurally characterized terminal Co-carbyne complex.[7]

4.2.3 Electronic Structure Comparison Across Pseudotetrahedral Co≡E Complexes

In reports of heteroatom-substituted carbynes of Fe (and most recently, Co), we and others have argued that complexes akin to **4.6** can be described with a formally low-valent metal center π-backdonating into a strongly accepting and hence Fischer-type carbyne ligand.[15a,7] In a limiting sense, this suggests that the electronic structure of **4.6** relates more closely to that of its precursor **4.5** than structurally-related Co(III) imido or oxo species. This idea is partially borne out in a computational comparison of a series of pseudotetrahedral Co complexes, including previously reported Co(O)[5] and Co(NAd)[27] species, as well as compounds **4.5a** and **4.6b** (Figure 4). In considering the electronic

structures of these compounds, the key distinguishing interactions are the Co-ligand π interactions. Combined, the spectroscopic observations and the computational MO picture are consistent with strong M-to-L multiple bonding, as is the case for the Co(O) and Co(NAd) compounds, and distinct from the anionic CO complex. However, for the Co(O) and Co(NAd) complexes, predominant localization of the vacant π* orbitals on Co, is consistent with π bonding interactions from the π-donating oxo and imido ligands to a relatively oxidized Co center. The polarity of these interactions is inverted in the carbyne complex **4.6b**, with π-donation from filled Co-localized orbitals into a strongly accepting carbyne ligand, akin to backbonding in the reduced carbonyl complex **4.5a**. While these comparisons suggest electronic structure perturbations across this series of compounds, simple consideration of formal oxidation state assignments fails to underscore the role of strong covalency required for the stabilization of these species.

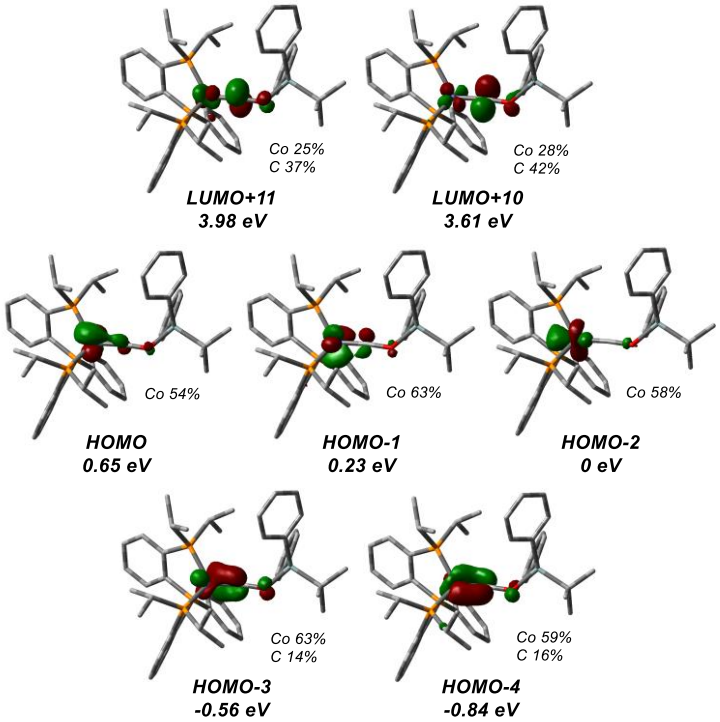

Figure 4.4. Select MOs derived from the DFT-optimized structure of **4.6b**. Orbital energies are listed relative to the HOMO-2 orbital in eV. Calculated contribution of Co d-orbitals for each MO are noted. C p-orbital contributions are noted where ≥ 10%. Lobal representations are shown with 0.07 isocontours.

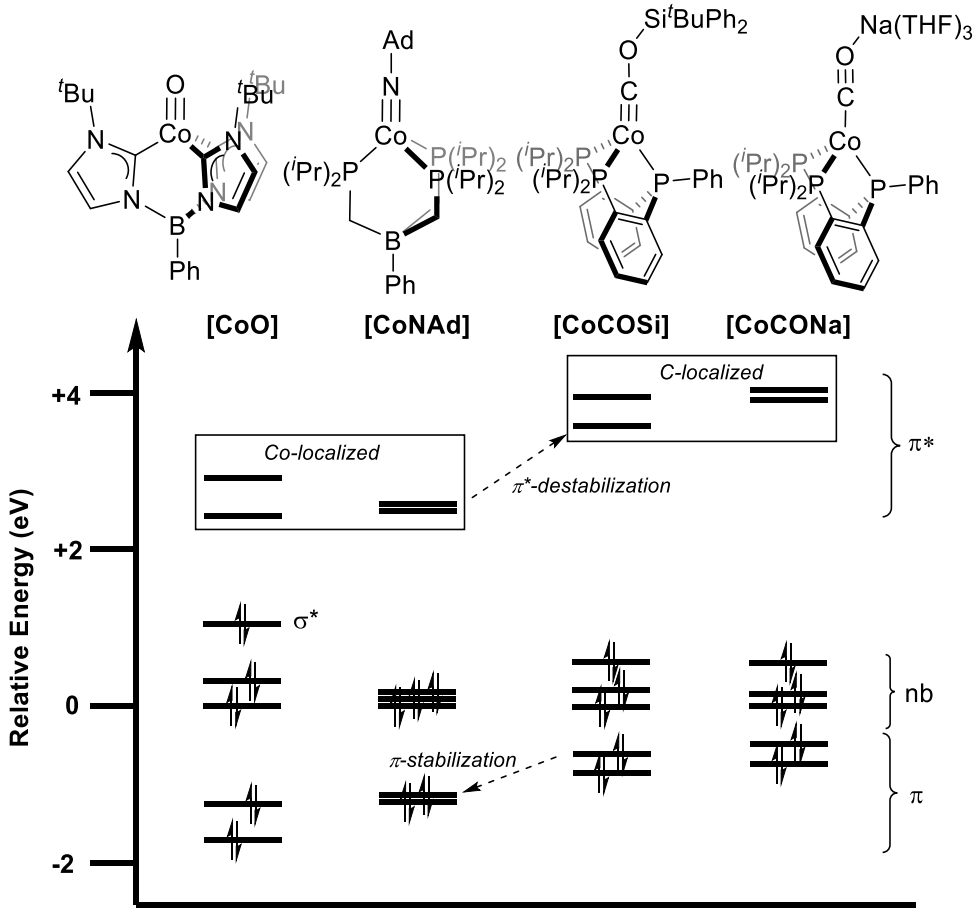

Figure 4.5. Comparison of MO splitting diagrams for pseudotetrahedral Co complexes obtained computationally (M06-L functional: def2tzvp (Co), def2svp (all other atoms)).[5,27] Relative orbital energies are referenced to the lowest energy Co-localized non-bonding orbital, in each case the HOMO-2 (see the Supporting Information for additional computational details).

4.3 Conclusions

To conclude, we have prepared a series of Co(CO) complexes, which, in the most reduced state, support a remarkable degree of terminal CO activation. This highly-reduced state is reactive towards O-functionalization with a silyl triflate electrophile to generate a very rare example of a terminal Co-carbyne complex. Like related iron and cobalt species, experimental and computational evidence support its assignment as a carbyne, with strong π-backdonation from Co to the carbyne ligand.

4.4 Experimental Section

4.4.1 General Considerations

All manipulations were carried out using standard Schlenk or glovebox techniques under an N_2 atmosphere. Solvents were deoxygenated and dried by thoroughly sparging with N_2 followed by passage through an activated alumina column in a solvent purification system by SG Water, USA LLC. Ethereal solvents (THF, Et_2O, DME) were dried further by stirring over Na/K alloy (>2 h) and were filtered through Celite prior to use. Deuterated benzene was purchased from Cambridge Isotope Laboratories, Inc., and dried by refluxing over Ca-H then distilled and stored over Na. Deuterated THF was purchased from Cambridge Isotope Laboratories and dried over Na/K alloy and was filtered through Celite prior to use. Reagents were purchased from commercial vendors and used without further purification unless otherwise noted. P_2^P was prepared according to a previously reported procedure.[17]

4.4.2 Physical Methods

NMR spectra (^1H, ^{13}C, and ^{31}P) were collected at room temperature (25 °C unless specified) on Varian 300 or 400 MHz spectrometers. ^1H and ^{13}C chemical shifts are reported in ppm, relative to tetramethylsilane using residual proton and ^{13}C resonances from solvent as internal standards. ^{31}P chemical shifts are reported in ppm relative to 85% aqueous H_3PO_4. IR spectra were obtained using a Bruker Alpha Platinum ATR spectrometer with OPUS software in a glovebox under an N_2 atmosphere. X-band EPR spectra were obtained on a Bruker EMX spectrometer with the samples prepared in a 2-MeTHF glass.

X-Ray diffraction and combustion analysis measurements were carried out in the Beckman Institute Crystallography Facility. XRD measurements were collected using a dual source Bruker D8 Venture, four-circle diffractometer with a PHOTON II detector or a Bruker D8 KAPPA with a PHOTON 100 detector. Structures were solved using SHELXT and refined against F^2 on all data by full-matrix least squares with SHELXL. The crystals were mounted on a glass fiber under Paratone N oil. See below for any special refinement details for individual data sets. Combustion analysis measurements were collected using a PerkinElmer 2400 Series II CHN Elemental Analyzer by facility staff.

4.4.3 Computational Methods

Geometry optimization and frequency calculations were carried out using the Gaussian 09 program.[28] The crystal structure coordinates of 3 and 5b were used in the input files. Reported DFT coordinates were used in the input file for the $PhB(^{t}BuIm)_3CoO$ complex.[5] The crystal coordinates of 4a were used in the input file, but the Na-coordinated DME molecules were replaced with THF molecules for optimization. For $BP_3Co(NAd)$ the crystal coordinates of the corresponding Fe complex[13a] were used in the input file, replacing Fe with Co. The M06-L functional[29] with def2-TZVP[30] basis set was used on Co with the def2-SVP basis set used on all other atoms.

4.4.4 Synthetic Details

4.4.4.1 P_2^PCoBr 4.1.

P_2^P (705.5 mg, 1.43 mmol) and $CoBr_2$ (312.0 mg, 1.43 mmol) were combined in THF (40 mL) in a 100 mL Schlenk tube, rapidly turning a muddy purple-brown color. Concurrently, a solution of sodium naphthalenide was prepared by stirring naphthalene (192.0 mg, 1.50 mmol, 1.05 equiv) over an excess of Na metal in THF (12 mL) over the course of 4 h. The naphthalenide solution was pipetted away from the excess Na metal and added to the prechilled Schlenk tube at -78 °C; this mixture was warmed to room temperature and then stirred for 3 h, yielding a dark red solution. The solvent was removed *in vacuo*, and the residue was triturated and then washed with pentane (2 x 10 mL). The dark residue was extracted into benzene and filtered through celite, with iterative addition of benzene to the dark residue until no additional colored material was brought into solution (~50 mL total). Concentration of this benzene solution and then crystallization by layering with pentane overnight allowed for the isolation of the product as a dark red crystalline solid (641.9 mg, 71%); crystals suitable for XRD were grown in an analogous fashion. Additional crystalline material could be isolated from the mother liquor by removing the solvent *in vacuo*, redissolving the residue in a minimal amount of benzene and layering with pentane. ^{1}H NMR (400 MHz, C_6D_6): δ 172.1, 94.1, 20.1, 10.1, 9.3, 8.4, 3.7, -0.8, -2.2, -8.9, -16.6. Solution magnetic moment (Evans Method): 25 °C: 2.7μ_B; -80 °C: 3.0 μ_B. Anal. Calcd. for $C_{30}H_{41}BrCoP_3$: C, 56.89; H, 6.52; N, 0.00. Found: C, 57.12; H, 6.52; N, < 0.1.

4.4.4.2 $P_2^PCoBr(CO)$ 4.2.

P_2^PCoBr **4.1** (244.9 mg, 0.387 mmol) was dissolved in benzene (30 mL) and transferred to a Schlenk tube. The solution was frozen and the headspace was evacuated; after thawing the solution, it was exposed to an atmosphere of CO. The tube was mixed vigorously at room temperature for 5 minutes before the solvent was removed *in vacuo*. The residue was washed with pentane (~10 mL) and the red-orange residue was extracted into benzene (~3 x 15 mL). Solvent removal by lyophilization yielded the product as an orange-red powder (244.2 mg, 95%). Consistent observation of two sets of ^{31}P resonances (~6:1) was attributed to the presence of two isomers of this complex. Resonances for both species are noted for the ^{31}P NMR spectrum including their approximate relative integrations. By ^{1}H NMR, only the ^{i}Pr methyl resonances are well resolved between the two species, so both sets are noted. Crystals suitable for XRD were grown by layering a concentrated toluene solution of **4.2** with pentane at -35 °C. ^{1}H NMR (400 MHz, C_6D_6): δ 7.55 (t, *J* = 7 Hz, 2H), 7.33 (d, *J* = 7 Hz, 2H), 7.26 (dd, *J* = 11, 7 Hz, 2H), 7.08-6.85 (overlapping m, 7H), 2.68 (m, *J* = 7Hz, 2H), 2.52 (br, 2H), 1.70 (q, *J* = 7 Hz, minor isomer), 1.59 (q, *J* = 7 Hz, 6H), 1.30 (q, *J* = 7 Hz, 6H), 1.23 (q, *J* = 7 Hz, minor isomer), 1.12 (q, *J* = 7 Hz, minor isomer), 1.04 (q, *J* = 7 Hz, minor isomer), 0.94 (q, *J* = 7 Hz, 6H), 0.88 (q, *J* = 7 Hz, 6H). $^{31}P\{^{1}H\}$ NMR (162 MHz, C_6D_6): δ 116.1 (t, *J* = 55 Hz, ~0.5P), 102.0 (t, *J* = 70 Hz, ~3P), 88.4 (d, *J* = 69 Hz, ~6P), 78.2 (d, *J* = 56 Hz, ~1P). $^{31}P\{^{1}H\}$ NMR (162 MHz, C_6D_6, ^{13}CO-labeled): δ 116.1 (m), 102.0 (apparent q, *J* = 70 Hz), 88.4 (dd, *J* = 70, 30 Hz), 78.2 (dd, *J* = 55, 37 Hz). $^{13}C\{^{1}H\}$ NMR (101 MHz, C_6D_6, ^{13}CO-labeled): δ 222.0 (dt, *J* = 62, 30 Hz). IR (thin film): ν_{CO} = 1928 cm^{-1}. IR (thin film, ^{13}CO): ν_{CO} = 1884 cm^{-1}. Anal. Calcd. for $C_{31}H_{41}BrCoOP_3$: C, 56.29; H, 6.25; N, 0.00. Found: C, 57.00; H, 6.24; N, < 0.1.

4.4.4.3 $P_2^PCo(CO)$ 4.3.

A solution of naphthalene (8.4 mg, 1 equiv) in THF (2 mL) was reduced by stirring over an excess of Na for 4 h. A red solution of $P_2^PCoBr(CO)$ **4.2** (43.5 mg, 1 equiv) in THF (3 mL) was cooled to -78 °C in the glovebox coldwell and the naphthalenide solution was decanted away from the excess Na metal and added. The mixture was allowed to stir at low temperature for an hour and then at room temperature for an additional 30 min, turning orange-red. The solvent was removed *in vacuo*, and the residue was triturated with pentane

(~1 mL) to give a red residue. The residue was then washed with pentane (3 x 1 mL) and then extracted into benzene (~5 mL). This solution was frozen and then lyophilized to yield the product as an orange-red powder (31.0 mg, 81%). Crystals suitable for XRD could be grown by evaporation of an Et_2O solution of **4.3** into MeCy. ^{1}H NMR (300 MHz, C_6D_6): δ 14.4 (br), 12.3 (br), 6.2 (br), 5.1 (br), 4.5 (br), -7.5 (br). IR (thin film): ν_{CO} = 1866 cm^{-1}. IR (thin film, ^{13}CO): ν_{CO} = 1824 cm^{-1}. Solution magnetic moment (Evans Method; 25 °C): 1.8 μ_B. Anal. Calcd. for $C_{31}H_{41}CoOP_3$: C, 64.03; H, 7.11; N, 0.00. Found: C, 64.07; H, 6.97; N, < 0.2.

4.4.4.4 $P_2^PCo(H)(CO)$ 4.4.

A solution of $P_2^PCoBr(CO)$ **4.2** (39.6 mg, 1 equiv) was prepared in THF and cooled to -78 °C. A slight excess of 1 M $KHBEt_3$ in THF (66 μL, 1.1 equiv) was added and the solution was stirred at low temperature for 1 h and then warmed to room temperature and stirred for an additional 1 h. The solvent was removed and the residue was washed with pentane and then extracted into benzene, yielding the desired product upon lyophilization. The hydride product is observed as a mixture of isomers in solution, with a minor component (<5%) reproducibly observed in the ^{1}H and ^{31}P NMR spectra of this compound. Given the small fraction of the material observed as the minor isomer, NMR data is listed only for the major isomer. Crystals suitable for XRD could be grown by evaporation of an Et_2O solution of the complex into MeCy. ^{1}H NMR (400 MHz, C_6D_6): δ 7.68 (t, *J* = 7 Hz, 2H), 7.51 (m, 2H), 7.37 (d, *J* = 7 Hz, 2H), 7.09-6.93 (m, 7H), 2.26 (overlapping hept, *J* = 7 Hz, 4H), 1.30 (q, *J* = 7 Hz, 6H), 1.03 (m, 12H), 0.77 (q, *J* = 7 Hz, 6H), -11.28 (dt, *J* = 70, 50 Hz, 1H). ^{31}P{^{1}H} NMR (162 Hz, C_6D_6): δ 115.3 (br, 1P), 107.4 (br, 2P). IR (thin film): ν_{CO} = 1901 cm^{-1}.

4.4.4.5 $[P_2^PCo(CO)][Na(S)_n]$ 4.5a.

An excess of Na metal was added to a THF solution (5 mL) of $P_2^PCoBr(CO)$ **2** (53.5 mg) and was stirred at room temperature turning very dark brown/black over the course of several hours. Thin film IR spectra of reaction aliquots were collected to monitor the conversion of **4.2** to **4.5a** over time. Once the reaction proceeded to completion, the solvent was transferred away from remaining Na and then removed *in vacuo*. The resultant residue was triturated and then washed with pentane. Subsequent extraction into benzene and

lyophilization yielded the desired product as a dark brown powder (53.2 mg; ~80% yield assuming $(S)_n$ = $(THF)_3$). Crystals suitable for XRD could be grown by dissolving the complex in a minimum of 1:1 toluene/DME and layering with pentane at -35 °C. The 12-crown-4 salt **4.5b** could be prepared by addition of 12-crown-4 (2 equiv) to a THF solution of the complex and then removing the solvent *in vacuo* and washing with benzene. ^{31}P NMR spectra of the complex **4.5a** were consistently very broad. ^{1}H NMR (400 MHz, C_6D_6): δ 7.81 (s, 2H), 7.59 (d, *J* = 7 Hz, 2H), 7.37 (m, 2H), 7.1-6.9 (overlapping m, 7H), 2.49 (br, 2H), 2.27 (br, 2H), 1.41 (br, 6H), 1.10 (br, 6H), 1.03 (br, 6H), 0.89 (br, 6H). ^{31}P{^{1}H} NMR (162 Hz, C_6D_6/THF): δ 80-120 (br). ^{13}C{^{1}H} NMR (101 Hz, C_6D_6): δ 227.2 (^{13}CO). IR (thin film): 1731 cm^{-1}. IR (thin film, ^{13}CO): 1691 cm^{-1}. IR (thin film, **4.5b**): 1752 cm^{-1}. Anal. Calcd. for . $C_{47}H_{73}CoNaO_9P_3$ **4.5b**: C, 58.99; H, 7.69; N, 0.00. Found: C, 58.51; H, 7.74; N, < 0.25.

4.4.4.6 $P_2^PCo(COSi^iPr_3)$ 4.6a.

A solution of $P_2^PCoBr(CO)$ **4.2** (40.5 mg, 1 equiv) was stirred over an excess of Na metal in THF (5 mL) until conversion to **4.5a** was observed with darkening of the reaction mixture. Complete conversion was confirmed by obtaining a thin film IR spectrum of a reaction aliquot. The resulting solution was decanted away from residual Na metal and cooled to -78 °C in a glovebox cold well. To the cooled solution, neat $^{i}Pr_3SiOTf$ (16.5 µL, 1 equiv) was added and the mixture was stirred at -78 °C for 15 min and then at room temperature for an additional 15 min, turning deep red. The solvent was removed *in vacuo* and then the residue was triturated with pentane (2 mL) and then extracted into pentane (5 mL). Removal of the solvent *in vacuo* yielded the product as a red foam (44.3 mg, > 95%). Minor quantities of products of unproductive reactivity (<5%) were typically observed in spectra of the isolated materials. ^{1}H NMR (400 MHz, C_6D_6): δ 7.82 (t, *J* = 6 Hz, 2H), 7.75 (t, *J* = 8 Hz, 2H), 7.64 (d, *J* = 7 Hz, 2H), 7.22-7.05 (overlapping m, 7H), 2.68 (hept, *J* = 7 Hz, 2H), 2.34 (hept, *J* = 7 Hz, 2H), 1.59 (dd, *J* = 15, 7 Hz, 6H), 1.37-1.09 (overlapping m, 33H), 1.01 (dd, *J* = 12, 6 Hz, 6H). ^{31}P{^{1}H} NMR (162 Hz, C_6D_6): δ 103.3 (br, 2P), 97.2 (br, 1P). ^{13}C{^{1}H} NMR (101 Hz, C_6D_6): 229.8 (^{13}CO). IR (thin film): ν_{CO} = 1387 cm^{-1}. IR (thin film, ^{13}CO): ν_{CO} = 1347 cm^{-1}.

4.4.4.7 $P_2^PCo(COSi^tBuPh_2)$ 4.6b.

As for **4.6a**, a solution of the reduced CO complex **4.5a** was prepared from **4.2** (56.5 mg, 0.085 mmol, 1 equiv) in THF (5 mL). Neat ^{t}BuPh$_2$SiOTf (33.2 mg, 1 equiv) was added to a stirring solution **4.5a** at -78 °C and allowed to stir for 15 min and then was warmed to room temperature and stirred for an additional 15 min, turning red. The solvent was removed *in vacuo* and then the residue was triturated with pentane (2 mL) and then extracted into pentane (5 mL). Removal of the solvent *in vacuo* yielded the product as a red foam (65.8 mg, 94%). Crystals suitable for X-ray diffraction were obtained by slow evaporation of a pentane solution into MeCy. Minor quantities of products of unproductive reactivity (<5%) were typically observed in spectra of the isolated materials. ^{1}H NMR (400 MHz, C_6D_6): δ 7.91 (m, 4H), 7.82-7.68 (overlapping m, 5H), 7.51 (dd, *J* = 6, 3 Hz, 2H), 7.15-7.06 (m, 8H), 7.01 (m, 4H), 2.42 (hept, *J* = 7 Hz, 2H), 2.21 (hept, *J* = 7 Hz, 2H), 1.26 (dd, *J* = 16, 7 Hz, 6H), 1.15-1.07 (dd, 6H), 1.12 (s, 9H), 1.02 (dd, *J* = 12, 7 Hz, 6H), 0.90 (dd, *J* = 12, 7 Hz, 6H). ^{31}P{^{1}H} NMR (162 Hz, C_6D_6): δ 103.8 (br, 2P), 97.4 (br, 1P). Anal. Calcd. for $C_{47}H_{60}CoOP_3Si$: C, 68.77; H, 7.37; N, 0.00. Found: C, 68.86; H, 7.78; N, < 0.20.

4.5 References and Notes

(1) Nugent, W. A.; Mayer, J. M. *Metal-ligand Multiple Bonds*, Wiley, New York, 1988.

(2) (a) Hartwig, J. F. *Organotransition Metal Chemistry: From Bonding to Catalysis*, University Science, 2010. (b) Gray, H. B.; Stiefel, E. I.; Valentine, J. S.; Bertini, I. *Biological Inorganic Chemistry: Structure and Reactivity*, University Science, 2006.

(3) For reviews, see: (a) Saouma, C. T.; Peters, J. C. *Coord. Chem. Rev.* **2011**, *255*, 920-937. (b) Ray, K.; Heims, F.; Pfaff, F. F. *Eur. J. Inorg. Chem.* **2013**, *2013*, 3784-3807.

(4) For select early examples of metal-to-ligand multiple bonding in late metal systems, see: (a) Glueck, D. S.; Hollander, F. J.; Bergman, R. G. *J. Am. Chem. Soc.* **1989,** *111***,** 2719-2721. (b) Hay-Motherwell, R. S.; Wilkinson, G.; Hussain-Bates, B.; Hursthouse, M. B. *Polyhedron* **1993**, *12*, 2009-2012. (c) Mindiola, D. J.; Hillhouse, G. L. *J. Am. Chem. Soc.* **2001**, *123*, 4623-4624. (d) Jenkins, D. M.; Betley, T. A.; Peters, J. C. *J. Am. Chem. Soc.* **2002**, *124*, 11238-11239. (e) Poverenov, E.; Efremenko, I.; Frenkel, A. I.; Ben-David, Y.; Shimon, L. J. W.; Leitus, G.; Konstantinovski, L.; Martin, J. M. L.; Milstein, D. *Nature* **2008**, *455*, 1093-1096.

(5) (a) Goetz, M. K.; Hill, E. A.; Filatov, A. S.; Anderson, J. S. *J. Am. Chem. Soc.* **2018**, *140*, 13176-13180. (b) Goetz, M. K.; Anderson, J. S.; *J. Am. Chem. Soc.* **2019**, *141*, 4051-4062.

(6) For reports of transient Co-oxo complexes, see: (a) Wang, B.; Lee, Y.-M.; Tcho, W.-Y.; Tussupbayev, S.; Kim, S.-T.; Kim, Y.; Seo, M. S.; Cho, K.-B.; Dede, Y.; Keegan, B. C.; Ogura, T.; Kim, S. H.; Ohta, T.; Baik, M.-H.; Ray, K.; Shearer, J.; Nam, W. *Nat. Commun.* **2017**, *8*, 14839. (b) Andris, E.; Navrátil, R.; Jašik, J.; Srnec, M.; Rodríguez, M.; Costas, M.; Roithová, J. *Angew. Chem. Int. Ed.* **2019**, *58*, 9619-9624.

(7) Mokhtarzadeh, C. C.; Moore, C. E.; Rheingold, A. L.; Figueroa, J. S. *J. Am. Chem. Soc.* **2018**, *140*, 8100-8104.

(8) Note that Fortune and Manning reported the first generation of a Co-carbyne species via S-methylation of a terminal CS complex. However, the data available are insufficient to reliably distinguish the terminal $Co{\equiv}CSMe^{+}$ carbyne formulation from an η^2-bound $Co\{CS(Me)\}^{+}$ isomer, where the methyl is instead bound to carbon to give a thioacyl complex, as noted by Hill (Ref. 9). See: Fortune, J.; Manning, A. R. *Organometallics* **1983**, *2*, 1719-1723.

(9) (a) Hill, A. F. In *Transition Metal Carbyne Complexes*, ed. Kreißl, F.R.; Springer, Dordrecht, Diversions *En Route* to Alkylidyne Complexes of Iron, 1993. (b) Cade, I. A.; Hill, A. F.; McQueen, C. M. A. *Dalton Trans.* **2019**, *48*, 2000-2012.

(10) Zolnhofer, E. M.; Käß, M.; Khusniyarov, M. M.; Heinemann, F. W.; Maron, L.; van Gastel, M.; Bill, E.; Meyer, K. *J. Am. Chem. Soc.* **2014**, *136*, 15072-15078.

(11) (a) Rapport, T.; Nürnberg, O.; Mahr, N.; Wolf, J.; Werner, H. *Organometallics* **1992**, *11*, 4156-4164. (b) Pell, C. J.; Zhu, Y.; Huacuja, R.; Herbert, D. E.; Hughes, R. P.; Ozerov, O. V. *Chem. Sci.* **2017**, *8*, 3178-3186. (c) Cho, H.-G.; Andrews, L. *Organometallics* **2010**, *29*, 2211-2222.

(12) Luecke, H. F.; Bergman, R. G. *J. Am. Chem. Soc.* **1998**, *120*, 11008-11009.

(13) (a) Betley, T. A.; Peters, J. C. *J. Am. Chem. Soc.* **2003**, *125*, 10782-10783. (b) Hu, X.; Meyer, K. *J. Am. Chem. Soc.* **2004**, *126*, 16322-16323. (c) Shay, D. T.; Yap, G. P. A.; Zakharov, L. N.; Rheingold, A. L.; Theopold, K. H. *Angew. Chem. Int. Ed.* **2005**, *44*, 1508-1510. (d) Mehn, M. P.; Brown, S. D.; Jenkins, D. M.; Peters, J. C.; Que, L. *Inorg. Chem.* **2006**, *45*, 7417-7427. (e) Cowley, R. E.; Bontchev, R. P.; Sorrell, J.; Sarracino, O.; Feng, Y.; Wang, H.; Smith, J. M. *J. Am. Chem. Soc.* **2007**, *129*, 2424-2425. (f) Wu, B.; Hernández-Sánchez, R.; Bezpalko, M. W.; Foxman, B. M.; Thomas, C. M. *Inorg. Chem.* **2014**, *53*, 10021-10023. (g) Liu, Y.; Du, J.; Deng, L. *Inorg. Chem.* **2017**, *56*, 8278-8286.

(14) For select examples, see: (a) Carnahan, E. M.; Protasiewicz, J. D.; Lippard, S. J. *Acc. Chem. Res.* **1993**, *26*, 90-97. (b) Pombeiro, A. J. L.; Hughes, D. L.; Pickett, C. J.; Richards, R. L. *J. Chem. Soc., Chem. Commun.* **1986**, 246-247. (c) Hughes, D. L.; Mohammed, M.

Y.; Pickett, C. J. *J. Chem. Soc., Chem. Commun.* **1989**, 1399-1400. (d) Hughes, D. L.; Ibrahim, S. K.; Ali, H. M.; Pickett, C. J. *J. Chem. Soc., Chem. Commun.* **1994**, 425-427.

(15) For carbynes derived from CO/CN functionalization at Fe, see: (a) Lee, Y.; Peters, J. C. *J. Am. Chem. Soc.* **2011**, *133*, 4438-4446. (b) Suess, D. L. M.; Peters, J. C. *J. Am. Chem. Soc.* **2013**, *135*, 12580-12583. (c) Rittle, J.; Peters, J. C. *Angew. Chem. Int. Ed.* **2016**, *55*, 12262-12265. (d) Rittle, J.; Peters, J. C. *J. Am. Chem. Soc.* **2017**, *139*, 3161-3170.

(16) Whited, M. T.; Mankad, N. P.; Lee, Y.; Oblad, P. F.; Peters, J. C. *Inorg. Chem.* **2009**, *48*, 2507-2517.

(17) (a) Buscagan, T. M.; Oyala, P. H.; Peters, J. C. *Angew. Chem. Int. Ed.* **2017**, *56*, 6921-6926. (b) Schild, D. J.; Peters, J. C. *ACS Catal.* **2019**, *9*, 4286-4295.

(18) (a) Vela, J.; Stoian, S.; Flaschenriem, C. J.; Münck, E.; Holland, P. L. *J. Am. Chem. Soc.* **2004**, *126*, 4522-4523. (b) Vela, J.; Cirera, J.; Smith, J. M.; Lachicotte, R. J.; Flaschenriem, C. J.; Alvarez, S.; Holland, P. L. *Inorg. Chem.* **2007**, *46*, 60-71.

(19) Addison, A. W.; Rao, T. N.; Reedijk, J.; van Rijn, J.; Verschoor, G. C. *J. Chem. Soc., Dalton Trans.* **1984**, 1349-1356.

(20) A second, minor component (~4%) was present in the crystal structure of this complex (see SI).

(21) For select examples of zerovalent Co compounds, see: (a) Keller, H. J.; Wawersik, H. *Z. Naturforsch., B: J. Chem. Sci.* **1965**, *20*, 938-942. (b) Crichton, O.; Poliakoff, M.; Rest, A. J.; Turner, J. J. *J. Chem. Soc., Dalton Trans.* **1973**, *12*, 1321-1324. (c) Margulieux, G. W.; Weidemann, N.; Lacy, D. C.; Moore, C. E.; Rheingold, A. L.; Figueroa, J. S. *J. Am. Chem. Soc.* **2010**, *132*, 5033-5035. (d) Ung, G.; Rittle, J.; Soleilhavoup, M.; Bertrand, G.; Peters, J. C. *Angew. Chem. Int. Ed.* **2014**, *53*, 8427-8431. (e) Rudd, P. A.; Liu, S.; Gagliardi, L.; Young, V. G.; Lu, C. C. *J. Am. Chem. Soc.* **2011**, *133*, 20724-20727. (f) Mo, Z.; Chen, D.; Leng, X.; Deng, L. *Organometallics* **2012**, *31*, 7040-7043.

(22) For factors contributing to structural distortions of four-coordinate Co complexes see: (a) Detrich, J. L.; Konečný, R.; Vetter, W. M.; Doren, D.; Rheingold, A. L.; Theopold, K. H. *J. Am. Chem. Soc.* **1996**, *118*, 1703-1712. (b) DuPont, J. A.; Yap, G. P. A.; Riordan, C. G. *Inorg. Chem.* **2008**, *47*, 10700-10707. (c) Jenkins, D. M.; Di Bilio, A. J.; Allen, M. J.; Betley, T. A.; Peters, J. C. *J. Am. Chem. Soc.* **2002**, *124*, 15336-15350.

(23) The bond distances for **4.3** are listed for one of two structurally similar molecules in the asymmetric unit.

(24) Use of the crown-encapsulated salt **4.5b** led to the formation of a mixture of carbyne **4.6** and carbonyl **4.3**.

(25) (a) Shaterian, H. R.; Shahrekipoor, F.; Ghashang, M. *J. Mol. Catal. A: Chem.* **2007**, *272*, 142-151. (b) Günzler, H.; Gremlich, H.-U. *IR Spectroscopy,* Wiley-VCH, Weinheim, 2002.

(26) (a) Fischer, E. O.; Schneider, J.; Neugebauer, D. *Angew. Chem., Int. Ed. Engl.* **1984**, *23*, 820−821. (b) Anderson, S.; Hill, A. F. *J. Organomet. Chem.* **1990**, *394*, C24-C26. (c) Anderson, S.; Hill, A. F.; Ng, Y. T. *Organometallics* **2000**, *19*, 15-21. (d) Mokhtarzadeh, C. C.; Moore, C. E.; Rheingold, A. L.; Figueroa, J. S. *Angew. Chem. Int. Ed.* **2017**, *56*, 10894-10899.

(27) Betley, T. A. Ph.D. Dissertation, California Institute of Technology, 2005.

(28) Gaussian 09, Revision B.01, M. J. Frisch, G. W. Trucks, H. B. Schlegel, G. E. Scuseria, M. A. Robb, J. R. Cheeseman, G. Scalmani, V. Barone, B. Mennucci, G. A. Petersson, H. Nakatsuji, M. Caricato, X. Li, H. P. Hratchian, A. F. Izmaylov, J. Bloino, G. Zheng, J. L. Sonnenberg, M. Hada, M. Ehara, K. Toyota, R. Fukuda, J. Hasegawa, M. Ishida, T. Nakajima, Y. Honda, O. Kitao, H. Nakai, T. Vreven, J. A. Montgomery Jr., J. E. Peralta, F. Ogliaro, M. Bearpark, J. J. Heyd, E. Brothers, K. N. Kudin, V. N. Staroverov, R. Kobayashi, J. Normand, K. Raghavachari, A. Rendell, J. C. Burant, S. S. Iyengar, J. Tomasi, M. Cossi, N. Rega, J. M. Millam, M. Klene, J. E. Knox, J. B. Cross, V. Bakken, C. Adamo, J. Jaramillo, R. Gomperts, R. E. Stratmann, O. Yazyev, A. J. Austin, R. Cammi, C. Pomelli, J. W. Ochterski, R. L. Martin, K. Morokuma, V. G. Zakrzewski, G. A. Voth, P. Salvador, J. J. Dannenberg, S. Dapprich, A. D. Daniels, Ö. Farkas, J. B. Foresman, J. V. Ortiz, J. Cioslowski, D. J. Fox, Gaussian, Inc., Wallingford CT, 2009.

(29) Zhao, Y.; Truhlar, D. G. *J. Chem, Phys.* **2006**, *125*, 194101.

(30) Weigend, F.; Ahlrichs, R. *Phys. Chem. Chem. Phys.* **2005**, *7*, 3297-3305.

Chapter 5

UNUSUAL REACTIVITY MODES OF NON-CLASSICAL DIHYDROGEN COMPLEXES

5.1 Introduction

Longstanding interest in the study of non-classical dihydrogen adducts and isomeric transition metal dihydrides derives from their ubiquity in H_2-consuming or evolving processes.[1,2] Transition metal hydrides access diverse reactivity patterns, with the ability to serve as a source of protons,[3] H-atoms,[4] or hydrides[5] depending on the nature of the hydride-ligated transition metal center and supporting ligands. In contrast, typical reactivity patterns of intact non-classical adducts are far less diverse, despite dihydrogen's remarkable flexibility as a weak ligand, with the ability to interact with nearly any system with an open coordination site. This can be rationalized by consideration of the canonical bonding description for dihydrogen adducts, where σ-donation to Lewis acidic, often cationic transition metal centers imparts substantial acidic character to the coordinated H_2 ligand. In contrast, increased π-backdonation in electron rich systems elongates the H-H distance, ultimately yielding the dihydride products of oxidative addition, rather than stabilizing 'hydridic' H_2 adducts.

Like Kubas's seminal complex,[6] the majority of non-classical H_2 adducts that have been studied are stabilized by coordinatively saturated d^6 systems of the 4d and 5d metals.[1,2] More recent work has led to the discovery of comparatively exotic non-classical adducts of Fe, Co, and Ni, including the first well-characterized doublet[7], anionic[8], and formally d^{10} H_2 adducts[9] of any transition metal (Figure 5.1). Given the unusual nature of these species, we wondered whether they might access reactivity patterns distinct from more typical H_2 adducts, which have been frequently studied as Brønsted acids. Drawing a simple analogy to the chemistry of transition metal hydrides, we hypothesized that coordination of H_2 to either a half-integer spin or anionic metal center might impart significant H-atom donor ability or hydricity, respectively, to the intact H_2 ligand (Figure 5.1D).

In this chapter, we describe the reactivity of isostructural $[Co(H_2)]^{\bullet}$ and $[Co(H_2)]^{1-}$ complexes toward H-atom and hydride transfer reactivity. The radical H_2 adduct is found

to serve as a competent H-atom donor to well-defined organic radicals (TEMPO•, $^{t}Bu_3ArO$•). Further, the anionic H_2 adduct proves to be a remarkably strong hydride donor, serving as a suitable precursor for the transfer of a hydride equivalent to a variety of acceptors, including BEt_3 to generate a borohydride ($KHBEt_3$) equivalent. Combined these transformations establish the thermodynamic viability of H_2 adducts as H-atom or hydride donors. The central question in this chemistry is whether these transformations can proceed directly from intact H_2 adducts rather than through their dihydride isomers generated *via* initial oxidative addition steps. For the reactions described here, the kinetically preferred pathways are not experimentally discernable. As such, discussion of these reactions is augmented by consideration of factors dictating the kinetically preferred pathway for M-H_2 deprotonation chemistry and the extent to which these factors are relevant to H-atom and hydride transfer reactivity.

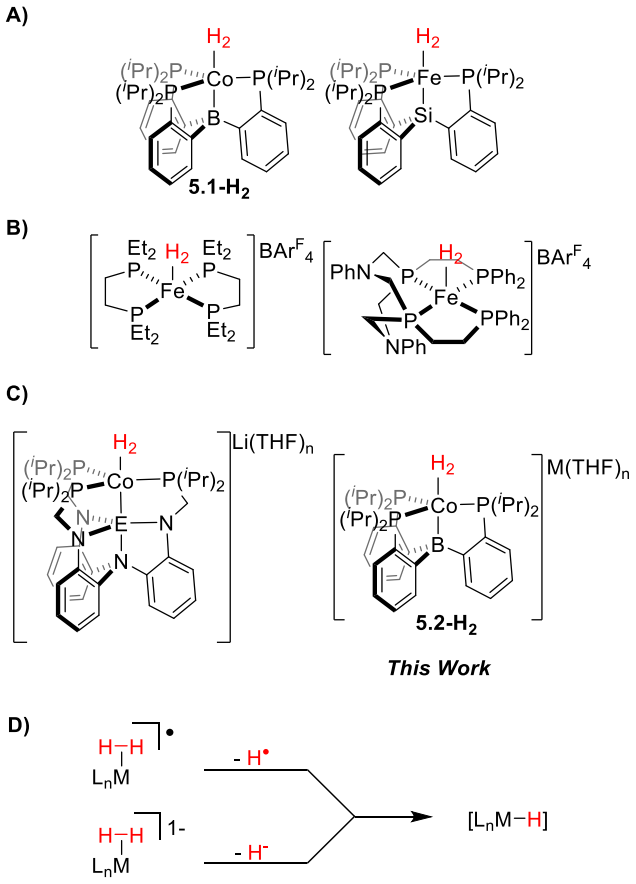

Figure 5.1. Examples of (**A, B**) half-integer spin[7] and (**C**) anionic[8] non-classical H_2 adducts (E = Al, Ga, In; M = Na, K). (**D**) General reactivity patterns targeted for radical and anionic dihydrogen adducts.

5.2 Results and Discussion

5.2.1 Synthesis of $[P_3^BCo\text{-}H_2]^{0/1-}$ Complexes

Towards exploring unusual reactivity patterns of H_2 adducts, we targeted the study of a system where isostructural half-integer spin and anionic H_2 adducts could be supported. While no such redox pairs have been reported, we postulated that one-electron reduction of $P_3^BCo(H_2)$ **5.1-H₂**, a well-characterized example of an $S = 1/2$ H_2 adduct[77b,c] would yield the anionic non-classical adduct bearing significant structural analogy to the complexes reported by Lu and coworkers (Figure 5.1C).[8] Accordingly, access to the anionic Co-H_2 adduct **5.2-H₂** was provided by reduction of P_3^BCoBr with strong reductants, such as K metal or Na naphthalenide under an H_2 atmosphere.[7b,10] NMR spectroscopic characterization of the resultant deep red solution showed the clean generation of a new diamagnetic species, $[P_3^BCo(H_2)][M(THF)_n]$ **5.2-H₂**. In the ^1H NMR spectrum of **5.2-H₂** the dihydrogen peak is observed at -8.58 ppm, with measurement of a short relaxation time (T_{1min} = 26 ms, 500 MHz) for this resonance consistent with its assignment as an intact H_2 ligand. Complex **5.2-H₂** was found to be stable to vacuum, but irreversibly formed the N_2 adduct $[P_3^BCo(N_2)][K(THF)_n]$ **5.2-N₂** when exposed to N_2.[11] Further corroboration of its assignment as the intact H_2 adduct was provided by preparation of the analogous H-D complex **5.2-HD** by exposure of **5.2-H₂** to a 1:1 mixture of H_2 and D_2, with J_{HD} = 29.5(4) Hz.[12] From the measured values of T_{1min} (corrected for dipolar interactions) and J_{HD}, predicted H-H distances were found to be 0.93(1) Å and 0.94(1) Å, respectively (see Appendix B for details).[13]

Table 5.1. Comparison of NMR parameters for anionic H_2 adducts of Co (Figure 5.1C). The value *r* is the ratio of the Co-M distance to the sum of the atomic radii.[8] [a]Determined computationally.

Parameter	5.2-H₂	M = Al	M = Ga	M = In
J_{HD}	29.5(4)	28.5(3)	27.6(16)	26.3(8)
T_{1min}	26	26	27	29
$T_{1min(corr)}$	34	44	45	52
d_{HH} (J_{HD})	0.94(1)	0.96(1)	0.98(3)	1.00(1)
d_{HH} ($T_{1\,min(corr)}$)	0.93(1)	0.97(1)	0.98(1)	1.00(1)
Co-M (Å)	2.252[a]	2.471(2)	2.383(5)	2.465(1)
r	1.07	1.00	0.96	0.92

With the complexes reported by Lu and coworkers, **5.2-H₂** completes a series of group 13 element-anchored trisphosphine Co complexes that stabilize anionic, non-

classical H_2 adducts (Figure 5.1C; Table 5.1). Complex **5.2-H₂** fits the trend described by Lu, where traversing down group 13, an increase in Co-E bonding is observed with concomitant weakening of the H-H bond. They have attributed this observation to a "pull-pull" effect, with an increase in σ-donation from Co to E contributing to an increase in σ-donation from H_2 to Co.[8] Thus, across this series of anionic dihydrogen adducts, the H-H bond of **5.2-H₂** is the least activated of these complexes. Attributing this effect primarily to a change in σ-donation from H_2 to Co suggests that the B-anchored complex **5.2-H₂** is also the most hydridic of this series.

5.2.2. Synthesis and Characterization of $P_3^BCo(H)$

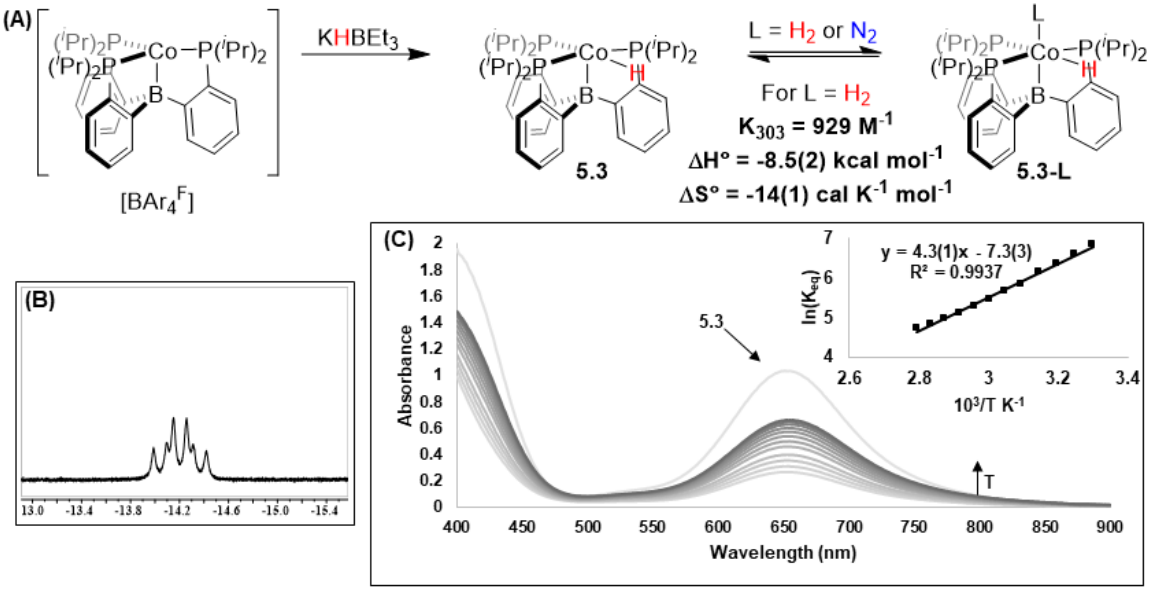

Figure 5.2. (**A**) Synthesis of **5.3** and weak ligand binding to generate **5.3-L** (L = H_2 or N_2). (**B**) ^{1}H NMR resonance of the hydride ligand of **5.3** collected at -60 °C in toluene under vacuum, exhibiting inequivalent ^{31}P coupling. (**C**) Variable temperature UV-Visible spectra of **5.3** collected under an H_2 atmosphere from 30 °C to 80 °C in toluene, with inset van't Hoff plot. Darker traces correspond to spectra collected at higher temperatures; the room temperature spectrum of **5.3** under vacuum is shown for reference.

Before assessing the reactivity of dihydrogen complexes **5.1-H₂** and **5.2-H₂**, we set out to independently synthesize the anticipated hydride product of these reactions, P_3^BCo-H **5.3**. The green hydride complex **5.3** could be conveniently prepared by treating the cationic complex $[P_3^BCo][BAr_4^F]$[11] with an equivalent of $KHBEt_3$ (Figure 5.2A) at low temperature. The hydride ligand of **5.3** is observable by both ^{1}H NMR (-14.2 ppm, -60 ºC) and IR (ν_{Co-H} = 1943 cm^{-1}) spectroscopies. Computationally, the hydride ligand of **5.3** preferentially lies co-planar with the phosphine ligands, with an overall square-pyramidal

geometry that readily accommodates the binding of an additional ligand *trans* to the boron anchor.[14] This along with the broad features in the NMR spectrum of **5.3** and their dependence on the presence of N_2 or H_2, prompted us to more closely study binding of these weak ligands to generate the coordinatively saturated complexes **5.3-H₂** and **5.3-N₂**. At low temperature under vacuum, NMR spectra of **5.3** show inequivalent ^{31}P couplings to the hydride ligand (td, $J = 81$, 53 Hz; Figure 5.2B), providing further evidence for its square pyramidal structure, where the hydride ligand is coplanar with the Co-bound phosphines. Temperature dependent binding of N_2 and H_2 is observed by both NMR and UV-Visible spectroscopy (see Appendix B), with thermochemical parameters for H_2 binding obtained from van't Hoff analysis of variable temperature UV-Visible spectra of this complex under an H_2 atmosphere in toluene ($\Delta H° = -8.5(2)$ kcal mol^{-1}; $\Delta S° = -14(1)$ cal mol^{-1} K^{-1}; Figure 5.2C).

5.2.3. Accessing H-Atom and Hydride Transfer Reactivity from H_2 Adducts

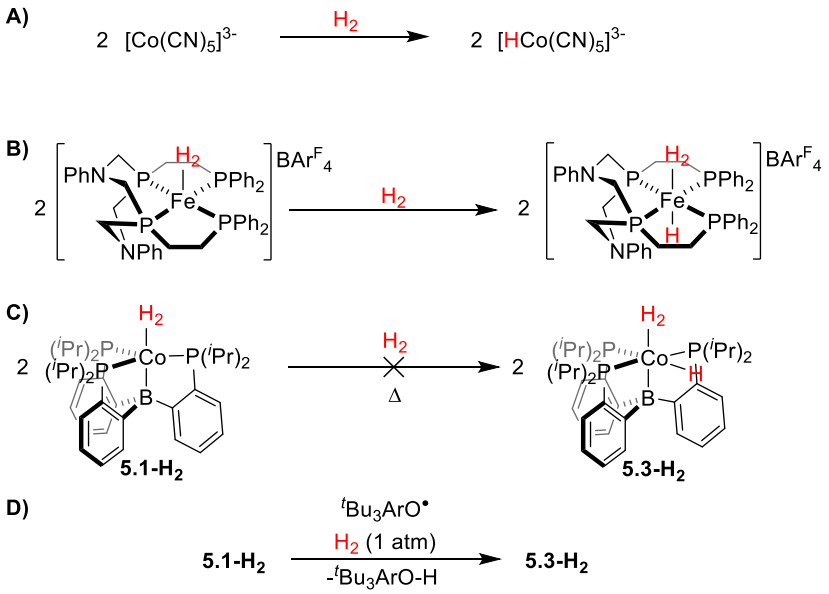

Scheme 5.1. (**A**) Representative example of bimolecular, homolytic H_2 activation by transition metal radicals.[15c] (**B**) Example of homolytic H_2 activation from a radical adduct precursor.[7e] (**C**) Unobserved bimolecular H_2 activation by **5.1-H₂** to generate **5.3-H₂**. (**D**) Reaction of **5.1-H₂** with ^{t}Bu$_3$ArO• to generate **5.3-H₂**.

While examples of homolytic H_2 activation by reactive transition metal radicals have been known for decades[15,16] (Scheme 5.1A), only recently has this type of reactivity been extended to observable H_2 adducts. In two recent reports, structurally-related cationic Fe^I-H_2 radicals (Figure 5.1B; Scheme 5.1B) were found to slowly promote net bimolecular

H_2 activation to generate an $[Fe^{II}\text{-}H]^+$ complex;[7d,e] a conceptually related transformation has been described for a $Co^{I}\text{-}H_2$ complex.[17] Reactivity observed in these systems contrast with the trigonal bipyramidal Fe and Co radical H_2 adducts reported previously by our group (Figure 5.1A), which have not been shown to spontaneously promote bimolecular H_2 activation (Scheme 5.1C).[18]

To access net HAT reactivity using **5.1-H₂** as a precursor, we explored its reactivity with well-defined H-atom acceptors. Treating **5.1-H₂** with the stable phenoxyl radical ^{t}Bu$_3$ArO• at room temperature resulted in its rapid conversion to the hydride complex **5.3-H₂** and ^{t}Bu$_3$ArOH (85% yield; Scheme 5.1D).[19] Under a D_2 atmosphere, deuterium is incorporated as anticipated, with the generation of ^{t}Bu$_3$ArOD and **5.3(D)-(D₂)**.[20] Moving to a weaker H-atom acceptor, TEMPO•, still affected the slow conversion (days) of **5.1-H₂** to generate some of the hydride complex **5.3** (10-15%) and TEMPO-H, but kinetically competitive decomposition pathways complicate further analysis of this transformation.

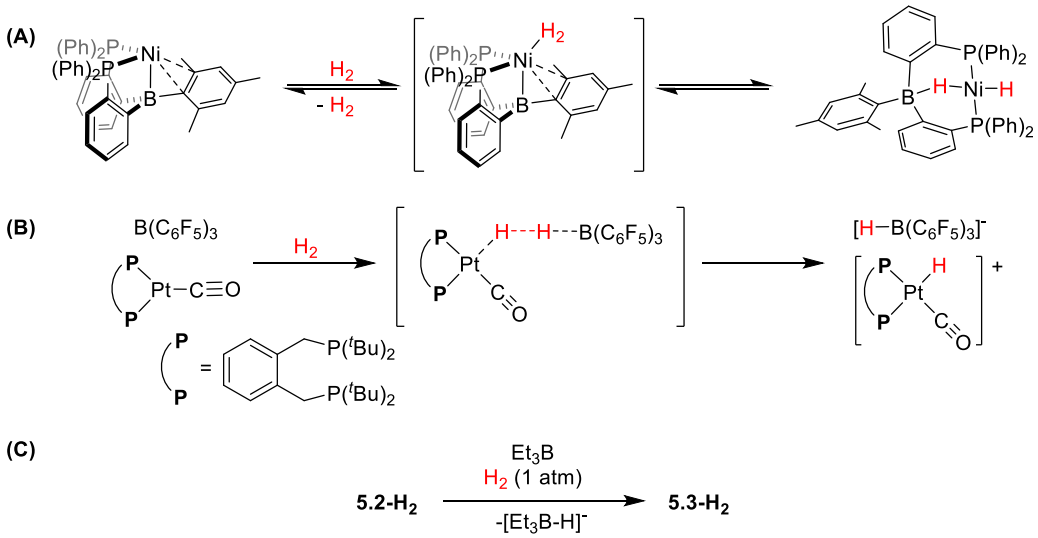

Scheme 5.2. (**A**) Metal-ligand cooperative activation of H_2 with inner sphere hydride transfer to ligand. (**B**) Frustrated Lewis pair activation of H_2 with transition metal Lewis bases. (**C**) Reaction of **5.2-H₂** with BEt_3 to generate $[HBEt_3]^-$ and **5.3-H₂**.

Concurrently, we were interested in establishing the viability of hydride transfer reactivity from the anionic complex, **5.2-H₂**, which we anticipated should serve as a thermodynamically suitable hydride source. Heterolytic activation of non-classical H_2 adducts is quite common, but is assumed to proceed with proton rather than hydride transfer to an outer-sphere substrate; to our knowledge, no examples have been reported where the

direct inverse of this reactivity is observed. Conceptually related reactions have been described, where inner-sphere H_2 activation has been observed to proceed with partial hydride transfer to a supporting borane ligand, generating a metal-bound borohydride (Scheme 5.2A).[21,22] In transition metal FLP reactivity, net proton transfer to transition metal Lewis bases has been observed, albeit without the assumed intermediacy of an H_2 adduct (Scheme 5.2B).[23]

Canvassing the reactivity of **5.2-H₂**, we found a propensity for this complex to promote net hydride transfer to a range of acceptors to generate **5.3-H₂**; molecules that accept a hydride equivalent from **5.2-H₂** include CO_2 and triarylboranes (BPh_3, $B(C_6H_4F)_3$). The rapid net hydride transfer to these substrates, in particular the non-coordinating Lewis acids, was an promising initial hit, but the exceptionally rapid kinetics of these transformations complicated attempts to study the kinetics of these transformations. Given the exceptionally facile nature of the reactivity with these substrates, we next examined reactivity with the quite poor hydride acceptor, BEt_3. In this case, **5.2-H₂** was observed to slowly transfer a hydride equivalent to BEt_3, generating an equivalent of $KHBEt_3$ and **5.3-H₂** in good yields (85%; Scheme 5.2C). The reverse reaction to generate **5.2-H₂** from $KHBEt_3$ and **5.3-H₂** was not accessible under an H_2 atmosphere, but could be driven in the presence of N_2, with the irreversible formation of the anionic N_2 adduct **5.2-N₂**.[24] Remarkably, this suggests that the thermodynamic hydricity of **5.2-H₂** is among those of quite strong main group hydride donors and some of the most hydridic transition metal complexes for which hydricities have been measured.[5] Provided that H_2 adducts are not generally thought to be hydridic, we find this observation, on its own, to be remarkable.

5.2.4. Thermodynamic and Kinetic Considerations for H•/H⁻ Transfer from M(H₂)

The possibility that a non-classical H_2 adduct could serve as a precursor for outer-sphere H-atom or hydride transfer to a thermodynamically suitable acceptor molecule is a fundamentally simple idea, yet σ-adducts have been studied almost exclusively as acids. We attribute the tendency to consider dihydrogen complexes as acids to the ubiquity of thermodynamically acidic systems to stabilize H_2 adducts over their dihydride tautomers rather than an inherently enhanced acidity for non-classical adducts. The critical factor that allows us to access net H-atom and hydride transfer reactivity from **5.1-H₂** and **5.2-H₂**,

respectively, is the unusual stability of these H_2 adducts over their dihydride isomers for systems that are thermodynamically predisposed to accessing H-atom and hydride transfer to stable acceptor molecules.

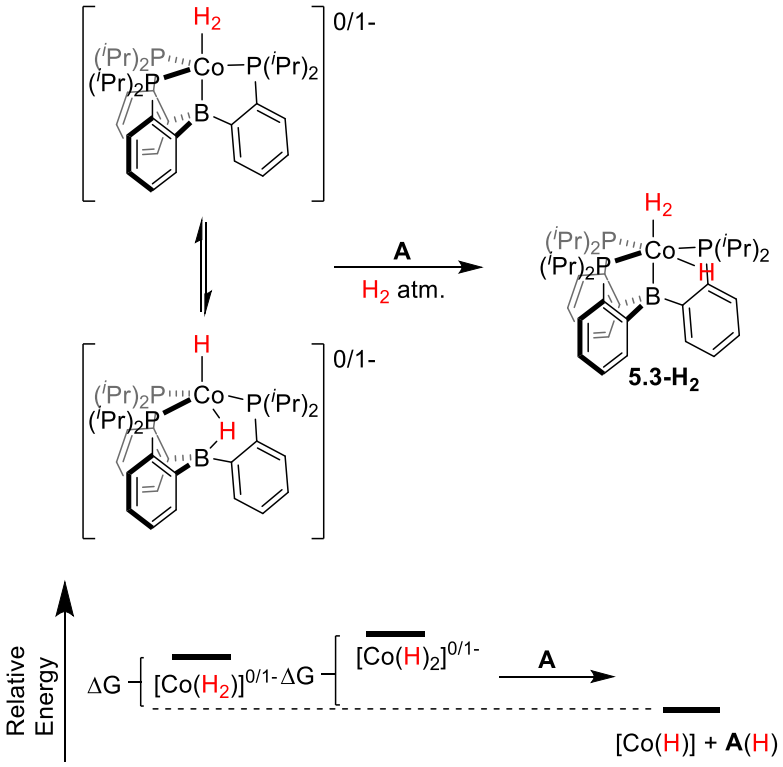

Figure 5.3. Representation of the tautomeric equilibrium between the non-classical adduct and dihydride isomers of **5.1** and **5.2** and their reaction with a suitable acceptor molecule (A) to generate the hydride product **5.3-H₂** (top). For a thermodynamically favored reaction, a representation of the relative energetics of $H^{\bullet}/H^{-}$ transfer from either isomer (bottom).

A central thermodynamic question is whether a non-classical adduct or its dihydride tautomer is predicted to be a stronger H-atom or hydride donor. From simple analysis, the answer to this question is obvious but frequently overlooked—for tautomers, it must be the case that the thermodynamically preferred isomer is simultaneously a poorer proton, H-atom, and hydride donor.[25] This is required because the product of deprotonation (or H-atom/hydride transfer) from either tautomer is identical, where the overall energetics of the reaction are dictated by the difference in energy between the two tautomers (Figure 5.3). We anticipate that both **5.1-H₂** and **5.2-H₂** are in rapid tautomeric equilibrium with their dihydride isomers. Consistent with this postulate is the observation that both of these complexes promote rapid scrambling of H_2 and D_2, which may proceed through a dihydride

intermediate.[7b,26] Computationally, local minima for both possible isomers were located for the neutral and anionic complexes. For the anionic complex, a slight preference for the non-classical adduct was determined (by 1.9 kcal/mol),[27] while the possible isomers of the neutral radical were computed to have nearly identical energies.[28]

Of course, the relative thermodynamics of H-atom or hydride transfer from a non-classical adduct and its dihydride isomer do not dictate the kinetically preferred pathway for H_2 activation. In a limiting sense, these transformations could proceed with direct cleavage of an H_2 adduct or *via* an initial oxidative addition pathway, where the barrier to this step and subsequent H-atom/hydride transfer is lower than direct reactivity from an intact H_2 ligand. Before considering these possibilities for our system and in a more general sense, two recently reported systems that have been shown to access bimolecular HAT steps from H_2 adduct precursors warrant additional comment.

In a recent report from Bullock and coworkers, net bimolecular H_2 oxidative addition was reported (Scheme 5.1B) with mixed order kinetic behavior observed for H_2 activation in this system.[7e] At early reaction times, the transformation is 2nd order in concentration of the Fe^{I} precursor, with a 1st order process dominating as the starting material is consumed and the reaction proceeds to completion. In their report, they provide a well-reasoned argument based on combined experimental and theoretical data that the observed 1st order process is the oxidative addition of H_2 at the Fe^{I} center to generate an $Fe^{III}(H)_2$ intermediate. They then propose that the 2nd order rate term is attributable to bimolecular HAT between this dihydride intermediate and a second $Fe^{I}(H_2)$ or $Fe^{III}(H)_2$ equivalent to generate two equivalents of the terminal Fe^{II} product upon facile H_2 binding (Scheme 5.3A). This sequential mechanism is inconsistent with the 2nd order term dominating the overall reaction profile at *early* times. Instead, the observed kinetics are consistent with competing 1st and 2nd order pathways, where the 2nd order reaction dominates at high Fe^{I} concentrations. As such, we suggest an alternative mechanism, where direct HAT from the intact H_2 adduct dominates the kinetics at high concentrations of the Fe^{I} precursor with a pathway proceeding *via* an initial oxidative operative as the reaction proceeds to completion (Scheme 5.3B).[29]

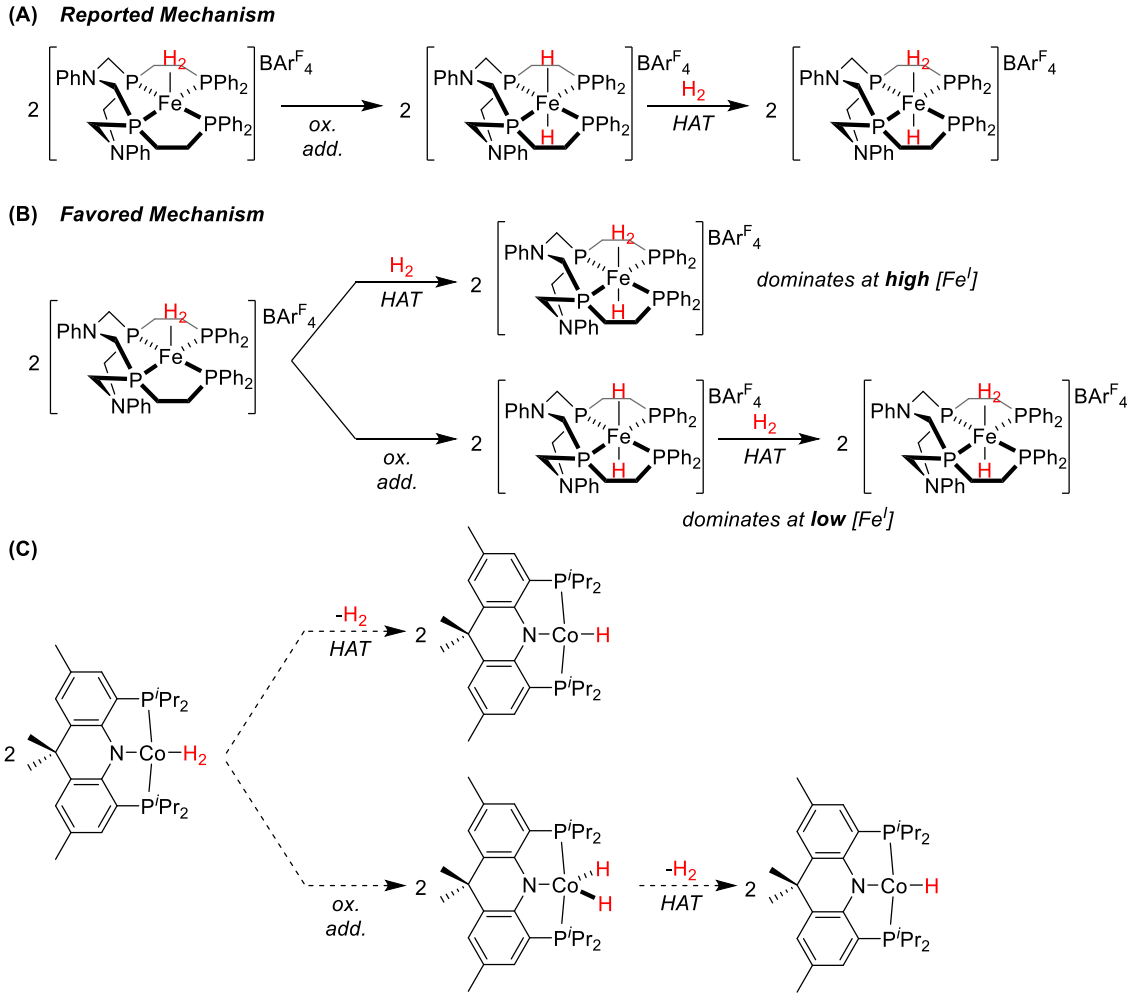

Scheme 5.3. (**A**) Simplified representation of the reported mechanism for net bimolecular H_2 oxidative addition from an $Fe^{I}(H_2)$ adduct precursor as proposed by Bullock and coworkers.[7e] (**B**) An alternative mechanistic scenario for this transformation that is preferred based on reported experimental data. (**C**) Plausible limiting mechanisms for net bimolecular H_2 oxidative addition from a putative $Co^{I}(H_2)$ adduct precursor. No reported experimental or computational results distinguish between these possible pathways.[17]

A second example of this reactivity pattern was reported recently by Choi and Lee, where net HAT is observed from a putative $Co^{I}(H_2)$ adduct precursor, where a key conclusion drawn by the authors is that the complex promotes HAT rather than simply undergoing oxidative addition.[17] For the $Co^{I}(H_2)$ complex, reliable solution NMR characterization data could not be obtained to unequivocally assign this species because of rapid H_2 exchange. A major component of the argument provided to support its assignment and the proposed reaction pathway was the characterization of a structurally related silane σ-adduct and study of its HAT reactivity. In the solid-state, the silane complex was

structurally characterized as a σ-adduct, but the solution-phase spectroscopic data provided are more consistent with a Co^{III}-silyl/hydride complex.[30] Specifically, few intact silane adducts have been reported to have such small Si-H couplings (28 Hz), and, to our knowledge, no intact adducts have been reported with Si-H ^{1}H NMR chemical shifts upfield of roughly -20 ppm, where the critical resonance for their complex is observed at nearly 10 ppm further upfield (-28.76 ppm).[31] It is often the case that hydrides and silane adducts fall in the same spectroscopic region and cannot reliably be distinguished simply by their ^{1}H NMR chemical shifts, but bona fide hydride ligands can fall well outside the region where reliably characterized silane adducts have previously been observed. Thus, based on the available data and literature precedent, we prefer a solution phase assignment for this species as the Co^{III} product of silane oxidative addition. Setting its uncertain assignment aside, demonstrating that this species undergoes net homolytic activation does not provide any information about the mechanism of H_2 activation, particularly with respect to the possible intermediacy of a Co^{III}-$(H)_2$ (Scheme 5.3C).

As we have suggested, for the transformations of interest, the central mechanistic question is whether H-atom and hydride transfer reactions can proceed directly from intact H_2 adducts. Notably, for well-studied heterolytic H_2 activation, systems tailored to probing the mechanism of H_2 activation have shown a kinetic preference for direct reactivity of the dihydrogen adduct, and this is assumed to be generally applicable.[32] This can be readily intuited where the microscopic reverse of this transformation is considered, with protonation directly at the M-H bond preferred, as significant structural and electronic structure reorganization is often required for direct metal-centered protonation. Exceptions to this generalization are known, specifically where a metal-centered protonation can proceed directly without requiring significant reorganization energy.[33]

Considering, instead, the microscopic reverse of H-atom or hydride transfer from non-classical H_2 adducts, the intuitive argument for preferred reactivity at the M-H bond rather than at the metal center no longer rings true. Inherent to the addition of an H-atom or hydride equivalent rather than a simple proton is the necessity of accommodating both the added electron(s) and proton. In this case, changes to the electronic structure are anticipated for both metal or M-H centered reactivity. Further, many H_2 adducts that are studied for their Brønsted acidities are often coordinatively saturated systems that, for the

reverse reaction, require structural perturbations to accommodate direct metal-centered protonation reactivity. For the H_2 adducts discussed here as H-atom and hydride transfer reagents, the initial hydride products of H-atom/hydride loss are inherently coordinatively unsaturated; thus direct metal-centered reactivity is intuited to be more facile, as reactivity can proceed at vacant coordination sites or with displacement of a weakly-bound or labile ligand (*i.e.,* N_2 or H_2).

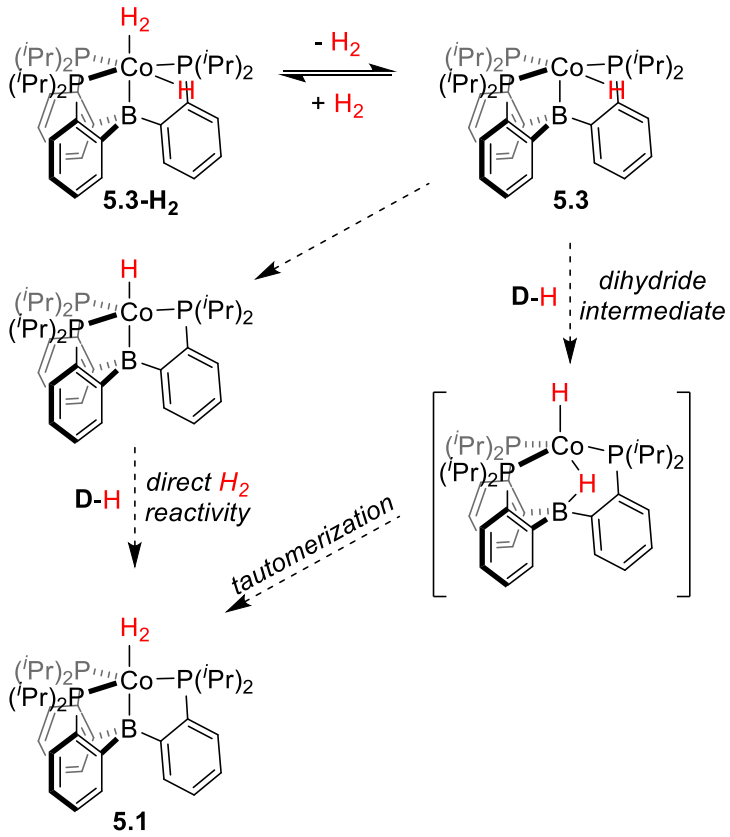

Scheme 5.4 Plausible pathways for the generation of **5.1** upon the addition of a suitable H-atom donor (D-H) to the hydride complex **5.3-H₂**.

Attempts to obtain kinetic data for the transformations of **5.1-H₂** or **5.2-H₂** to **5.3-H₂** that distinguishes between these limiting pathways have been unsuccessful. For the reaction of **5.1-H₂** with ^{t}Bu$_3$ArO•, attempts to obtain reproducible kinetic data at low temperature have been unsuccessful. We speculate that for this system multiple mechanisms are operative, which possibly include impurity mediated pathways.[34] Nevertheless, we consider which of the two limiting mechanistic pathways is preferred as an intriguing thought experiment. Above we reasoned that tautomerization for both **5.1-H₂** and **5.2-H₂** is facile. Given this and the microscopic reversibility discussion outlined above,

we hypothesize that for both H-atom and hydride transfer reactions observed for $[P_3^BCo(H_2)]^{0/-1}$ there should be a kinetic preference for reactivity from the dihydride state. Speculatively, we predict that, if our reasoning is correct, this should be generalizable for systems that both access facile tautomeric equilibria and exhibit H-atom/hydride transfer reactivity. Exceptional cases where direct H-atom or hydride transfer are accessible from H_2 adducts are anticipated where the barrier to tautomerization is high. Indeed, the modified mechanism proposed above for the Fe system initially reported by Bullock and coworkers[7e] may be a representative example of this phenomenon.

5.3. Conclusions

In this study, we describe the chemistry of an unusual redox pair of radical and anionic non-classical dihydrogen adducts, **5.1-H₂** and **5.2-H₂**. These complexes demonstrate the viability of H-atom and hydride transfer from dihydrogen σ-adduct precursors, which are highly unusual reactivity patterns for these structure types. Given the limited precedent for these reactivity profiles, the exceptional hydricity of **5.2-H₂** is worth reemphasizing. We discuss in some detail limiting thermodynamic and kinetic factors for these transformations that led us to our current hypothesis that reactivity in these systems should proceed preferentially from dihydride intermediates. We remain interested in the development of novel systems that promote related transformations, especially those that are more amenable to providing experimentally practical mechanistic insight.

5.4. Synthetic Details

5.4.1 $[P_3^BCo(H_2)][K(THF)_n]$ 5.2-H₂: Solutions of **5.2-H₂** for spectroscopic characterization and reactivity studies were prepared *in situ*. Rigorous exclusion of N_2 from these reactions is necessary to avoid formation of **5.2-N₂**. When Na naphthalenide was used as the reductant, it was prepared as a stock solution of known concentration in a septum-capped vial and stored under an Ar atmosphere at -35 ºC. A solution of P_3^BCoBr was prepared in THF and transferred to a Schlenk tube with a Kontes valve seal. This solution was degassed by three freeze-pump-thaw cycles and backfilled with an atmosphere of H_2. Against positive H_2 pressure 2.05 equivalents of Na naphthalenide were added *via* syringe and the mixture was mixed at room temperature, rapidly turning dark red. For reductions using Na or K metal, an excess of the solid reductant was added to the Schlenk tube, which was then sealed, rapidly transferred from the glovebox and frozen. The solutions were

degassed by three freeze-pump-thaw cycles then backfilled with H_2 and stirred at room temperature overnight. Manipulations of the product including transfers to alternative vessels for characterization and reactivity studies were carried out *via* syringe with high overpressures of H_2. ^{1}H NMR (THF-d_8, 400 MHz): δ 7.38 (3H), 6.90 (3H), 6.61 (3H), 6.45 (3H), 1.98 (6H), 0.84 (18H), 0.34 (18H), -8.60 (br, 2H).^{1}H NMR (THF-d_8, 400 MHz; HD): δ -8.6 (J_{HD} = 29.5 Hz). ^{31}P{^{1}H} NMR (THF, 121 MHz): δ 74.5. ^{11}B{^{1}H} NMR (THF-d_8, 128 MHz): δ 11.1.

5.4.2 $P_3^BCo(H)$ 5.3: A stirred solution of [P_3^BCo][BAr^F_4] (150.2 mg) in THF (8 mL) was cooled to -78 °C and a solution of $KHBEt_3$ in THF (1 M, 100 μL, 1 equiv) was added. The reaction mixture was allowed to warm slowly to room temperature overnight, turning dark green. The solvent was removed *in vacuo* and the dark green residue was triturated with pentane (~3 mL), which was subsequently removed *in vacuo*. The resultant dark green powder was extracted into pentane until washings became nearly colorless (~15 mL total), with removal of the solvent yielding the product in moderate yields (71%) and reasonable purities (~95% as judged by NMR spectroscopy). A minor amount of $P_3^BCo(N_2)$ **1-N_2** was typically observed in materials isolated according to this protocol. Further purification of **3** was achieved first by crystallizing the complex (evaporation of an Et_2O solution into MeCy) and then washing the resultant dark green crystals with pentane at -78 °C. The NMR behavior of this species is complicated by N_2/H_2 binding (see Appendix B). IR spectrum (thin film): $\nu_{Co\text{-}H}$ = 1943 cm^{-1}. Anal. Calcd. for $C_{36}H_{55}BCoP_3$: C, 66.47; H, 8.52; N, 0.00. Found: C, 66.50; H, 8.15; N, < 0.1.

5.5. Notes and References

---

(1) For a comprehensive review of H_2 chemistry predating 2001: Kubas, G. J. Metal Dihydrogen and σ-bond Complexes; Kluwer/ Plenum: New York, 2001.

(2) For additional reviews: (a) Kubas, G. J. *Chem. Rev.* **2007**, *107*, 4152-4205. (b) Crabtree, R. H. *Chem. Rev.* **2016**, *116*, 8750-8769. (c) Jessop, P. G.; Morris, R. H. *Coord. Chem. Rev.* **1992**, *121*, 155-284.

(3) Morris, R. H. *Chem. Rev.* **2016**, *116*, 8588-8654.

(4) (a) Hu, Y.; Shaw, A. P.; Estes, D. P.; Norton, J. R. *Chem. Rev.* **2016**, *116*, 8427-8462. (b) Eisenberg, D. C.; Norton, J. R. *Isr. J. Chem.* **1991**, *31*, 55-66.

(5) Wiedner, E. S.; Chambers, M. B.; Pitman, C. L.; Bullock, R. M.; Miller, A. J. M.; Appel, A. M. *Chem. Rev.* **2016**, *116*, 8655-8692.

(6) Kubas, G. J.; Ryan, R. R.; Swanson, B. I.; Vergamini, P. J.; Wasserman, H. J. *J. Am. Chem. Soc.* **1984**, *106*, 451-452.

(7) (a) Lee, Y.; Kinney, R. A.; Hoffman, B. M.; Peters, J. C. *J. Am. Chem. Soc.* **2011**, *133*, 16366-16369. (b) Suess, D. L. M.; Tsay, C.; Peters, J. C. *J. Am. Chem. Soc.* **2012**, *134,* 14158-14164. (c) Gunderson, W. A.; Suess, D. L. M.; Fong, H.; Wang, X.; Hoffman, C. M.; Cutsail III, G. E.; Peters, J. C.; Hoffman, B. M. *J. Am. Chem. Soc.* **2014**, *136*, 14998-15009. (d) Doyle, L. R.; Scott, D. J.; Hill, P. J.; Fraser, D.; Myers, W.; White, A. J. P.; Green, J.; Ashley, A. E. *Chem. Sci.* **2018**, *9*, 7362-7369. (e) Prokopchuk, D. E.; Chambers, G. M.; Walter, E. D.; Mock, M. T.; Bullock, R. M. *J. Am. Chem. Soc.* **2019**, *141*, 1871-1876.

(8) Vollmer, M. V.; Xie, J.; Lu, C. C. *J. Am. Chem. Soc.* **2017**, *139*, 6570-6573.

(9) (a) Harman, W. H.; Lin, T.-P.; Peters, J. C. *Angew. Chem. Int. Ed.* **2014**, *53*, 1081-1086. (b) Cammarota, R. C.; Lu, C.C. *J. Am. Chem. Soc*. **2015**, *137*, 12486–12489. (c) Cammarota, R. C.; Xie, J.; Burgess, S. A.; Vollmer, M. V.; Vogiatzis, K. D.; Yem J.; Linehan, J. C.; Appel, A. M.; Hoffmann, C.; Wang, X.; Young, V. G.; Lu, C. C. *Chem. Sci.* **2019**, *10*, 7029-7042.

(10) Initial generation of $P_3^BCo(H_2)$ by $P_3^BCo(N_2)$ according to the published protocol (Ref. 7b), followed by *in situ* reduction of this species invariably led to mixtures containing a minor product that could be identified as of $[P_3^BCo(N_2)]^{1-}$ (Ref. 11).

(11) Del Castillo, T. J.; Thompson, N. B.; Suess, D. L. M.; Ung, G.; Peters, J. C. *Inorg. Chem.* **2015**, *54*, 9256-9262.

(12) At room temperature, the free H_2 peak is not completely resolved, so the J_{HD} value may be slightly lower than the true value for the H_2 complex. Given that the H_2 peak is fully resolved at temperatures as high as 15 ºC and the predicted H-H distances are in good agreement between the $T_{1(min)}$ and $J_{H\text{-}D}$ values, the measured value is sufficient.

(13) (a) Heinekey, D. M.; Luther, T. A. *Inorg. Chem.* **1996**, *35*, 4396-4399. (b) Luther, T. A.; Heinekey, D. M. *Inorg. Chem.* **1998**, *37*, 127-132.

(14) This complex has been characterized in the solid state by XRD, but significant disorder and the inherently poor detection of hydride ligands limits its utility for locating the hydride ligand.

(15) For select examples, see: (a) Wayland, B. B.; Ba, S.; Sherry, A. E. *Inorg. Chem.* **1992**, *31*, 148-150. (b) Capps, K. B.; Bauer, A.; Kiss, G.; Hoff, C. D. *J. Organomet. Chem.* **1999**, *586*, 23-30. (c) Halpern, J.; Pribanić, M. *Inorg. Chem.* **1970**, *9*, 2616-2618.

(16) The intermediacy of H_2 adducts in these transformations has been suggested but is not required. For a relevant discussion, see: Norton, J. R.; Spataru, T.; Camaioni, D. M.; Lee, S.-J.; Li, G.; Choi, J.; Franz, J. A. *Organometallics* **2014**, *33*, 2496-2502.

(17) Choi, J.; Lee, Y. *Angew. Chem. Int. Ed.* **2019**, *58*, 6938-6942.

(18) Attempts to promote bimolecular H_2 activation by heating **5.1-H$_2$** or **5.3-H$_2$** under an H_2 atmosphere led to decomposition of the supporting ligand in these complexes, with no evidence for their interconversion.

(19) Addition of ^{t}Bu$_3$ArO• to **5.3-H$_2$** was not observed to abstract an H-atom to generate **5.1-H$_2$**. After mixing for 1 h at room temperature, **5.3-H$_2$** was largely unreacted (~90%), with minor decomposition to an unknown paramagnetic species.

(20) We note that under an H_2 atmosphere, rapid scrambling of H is observed into the hydride position of **5.3(D)**.

(21) (a) Harman, W. H.; Peters, J. C. *J. Am. Chem. Soc.* **2012**, *134*, 5080-5082. (b) Li, Y.; Hou, C.; Jiang, J.; Zhang, Z; Zhao, C.; Page, A. J.; Ke, Z. *ACS Catal.* **2016**, *6*, 1655-1662.

(22) Examples of inner-sphere hydride transfer to substrate from dihydrogen adduct precursors have been observed, but these processes follow initial coordination induced oxidative addition steps, see: (a) Vigalok, A.; Ben-David, Y.; Milstein, D. *Organometallics* **1996**, *15*, 1839-1844. (b) Huang, K.-W.; Han, J. H.; Musgrave, C. B.; Fujita, E. *Organometallics* **2007**, *26*, 508-513. (c) Tokmic, K.; Fout, A. R. *J. Am. Chem. Soc.* **2016**, *138*, 13700-13705.

(23) (a) Forrest, S. J. K.; Clifton, J.; Fey, N.; Pringle, P. G.; Sparkes, H. A.; Wass, D. F. *Angew. Chem. Int. Ed.* **2015**, *54*, 2223-2227. (b) Campos, J. *J. Am. Chem. Soc.* **2017**, *139*, 2944-2947. (c) Habraken, E. R. M.; Jupp, A. R.; Brands, M. B.; Nieger, M.; Ehlers, A. W.; Slootweg, J. C. *Eur. J. Inorg. Chem.* **2019**, *2019*, 2436-2442.

(24) We note that the anionic H_2 adducts reported by Lu are synthesized by metalating under reductive conditions with MHBEt$_3$ (See Ref. 8).

(25) This has been discussed previously in the context of proton transfer from H_2 adducts, see: Kristjánsdóttir, S. S.; Norton, J. R. Acidity of Hydrido Transition Metal Complexes in Solution. In *Transition Metal Hydrides*; Dedieu, A., E.; VCH Publishers: New York; p 309-360.

(26) Mechanisms for the scrambling of H_2 and D_2 that do not require the intermediacy of a dihydride are difficult to rule out.

(27) A similar conclusion was drawn concerning the thermal accessibility of dihydride isomers for the structurally-related complexes reported by Lu and coworkers (Ref. 8).

(28) For the neutral complex, the dihydride isomer is preferred by 0.3 kcal/mol. For either species, the calculated energy difference is within the error of the calculation.

(29) This mechanism is consistent with the rate law derived in the Supporting Information for their manuscript. The assumptions made in their derivation are an oversimplification for the proposed mechanism and should instead apply the steady-state approximation.

(30) The solution and solid-state structures of this compound are not necessarily the same. A relevant example contributed to the solution-phase misassignment of a $Co^{I}(H_2)/Co^{III}(H)_2$ non-classical adduct. (a) Bianchini, C.; Mealli, C.; Meli, A.; Bianchini, C.; Mealli, C.; Meli, A.; Peruzzini, M.; Zanobini, F. *J. Am. Chem. Soc.* **1988**, *110*, 8725−8726. (b) Heinekey, D.; Liegeois, A.; van Roon, M. *J. Am. Chem. Soc.* **1994**, *116*, 8388−8389. (c) Heinekey, D.; van Roon, M. *J. Am. Chem. Soc.* **1996**, *118*, 12134−12140.

(31) (a) Corey, J. Y.; Braddock-Wilking, J. *Chem. Rev.* **1999**, *99*, 175-292. (b) Corey, J. Y. *Chem. Rev.* **2016**, *116*, 11291-11435.

(32) (a) Chinn, M. S.; Heinekey, D. M. *J. Am. Chem. Soc.* **1987**, *109*, 5865-5867. (b) Crabtree, R. H.; Lavin, M.; Bonneviot, L. *J. Am. Chem. Soc.* **1986**, *108*, 4032-4037.

(33) (a) Conroy-Lewis, F. M.; Simpson, S. J. *J. Chem. Soc., Chem. Commun.* **1987**, 1675-1676. (b) Scharrer, E.; Chang, S.; Brookhart, M. *Organometallics* **1995**, *14*, 5686-5694.

(34) Final data collection for the transformation from **5.2-H$_2$** to **5.3-H$_2$** are ongoing.

Chapter 6

FUNCTIONALIZATION OF IRON THIOCARBONYL COMPLEXES: TOWARD A TERMINAL IRON CARBIDE

6.1 Introduction

The Fischer-Tropsch process was developed to control the reduction of CO by H_2 to generate C-C coupled products at elevated temperatures and pressures and is most often catalyzed by heterogeneous Fe or Co catalysts (Figure 6.1A).[1] It was discovered recently that biological nitrogenase enzymes are similarly capable of mediating the reduction of CO to C-C coupled products upon the addition of H^+ and e^- equivalents (Figure 6.1B).[2] Remarkably, both of these processes yield products that require complete cleavage of the exceptionally strong C-O triple bond of carbon monoxide (256 kcal/mol). Together these transformations motivate our group's interest in modeling aspects of CO functionalization and cleavage by well-defined complexes of Co[3] and especially Fe.[4] To this end, we have developed phosphine-supported Fe systems that are able to support O-functionalization of Fe-CO complexes,[5] including in systems that are able to access downstream reactivity, including C-C coupling[6] and C-H bond forming steps.[7] To date, despite some effort, these systems have not been amenable to accessing C-O bond cleavage chemistry to generate a terminal Fe(C).[8] In fact, as of yet, there are no reported examples of terminally-bound carbides of any first row transition metals and, as such, these species remain compelling synthetic targets.

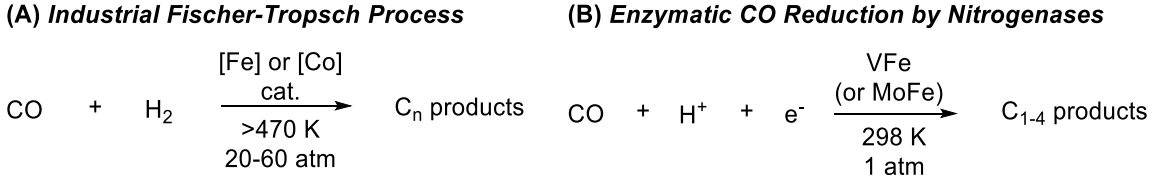

Figure 6.1. Addition of H-atom equivalents for the (**A**) industrial and (**B**) enzymatic reduction of CO.

One of the primary barriers to the preparation of molecular metal carbides is a lack of generalizable approaches to their synthesis. Cummins and coworkers reported the synthesis of the first terminal transition metal carbide that was prepared, in this case, *via* deoxygenation of a Mo(CO) complex.[9,10] An alternative approach to the synthesis of this

complex was demonstrated through application of a methylidyne transfer reagent that generates a "C-H" fragment concurrent with the aromatization of benzene (Scheme 6.1A).[11] To extend these unusual structural motifs to group 8 systems, terminal Ru carbides were first prepared through olefin metathesis between Ru carbene precursors and reaction partners that can serve as direct carbide precursors (Scheme 6.1B).[12] An alternative route to the synthesis of terminal Ru and Os carbides was demonstrated *via* S-atom abstraction from thiocarbonyl complexes (Scheme 6.1B).[13] To date, the successful application of these and alternative approaches[14] remain limited.

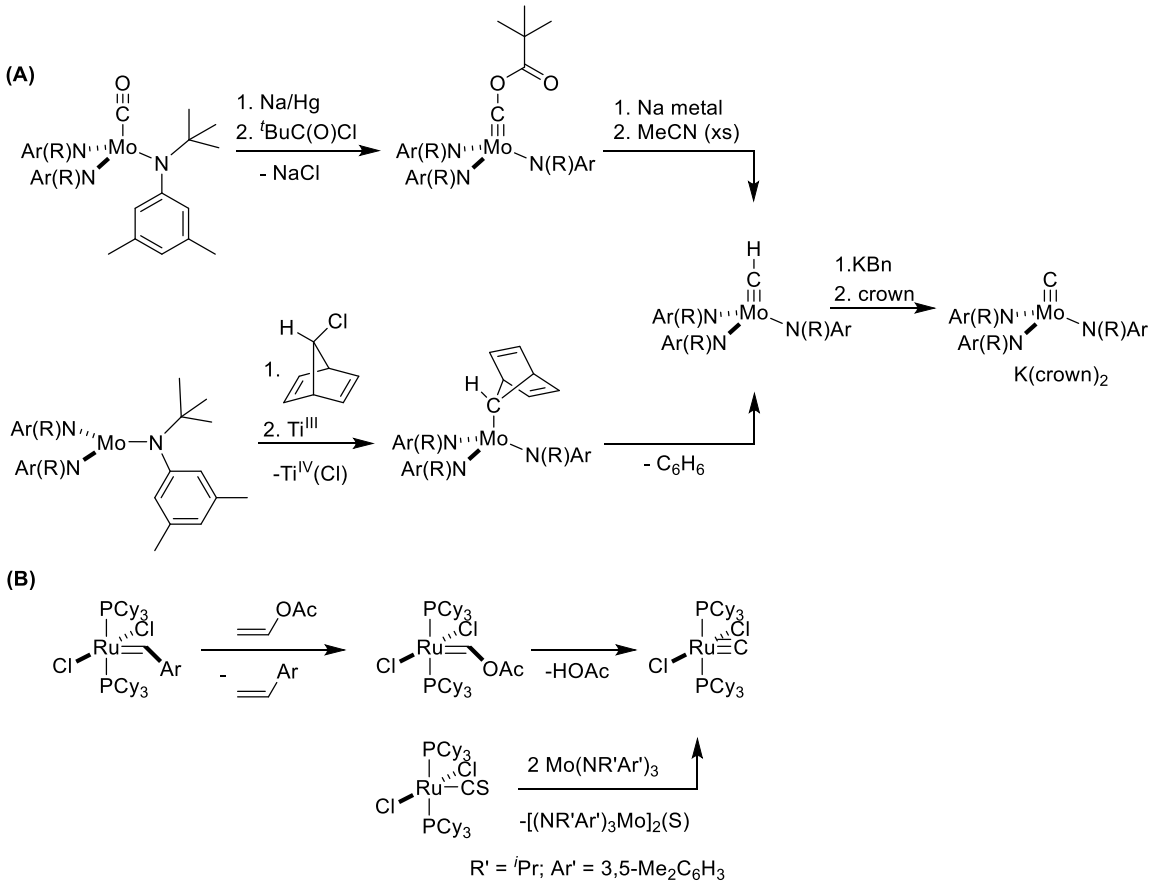

Scheme 6.1. Representative synthetic strategies for the synthesis of (**A**) group 6[9,10] and (**B**) group 8[12,13] terminal metal carbides.

Herein, we describe our efforts targeting the synthesis of a terminal Fe-carbide complex. Given that efforts from our group to cleave the strong C-O bond in Fe-carbonyl complexes have not yet been fruitful, we hypothesized that moving to the corresponding thiocarbonyl complexes would provide access to S-functionalization reactivity and that

these systems might be amenable to cleavage of the far weaker C-S bond.[15] In this chapter, we describe the synthesis of Fe-CS complexes supported by two different trisphosphine ligand frameworks. In a reduced state, these complexes are amenable to S-functionalization reactivity upon treatment with alkyl-triflate electrophiles, which provides synthetic access to a series of terminal thiocarbynes. In one case, a surprising C-S bond cleavage pathway is observed, but proceeds without the intermediacy of a terminal Fe-carbide. Additional approaches to generating a terminal carbide in these systems are discussed, which emphasize limiting factors that have, to date, precluded the generation of the target species.

6.2 Results and Discussion

6.2.1 Synthesis and Characterization of $P_3^BFe(CS)$ Complexes

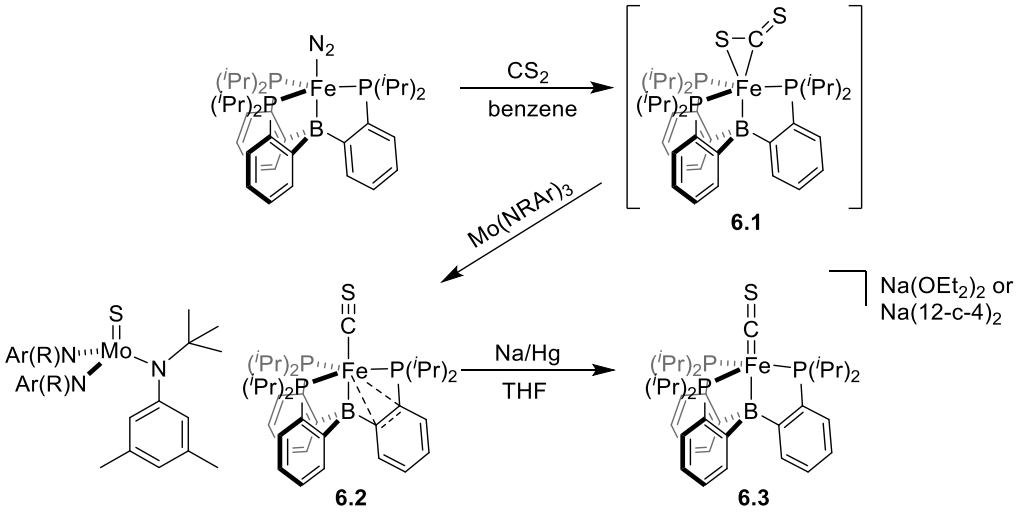

Scheme 6.2. Approach to the synthesis of $P_3^BFe(CS)$ complexes.

One of the systems we initially targeted for the preparation of Fe-CS complexes as prospective precursors to S-functionalization and C-S cleavage was the P_3^BFe platform.[16] Previous research from our group has established that this system is able to support an array of transformations of N_2,[17] and, as such, we thought it might be a suitable starting point for accessing the desired CS functionalization and cleavage chemistry. Initial access to thiocarbonyl chemistry on this platform was provided by treating the previously reported $P_3^BFe\text{-}N_2$ complex with an equivalent of CS_2 to cleanly generate $P_3^BFe\text{-}CS_2$ **6.1**. The CS_2 adduct **6.1** has a paramagnetically shifted ^1H NMR spectrum and Mössbauer parameters consistent with the formation of a new triplet species (δ = 0.44 mm/s; ΔE_Q = 2.55 mm/s).

This compound decays in solution over time, but can be directly generated *in situ* as a precursor to thiocarbonyl complexes (Scheme 6.2).

Treating the CS_2 adduct **6.1** with an equivalent of $Mo(NRAr)_3$ (R = ^{t}Bu; Ar = 3,5-dimethylphenyl)[18] in benzene led to an instantaneous reaction. NMR spectroscopic analysis of the resultant reaction mixture confirmed the formation of the previously reported Mo=S complex[19] with concurrent formation of a new, diamagnetic Fe species, $P_3^BFe(CS)$ **6.2**.[20] The similar solubility properties of the two transition metal products of this transformation precludes their direct separation. Instead, reduction of the product mixture over an excess of Na/Hg amalgam in THF gave selective one-electron reduction of the Fe complex, which could be isolated following crystallization as its Et_2O solvate $[P_3^BFe(CS)][Na(Et_2O)_2]$ **6.3** or by precipitating the crown ether encapsulated salt $[P_3^BFe(CS)][Na(12\text{-crown-}4)_2]$ **6.3'** from Et_2O (Scheme 6.2). Solid state structural characterization of the Na-capped complex **6.3** shows significant activation of the CS ligand (Figure 6.4). Specifically, the Fe-C bond distance of 1.703(2) Å is only slightly longer than typical Fe-carbynes[21,22] (1.63-1.7 Å), suggesting there is significant Fe-to-C multiple bond character in this species. Corresponding elongation of the C-S bond to 1.663(2) Å is observed, which is longer than most structurally characterized thiocarbonyl complexes (typically ~1.5-1.6 Å).[23]

The isolated anionic Fe-CS complex **6.3** (or **6.3'**) undergoes one electron oxidation upon treatment with $[Cp_2Co][PF_6]$ to cleanly generate the neutral Fe-CS complex **6.2** (Scheme 6.3). Like the corresponding Fe-CO complex, this species is diamagnetic, with an interaction observed between the Fe-center and one of the ligand arenes in its solid-state structure (Figure 6.2).[16] Solution three-fold symmetry is observed by room temperature NMR spectroscopy, indicating that this interaction is fluctional in solution on the NMR time scale. Bonding in the Fe-C≡S unit of **6.2** is similar to other structurally characterized thiocarbonyl complexes, with a C-S distance of 1.591(2) Å. The Fe-C distance in **6.2** (1.734(2) Å) is slightly contracted when compared to the isostructural Fe-CO complex (1.752(3) Å).[16] An additional reduction event is accessible when **6.3** is treated with an excess of KC_8 to putatively generate a dianionic thiocarbonyl complex **6.4** (Scheme 6.3).[24] This dianionic complex is three-fold symmetric in solution, as judged NMR spectroscopy.

Efforts to isolate and fully characterize **6.4** are ongoing, but have been limited by the highly reactive nature of this complex.

6.2.2 S-Functionalization to Generate Thiocarbyne Complexes

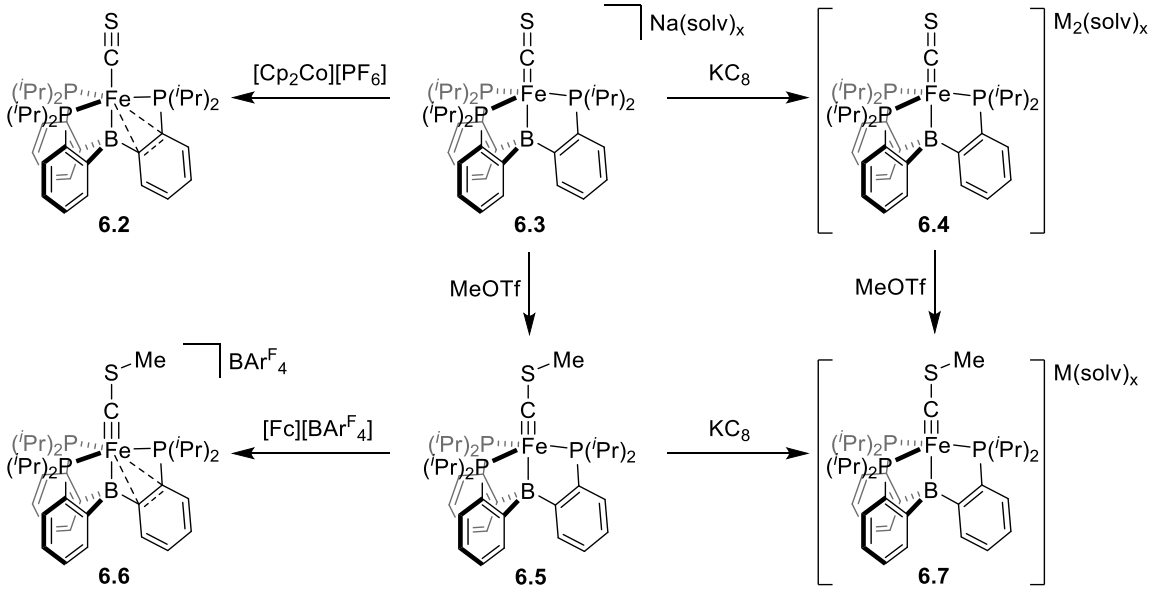

Scheme 6.3. Synthesis of Fe-CS and Fe≡C-SMe complexes across three oxidation states.

Treating the anionic Fe-CS complex **6.3** with an equivalent of MeOTf at low temperature led to the rapid consumption of the starting material (Scheme 6.3). The product of this transformation is a new doublet species, with the incorporation of the methyl group in this species initially confirmed by using ^{13}C-labeled MeOTf, which strongly couples to one of the paramagnetically shifted ^{1}H NMR resonances. Structural characterization of the product confirmed the assignment of this species as the terminal thiocarbyne complex P_3^BFe≡C-SMe **6.5**. Methylation of the CS ligand results in further activation of the C-S bond, with contraction of the Fe-C distance to 1.688(2) Å and elongation of the C-S distance to 1.706(2) Å, consistent with the formation of a bona fide carbyne ligand (Figure 6.2). The contracted C-S-C angle of 103.4(1)º is comparable to previously reported thiocarbynes of Mo and W and is consistent with little contribution of heteroatom π-stabilization for S-substituted carbyne ligands.[25] We note that complex **6.5** is a relatively unusual example of a paramagnetic carbyne complex, though structurally-related species have been described recently by our group.[26] When isolated in the solid state **6.5** is a stable

species, but slowly decomposes in solution over time with formal methyl radical loss to regenerate the neutral thiocarbonyl complex **6.2**.

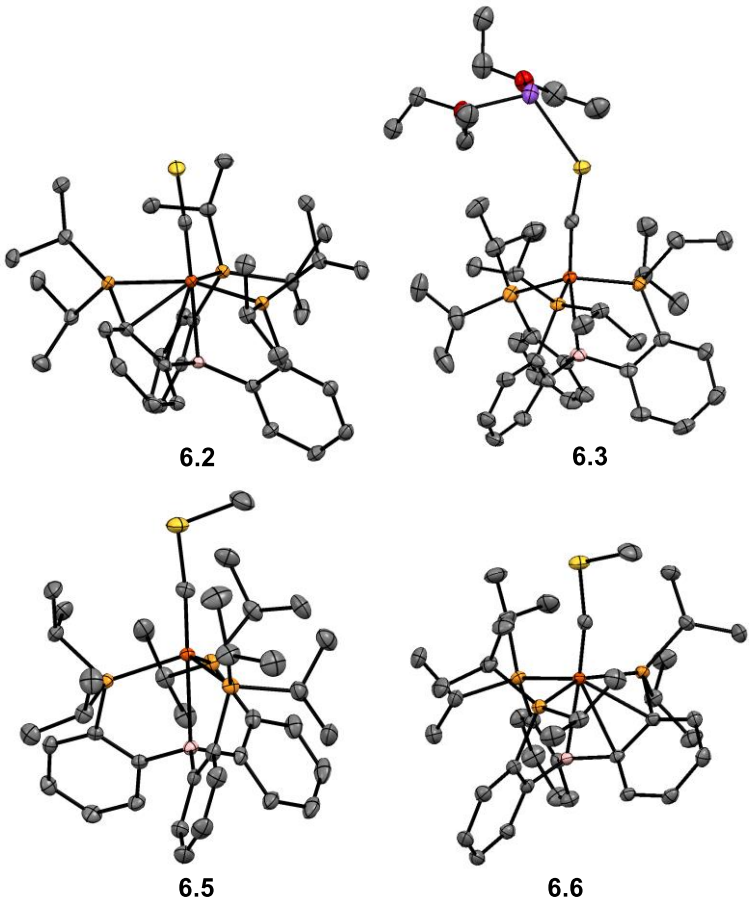

Figure 6.2. Crystal structures of the neutral (**6.2**) and anionic (**6.3**) thiocarbonyl complexes (top), as well as the neutral (**6.5**) and cationic (**6.6**) thiocarbyne complexes. C-bound H-atoms and the BAr^F_4 countercation of **6.6** are omitted for clarity.

One electron oxidation of the neutral carbyne complex **6.5** was accessed upon treatment with an equivalent of [Fc][BAr^F_4] to generate the dark green cationic carbyne complex [$P_3{}^B$Fe≡C-SMe][BAr^F_4] **6.6** (Scheme 6.3). The methyl peak of the thiocarbyne ligand is readily identified in the ^{1}H NMR spectrum of this complex with a sharp singlet resonance at 3.10 ppm. Characterization of this complex in the solid state showed only small perturbations to the bonding in the [Fe≡C-SMe] unit upon oxidation (Figure 6.2), with slight contraction of both the Fe-C (1.677(2) Å) and C-S (1.683(2) Å) bonds in **6.6** relative to the neutral precursor and a similar C-S-C angle (103.9(1) º). Like the neutral thiocarbonyl complex **6.2**, an interaction between the Fe center and one of the arene rings

of the supporting ligand is observed in the solid-state structure of **6.6**; this complex is symmetric in solution on the NMR time scale.

An additional thiocarbyne complex is accessible in this system by reduction of **6.5** with an excess of KC_8 at low temperature to putatively generate the anionic carbyne complex **6.7**. This complex can also be prepared by treating the dianionic thiocarbonyl complex **6.4** with an equivalent of MeOTf (Scheme 6.3). In solution, this species is thermally unstable and regenerates the anionic thiocarbonyl complex **6.3** upon warming to room temperature, with formal loss of an equivalent of methyl radical. In the presence of a second equivalent of MeOTf, warming this complex to room temperature results in its one electron oxidation to the neutral thiocarbyne complex **6.5**. The thermal instability of complex **6.7** has, to date, limited our ability to isolate and characterize this complex, but we are currently pursuing approaches to more thoroughly characterize this species. This series of complexes represents a unique case where carbyne species can be stabilized across three formal oxidation states.[27]

6.2.3 Approaches to Carbide Generation from $P_3^BFe{\equiv}CSMe$ Complexes

The first strategy targeted for generating $P_3^BFe(C)$ was further derivatization at the thiocarbyne S-atom to generate a prospective thioether leaving group. With the thiocarbyne complexes accessible across three charge states that could react with nucleophiles for the cationic complex **6.6**, electrophiles for the anionic complex **6.7**, or radicals for the neutral complex **6.5**. Ultimately, despite many attempts these approaches proved to be unsuccessful; the charged complexes **6.6** and **6.7** typically accessed net one-electron redox events to regenerate the neutral carbyne complex. The neutral radical complex itself was unreactive toward prospective transition metal radical "•S-Me" abstractors and transiently generated alkyl radicals. For these systems, we hypothesize that the extent to which charge or radical character is delocalized onto the thiocarbyne ligand is limited and, as a result, the reactivity of these systems toward further productive reactivity at S is negligible. As an alternative approach to carbide generation we considered strategies to promote the loss of thioformaldehyde, which rapidly trimerizes, derived from the -SMe unit. For the cationic thiocarbyne complex **6.6**, deprotonation of the -SMe group could lead to this type of

reactivity, but attempts to deprotonate this species with strong, non-nucleophilic bases were also unsuccessful (Scheme 6.4).

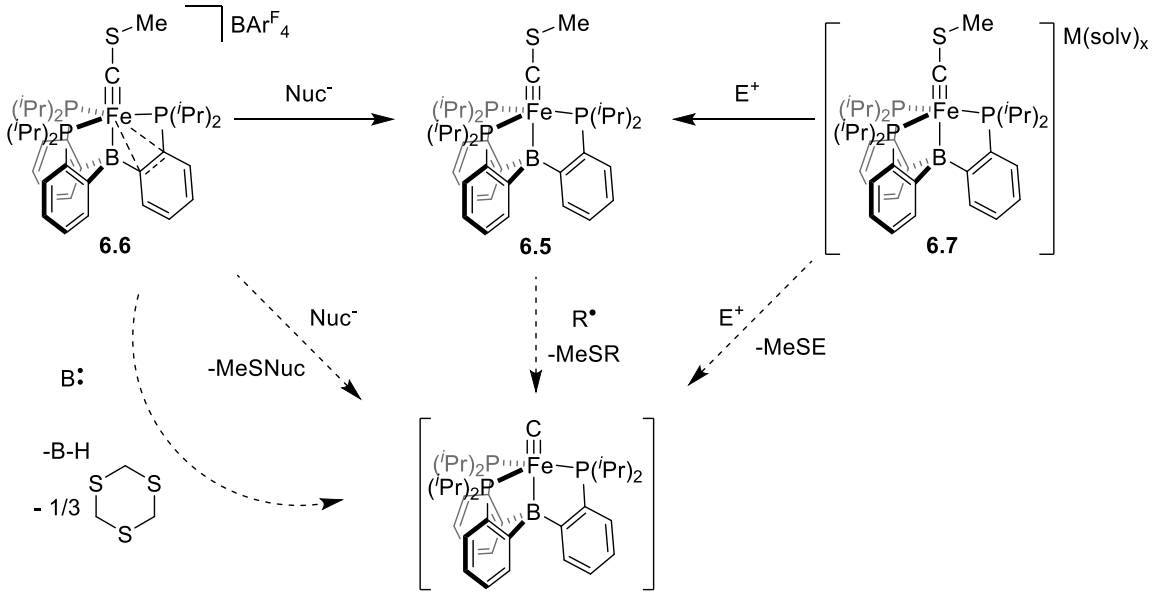

Scheme 6.4. General, unsuccessful approaches to generate a terminal Fe-carbide complex. (Nuc^- = nucleophile; B: = base; $R^\bullet$ = alkyl radical; E^+ = electrophile).

Species that are able to cleanly S-functionalize the reduced thiocarbonyl complexes **6.3** and **6.4** have thus far been limited to alkyl triflate electrophiles. Among alternatives we have explored are alkyl tosylates, aryl iodoniums, and acyl halides, which putatively give mixtures of S-functionalized and oxidized products whose similar solubilities prevent their facile separation. Given this limitation, we are currently pursuing reactivity with alkyl triflate electrophiles that incorporate groups that can be targeted for cleavage including Me_3SiCH_2OTf and $H_2C(OTf)_2$.

6.2.4 Synthesis of $P_2^PFe(CO)$ Complexes

Concurrent to our studies of the thiocarbonyl chemistry of the $[P_3^BFe]$ system, we pursued thiocarbonyl complexes supported by $[P_2^PFe]$. Prior to these studies, we synthesized and characterized the corresponding carbonyl complexes for this system.[28] These complexes provide a useful spectroscopic handle for the generation of the comparatively ill-behaved thiocarbonyl complexes; we will briefly detail their synthesis and characterization. Monocarbonyl chemistry in this system was initially accessed by stirring a benzene solution of $P_2^PFeBr_2$ under a CO atmosphere to generate $P_2^PFeBr_2(CO)$

6.8 (Scheme 6.5) with a single predominant isomer as judged by ^{31}P NMR spectroscopy.[29] Consistent with this assignment, the IR spectrum of **6.8** features a sharp CO stretch at 1938 cm^{-1}, indicating the formation of the monocarbonyl complex.

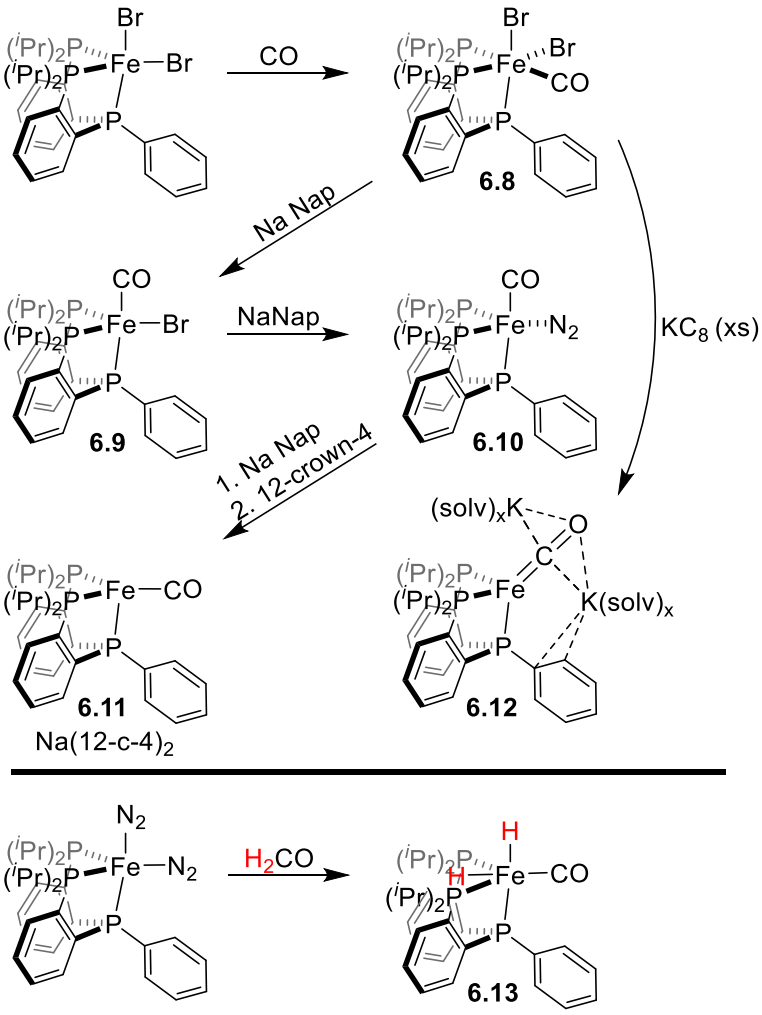

Scheme 6.5. Synthesis of $P_2^PFe(CO)$ complexes.

One electron reduction of **6.8** with an equivalent of Na naphthalenide cleanly generates the doublet $P_2^PFe^IBr(CO)$ **6.9** (Scheme 6.5). Upon one electron reduction, an increase in CO activation is observable by IR spectroscopy (ν_{CO} = 1886 cm^{-1}), with this five-coordinate complex isostructural with $P_2^PCo^IBr(CO)$ (Figure 6.3).[3] Treating this species with an additional equivalent of Na naphthalenide generates the diamagnetic Fe^0 complex **6.10** that binds an equivalent of N_2 (Scheme 6.5). This is readily observed in both the IR spectrum of this complex (ν_{CO} = 1855 cm^{-1}; ν_{NN} = 2062 cm^{-1}) and its solid state structure, with the CO ligand located *trans* to the central P^{Ph} of the supporting ligand and

the N_2 ligand coplanar with the two P^{iPr} ligands in an overall trigonal bipyramidal geometry (Figure 6.3); we note that structurally-characterized transition metal complexes with both CO and N_2-bound are relatively unusual.[30]

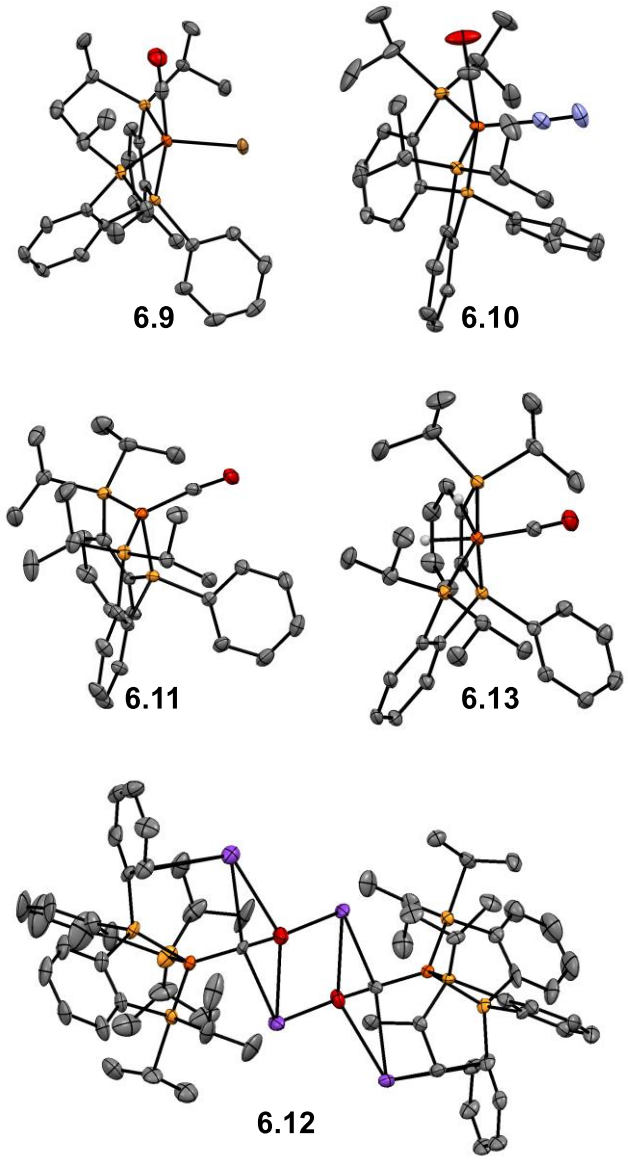

Figure 6.3. Crystal structures of $P_2^PFe(CO)$ complexes. The crown encapsulated counter cation of **6.11**, C-bound H-atoms, solvent molecules, and disorder are omitted for clarity.

Two additional reduction events are accessible to complete the series of P_2^PFe-CO complexes. Treating $P_2^PFe(CO)(N_2)$ with an equivalent of Na naphthalenide followed by two equivalents of 12-crown-4 allowed for clean isolation of the monoanionic carbonyl complex **6.11** as the crown-ether encapsulated Na salt (Scheme 6.5). Complex **6.11** features

a quite activated terminally-bound CO ligand (ν_{CO} = 1715 cm^{-1}). In the solid state, this complex adopts a distorted trigonal pyramidal geometry (Figure 6.3), similar to that observed for the d^9 Co complex $P_2^PCo(CO)$. One additional reduction event was accessible in this system. The dianionic complex $[P_2^PFe(CO)][K_2(solv)_x]$ **6.12** could be accessed readily upon the addition of an excess of KC_8 to the Fe^{II} precursor **6.8** (Scheme 6.5). The resultant complex features an exceptionally activated CO ligand, with an Fe-C distance of 1.71 Å and C-O distance of 1.24 Å stabilized in a Fe_2K_4 cluster in the solid-state, with each C-O ligand interacting with three K cations (Figure 6.3).[31,32] This could also be observed in the IR spectrum of **6.12**, with a broad highly-activated C-O stretch observed for this complex at 1536 cm^{-1}. Combined, these observations suggest that **6.12** is best described with approximate double bond character in both the Fe-C and C-O bonds.

An additional species that we ultimately became interested in generating for comparison to related Fe-CS compounds was $P_2^PFe(H)_2(CO)$ **6.13.** Complex **6.13** was prepared most readily by reacting $P_2^PFe(N_2)_2$ with excess paraformaldehyde, with broad hydridic resonances observable in the ^1H NMR spectrum of this complex at -10.5 and -14.0 ppm. We note that the reactivity of these complexes was explored and conditions amenable to productive O-functionalization were not elucidated. For this system, a propensity for competitive Fe- and O-centered reactivity and/or poor stability of the carbyne complexes proved to be problematic.

6.2.5 Synthesis of $P_2^PFe(CS)$ Complexes

Initial access to thiocarbonyl chemistry on this platform was provided by treating the previously reported complex $P_2^PFe(N_2)_2$ with $(PhO)_2C{=}S$ in pentane, which cleanly precipitates $P_2^PFe(OPh)_2(CS)$ **6.14** (Scheme 6.6).[33] The purity of the precipitated solid was confirmed by Mössbauer spectroscopy, with parameters (δ = 0.04 mm/s; ΔE_Q = 0.76 mm/s) consistent with the generation of a this species. Solution NMR characterization of the pink-brown material shows a clean diamagnetic signature; this complex slowly decays in solution over time, which has limited our ability to structurally characterize this species. A related species, $P_2^PFeCl_2(CS)$ **6.14'** has been structurally-characterized (Figure 6.4A), but the approach that generates **6.14'** is of low synthetic utility and its structure is otherwise unremarkable.[33] We attribute the solution instability of **6.14** to formal loss of PhO•, which

generates $P_2^PFe(OPh)(CS)$ **6.15** concurrent with partial demetallation to generate free ligand and an additional unidentified Fe-containing byproduct. Independent generation of **6.15** is accessible by reducing **6.14** with Na/Hg amalgam in benzene, which circumvents its unproductive decomposition.[34] Direct reduction of **6.14** instead with Na/Hg amalgam in THF gives rise to a new diamagnetic species with a diamagnetic NMR spectroscopic initially similar to the $Fe(CO)(N_2)$ complex **6.10** (Scheme 6.6). By IR spectroscopy, the ligation of N_2 to the newly generated species is confirmed by the presence of an intense N-N stretch observed at 2077 cm^{-1}, consistent with the assignment of this complex as $P_2^PFe(N_2)(CS)$ **6.16**. This species was observed to reproducibly decay in solution over time, generating an apparent mixture of unidentified species with no terminal N_2 stretch observed in the IR spectrum of the decay product(s).

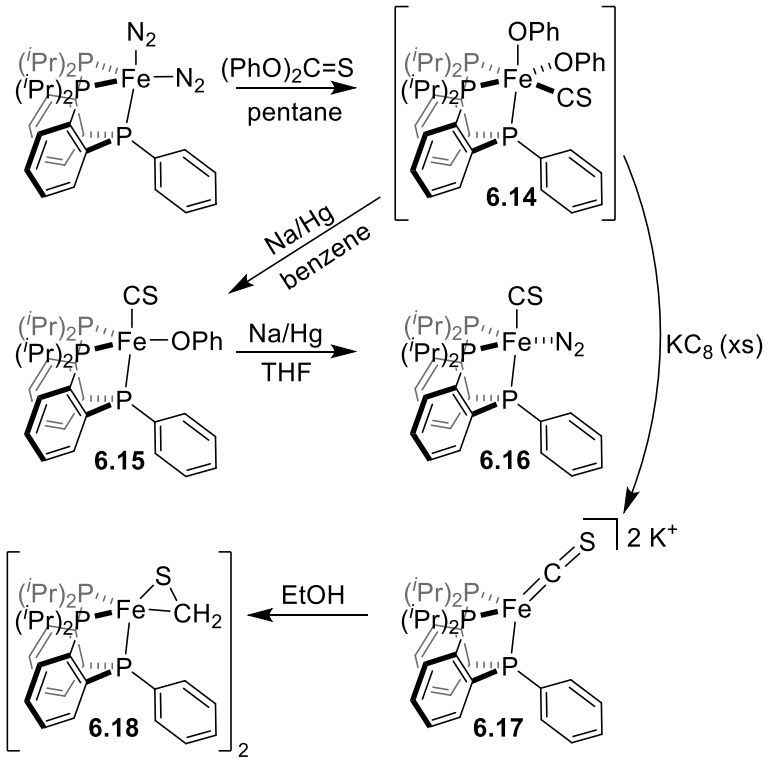

Scheme 6.6. Synthesis of $P_2^PFe(CS)$ complexes.

Towards the generation of a species that might be amenable to S-functionalization reactivity, we next explored approaches to the clean generation of anionic CS complexes supported by this platform. As such, treating complex **6.14** with an excess of KC_8 cleanly generates a new diamagnetic complex that we assigned as the formally $Fe^{-2}(CS)$ complex

6.17 (Scheme 6.6). The relatively unusual Mössbauer spectrum of this complex exhibits a quite low isomer shift ($\delta \sim 0$ mm/s) and a near negligible quadrupole splitting ($\Delta E_Q \sim 0.15$ mm/s) consistent with generation of a highly-reduced d^{10} complex in a roughly symmetric tetrahedral ligand field (Figure 6.4B); a similar spectrum is observed for the structurally-related N_2 complex.[28b] Thus far, attempts to structurally characterize this complex have resulted in its decay to a doubly protonated product, presumably generated in the presence of adventitious water. The structure observed in this case is not a dihydride akin to **6.13**, but instead the bridged thioformaldehyde product $[P_2^PFe(CH_2S)]_2$ **6.18**, with net addition of both proton equivalents at the thiocarbonyl C-atom (Figure 6.4C).[35] This species could be independently generated by treating the dianionic precursor with a EtOH saturated N_2 stream (Scheme 6.6).

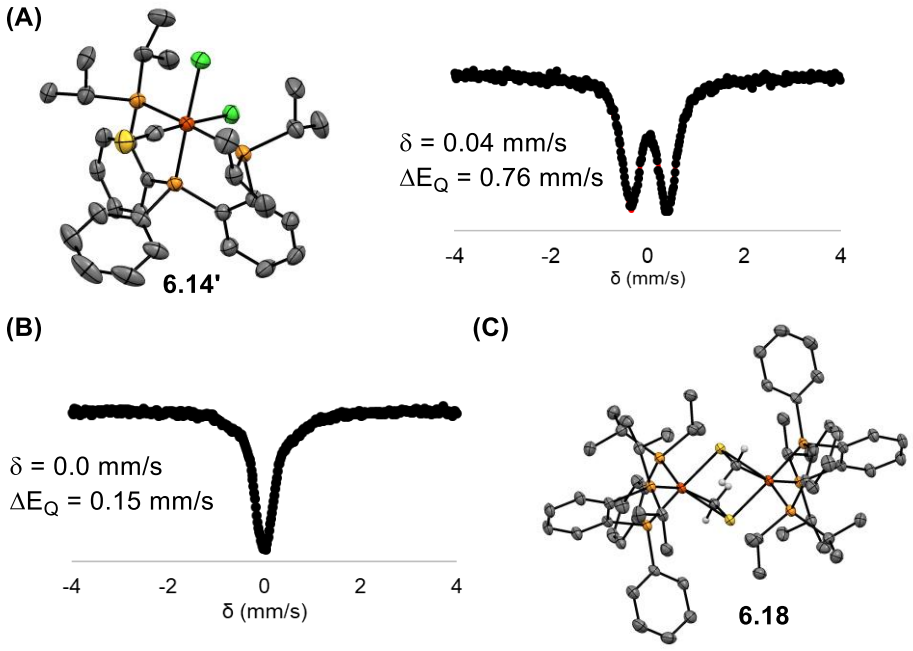

Figure 6.4. (**A**) Crystal structure of **6.14'** and Mössbauer spectrum of **6.14**, (**B**) Mössbauer spectrum of the dianionic complex **6.17,** and (**C**) structure of its decomposition product the bridged thioformaldehyde complex **6.18**.

6.2.6 S-Functionalization at P_2^PFe Thiocarbonyl Complexes

The accessible chemistry for the reduced complex **6.17** contrasts with the P_3^BFe-CS chemistry described above as this platform does not support tractable CS monofunctionalization. Given this limitation, we instead set out to explore the reactivity of

the dianionic complex **6.17** toward direct difunctionalization with suitable electrophiles, our rationalization being that a transient S-functionalized complex may be reactive toward a second alkylation/protonation event. In this chemistry, we were initially surprised to find that treating **6.17** with two equivalents of $[H(OEt_2)_2][BAr^F{}_4]$ gave rise to a major Fe-containing paramagnetic species, **6.19**, and not the product of double protonation **6.18** or two electron oxidation **6.16**. The same complex could also be generated by treating the dianionic precursor **6.17** with two equivalents of MeOTf. That these disparate electrophiles gave rise to the same product initially suggested to us that the terminal product **6.19** might be derived from C-S cleavage chemistry, where the added acid or alkyl electrophile equivalents cannot be incorporated in **6.19**. This prompted us to more closely examine this overall transformation.

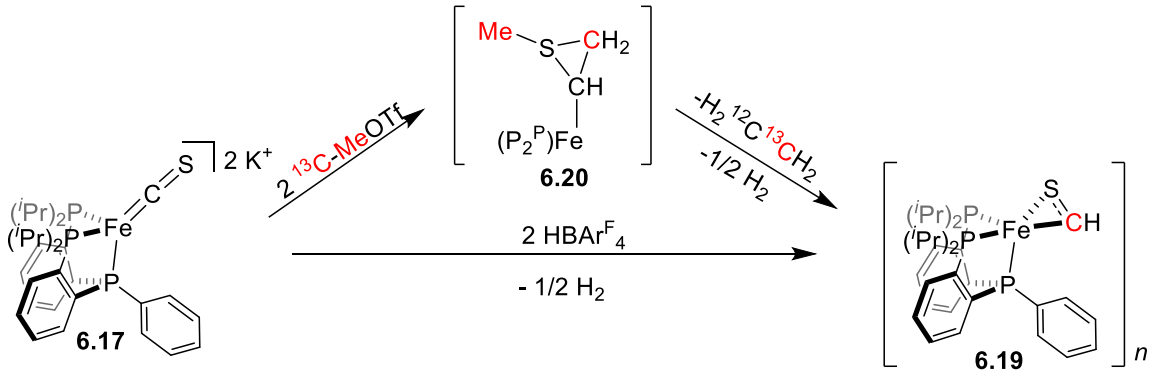

Scheme 6.7. Proposed pathway for the reaction of **6.17** with alkyl and acid electrophiles.

The reaction of **6.17** with two equivalents of acid at low temperature rapidly generates **6.19**. When **6.17** is instead treated with two equivalents MeOTf conversion to the terminal Fe product is slow, with the intermediacy of an observable asymmetric diamagnetic complex **6.20** (^{31}P NMR: 132.4, 109.2, and 89.6 ppm).[36] Use of ^{13}C-labeled MeOTf to generate this species allowed us to track the added methyl equivalents. In this case, two distinct ^{13}C-labeled peaks are observed in the ^{13}C NMR spectrum of this complex at 23.8 and 10.4 ppm, with one of these resonances (at 23.8 ppm) exhibiting strong coupling to only two protons, with apparent cleavage of the third methyl-derived C-H bond. The unaccounted-for proton resonates in the ^{1}H NMR spectrum at 4.00 ppm and correlates with a ^{13}C NMR peak at 61 ppm in the HSQC spectrum which is likely derived from the CS C-

atom. Based on these and additional spectroscopic observations, one speculative assignment for **6.20** is shown in Scheme 6.7.

As the intermediate **6.20** is converted to the paramagnetic Fe product **6.19**, the only observed ^{13}C-labeled product is ethylene. The ^{1}H NMR signature of this product surprisingly revealed that it is half-labeled ($H_2{}^{12}C={}^{13}CH_2$), where the second C-atom incorporated in the organic product is presumably derived from the thiocarbonyl C-atom (Scheme 6.7). While the identity of the terminal Fe-containing product has not been reliably determined, these experiments suggest that the product derived from double protonation of the dianionic precursor **6.17** does not arise from C-S bond cleavage. We hypothesize that **6.19** is the thioformyl complex [$P_2{}^{P}$Fe(CHS)] or a product of its decay, generated by protonation and one-electron oxidation of **6.17** with loss of half of an equivalent of H_2. To account for formation of the same product in the MeOTf case requires that the thioformyl C-atom in **6.19** is derived from one of the MeOTf equivalents; loss of half an equivalent of H_2 in the conversion from **6.20** to **6.19** balances this reaction (Scheme 6.7). Overall this transformation remarkably proceeds with the activation of three of the six C-H bonds derived from the MeOTf precursor with concurrent cleavage of the thiocarbonyl C-S bond.

6.3 Conclusions

In this chapter, we detailed the synthesis of a number of Fe-thiocarbonyl complexes supported by polydentate phosphine ligands. The [$P_3{}^{B}$Fe(CS)] complexes are amenable to S-functionalization, which generates an unique series of carbyne complexes that can be characterized across three oxidation states. For the [$P_2{}^{P}$Fe] platform, the synthesis of a series of carbonyl complexes and their more fickle thiocarbonyl analogs was acheived. When treated with two equivalents of MeOTf, the most reduced thiocarbonyl complex supported by this ligand platform accesses C-S bond cleavage *via* a surprising reaction pathway that incorporates the thiocarbonyl-derived C-atom in a generated ethylene equivalent. Thus far, C-S cleavage to generate a terminal Fe-carbide has not been achieved, but ongoing research efforts in our group are targeting alternative avenues to such a species.

6.4 Synthetic Details

6.4.1 [$P_3^BFe(CS)$][$Na(Et_2O)$] 6.3 *In situ* generation of $P_3^BFe(CS_2)$ **6.1** was carried out by adding CS_2 (5 M in THF; 1.05 equiv, 65 μL, 0.328 mmol) to a solution of $P_3^BFe(N_2)$ (210.4 mg, 0.312 mmol) in benzene (7 mL), which yielded a red solution after stirring at room temperature for 20 min. This solution was then transferred to a second vial containing $Mo(NRAr)_3$ (1.05 equiv, 204.6 mg, 0.328 mmol) and the resultant solution was stirred for an additional 30 min, turning dark brown. The solvent was removed *in vacuo* and the residue was redissolved in THF (7 mL) and stirred vigorously over an excess of Na/Hg amalgam for 1 h, giving a dark red-brown solution. This solution was decanted away from the residual Na/Hg and the solvent was removed *in vacuo*, leaving a dark residue. The residue was triturated and then washed with pentane until the washes were colorless or slightly yellow. The residue was then extracted into Et_2O, concentrated, and then layered with pentane at -30 ºC to yield the product as a dark crystalline solid (107.2 mg; 40% over three steps). To isolate this species as the 12-crown-4 encapsulated sodium salt **6.3'**, the residue obtained following the Na/Hg amalgam reduction was dissolved in Et_2O and 12-crown-4 (2 equiv) was added. This mixture was stirred at room temperature for 30 min, with the precipitation of **6.3'** in this time. The mixture was filtered and the solid was washed with pentane and then benzene. Extraction of the solid into THF followed by solvent removal *in vacuo* yielded the product as a dark orange powder. Crystalline material could be obtained by layering a THF solution of **6.3'** with pentane at -30 ºC.

6.4.2 $P_3^BFe{\equiv}CSMe$ 6.5 An orange solution of **6.3** (49.7 mg, 0.0924 mmol) was prepared in THF (3 mL) and stirred at -78 ºC in the glovebox coldwell. To the prechilled solution, MeOTf (10.6 μL, 0.0970 mmol, 1.05 equiv) was added *via* syringe, resulting in an immediate darkening of the solution. After stirring at -78 ºC for 10 min, the solution was warmed to room temperature and the solvent was removed *in vacuo*. The residue was extracted into pentane and the solvent was removed, yielding the product as a brown powder (49.7 mg, 76%). ^{1}H NMR (400 MHz, c_6d_6) δ 16.09, 12.32, 10.22, 4.45, 2.18 -1.05, -2.89, -3.64, -6.09.

6.4.3 [$P_3^BFe{\equiv}CSMe$][BAr^F_4] 6.6 A solution of **6.5** (28.7 mg, 0.041 mmol) was prepared in Et_2O (2 mL) and cooled to -78 ºC in the glovebox coldwell. A similarly prechilled

solution of [Fc][BAr^F_4] (1 equiv, 42.7 mg, 0.041 mmol) in Et_2O (2 mL) was added and the mixture was stirred at -78 ºC for 1 h. The solvent was removed *in vacuo* and the resultant residue was washed with pentane and then benzene until the washes were colorless. The resultant green residue was extracted into a 1:1 Et_2O/THF mixture, giving the desired product **6.6** as a dark green powder following solvent removal. The product could be obtained as a crystalline solid by layering a THF solution of the product with pentane at -30 ºC. No ^{31}P resonance is observed for this species at room temperature, presumably because of the equilibrating Fe-arene interaction. ^1H NMR (400 MHz, THF-d_8): δ 7.86 – 7.76 (s, 8H, BAr^F_4), 7.71 (t, *J* = 6.8 Hz, 3H), 7.57 (s, 4H, BAr^F_4), 7.53 (overlapping, 3H), 7.45 (t, *J* = 7.1 Hz, 3H), 7.25 (d, *J* = 7.7 Hz, 3H), 3.10 (s, 3H, SMe), 2.77 (br, 3H), 1.66-1.59 (overlapping, *J* = 14.7, 14.0, 7.2 Hz, 18H), 1.00 (dd, *J* = 15.2, 6.8 Hz, 9H), 0.78 (br, 3H), 0.64 (dd, *J* = 13.1, 6.4 Hz, 9H).

6.4.5 $P_2^PFe(CS)(OPh)_2$ 6.14 $P_2^PFe(N_2)_2$ (96.1 mg, 0.158 mmol) and $(PhO)_2C{=}S$ (36.5 mg, 0.158 mmol) were combined as solids in a vial and pentane (10 mL) was added. The resultant mixture was stirred for 2 h at room temperature, with precipitation of a fine powder observed over this time. Filtering the reaction mixture yielded the product as a pink-brown powder (60 mg, 49%). ^1H NMR (400 MHz, C_6D_6) δ 7.89 (d, *J* = 8.0 Hz, 2H), 7.74 (br, 2H), 7.53 (t, *J* = 7.5 Hz, 2H), 7.36 (br, 2H), 7.02 (s, 4H), 6.89 (t, *J* = 7.8 Hz, 2H), 6.85 – 6.71 (m, 3H), 6.62 (t, *J* = 8.2 Hz, 2H), 6.49 (t, *J* = 7.0 Hz, 1H), 6.36 (d, *J* = 8.0 Hz, 2H), 3.11 (br, 3H), 2.43 (br, 3H) 1.48 (q, 12H), 1.34-1.16 (overlapping solv, 12H), 1.10 (q, 12H). $^{31}P\{^1H\}$ NMR (162 MHz, C_6D_6): δ 99.13 (t, *J* = 40 Hz), 72.80 (d, *J* = 40 Hz). Mössbauer parameters (frozen benzene solution): δ = 0.04 mm/s, ΔE_Q = 0.76 mm/s.

6.4.6 $P_2^PFe(CS)(OPh)$ 6.15 A solution of **6.14** (60 mg, 0.077 mmol) was prepared in benzene (3 mL) and Na/Hg amalgam was quickly added. This mixture was vigorously stirred for 2 h and the resultant solution was decanted away from excess Na/Hg amalgam. The solvent was removed and the residue was triturated and then washed with pentane Extracting the residue into benzene and then lyophilized to yield the product as a brown powder. ^1H NMR (400 MHz, C_6D_6): δ 10.2, 7.8, 6.2, 5.4, -1.36, -3.30.

6.4.7 $[P_2^PFe(CS)][K_2(solv)_x]$ 6.17 Given the extreme sensitivity of **6.17**, solutions of this complex for reactivity studies and characterization were typically prepared *in situ*. Separate

vials containing solid **6.14** and THF were chilled to -78 ºC in the glovebox coldwell. After equilibrating at that temperature for 10 min, the solid was dissolved in the prechilled THF and an excess of KC_8 (10 equiv) was added immediately. The reaction mixture darkened upon addition of reductant, was stirred briefly until it became a homogeneous suspension, and was then passed through a prechilled celite pipette filter, yielding the product as a dark brown/black THF solution. The product **6.17** is thermally stable in sealed solutions, but slowly picks up proton equivalents when manipulated under a nominally inert atmosphere. $^{31}P\{^1H\}$ NMR (162 MHz, THF): δ 122.0 (d, *J* = 12 Hz, 2P), 104.8 (t, *J* = 12 Hz, 1P). Mössbauer parameters (frozen THF solution): $\delta = 0.0$ mm/s, $\Delta E_Q = 0.15$ mm/s.

6.5 Notes and References

(1) (a) Rofer-DePoorter, C. K. *Chem. Rev.* **1981**, *81*, 447-474. (b) Maitlis, P. M.; Zanotti, V. *Chem. Commun.* **2009**, 1619-1634.

(2) (a) Lee, C. C.; Hu, Y.; Ribbe, M. W. *Science* **2010**, *329*, 642. (b) Hu, Y.; Lee, C. C.; Ribbe, M. W. *Science* **2011**, *333*, 753-755. (c) Lee, C. C.; Hu, Y.; Ribbe, M. W. *Angew. Chem. Int. Ed.* **2012**, *51*, 1947-1949. (d) Lee, C. C.; Hu, Y.; Ribbe, M. W. *Angew. Chem. Int. Ed.* **2015**, *54*, 1219-1222. (e) Lee, C. C.; Fay, A. W.; Weng, T.-C.; Krest, C. M.; Hedman, B.; Hodgson, K. O.; Hu, Y.; Ribbe, M. W. *Proc. Natl. Acad. Sci.* **2016**, *112*, 13845-13849. (f) Lee, C. C.; Tanifuji, K.; Newcomb, M.; Liedtke, J.; Hu, Y.; Ribbe, M. W. *ChemBioChem* **2018**, *19*, 649-653.

(3) See Chapter 4 and: Deegan, M. M.; Peters, J. C. *Chem. Commun.* **2019**, *55*, 9531-9534.

(4) For a recent review of molecular FT model chemistry see: West, N. M.; Miller, A. J. M.; Labinger, J. A.; Bercaw, J. E. *Coord. Chem. Rev.* **2011**, *255*, 881-898.

(5) Lee, Y.; Peters, J. C. *J. Am. Chem. Soc.* **2011**, *133*, 4438-4446.

(6) Suess, D. L. M.; Peters, J. C. *J. Am. Chem. Soc.* **2013**, *135*, 12580-12583.

(7) See Chapter 2 and: Deegan, M. M.; Peters, J. C. *J. Am. Chem. Soc.* **2017**, *139*, 2561-2564.

(8) In related chemistry, complete cleavage of the C-N bond is observed upon proton-coupled reduction of a phosphine-supported Fe-CN complex. In this chemistry, there is no direct evidence for the intermediacy of a terminal Fe(C). See: (a) Rittle, J.; Peters, J. C. *J. Am. Chem. Soc.* **2017**, *139*, 3161-3170. (b) Rittle, J.; Peters, J. C. *Angew. Chem. Int. Ed.* **2016**, *55*, 12262-12265.

(9) Peters, J. C.; Odom, A. L.; Cummins, C. C. *Chem. Commun.* **1997**, 1995-1996.

(10) Related reactivity has been reported more recently for phosphine-supported Mo complexes, see: (a) Buss, J. A.; Agapie, T. *Nature* **2016**, *529*, 72-75. (b) Buss, J. A.; Agapie, T. *J. Am. Chem. Soc.* **2016**, *138*, 16466-16477.

(11) For examples of reagents that have been explored for $C(H)_{0-2}$ transfer, see: (a) Agapie, T.; Diaconescu, P. L.; Cummins, C. C. *J. Am. Chem. Soc.* **2002**, *124*, 2412-2413. (b) Joost, M.; Nava, M.; Transue, W. J.; Cummins, C. C. *Chem. Commun.* **2017**, *53*, 11500-11503. (c) Martinez, J. L.; Lin, H.-J.; Lee, W.-T.; Pink, M.; Chen, C.-H.; Gao, X.; Dickie, D. A.; Smith, J. M. *J. Am. Chem. Soc.* **2017**, *139*, 14037-14040. (d) Joost, M.; Transue, W. J.; Cummins, C. C. *Chem. Sci.* **2018**, *9*, 1540-1543.

(12) (a) Carlson, R. G.; Gile, M. A.; Heppert, J. A.; Mason, M. H.; Powell, D. R.; Vander Velde, D.; Vilain, J. M. *J. Am. Chem. Soc.* **2002**, *124*, 1580-1581. (b) Hejl, A.; Trnka, T. M.; Day, M. W.; Grubbs, R. H. *Chem. Commun.* **2002**, 2524-2525. (c) Caskey, S. R.; Stewart, M. H.; Kivela, J. E.; Sootsman, J. R.; Johnson, M. J. A.; Kampf, J. W. *J. Am. Chem. Soc.* **2005**, *127*, 16750-16751.

(13) See Ref. 12c and: Stewart, M. H.; Johnson, M. J. A.; Kampf, J. W. *Organometallics* **2007**, *26*, 5102-5110.

(14) Enriquez, A. E.; White, P. S.; Templeton, J. L. *J. Am. Chem. Soc.* **2001**, *123*, 4992-5002.

(15) For reviews of thiocarbonyl chemistry, see: (a) Petz, W. *Coord. Chem. Rev.* **2008**, *252*, 1689-1733. (b) Broadhurst, P. V. *Polyhedron* **1985**, *4*, 1801-1846.

(16) Moret, M.-E.; Peters, J. C. *Angew. Chem. Int. Ed.* **2011**, *50*, 2063-2067.

(17) (a) Moret, M.-E.; Peters, J. C. *J. Am. Chem. Soc.* **2011**, *133*, 18118-18121. (b) Anderson, J. S.; Cutsail, G. E.; Rittle, J.; Connor, B. A.; Gunderson, W. A.; Zhang, L.; Hoffman, B. M.; Peters, J. C. *J. Am. Chem. Soc.* **2015**, *137*, 7803-7809. (c) Thompson, N. B.; Green, M. T.; Peters, J. C. *J. Am. Chem. Soc.* **2017**, *139*, 15312-15315. (d) Deegan, M. M.; Peters, J. C. *Chem. Sci.* **2018**, *9*, 6264-6270. (e) Thompson, N. B.; Oyala, P. H.; Dong, H. T.; Chalkley, M. J.; Zhao, J.; Alp, E. E.; Hu, M.; Lehnert, N.; Peters, J. C. *Inorg. Chem.* **2019**, *58*, 3535-3549. (f) Nesbit, M. A.; Oyala, P. H.; Peters, J. C. *J. Am. Chem. Soc.* **2019**, *141*, 8116-8127.

(18) See Ref. 13 and: (a) Laplaza, C. E.; Odom, A. L.; Davis, W. M.; Cummins, C. C. *J. Am. Chem. Soc.* **1995**, *117*, 4999-5000. (b) Laplaza, C. E.; Cummins, C. C. *Science* **1995**, *268*, 861-863.

(19) Johnson, A. R.; Davis, W. M.; Cummins, C. C.; Serron, S.; Nolan, S. P.; Musaev, D. G.; Morokuma, K. *J. Am. Chem. Soc.* **1998**, *120*, 2071-2085.

(20) This complex is spectroscopically similar to the previously reported $P_3^BFe(CO)$ complex, see Ref. 16.

(21) See Ref. 5, 6, and: (a) Fischer, E. O.; Schneider, J.; Neugebauer, D. *Angew. Chem., Int. Ed. Engl.* **1984**, *23*, 820−821. (b) Anderson, S.; Hill, A. F. *J. Organomet. Chem.* **1990**, *394*, C24-C26. (c) Anderson, S.; Hill, A. F.; Ng, Y. T. *Organometallics* **2000**, *19*, 15-21. (d) Mokhtarzadeh, C. C.; Moore, C. E.; Rheingold, A. L.; Figueroa, J. S. *Angew. Chem. Int. Ed.* **2017**, *56*, 10894-10899. (e) Citek, C. T.; Oyala, P. H.; Peters, J. C. *J. Am. Chem. Soc.* Accepted Article. doi: 10.1021/jacs.9b06987

(22) Reported amino carbynes from our group have longer Fe-C distances (see Ref. 8). See also: Rittle, J. D. Ph.D. Dissertation, California Institute of Technology, 2015.

(23) These are discussed in Ref. 15. For examples of structurally-characterized Fe-CS complexes, see: (a) Conway, P.; Manning, A. R.; Stephens, F. S. *J. Organomet. Chem.* **1980**, *186*, C64-C66. (b) Scheidt, W. R.; Geiger, D. K. *Inorg. Chem.* **1982**, *21*, 1208-1211. (c) Touchard, D.; Fillaut, J.-L.; Dixneuf, P. H.; Toupet, L. *J. Organomet. Chem.* **1986**, *317*, 291-299. (d) Richardson, J. W.; Angelici, R. J.; Jacobson, R. A. *Inorg. Chem.* **1987**, *26*, 452-454. (e) Cao, C.; Dahal, S.; Shang, M.; Beatty, A. M.; Hibbs, W.; Schulz, C. E.; Scheidt, W. R. *Inorg. Chem.* **2003**, *42*, 5202-5210.

(24) The corresponding dianionic Fe-N_2 complex has previously been described, see Ref. 17c.

(25) (a) Greaves, W. W.; Angelici, R. J.; Helland, B. J.; Klima, R.; Jacobson, R. A. *J. Am. Chem. Soc.* **1979**, *101*, 7618-7620. (b) Desmond, T.; Lalor, F. J.; Ferguson, G.; Parvez, M. *J. Chem. Soc., Chem. Commun.* **1984**, 75-77. (c) Angelici, R. J.; Doyle, R. A. *J. Am. Chem. Soc.* **1990**, *112*, 194-198. (d) Cordiner, R. L.; Hill, A. F.; Wagler, J. *Organometallics* **2008**, *27*, 4532-4540.

(26) See Ref. 8, 21e, and: (a) Felixberger, J. K.; Kiprof, P.; Herdtweck, E.; Herrmann, W. A.; Jakobi, R.; Gütlich, P. *Angew. Chem. Int. Ed.* **1989**, *28*, 334-337. (b) Lemos, M. A. N. D. A.; Pombeiro, A. J. L.; Hughes, D. L.; Richards, R. L. *J. Organomet. Chem.* **1992**, *434*, C6-C9. (c) van der Eide, E. F.; Piers, W. E.; Parvez, N.; McDonald, R. *Inorg. Chem.* **2007**, *46*, 14-21. (d) Leep, C. J.; Kingsbury, K. B.; McElwee-White, L. *J. Am. Chem. Soc.* **1988**, *110*, 7535-7536.

(27) A structurally-related series of $[Fe{\equiv}NNMe_2]^{+/0/-}$ complexes supported by this ligand system reported recently by our group. See Ref. 17e.

(28) Many related Fe-N_2 complexes on this platform have been described, see: (a) Buscagan, T. M.; Oyala, P. H.; Peters, J. C. *Angew. Chem. Int. Ed.* **2017**, *56*, 6921-6926. (b) Schild, D. J.; Peters, J. C. *ACS Catal.* **2019**, *9*, 4286-4295.

(29) This species tends to add a second equivalent of CO, especially when generated in more polar solvents (*i.e.*, THF, DCM), with displacement of one of the halide ligands. The resultant species is very insoluble in THF and benzene and can readily be removed from the monocarbonyl complex. A closely related species has previously been described, see: Li, P.; de Bruin, B.; Reek, J. N. H.; Dzik, W. I. *Organometallics* **2015**, *34*, 5009-5014.

(30) (a) Sato, M.; Tatsumi, T.; Kodama, T.; Hidai, M.; Uchida, T.; Uchida, Y. *J. Am. Chem. Soc.* **1978**, *100*, 4447-4452. (b) Luo, X.-L.; Kubas, G. J.; Burns, C. J.; Eckert, J. *Inorg. Chem.* **1994**, *33*, 5219-5229. (c) Kandler, H.; Gauss, C.; Bidell, W.; Rosenberger, S.; Bürgi, T.; Eremenko, I. L.; Veghini, D.; Orama, O.; Burger, P.; Berke, H. *Chem. Eur. J.* **1995**, *1*, 541-548. (d) Zhang, J.; Barakat, K. A.; Cundari, T. R.; Gunnoe, T. B.; Boyle, P. D.; Petersen, J. L.; Day, C. S. *Inorg. Chem.* **2005**, *44*, 8379-8390. (e) Kirillov, A. M.; Haukka, M.; Guedes da Silva, M. F. C.; Fraústo da Silva, J. J. R.; Pombeiro, A. J. L. *J. Organomet. Chem.* **2006**, *691*, 4153-4158. (f) Lee, J. P.; Ke, Z.; Ramírez, M. A.; Gunnoe, T. B.; Cundari, T. R.; Boyle, P. D.; Petersen, J. L. *Organometallics* **2009**, *28*, 1758-1775.

(31) This complex is unstable to the addition of crown ethers.

(32) Noted bond distances are an average of two crystallographically distinct Fe-centers in the asymmetric unit.

(33) We explored a few alternatives to $(PhO)_2C=S$. Use of thiophosgene $Cl_2C=S$ led predominantly to oxidation chemistry, yielding $P_2^PFeCl_2$ as the major product. Use of the asymmetric variant of this reagent, (PhO)ClC=S, led initially to productive chemistry. The product of this transformation disproportionates to give partial demetallation and $P_2^PFeCl_2(CS)$, which was crystallographically characterized when generated *via* this synthetic route. Thiocarbonyl diimidazole led predominantly to demetallation, with free ligand observed.

(34) Attempts to structurally characterize this complex have invariably yielded twinned crystals. Data of sufficient quality to confirm the identity of this complex.

(35) The propensity of thiocarbonyl compounds to undergo migratory insertion reactivity is well-precedented, see Ref. 15 for reviews and for an early example, see: Roper, W. R.; Town, K. G. *J. Chem. Soc., Chem. Commun.* **1977**, 781-782.

(36) Spectroscopically similar intermediates arise from functionalization with $[Et_3O][BAr^F_4]$ or the tethered bistriflate electrophile $TfO(CH_2)_4OTf$.

Appendix A

MODIFICATION OF LIGAND ELECTRONIC PROFILES IN N_2 FIXATION CATALYSIS

A1.1 Introduction

The essential nature of N_2 fixation processes in supporting human life have made the industrial Haber-Bosch process and biological nitrogenase enzymes the focus of intense scientific inquiry.[1] Through these investigations, the mechanism of industrial N_2 fixation has been well understood for some time,[2] but the current mechanistic understanding of the enzymatic process remains limited.[3] Our specific interest in this area lies in the development of well-defined functional model systems that provide opportunities for study of detailed mechanistic pathways for N_2 conversion to NH_3.[4]

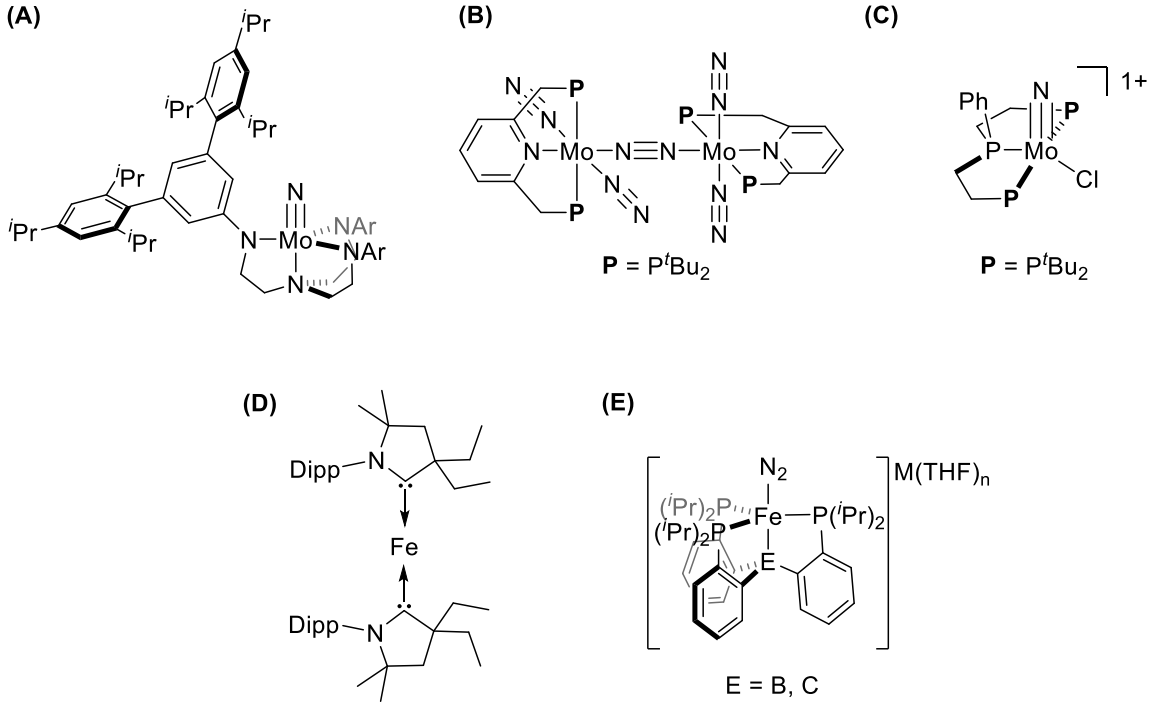

Figure A1.1. Select early examples of molecular catalysts that facilitate the reduction of N_2 to NH_3. **(A)** First molecular catalyst reported for N_2 reduction reported by Schrock.[5] **(B, C)** Additional pincer-supported Mo catalysts reported by Nishibayashi. **(D,E)** Molecular Fe-based catalysts reported by Peters.

The first examples of molecular model systems that facilitate the catalytic reduction of N_2 to NH_3 upon addition of proton and electron equivalents were reported only in the

last fifteen years. In 2003, the first example was described by Schrock and Yandulov where tris(amido)amine-supported Mo complexes were found to facilitate the conversion of N_2 to NH_3 upon the addition of excess acid and reductant (Figure A1.1A).[5] For this system, extensive stoichiometric reactivity studies have been carried out and provide evidence to support the feasibility of distal mechanism for this system.[6] Subsequently, the group of Nishibayashi demonstrated that pincer supported Mo complexes are also capable of facilitating the catalytic reduction of N_2 to NH_3 (Figure A1.1B, C).[7] In these systems (Figure A1.1B), experimental mechanistic studies are limited and outlined mechanistic pathways heavily depend on theoretical work.[8] Nevertheless, these studies provided evidence that support a rate limiting initial N_2 protonation step, which led to the rational improvement of the catalytic activity with the synthesis of more electron-rich variants of this catalyst.[7c]

Our group has a long-standing interest in developing chemistry relevant to N_2 fixation at Fe, as this is the only element required for both the Haber-Bosch process and biological N_2 fixation.[9] Recently, our group has reported a number of molecular Fe catalysts that facilitate N_2-to-NH_3 conversion (Figure A1.1D, E),[10] with additional examples provided more recently by the groups of Nishibayashi[11] and Ashley.[12] The most active and extensively studied of these systems the $(P_3^B)Fe$ ($P_3^B = B(o\text{-}P^iPr_2C_6H_4)_3$) system, which reacts with excess $HBAr_4^F$ ($HBAr_4^F = [H(OEt_2)_2][(3,5\text{-}(CF_3)_2C_6H_3)_4B)]$) and KC_8 at low temperatures to yield catalytic amounts of NH_3 (initially 7 equiv when supplied with 50 equiv of acid and reductant).[10a] In this case, little was known regarding the mechanism of the reaction until very recently.[13] Direct stoichiometric studies examining the reactivity of plausible intermediates have proven to be challenging for this system, as proposed intermediates are either synthetically inaccessible or kinetically unstable.[14] Previous efforts to modify the supporting ligand either at the anchor atom (E = Si, C, Al, Ga) or at the P-substituent (R = Cy, Ph) have invariably resulted in lower catalytic activity.[10b,15] These results suggest that the high catalytic turnover observed for $(P_3^B)Fe$ is, to some extent, inherent to the B-anchor atom, with some sensitivity to the steric and electronic profiles of the supporting scaffold.

With this in mind, we targeted ligand electronic modifications that would not perturb its steric profile or the primary coordination sphere, with the hope of providing

access to a more active catalyst or complementary mechanistic insight. Herein, we describe the synthesis of (P_3^B)Fe complexes with variably substituted phenylene linkers and examine the effect of these electronic perturbations on catalytic N_2 reduction.

A1.2 Synthesis and Characterization of Modified Ligands and Their Fe Complexes

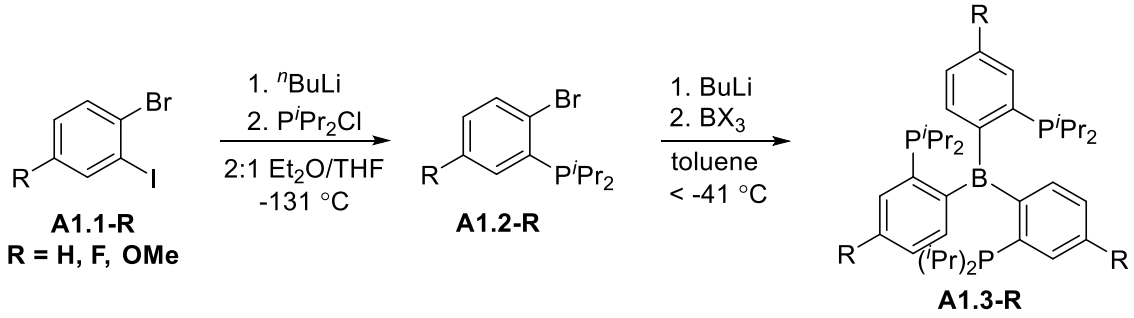

Scheme A1.1. Two-step synthesis of ligands **A1.3-R** from precursors **A1.1-R**.

Synthesis of a series of electronically modified R-P_3^B (R = F, OMe) ligands proceeds analogously to the synthesis of the parent P_3^B system initially reported by Bourissou and coworkers (Scheme A1.1).[16] Precursor substituted arenes were purchased (**A1.1-F**) or prepared using literature methods (**A1.1-OMe)**.[17] Selective lithium-halogen exchange proceeds upon the addition of ^{n}BuLi to a 2:1 Et_2O/THF solution of **A1.1-R** at -131 °C. Quenching with ^{i}Pr$_2$PCl yields the *o*-phosphinophenyl bromide product **A1.2-R** in good yields following purification. From **A1.2-R**, ligand assembly proved to be quite sensitive to arene substitution pattern and the choice of reaction conditions. For **A1.2-OMe**, lithium-halogen exchange was carried out with the addition of 2 equiv of ^{t}BuLi at -78 °C in toluene. Quenching the generated aryl-lithium *in situ* with $B(OMe)_3$ (1/3 equiv) yields the desired MeO-P_3^B product **A1.3-OMe**. For **A1.2-F**, lithium-halogen exchange was optimized with the addition of ^{n}BuLi (1.05 equiv) at -41 °C in a toluene solution. In this case, quenching the reaction mixture at -78 °C with BCl_3 (1/3 equiv) yields the F-P_3^B product **A1.3-F**.

Metallation of these ligands on Fe proceeds readily using the method previously reported for the related diphosphine borane (P_2^{BPh} = PhB(*o*-^{i}Pr$_2$PC$_6$H$_4$)$_2$) ligand.[18] Stirring a solution of **A1.3-R** with $FeBr_2$ in THF results in a color change to bright yellow upon formation of an $FeBr_2$ phosphine adduct, which was not isolated. Overnight reduction of this species with stoichiometric Na/Hg amalgam in benzene yields (R-P_3^B)FeBr **A1.4-R** (Scheme A1.2). Complexes **A1.4-OMe** and **A1.4-F** exhibit spectroscopic signatures

similar to the previously reported complex **A1.4-H** by UV-Vis and ^{1}H NMR, excepting the absence of one of the proton resonances in the paramagnetic region, whose loss was attributed to substitution in the ligand backbone.[19] The solution magnetic moments of these complexes were measured using the Evans Method and confirmed that **A1.4-OMe** and **A1.4-F** unsurprisingly adopt the same S = 3/2 ground state as **A1.4-H** (μ_{eff} = 4.3μ_B).[20] Solid-state structure determination by single crystal XRD confirmed that complexes **A1.4-OMe** and **A1.4-F** are isostructural to **A1.4-H**, with all of these species crystallizing in the triclinic space group P-1 (Figure A1.2A, B).

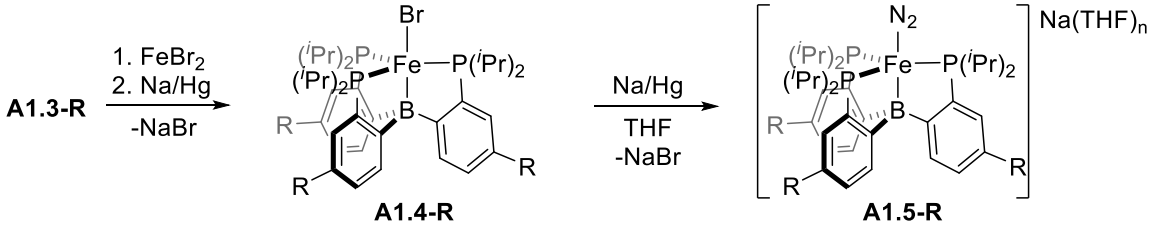

Scheme A1.2. Metallation of **A1.3-R** using $FeBr_2$, yielding **A1.4-R** and further reduction to the anionic N_2 complex **A1.5-R**.

Table A1.1. Comparison of complexes **A1.4-R**, **A1.5-R**, and **A1.6-R**. Stretching frequencies are for compounds in the solid state (thin film or KBr pellet). Data for **A1.4-H**, **A1.5-H**, and **A1.6-H** were previously reported.

	S =	$E°_{1/2}$ (V)	ν_{NN} (cm^{-1})	Fe-Br/N_2 (Å)	Fe-P_{ave} (Å)	Fe-B (Å)	Σ (C-B-C) (°)
A1.4-H	3/2	--	--	2.41	2.41	2.46	341.9
A1.4-OMe	3/2	--	--	2.43	2.43	2.445	336.9
A1.4-F	3/2	--	--	2.44	2.43	2.42	338
A1.5-H	1/2	--	1879	--	--	--	--
A1.6-H	1/2	-2.06	1905	1.78	2.25	2.29	331.0
A1.5-OMe	1/2	--	1873	--	--	--	--
A1.6-OMe	1/2	-2.09	1902	1.79	2.25	2.32	330.6
A1.5-F	1/2	--	1887	--	--	--	--
A1.6-F	1/2	-1.96	1916	1.8	2.24	2.29	329.8

Reduction of **A1.4-R** using excess Na/Hg amalgam (~4 equiv) in THF provides access to the anionic, Na-capped N_2 complex **A1.5-R** (Scheme A1.2). Intense N_{-N} stretches

can be observed in the IR spectra of these species at 1873 cm^{-1} for **A1.5-OMe** and 1887 cm^{-1} for **A1.5-F**. Layering an Et_2O solution of **A1.5-R** with a solution of 12-crown-4 yields the cation-encapsulated salt **A1.6-R** as a red microcrystalline solid. The expected shifts in the N-N stretching frequencies are observed upon encapsulation of the counter-cation, with N-N stretches at 1902 cm^{-1} for **A1.6-OMe** and 1916 cm^{-1} for **A1.6-F**. Solution magnetic moment data is consistent with the $S = 1/2$ spin-state predicted for a d^9 metal center ($\mu_{eff} = 1.8\mu_B$) and structure determination by XRD confirmed the identity of complexes **A1.6-OMe** and **A1.6-F** (Figure A1.2C, D). The electrochemistry of these N_2 complexes show a quasi-reversible event for the -1/0 redox couple at -2.09 V for **A1.6-OMe**, -2.06 for **A1.6-H**, and -1.96 V for **A1.6-F** (vs. Fc/Fc^+). An additional quasi-reversible oxidation event is observed at -1.51 V for **A1.6-OMe** and -1.47 V for **A1.6-H**, with an irreversible oxidative feature at approximately -0.4 V for **A1.6-F**.[21] The remarkable difference in the oxidation potential of **A1.6-F** is not readily explained given the otherwise similar properties of these complexes. It is worth noting here that the previously reported complexes $(P_3^B)Fe(CO)$ and $(P_3^B)Co(N_2)$ have similar, unusually positive oxidation events.[19,22]

Electronically varied compounds **A1.4-R**, **A1.5-R**, and **A1.6-R** can be compared across a series of parameters (Table A1.1). In all variants, the expected crystallographic trends are observed upon the reduction of **A1.4-R** to **A1.6-R**, with shortening of the Fe-P and Fe-B bonds and increased pyramidalization at B. This is consistent with increased π-backbonding to the phosphines and an increase in σ-donation to the borane ligand as anticipated upon reduction. Across the electronically varied series, for complexes **A1.4-R** or **A1.6-R** there are no consistent trends in the bond lengths, likely because the relatively small electronic perturbations are competing with crystal packing effects. More systematic trends are observed in the electrochemical and N_2 activation parameters for these complexes. For both the capped and uncapped complexes **A1.5-R** and **A1.6-R**, the degree of N_2 activation varies over 14 cm^{-1}, with the more electron rich MeO-substituted complexes exhibiting a greater degree of N_2 activation than either the unsubstituted complexes or the least activated F-substituted species. A consistent trend is observed in the reduction potentials of these compounds, which show that the comparatively electron-poor F-complexes are reduced most readily to the anionic N_2 species, with the reduction event 130 mV more reducing for the electron-rich MeO-variant. Further, both of these

measurements demonstrate that the MeO-congener is more similar to the original system than the F-congener, which is borne out in the catalytic reactivity profiles of these complexes discussed below. The total variation across the two parameters discussed here is similar to that reported for Nishibayashi's PNP-supported Mo complexes, which have reduction potentials that vary over 130 mV and N_2 stretching frequencies that vary over 18 cm^{-1}.[7c]

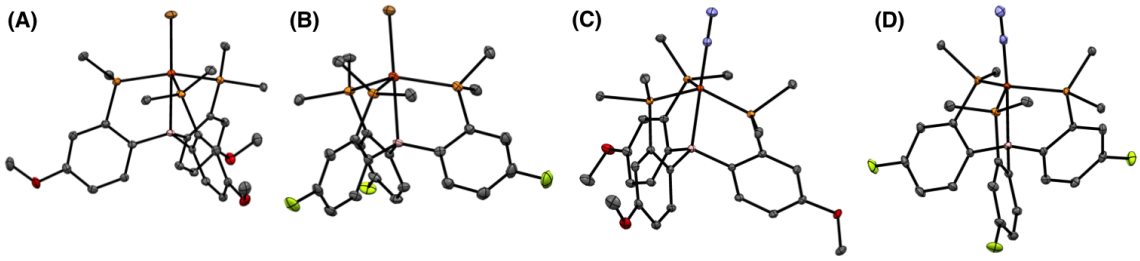

Figure A1.2. From left to right: Structures of **A1.4-OMe**, **A1.4-F**, **A1.6-OMe**, and **A1.6-F**. Solvent molecules, counter-cations, and hydrogen atoms have been omitted and ^{i}Pr groups have been truncated for clarity.

A1.3 Catalytic Reduction of N_2 to NH_3

Previous stoichiometric and kinetic studies have provided some insight with respect to plausible mechanistic pathways for the reduction of N_2 by **A1.6-H**. Direct stoichiometric studies demonstrate the viability of initial protonation steps to generate a Fe-hydrazido intermediate **A1.7-H** (Scheme A1.4A) and ultimately promote N-N bond scission to generate a terminal Fe-nitride **A1.8-H**.[14b,c] Kinetic studies have found that the overall reaction is first-order in Fe and zero-order in $HBAr_4^F$, suggesting that these and other protonation steps are of no kinetic consequence.[13] Later steps in a plausible cycle have also been demonstrated, with a terminal Fe-amido complex **A1.9-H** protonated to generate a cationic ammonia complex **A1.10-H**. Reduction of **A1.10-H** results in the dissociation of NH_3 and generation of an N_2 complex **A1.11-H** (Scheme A1.4B).[14a] Theoretical studies are underway to provide complementary support for plausible early stage mechanistic steps.[23] *In situ* Mössbauer spectroscopy has allowed our group to identify an Fe-H species **A1.12-H** as the catalyst resting state under turnover, with this species consumed as the reaction proceeds to completion. Stoichiometric reactivity of **A1.12-H** provides evidence for a kinetically accessible pathway to regenerate the precatalyst **A1.6-H** from this resting state (Scheme A1.4C). These kinetic studies also led to the discovery that **A1.6-H** is a more

robust catalyst than initially appreciated, yielding up to 60 equiv of NH_3 with higher reagent loadings (1500 equiv $HBAr^F$; 1800 equiv KC_8).[13]

Table A1.2 Results of catalytic runs using **A1.6-R** as the precatalyst under conditions optimized elsewhere for **A1.6-H**.* [a]Results reported elsewhere.[13]

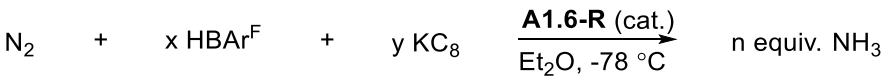

Run	Catalyst	$HBAr_4^F$ equiv	KC_8 equiv	Equiv NH_3/Fe	%Yield NH_3/H^+
Average[a]	**A1.6-H**	48	58	7.3 ± 0.5	45 ± 3
Average[a]	**A1.6-H**	1500	1800	59 ± 6	12 ± 1
1	**A1.6-OMe**	48	58	8.50	53.1
2	**A1.6-OMe**	48	58	7.62	47.6
Average	**A1.6-OMe**	48	58	8.06 ± 0.62	50.3 ± 3.9
1	**A1.6-OMe**	1500	1800	12.19	2.4
2	**A1.6-OMe**	1500	1800	15.92	3.2
Average	**A1.6-OMe**	1500	1800	14.1 ± 2.8	2.8 ± 0.5
1	**A1.6-F**	48	58	2.56	16.0
2	**A1.6-F**	48	58	3.40	21.2
Average	**A1.6-F**	48	58	2.98 ± 0.59	18.6 ± 3.7

*These experiments were carried out in collaboration with Niklas B. Thompson.

With this in mind, complexes **A1.6-OMe** and **A1.6-F** were used as precatalysts for the reduction of N_2 to NH_3 under the conditions previously reported for **A1.6-H** (Table A1.2).[13] We found that **A1.6-OMe** was an equally competent or slightly improved catalyst for N_2 reduction to NH_3, yielding 8.06 ± 0.62 equiv of NH_3 with 48 equiv of $HBAr^F$ as the limiting reagent. It is worth noting that, with the range of modified catalysts mentioned above, **A1.6-OMe** is the only variant that performs as well catalytically as **A1.6-H**. Given the nearly identical electronic and steric profiles of these complexes, it is unsurprising that **A1.6-OMe** shows similar activity, selectivity, and stability to **A1.6-H** under the standard reaction conditions. Given our recent discovery that **A1.6-H** is a much more robust catalyst than initially thought, we were interested in exploring whether **A1.6-OMe** showed similar behavior under higher reagent loading conditions. With 1500 equiv of $HBAr_4^F$, the yield was appreciably lower than that observed for **A1.6-H**, generating only 14.1 ± 2.8 equiv

NH_3. Clearly, **A1.6-OMe** is a far poorer catalyst than **A1.6-H** under the higher loading conditions, which may be consistent with additional catalyst decomposition pathways being turned on in the modified arene system.

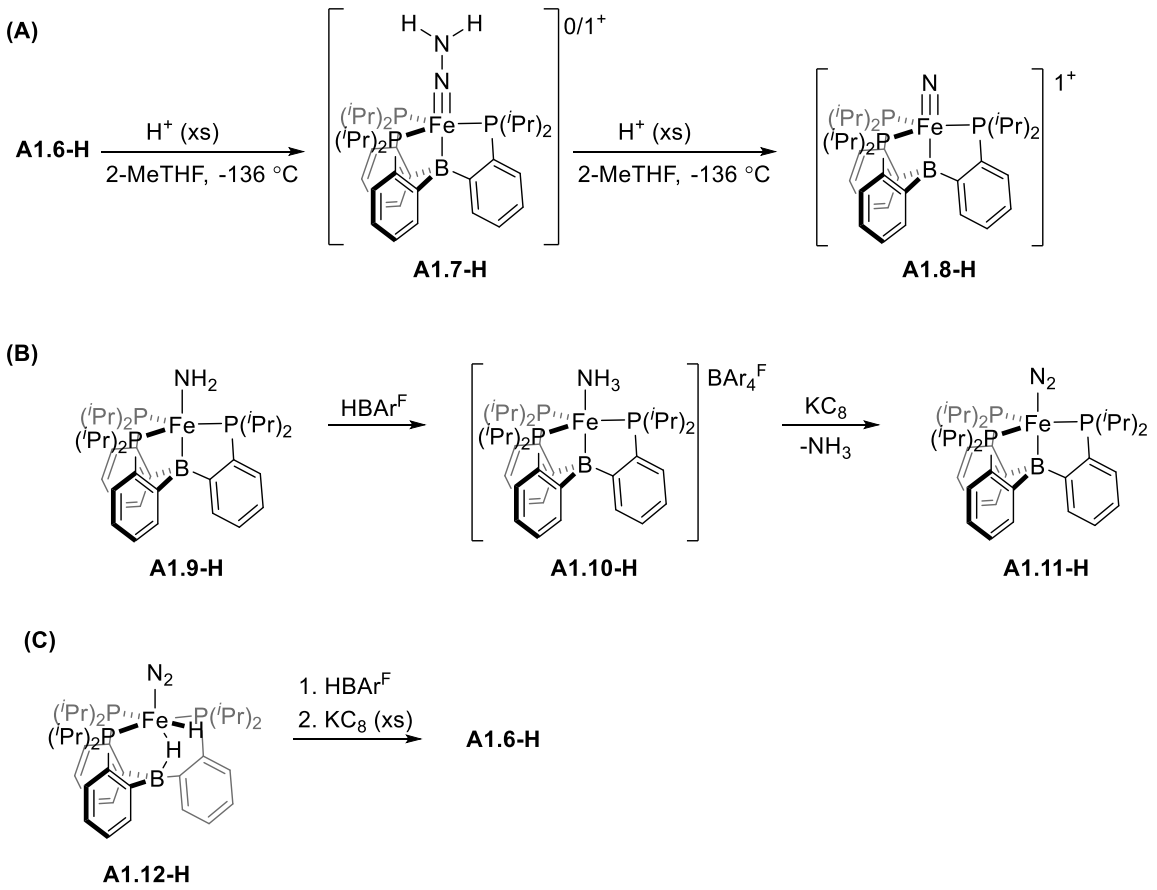

Scheme A1.3. Stoichiometric reactivity relevant to N_2 reduction by **A1.6-R**. (**A**) Protonation of **A1.6-H** to generate a hydrazido(2-) intermediate **A1.7-H** and promote N-N cleavage to generate a terminal nitride **A1.8-H**. (**B**) Regeneration of an Fe-N_2 complex **A1.11-H** from an Fe-NH_2 complex **A1.9-H**. (**C**) Regeneration of the precatalyst **A1.6-H** from the spectroscopically observed catalyst resting state **A1.12-H**.

Complex **A1.6-F** was found to be an appreciably worse catalyst under the same conditions, yielding only 2.98 ± 0.59 equiv of NH_3. With no additional experimental evidence, current hypotheses concerning the origin of this effect are entirely speculative. On the catalytic cycle, the less electron-rich complex is expected to more weakly activate π-acidic ligands (observed for **A1.6-F**) and stabilize strongly donating ligands. If we assume that the nature of the turnover-limiting step is unchanged with the slight electronic perturbation, the reduced reactivity with acid should not be kinetically relevant (Scheme

A1.3A, for instance). Further, the electron-withdrawing scaffold is predicted to facilitate reduction events, so the lower yield suggests that such an event is not the only important factor in determining the activity of **A1.6-F**. One plausible on-cycle origin of the reduced activity is slowed dissociation of the strongly σ-donating NH_3 product (Scheme A1.3B), with a similar effect demonstrated for an electron-poor variant of the Schrock system.[5b] An intriguing possibility concerns the recently reported off-cycle resting state of catalysis **A1.12-H**.[13] If this species is truly off-path, slight perturbations to this species that slows regeneration of catalytically active material could substantially lower selectivity for N_2 conversion (Scheme A1.3C). Additional, more detailed studies are necessary to draw more decisive conclusions about the origin of the attenuated activity of **A1.6-F**.

A1.4 Conclusions

In this report, we have synthesized a series of electronically varied P_3^B-supported Fe complexes to understand the effect of electronic perturbation on the efficiency of N_2 fixation for this system. Spectroscopic and electrochemical studies show that these complexes vary electronically over a relatively narrow range. Despite the similarity of these compounds, catalytic studies have demonstrated that there is some variation in their selectivities for N_2 fixation, most notably with a significant loss of activity for the most electron poor variant. As of yet, the origin of this effect is not well understood, but additional studies may provide insights that contribute to our understanding of N_2 reduction by Fe model complexes.

A1.5 Synthetic Procedures

F-$C_6H_3P^iPr_2Br$ (A1.2-F): A solution of F-C_6H_3BrI (10.72 g, 35.6 mmol, 1.0 equiv) in 2:1 Et_2O/THF (300 mL) was cooled to -120 °C in a liquid nitrogen/ethanol slush bath. A solution of *n*-BuLi (1.6 M in hexanes, 24.5 mL, 39.2 mmol, 1.1 equiv) was added over 20 min and the mixture was stirred at -120 °C for 3 h, becoming cloudy. A solution of P^iPr_2Cl (6.25 g, 41.0 mmol, 1.15 equiv) was added over 30 min and the solution was allowed to slowly warm to room temperature overnight. Degassed H_2O was added and the mixture was stirred for 10 min. The organic layer was transferred via cannula to a Schlenk tube and the solvents were removed, yielding the crude product as a cloudy oil. Filtration through a plug of alumina yielded the product as a colorless oil (9.28 g, 89%; distills at 135 °C under full vacuum). $^{31}P\{^1H\}$ NMR (C_6D_6, 400 MHz): δ 9.9. ^{19}F NMR (C_6D_6, 400 MHz): δ -115.8

(td, J = 8.4, 5.3 Hz). ^{1}H NMR (C_6D_6, 400 MHz): δ 7.17 (m, overlapping benzene, 1H), 7.0 (dd, J = 9.0, 3.1 Hz, 1H), 6.41 (td, J = 7.7, 3.1 Hz, 1H), 1.72 (hept, J = 7.0 Hz, 2H), 0.90 (ddd, J = 78.3, 13.2, 7.0 Hz, 12H).

MeO-$C_6H_3P^iPr_2Br$ (A1.2-OMe): A solution of MeO-C_6H_3BrI (15 g, 47.9 mmol)[17] in 2:1 Et_2O/THF (400 mL) was cooled to -131 °C in a liquid nitrogen/pentane slush bath. A solution of *n*-BuLi (1.6 M in hexanes, 32.9 mL, 52.7 mmol, 1.1 equiv) was added over 15 min and the mixture was stirred at -131 °C for 3 h, becoming cloudy. A solution of P^iPr_2Cl (8.41 g, 55.1 mmol, 1.15 equiv) in Et_2O (30 mL) was added to the mixture over 30 min and the solution was allowed to warm slowly to room temperature overnight. Degassed H_2O was added and the mixture was stirred for 10 min. The organic layer was transferred via cannula to a Schlenk tube and the solvents were removed, yielding a yellow oil. The oil was dissolved in pentane, filtered, and the solvent was removed yielding the crude product as a yellow oil. Vacuum distillation at 175 °C yielded the product as a colorless oil (9.64 g, 67%). $^{31}P\{^{1}H\}$ NMR (C_6D_6, 400 MHz): δ 9.7. ^{1}H NMR (C_6D_6, 400 MHz): δ 7.40 (dd, J = 8.7, 3.3, 1H), 7.02 (dd, J = 3.1, 1.3, 1H) 6.33 (dd, J = 8.8, 3.1, 1H), 3.20 (s, 3H), 1.91 (hept, J = 7.1 Hz, 2H), 1.00 (ddd, J = 46.5, 13.1, 7.0 Hz, 12H).

P_3^B-F (A1.3-F): A solution of F-$C_6H_3(P^iPr_2Br)$ (3.61 g, 12.4 mmol, 1.0 equiv) in toluene (200 mL) was cooled to -41 °C in a dry ice/acetonitrile bath and a solution of *n*-BuLi (1.6 M in hexanes, 8.53 mL, 13.6 mmol, 1.1 equiv) was added dropwise. The solution was stirred for 3 h and a solution of BCl_3 (1.0 M in heptane, 3.72 mL, 3.7 mmol, 0.3 equiv) was added dropwise via syringe. The mixture was allowed to warm slowly to room temperature overnight in a sealed vessel. The solvent was removed and the residue was dissolved in benzene and filtered through Celite. The benzene was removed yielding a sticky brown residue. The product was extracted with pentane, filtered, and the solvent was pumped down yielding a sticky orange solid. Addition of HMDSO resulted in the precipitation of the product as an off white solid after standing at -35 °C overnight. Additional product was isolated by concentration of the washes and storage at -35 °C over several days. $^{31}P\{^{1}H\}$ NMR (C_6D_6, 300 MHz): δ 4.6. ^{19}F NMR (C_6D_6, 300 MHz): δ -113.8. ^{1}H NMR (C_6D_6, 300 MHz): δ 7.83 (br, 1H), 7.18 (m, overlapping benzene, 1H), 6.93 (td, J = 8.6, 2.5 Hz, 1H), 1.76 (br m, 2H), 0.94-0.79 (overlapping m, 12H). ESI-MS (positive ion, amu): Calcd. 751.2, 753.2 ($[M\text{-}Ag]^+$); Found. 751.2, 753.2.

P_3^B-OMe (A1.3-OMe): A solution of MeO-$C_6H_3(P^iPr_2)Br$ (1.9 g, 6.3 mmol) in toluene was cooled to -78 °C in a dry ice/acetone bath and a solution of *t*-BuLi (845 mg, 13.2 mmol, 2.1 equiv) in toluene (20 mL) was added dropwise. The solution was stirred for 2 h, turning orange and cloudy. A solution of $B(OMe)_3$ (196 mg, 1.89 mmol, 0.3 equiv) in toluene (10 mL) was added in portions and the solution was allowed to slowly warm to room temperature overnight. The solvent was removed leaving an off-white solid. This was redissolved in Et_2O, filtered through Celite, and the solvent was removed leaving a sticky orange solid. The crude product was purified using column chromatography with alumina as the stationary phase and a 20:1 pentane/Et_2O mixture as the eluent. The product was obtained as an off-white solid (193 mg, 15%). $^{31}P\{^1H\}$ NMR (C_6D_6, 300 MHz): δ 2.5. ^1H NMR (C_6D_6, 300 MHz): δ 7.65 (br, 1H), 7.28 (br, 1H), 6.76 (dd, J = 8.5, 2.4 Hz, 1H), 3.38 (s, 3H), 2.04 (br, 2H), 1.16 – 0.95 (overlapping br m, 12H). ESI-MS (positive ion, amu): Calcd. 787.2, 789.2 ([M-Ag^+]). Found. 787.2, 789.2.

(P_3^B-F)FeBr (A1.4-F): P_3^B-F (420 mg, 65.2 mmol) and $FeBr_2$ (139 mg, 65.2 mmol) were stirred in THF (10 mL) until all solids had dissolved yielding an orange yellow solution. The solvent was removed yielding a yellow brown residue. The residue was redissolved in benzene (10 mL) and was added to a vial containing Na/Hg amalgam (1.0 equiv). After stirring overnight, the dark brown solution was filtered through Celite and the solvents were removed, yielding a dark brown oily solid. This solid was washed with HMDSO yielding the desired product as a yellow-brown solid (330 mg, 65%). X-Ray quality crystals were grown from a concentrated pentane solution at -35 °C. ^{19}F NMR (C_6D_6, 300 MHz): δ -153.0. ^1H NMR (C_6D_6, 300 MHz): 95.2, 32.4, 18.1, 6.5, 3.0, 1.8, 0.3, -1.2, -23.0. μ_{eff} (C_6D_6, Evans Method, 298 K): 4.3 μ_B. UV-Vis (THF, nm {$cm^{-1}\,M^{-1}$}): 560 {sh}, 800 {sh}, 985 {130}.

(P_3^B-OMe)FeBr (4-OMe): P_3^B-OMe (87 mg, 0.128 mmol) and $FeBr_2$ (27 mg, 0.128 mmol) were stirred in THF (5 mL) until all solids had dissolved and the solution had turned yellow. The solvent was removed, yielding an orange-red solid. The solid was dissolved in benzene (5 mL) and added to a vial containing Na/Hg amalgam (1.0 equiv). After stirring overnight, the dark brown solution was filtered through Celite and the solvents were removed, yielding a dark brown oily solid. Washing the oil with HMDSO yielded the desired product as a light brown solid (51 mg, 49%). X-Ray quality crystals were grown from a

concentrated 3:1 HMDSO/THF solution at -35 °C. ^{1}H NMR (C_6D_6, 400 MHz): δ 89.8, 33.4, 19.3, 7.4, 3.3, 1.5, 1.2, 0.6, -1.5, -22.8. μ_{eff} (C_6D_6, Evans Method, 298 K): 4.3 μ_B. UV-Vis (THF, nm {cm^{-1} M^{-1}}): 560 {sh}, 850 {sh}, 1030 {150}.

[(P_3^B-F)FeN_2][Na(12-c-4)$_2$] (A1.6-F): A solution of (P_3^B-F)FeBr in THF was added to a vial containing excess Na/Hg amalgam. The mixture was stirred for 1 h, turning dark red-brown. The solution was filtered through Celite and the solvent was removed, yielding a dark red solid. The solid was dissolved in Et_2O and layered with an Et_2O solution of 12-crown-4 (3 equiv). After standing for 3 h, pentane was added, resulting in the precipitation of a dark red solid. The mixture was filtered and washed with additional benzene yielding the desired product as a dark red powder. X-Ray quality crystals were grown from vapor diffusion of pentane into a concentrated THF solution of the product at -35 °C. IR (thin film): ν_{NN} = 1916 cm^{-1}.

[(P_3^B-OMe)FeN_2][Na(12-c-4)$_2$] (A1.6-OMe): A solution of (P_3^B-OMe)FeBr (50 mg, 0.0613 mmol) in THF was added to a vial containing excess Na/Hg amalgam. The mixture was stirred for 2 h, turning dark red. The solution was filtered through Celite and the solvent was removed yielding a red solid. The solid was dissolved in Et_2O and layered with an Et_2O solution of 12-crown-4 (5 equiv). After standing overnight, the solvent was decanted and the precipitate was washed with pentane yielding the desired product as a red crystalline solid (40 mg, 60%). X-Ray quality crystals were grown from vapor diffusion of pentane into a concentrated THF solution of the product. IR (thin film): ν_{NN} = 1902 cm^{-1}. ^{1}H NMR (THF-d_8, 300 MHz): δ 12.7, 6.8, 4.4, 3.8 (12-c-4), -0.2 -1.4. μ_{eff} (THF-d_8, Evans Method, 298 K): 1.8 μ_B.

A1.6 References and Notes

(1) Smil, V. *Enriching the Earth*. Cambridge: MIT Press, 2001.

(2) Ertl, G. *J. Vac. Sci. Technol. A* **1983**, *1*, 1247-1253.

(3) (a) Howard, J. B.; Rees, D. C. *Chem. Rev.* **1996**, *96*, 2965-2982. (b) Burgess, B. K.; Lowe, D. J. *Chem. Rev.* **1996**, *96*, 2983-3012. (c) Hoffman, B. M.; Lukoyanov, D.; Yang, Z.-Y.; Dean, D. R.; Seefeldt, L. C. *Chem. Rev.* **2014**, *114*, 4041-4062.

(4) For a recent review: Nishibayashi, Y. *Inorg. Chem.* **2015**, *54*, 9234-9247.

(5) (a) Yandulov, D. V.; Schrock, R. R. *Science* **2003**, *301*, 76-78. (b) Ritleng, V.; Yandulov, D. M.; Weare, W. W.; Schrock, R. R.; Hock, A. S.; Davis, W. M. *J. Am. Chem. Soc.* **2004**, *126*, 6150-6163.

(6) Schrock, R. R. *Angew. Chem. Int. Ed.* **2008**, *47*, 5512-5522.

(7) (a) Arashiba, K.; Miyake, Y.; Nishibayashi, Y. *Nat. Chem.* **2011**, *3*, 120-125. (b) Tanka, H.; Arashiba, K.; Kuriyama, S.; Sasada, A.; Nakajima, K.; Yoshizawa, K.; Nishibayashi, Y. *Nat. Commun.* **2014**, *5*, 3737. (c) Kuriyama, S.; Arashiba, K.; Nakajima, K.; Tanaka, H.; Kamaru, N.; Yoshizawa, K.; Nishibayashi, Y. *J. Am. Chem. Soc.* **2014**, *136*, 9719-9731. (d) Arashiba, K.; Kinoshita, E.; Kuriyama, S.; Eizawa, A.; Nakajima, K.; Tanaka, H.; Yoshizawa, K.; Nishibayashi, Y. *J. Am. Chem. Soc.* **2015**, *137*, 5666-5669.

(8) Tian, Y.-H.; Pierpont, A. W.; Batista, E. R. *Inorg. Chem.* **2014**, *53*, 4177-4183.

(9) Eady, R. R. *Chem. Rev.* **1996**, *96*, 3013-3030.

(10) (a) Anderson, J. S.; Rittle, J.; Peters, J. C. *Nature* **2013**, *501*, 84-87. (b) Creutz, S. E.; Peters, J. C. *J. Am. Chem. Soc.* **2014**, *136*, 1105-1115. (c) Ung, G.; Peters, J. C. *Angew. Chem. Int. Ed.* **2015**, *54*, 532-535. (d) Buscagan, T. M.; Oyala, P. H.; Peters, J. C. *Angew. Chem. Int. Ed.* **2017**, *56*, 6921-6926.

(11) Kuriyama, S.; Arashiba, K.; Nakajima, K.; Matsuo, Y.; Tanaka, H.; Ishii, K.; Yoshizawa, K.; Nishibayashi, Y. *Nat. Commun.* **2016**, *7*, 12181.

(12) Hill, P. J.; Doyle, L. R.; Crawford, A. D.; Myers, W. K.; Ashley, A. E. *J. Am. Chem. Soc.* **2016**, *138*, 13521-13524.

(13) Del Castillo, T. J.; Thompson, N. B.; Peters, J. C. *J. Am. Chem. Soc.* **2016**, *138*, 5341-5350.

(14) (a) Anderson, J. S.; Moret, M.-E.; Peters, J. C. *J. Am. Chem. Soc.* **2013**, *135*, 534-537. (b) Anderson, J. S.; Cutsail III, G. E.; Rittle, J.; Connor, B. A.; Gunderson, W. A.; Zhang, L.; Hoffman, B. M.; Peters, J. C. *J. Am. Chem. Soc.* **2015**, *137*, 7803-7809. (c) Thompson, N. B.; Green, M. T.; Peters, J. C. *J. Am. Chem. Soc.* **2017**, *139*, 15312-15315.

(15) For E = Si, R = Cy, Ph, see: (a) Anderson, J. S. PhD. Dissertation, California Institute of Technology, 2013. For E = Al, Ga, see: (b) Fajardo Jr., J. F.; Peters, J. C. Unpublished Results.

(16) Bontemps, S.; Bouhadir, G.; Dyer, P. W.; Miqueu, K.; Bourissou, D. *Inorg. Chem.* **2007**, *46*, 5149-5151.

(17) Bhunia, S.; Wang, K.-C.; Liu, R.-S. *Angew. Chem. Int. Ed.* **2008**, *47*, 5063-5066.

(18) Suess, D. L. M.; Peters, J. C. *J. Am. Chem. Soc.* **2013**, *135*, 4938-4941.

(19) Except where specifically mentioned, data from the Fe complexes supported by **3-H** is adopted from: Moret, M.-E.; Peters, J. C. *Angew. Chem. Int. Ed.* **2011**, *50*, 2063-2067.

(20) Evans, D. F. *J. Chem. Soc.* **1959**, 2003-2005.

(21) Electrochemistry data for **6-H** was recollected from Ref. 16 under the same conditions used for **6-OMe and 6-F**.

(22) Del Castillo, T. J.; Thompson, N. B.; Suess, D. L. M.; Ung, G.; Peters, J. C. *Inorg. Chem.* **2015**, *54*, 9256-9262.

(23) Matson, B. D.; Peters, J. C. *ACS Catal.* **2018**, *8*, 1448-1455.

Appendix B

SUPPLEMENTARY DATA FOR CHAPTER 2

B1. NMR Spectra

$[P_3^B(\mu\text{-H})Fe(H)(CO)][K_2(THF)_n]$ 2.2:

Figure B1.1: ^{1}H NMR (400 MHz) spectrum of **2.2** in THF-d_8.

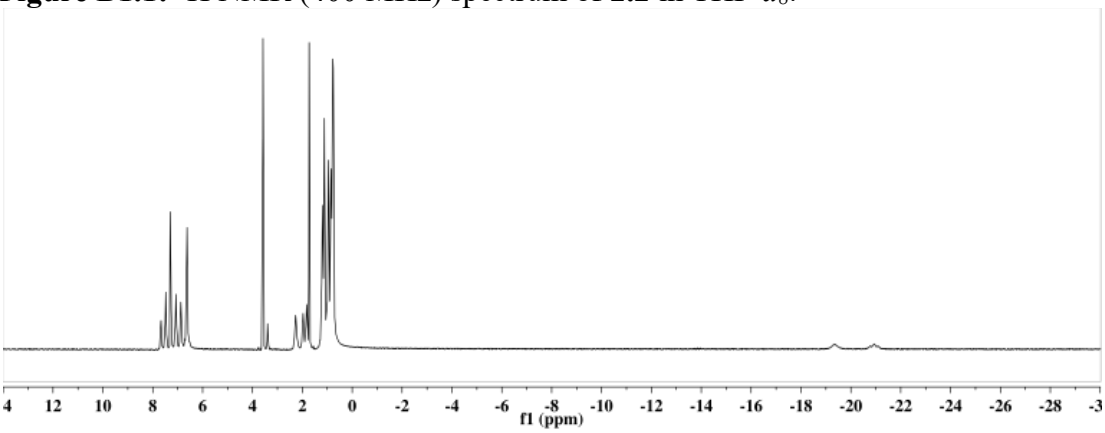

Figure B1.2: ^{31}P{^{1}H} NMR (162 MHz) spectrum of **2.2** in THF-d_8.

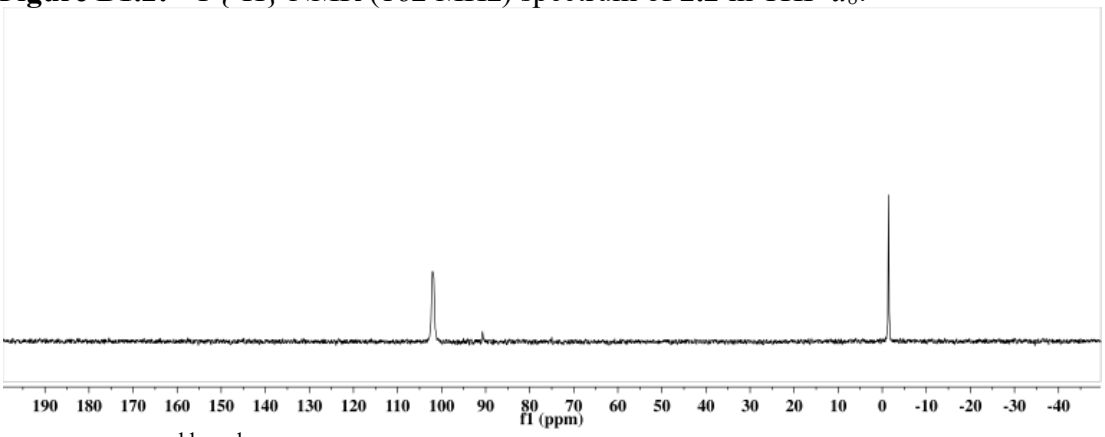

Figure B1.3: ^{11}B{^{1}H} NMR (128 MHz) spectrum of **2.2** in THF-d_8.

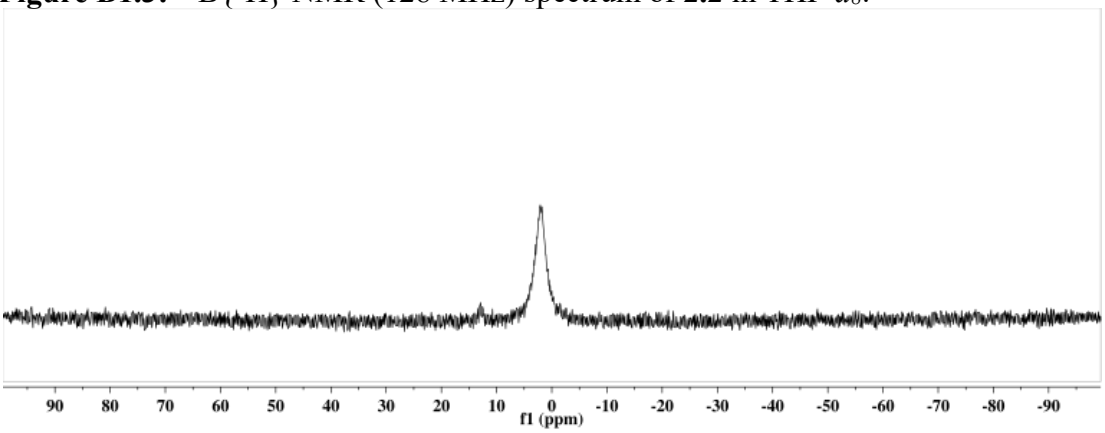

Figure B1.4: $^{13}C\{^{1}H\}$ NMR (101 MHz; ^{13}CO-labeled) spectrum of **2.2** in a mixture of THF and C_6D_6.

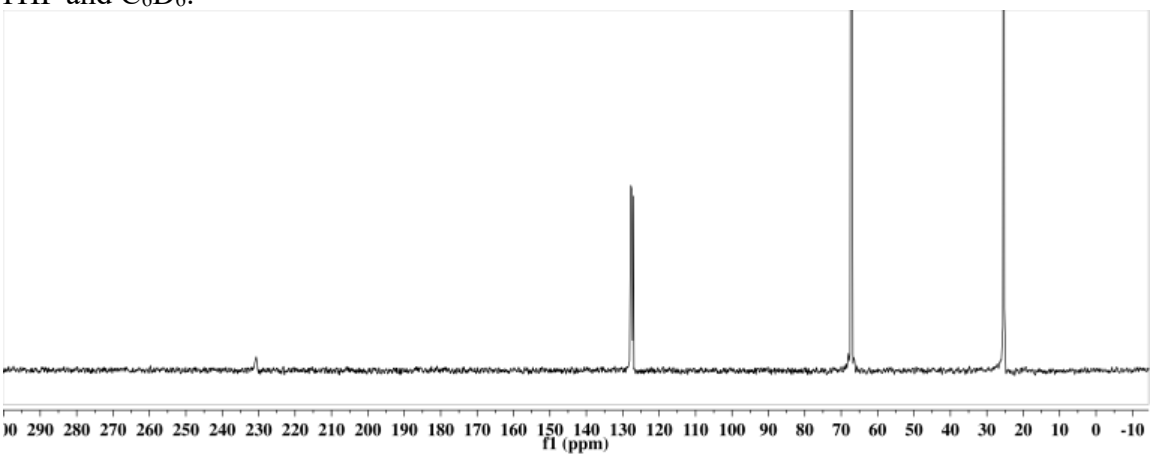

$[P_3^B(\mu\text{-}H)Fe(H)_2(CO)][K(THF)_n]$ 2.3:

Figure B1.5: ^{1}H NMR (400 MHz) spectrum of **2.3** in THF-d_8.

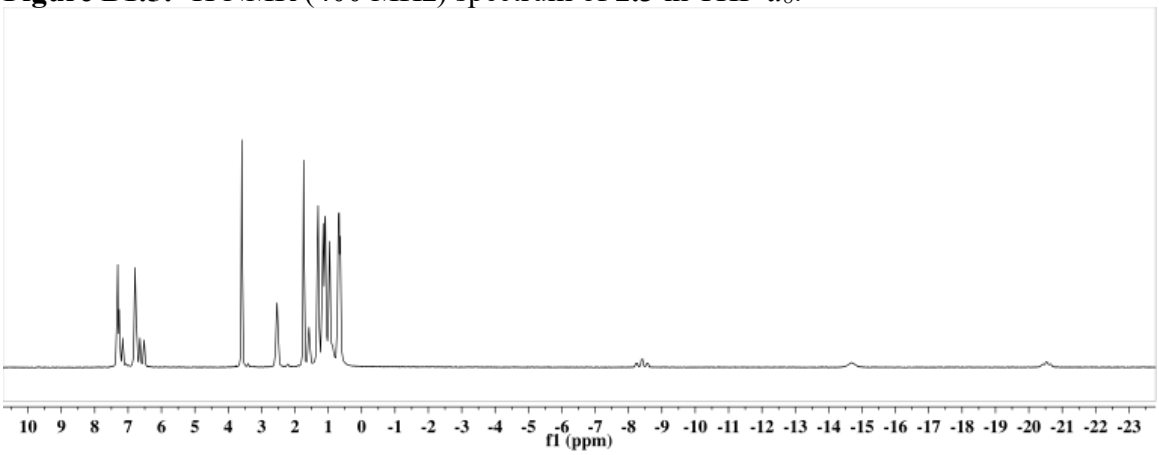

Figure B1.6: $^{31}P\{^{1}H\}$ NMR (162 MHz) spectrum of **2.3** in THF-d_8.

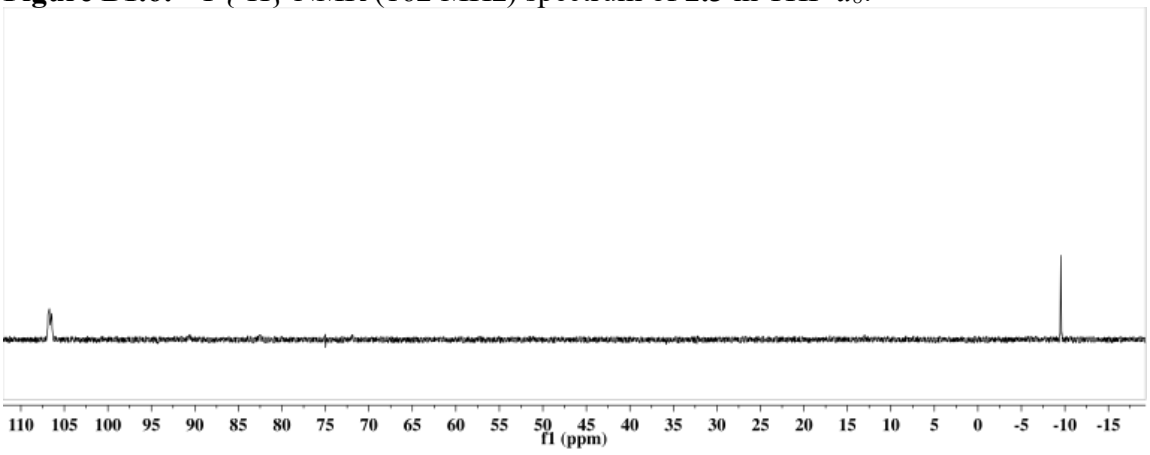

Figure B1.7: $^{11}B\{^{1}H\}$ NMR (128 MHz) spectrum of **2.3** in THF.

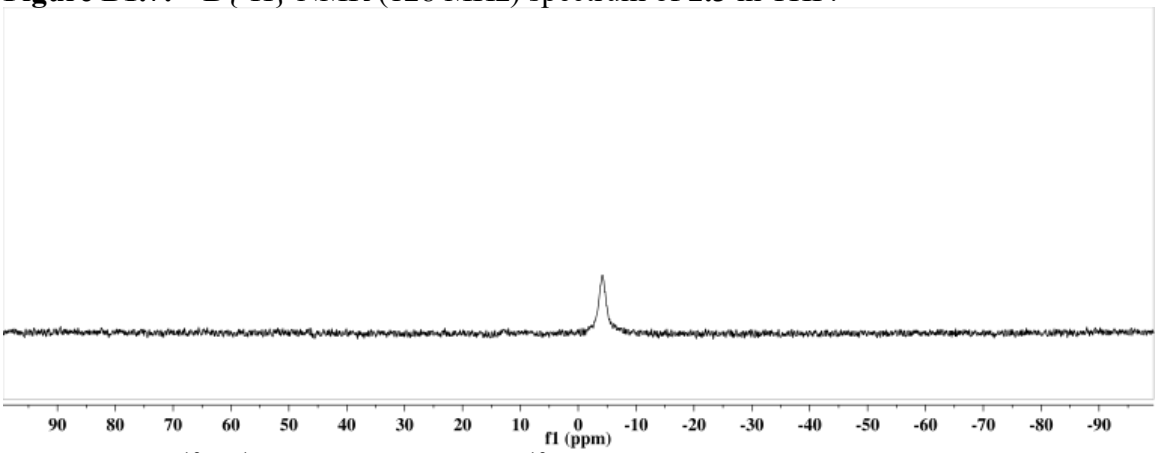

Figure B1.8: $^{13}C\{^{1}H\}$ NMR (101 MHz; ^{13}CO-labeled) spectrum of **2.3** in THF.

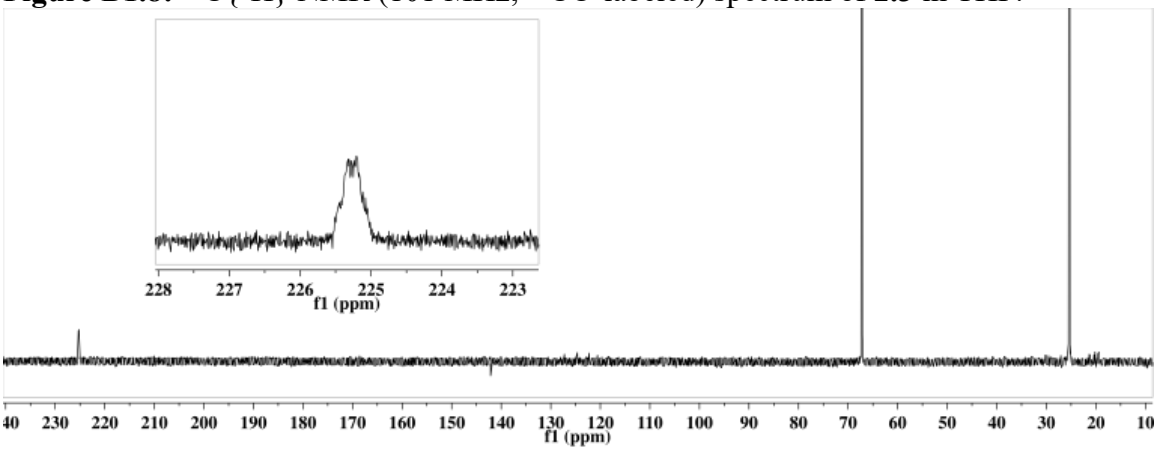

$[P_3^BFe(H)(CO)][K(THF)_n]$ 2.4:

Figure B1.9: ^{1}H NMR (400 MHz) spectrum of **2.4** in THF-d_8.

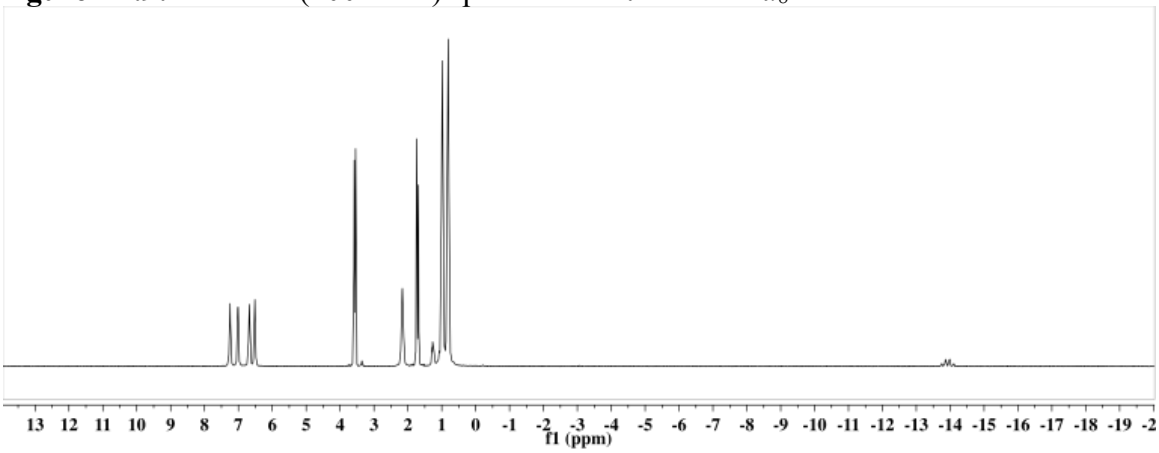

Figure B1.10: $^{31}P\{^{1}H\}$ NMR (162 MHz) spectrum of **2.4** in THF-d_8.

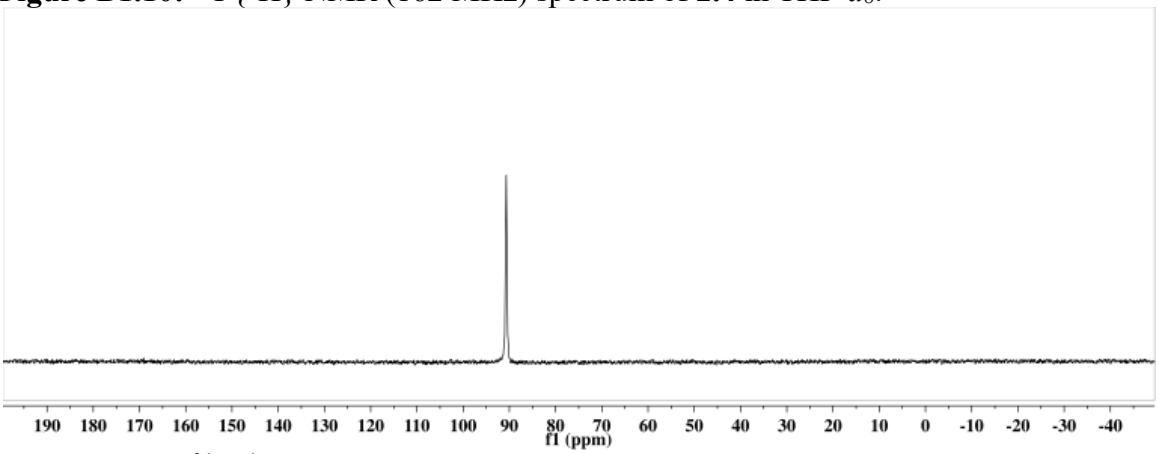

Figure B1.11: $^{31}P\{^{1}H\}$ NMR (202 MHz) spectrum of **2.4** in THF-d_8 collected at -80 °C.

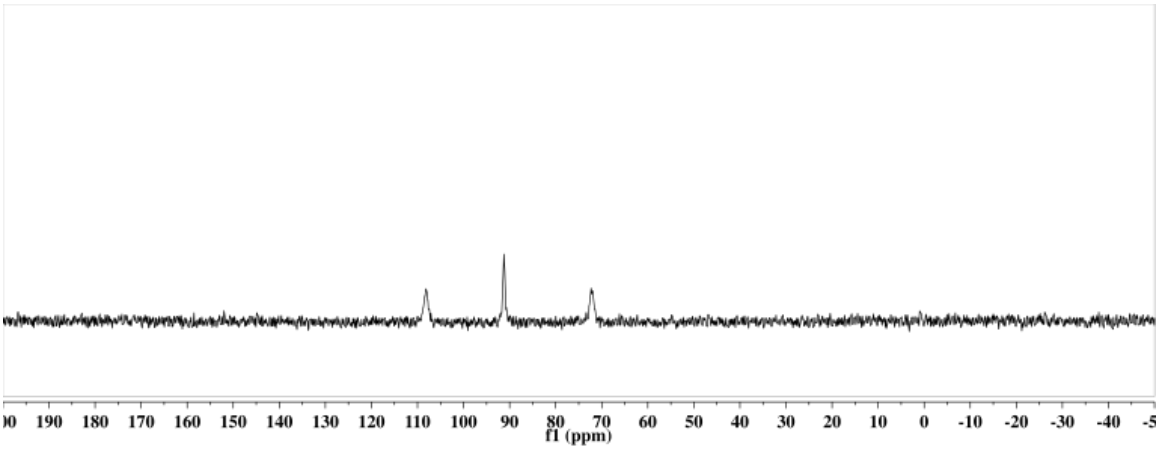

Figure B1.12: $^{11}B\{^{1}H\}$ NMR (128 MHz) spectrum of **2.4** in THF-d_8.

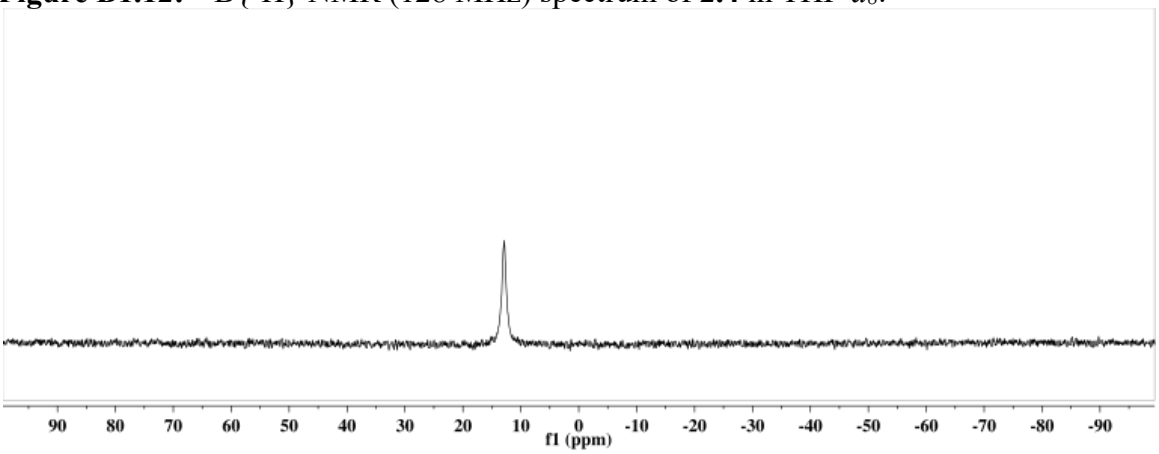

Figure B1.13: $^{13}C\{^{1}H\}$ NMR (101 MHz; ^{13}CO-labeled) spectrum of **2.4** in THF-d_8.

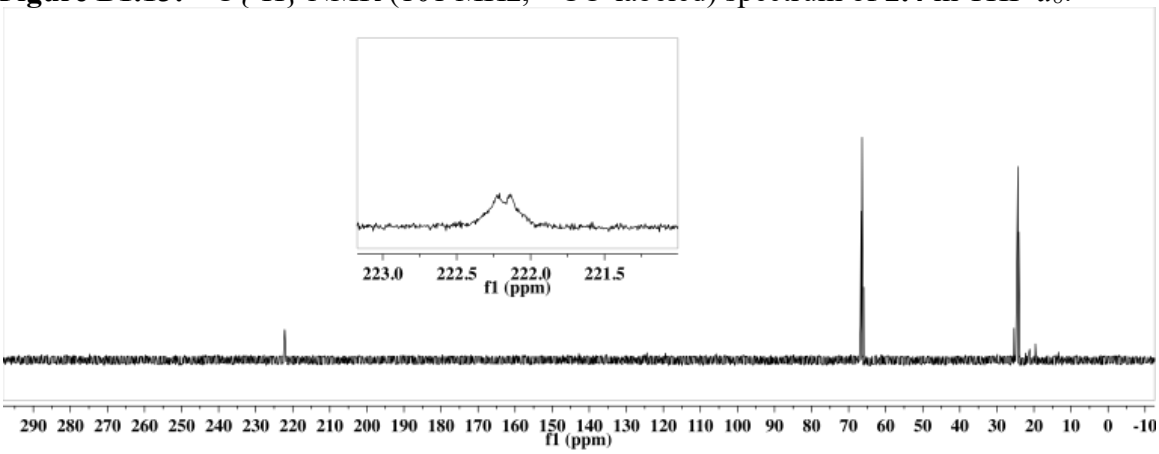

(P_3^B-H)Fe(CO) 2.5:

Figure B1.14: ^{1}H NMR (300 MHz) spectrum of **2.5** in C_6D_6 (Et_2O impurity observable).

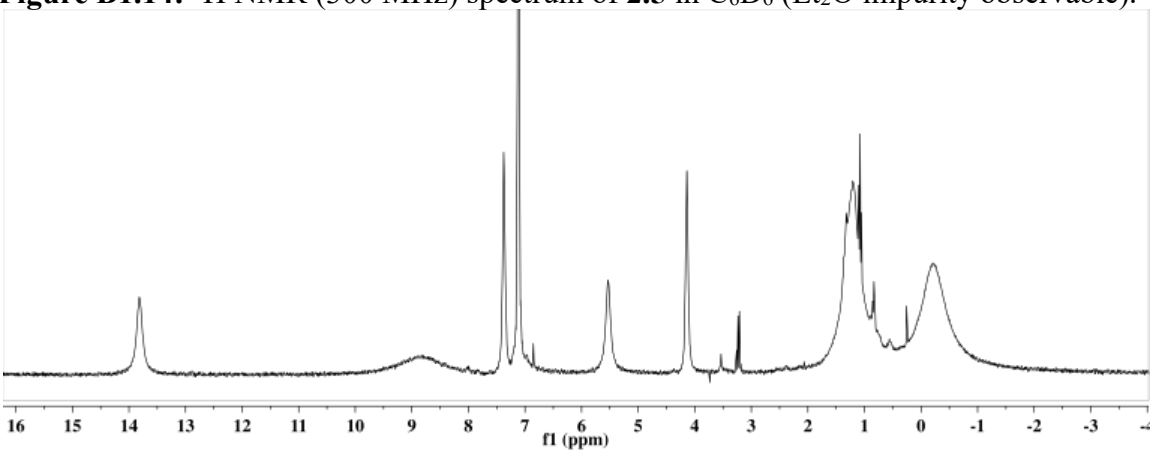

P_3^BFe(CH_2OSiMe_3) 2.6:

Figure B1.15: ^{1}H NMR (400 MHz) spectrum of **2.6** in C_6D_6.

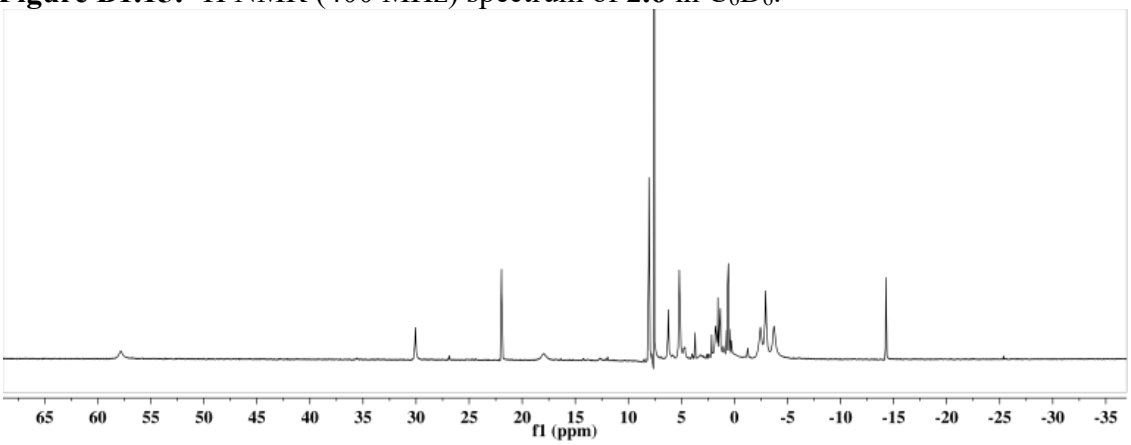

Figure B1.16: ^{1}H NMR (400 MHz) spectrum of the product mixture generated from the reaction of **2.6** with $PhSiH_3$. Additional, paramagnetically shifted resonances associated with the Fe-containing products are observable with a wider spectrum window.

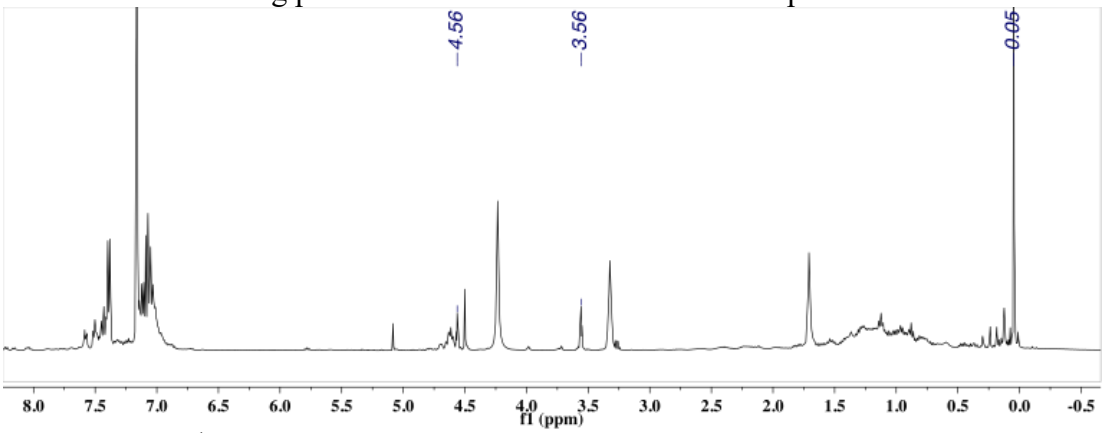

Figure B1.17: ^{1}H NMR (400 MHz) spectrum of the product mixture generated from the reaction of **2.6** with $PhSiH_3$ with isolation from iron-containing products *via* vacuum transfer.

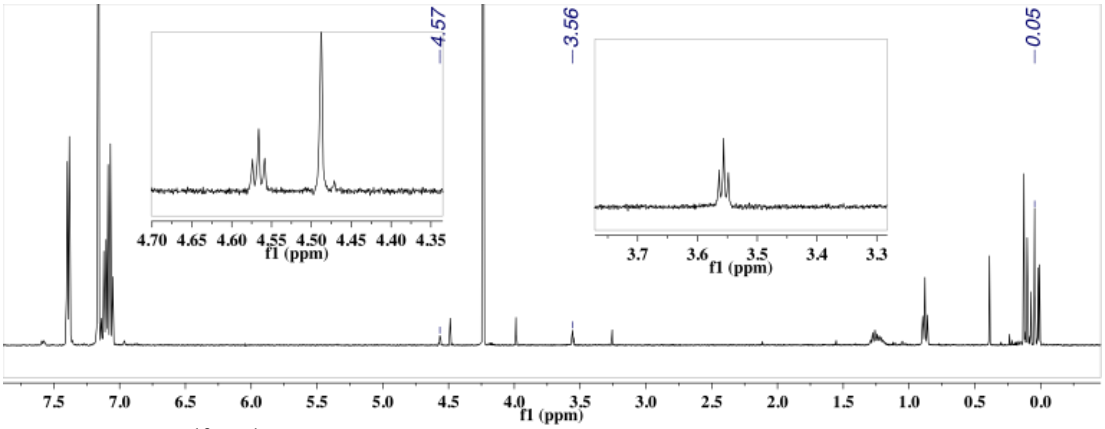

Figure B1.18: $^{13}C\{^{1}H\}$ NMR (101 MHz) spectrum of the product mixture generated from the reaction of **2.6-^{13}CO** with $PhSiH_3$.

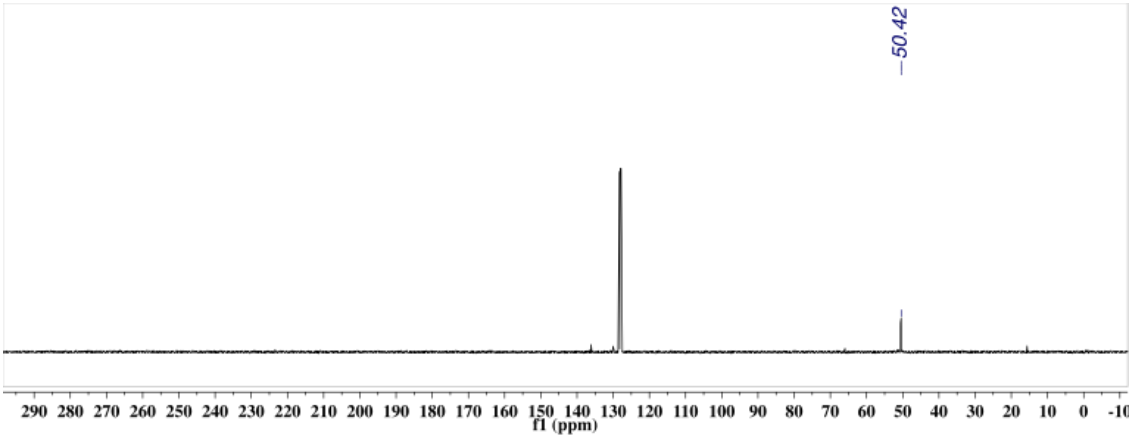

B2. IR Spectra

Figure B2.1: Thin film IR spectrum of **2.2**.

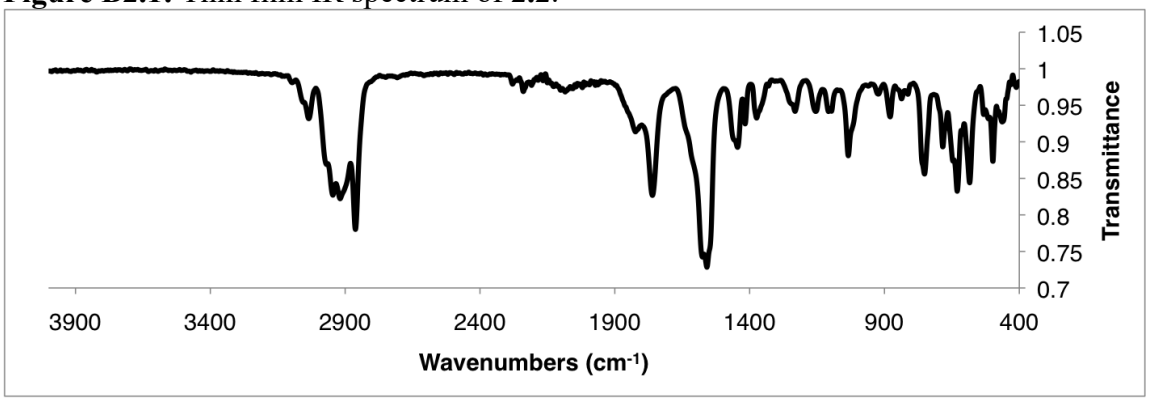

Figure B2.2: Thin film IR spectrum of **2.3**.

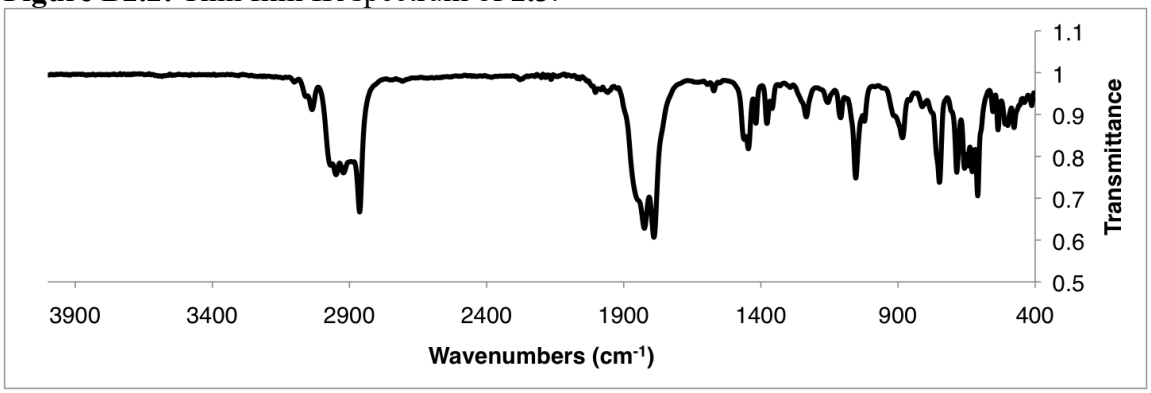

Figure B2.3: Thin film IR spectrum of **2.4**.

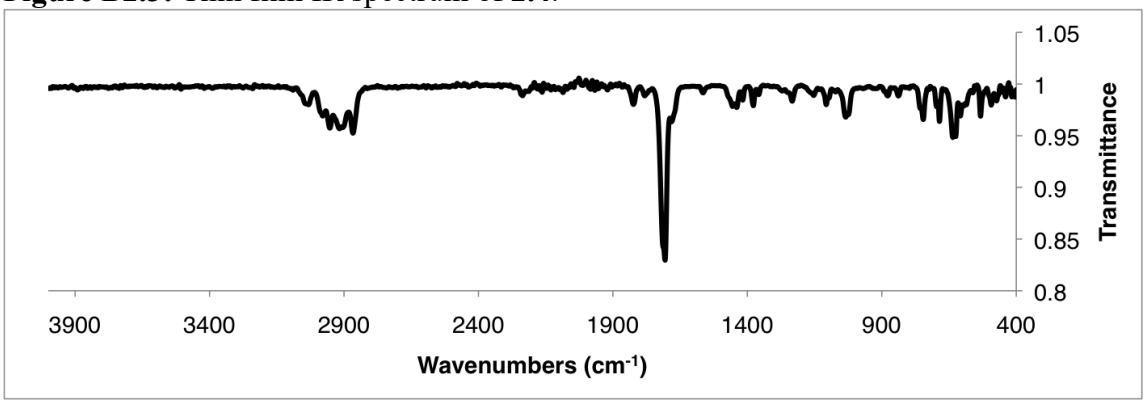

Figure B2.4: Thin film IR spectrum of **2.5**.

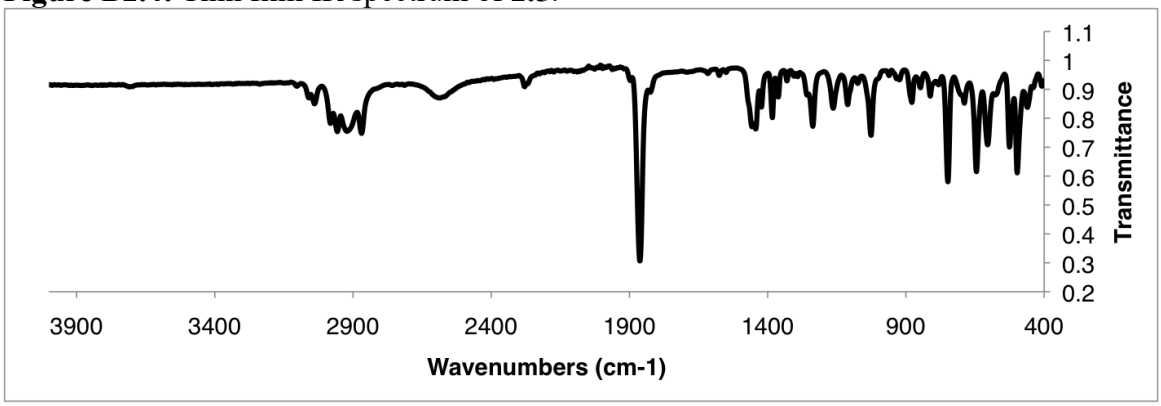

B3. UV-Vis Spectra in THF at 298 K

Figure B3.1: UV-Vis Spectrum of **2.2** in THF.

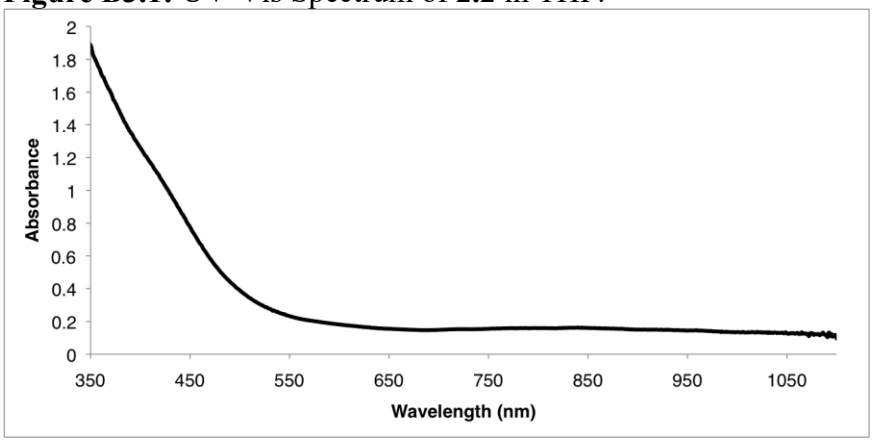

Figure B3.2: UV-Vis Spectrum of **2.4** in THF.

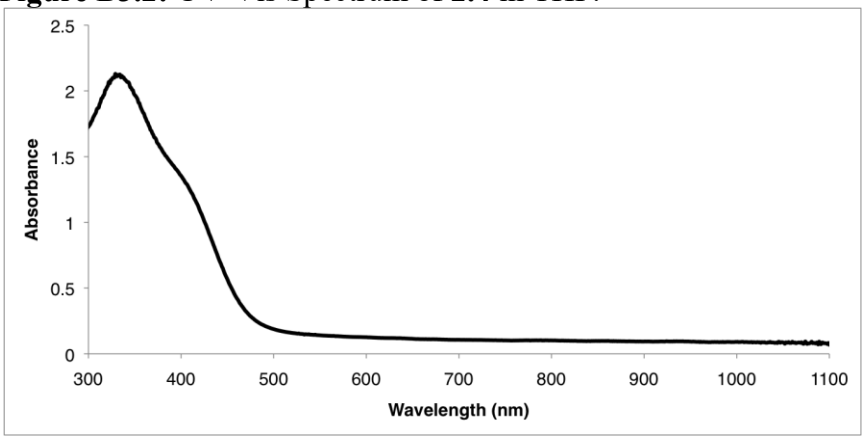

Figure B3.3: UV-Vis Spectrum of **2.5** in THF.

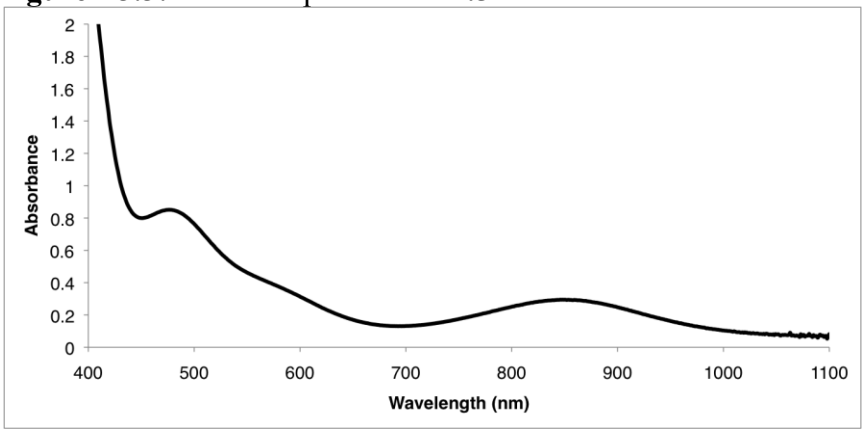

B4. EPR Spectrum

Figure B4.1: X-Band EPR Spectrum of **2.5** collected at 77K in a 2-MeTHF glass. Simulation parameters: g = [2.4 2.0322 2.0322]; lw = 5; HStrain = [300 200 175]

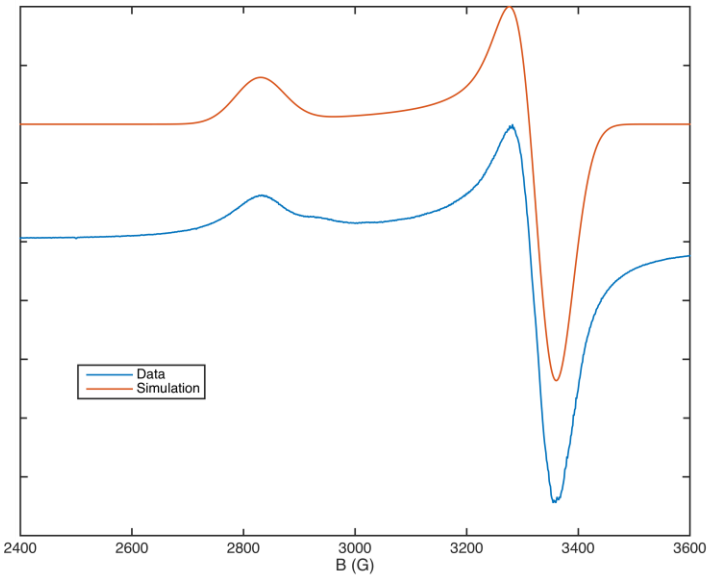

B5. Mössbauer Spectra

Figure B5.1: Spectrum of **2.1** collected at 80 K in benzene ($\delta = 0.01$; $\Delta E_Q = 1.09$).

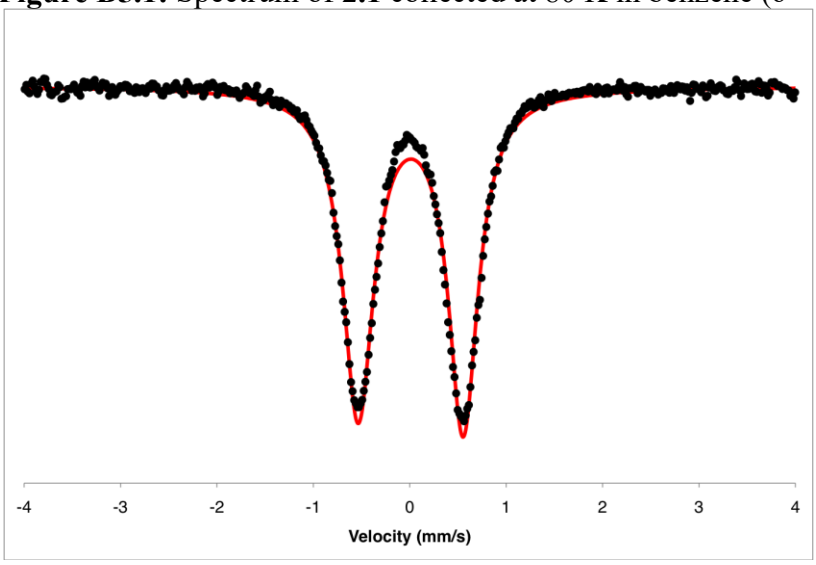

Figure B5.2: Spectrum of **2.2** collected at 80 K in THF ($\delta = 0.09$; $\Delta E_Q = 2.39$).

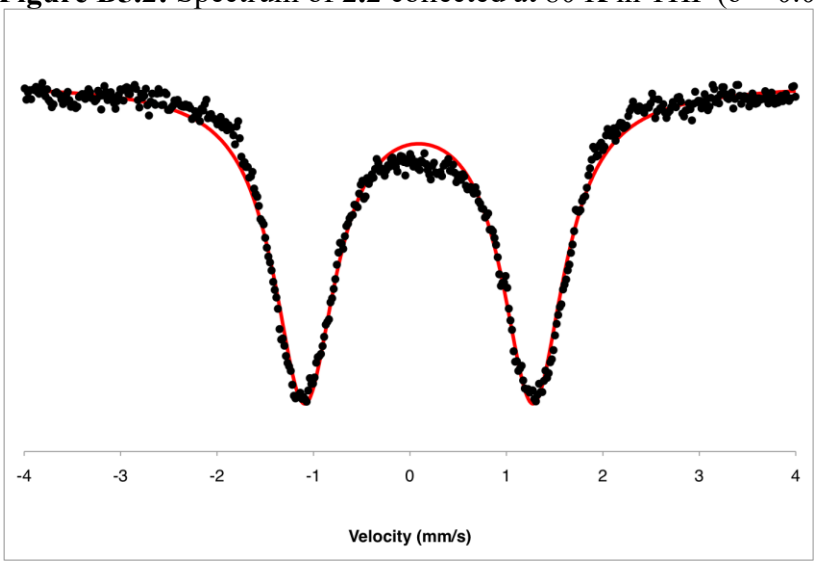

Figure B5.3: Spectrum of **2.4** collected at 80 K in a 2-MeTHF/benzene mixture ($\delta = 0.03$; $\Delta E_Q = 1.28$). Residual signal is consistent with the presence of a minor amount of **2.5** generated from oxidation during sample handling ($\delta = 0.19$; $\Delta E_Q = 0.47$).

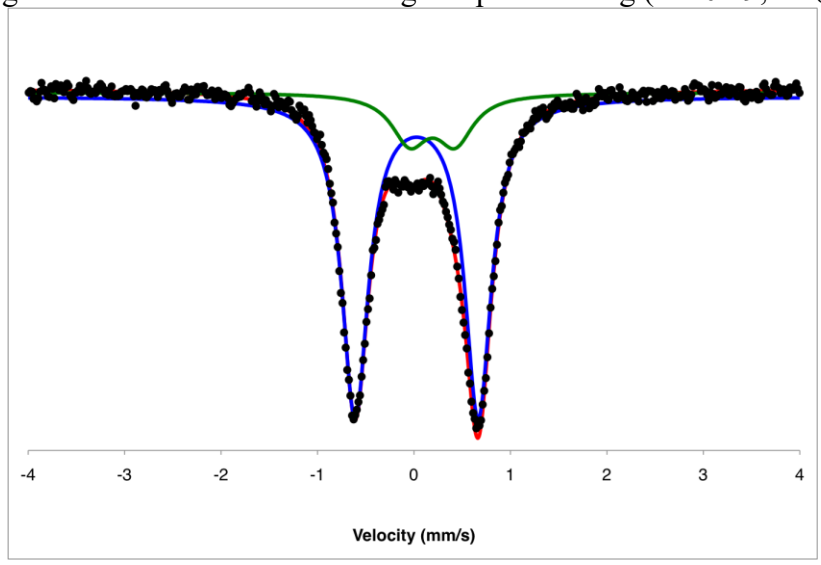

Figure B5.4: Spectrum of **2.5** collected at 80 K in frozen benzene with an applied 50 mT magnetic field ($\delta = 0.21$; $\Delta E_Q = 0.45$).

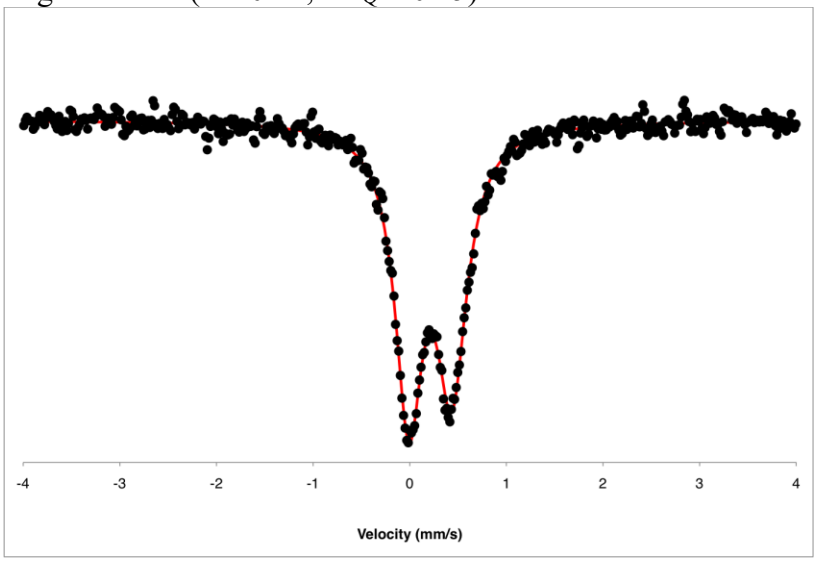

Figure B5.5: Spectrum of **2.5** collected at 80 K in frozen benzene ($\delta = 0.22$; $\Delta E_Q = 0.43$). Spectra collected with and without the magnet for **2.5** were collected on the same sample for approximately the same period of time.

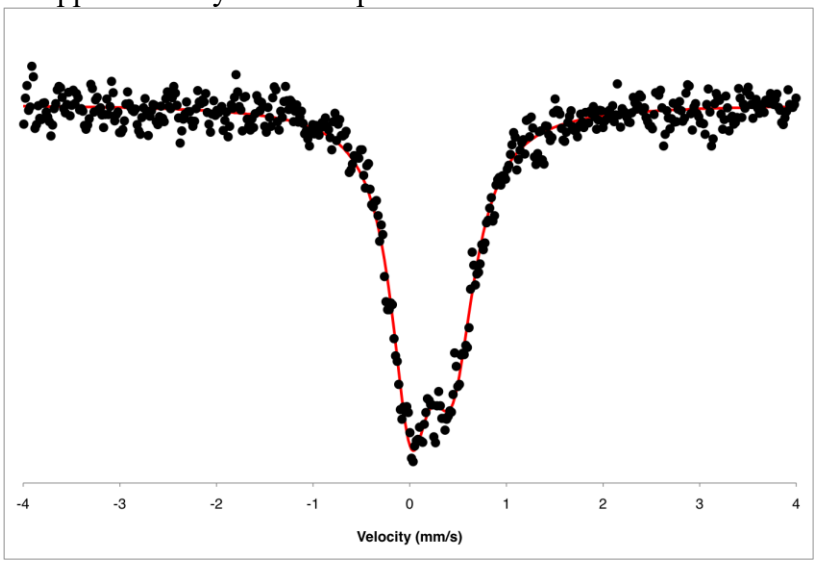

Figure B5.6: Spectrum of product mixture including **2.6** collected at 80 K in benzene) ($\delta = 0.49$; $\Delta E_Q = 2.05$; 78%). The minor component is likely representative of multiple species ($\delta = 0.19$; $\Delta E_Q = 0.65$; 22%).

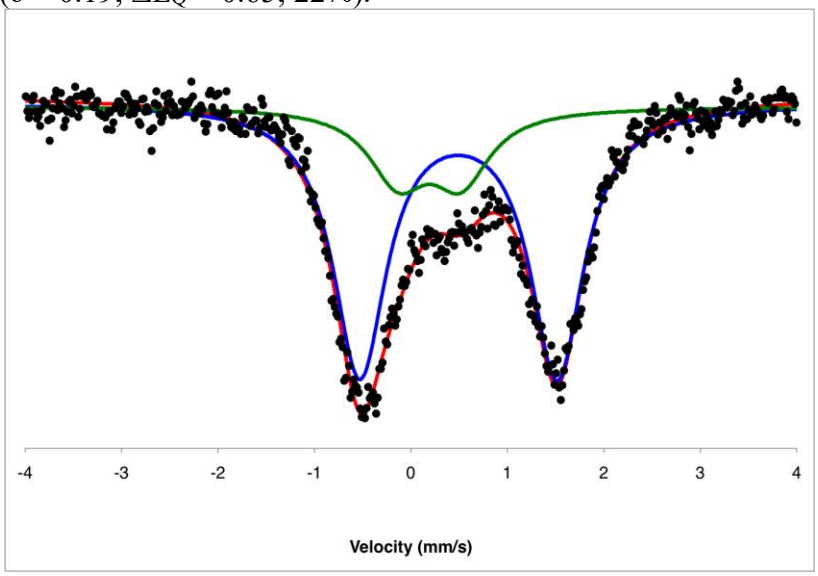

Figure B5.7: Spectrum of P_3^BFe-Me collected at 80 K in benzene ($\delta = 0.50$; $\Delta E_Q = 1.84$). Minor impurity: $\delta = 0.11$; $\Delta E_Q = 0.28$.

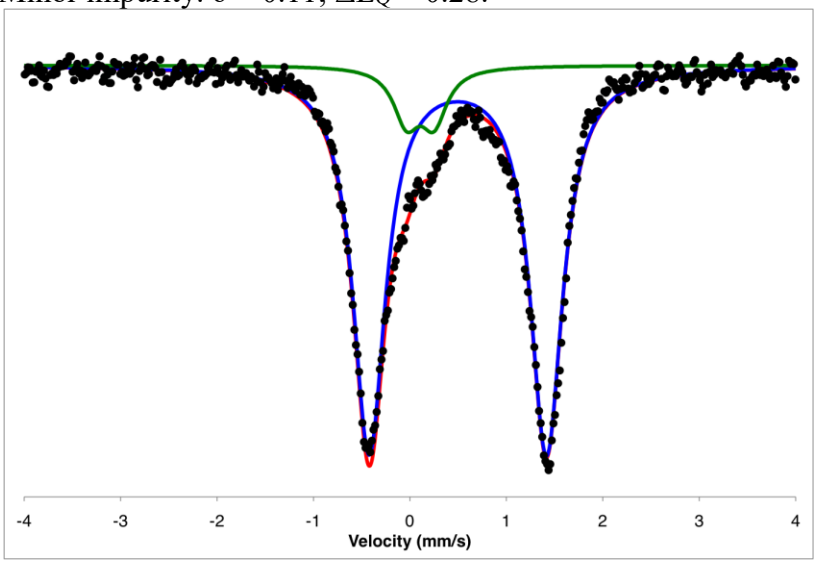

B6. Labeling Experiments

For these experiments, $P_3^BFeCH_2OSiMe_3$ **2.6** was prepared from $P_3^B(\mu\text{-H})Fe(H)(CO)$ **2.2-H2**, $P_3^B(\mu\text{-D})Fe(D)(CO)$ **2.2-D2**, or a mixture of both. The isolated products (10-20 mg), **2.6-H2**, **2.6-D2**, or **2.6-H2/D2** were dissolved in C_6D_6 and exposed to an atmosphere of H_2 or D_2 in a J. Young NMR tube. The solutions were mixed until full conversion of the starting material was observed (~24 h). Longer reaction times were not observed to change the product ratios or improve the yield of the CO-derived product. The resulting mixtures were vacuum transferred into a second J. Young NMR tube and the product ratios were determined by ^{1}H NMR integration. Integrations relative to the *Me*$_3$Si- peak were used to determine the amount of fully deuterated product in the samples. A small amount of Et_2O was observed in one case, which overlapped with the product peak, so ^{13}C-labeled compounds were used to obtain improved integrations.

Figure B6.1: ^{1}H NMR (400 MHz) spectrum of the product mixture generated from the reaction of **2.6** with H_2 (with Fc internal standard).

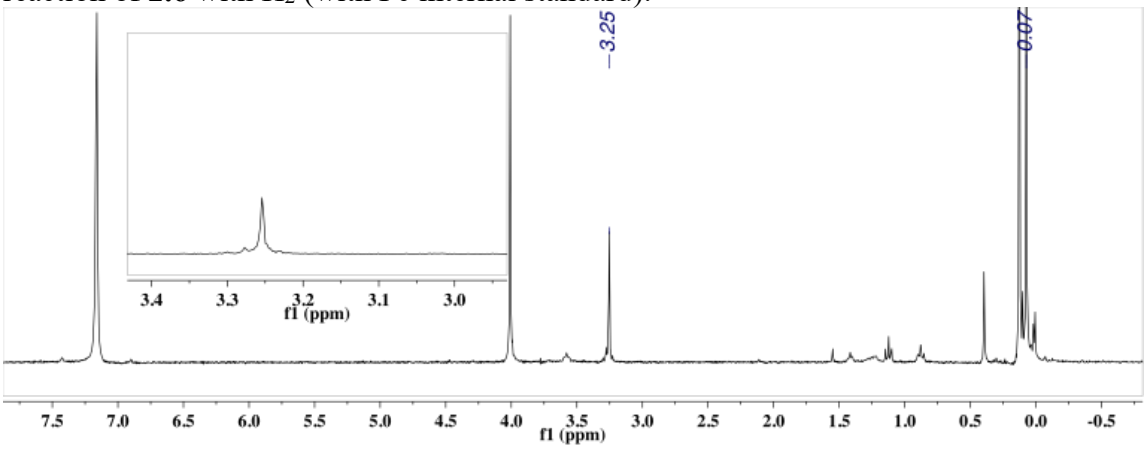

Figure B6.2: ^{1}H NMR (400 MHz) spectrum of the product mixture generated from the reaction of **2.6** with D_2.

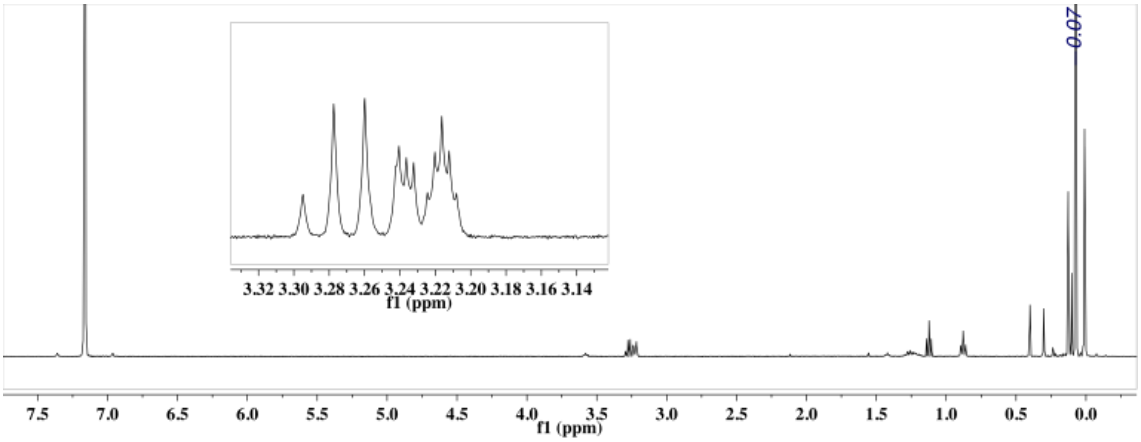

Figure B6.3: ^{1}H NMR (400 MHz) spectrum of the product mixture generated from the reaction of **2.6** with D_2 using ^{13}CO-labeled material.

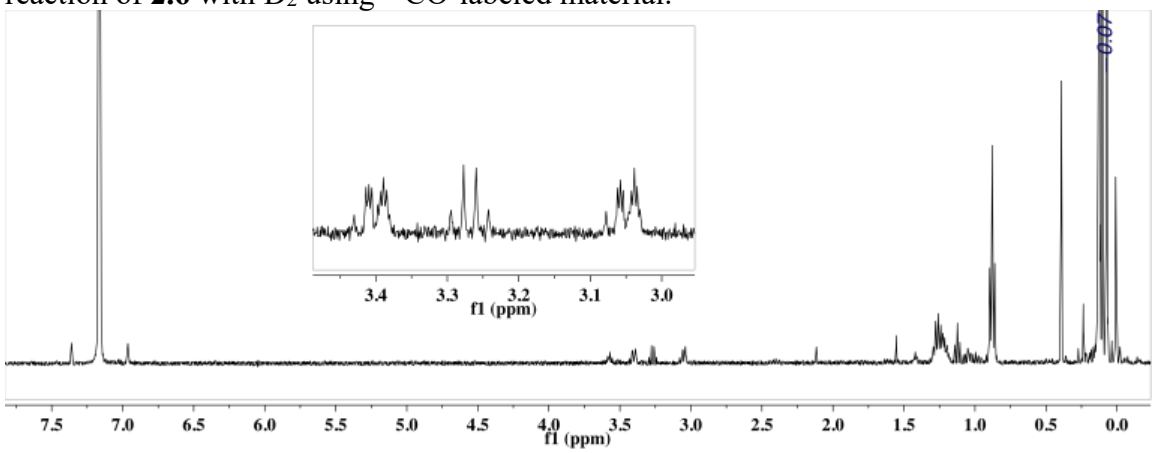

Figure B6.4: ^{1}H NMR (400 MHz) spectrum of the product mixture generated from the reaction of **2.6-D$_2$** with H_2.

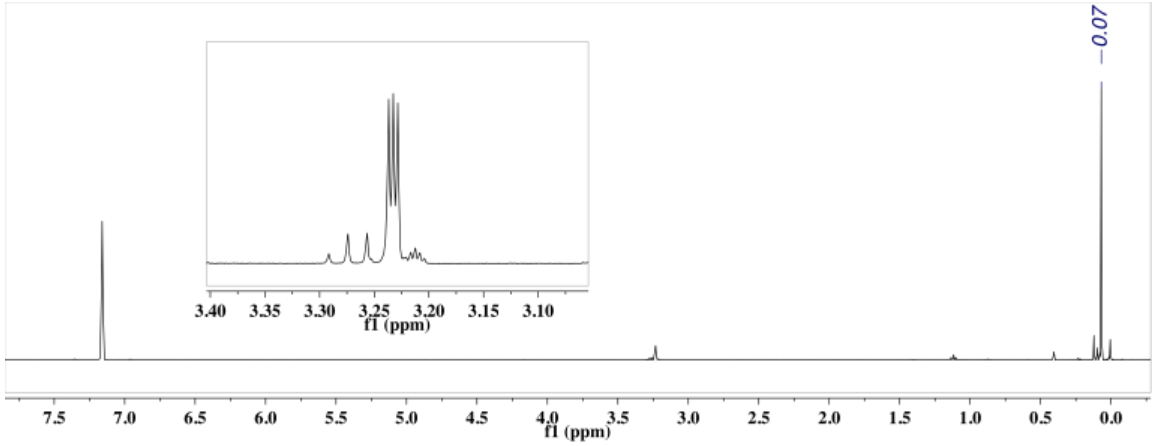

Figure B6.5: ^{13}C{^{1}H} NMR (101 MHz) spectrum of the product mixture generated from the reaction of **2.6-D$_2$** with H_2 using ^{13}CO-labeled material.

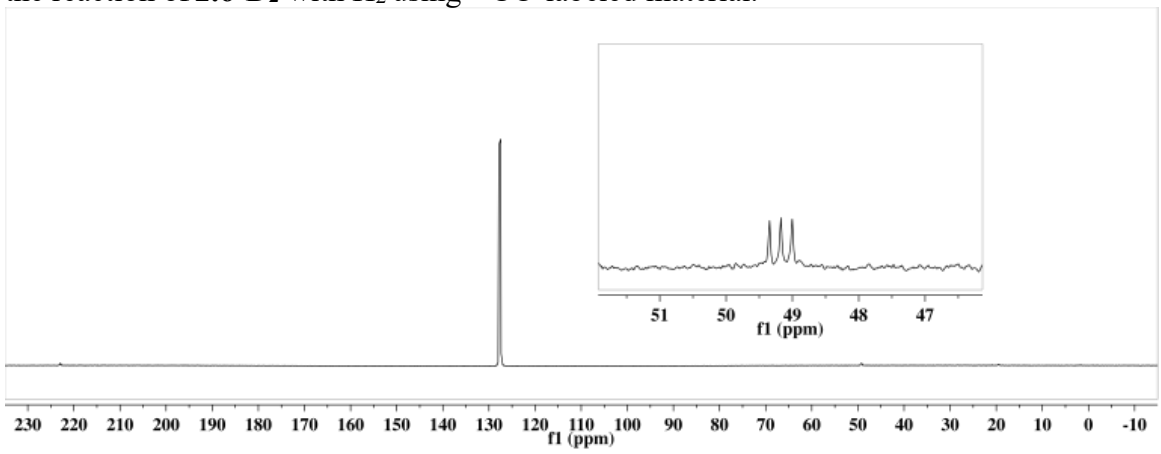

Figure B6.6: ^{1}H NMR (400 MHz) spectrum of the product mixture generated from the reaction of **2.6-D$_2$** with D_2

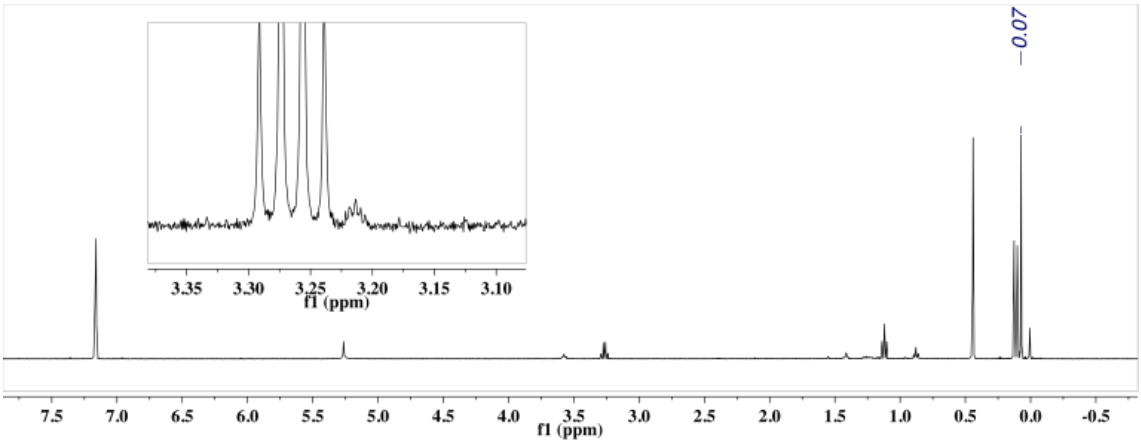

Figure B6.7: ^{1}H NMR (400 MHz) spectrum of the product mixture generated from the reaction of a mixture of **2.6** and **2.6-D$_2$** (1:1) with H_2.

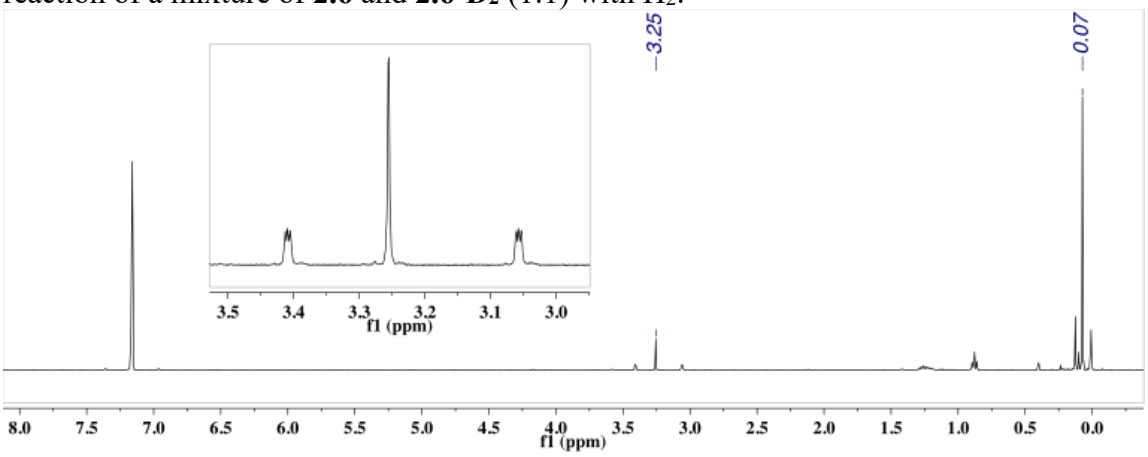

B7. Crystallographic Details

	2.2	**2.3**	**2.4**	**2.5**	**2.6**
Crystal system	Monoclinic	Monoclinic	Monoclinic	Monoclinic	Triclinic
Crystal size (mm)	0.11 x 0.18 x 0.42	0.20 x 0.21 x 0.27	0.12 x 0.17 x 0.20	0.14 x 0.14 x 0.22	0.13 x 0.21 x 0.27
Formula	$C_{197.8}H_{311.8}B_4Fe_4K_8O_{10}P_{12}$	$C_{41}H_{64}BFeKO_2P_3$	$C_{53}H_{87}BFeKO_5P_3$	$C_{37}H_{55}BFeOP_3$	$C_{41.3}H_{68.3}BFeO_{1.3}P_3Si$
Formula weight (g/mol)	3800.66	787.55	1002.89	675.38	773.74
Space group	P 21/c	P 21/n	P 21/c	P 21/c	P-1
a (Å)	18.8485(17)	14.965(2)	11.2309(19)	10.9781(13)	10.9056(7)
b (Å)	41.389(4)	19.074(3)	23.142(4)	15.8664(18)	11.3906(7)
c (Å)	26.821(3)	16.191(2)	20.143(3)	20.543(2)	20.2061(14)
α (deg)	90	90	90	90	78.666(2)
β (deg)	99.494(4)	103.987(5)	97.191(6)	103.016(4)	78.736(2)
γ (deg)	90	90	90	90	62.016(2)
Z	4	4	4	4	2
V (Å^3)	20638(3)	4484.6(11)	5194.1(15)	3486.3(7)	2157.9(2)
Indep. Reflections	51181	7998	25208	13298	8802
R(int)	0.139	0.072	0.073	0.040	0.130
R1	9.50	9.20	4.58	2.67	7.16
wR2	20.29	30.62	12.08	7.09	18.70
GOF	1.12	1.04	1.02	1.03	1.04

Remarks on Crystal Structures:

Figure B7.1: Asymmetric unit of the structure of **2.2** in which four Fe centers and eight K countercations crystallize in a cluster. Hydrogen atoms, five K-coordinated THF molecules, free solvent molecules, and a disordered isopropyl group are omitted.

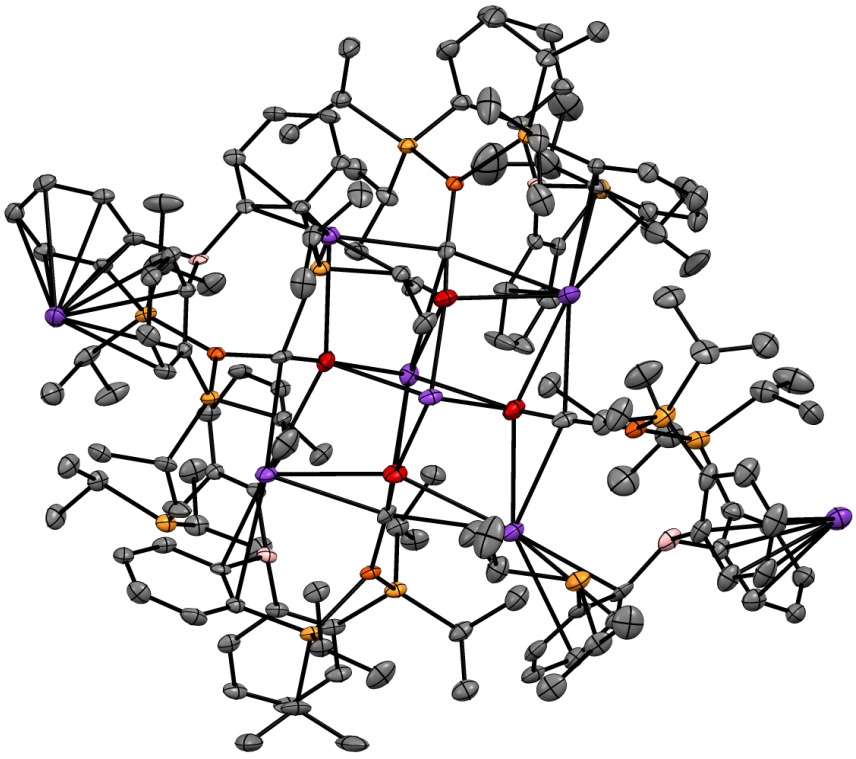

Compound 2.2. This compound crystallizes as a four Fe, eight K cluster, with four crystallographically independent Fe centers in the asymmetric unit as depicted above. The complex crystallizes with five K-coordinated THF molecules. Some of the hydride ligands could be located in the difference map and refined. For two of the iron centers, the terminal hydride could be refined; for one of the iron centers, the bridging borohydride could be refined; and for the final iron center, both the bridging and terminal borohydride ligands could be refined. One of the ligand isopropyl groups was disordered over two positions (60:40), with refinement aided by the application of a RIGU restraint. Free solvent molecules were found in six positions in the unit cell, including two benzene molecules. A third position was refined as a disordered pentane molecule (77:23). Two positions were refined as mixed THF/pentane disorders (77:23 and 64:36). The final position was refined as a partially occupied (0.7) disorder of benzene and THF (41:29). Refinement of these disorders was aided by the application of RIGU and SIMU restraints and EADP constraints where appropriate.

Compound 2.3 This compound crystallizes with a K-coordinated THF molecule in the asymmetric unit; it co-crystallizes with a minor component of an additional Fe complex that has an intact Fe-B interaction (likely **2.4** based on NMR obtained of crystalline material) (90:10). Only the heavy atoms of this minor component (Fe and 3 P) could be refined with the aid of a RIGU restraint. The phenylene rings associated with the Fe-coordinated phosphines are disordered over two positions (62:38 and 71:29). RIGU restraints and an AFIX 66 command aided with refinement of this disorder. The coordinated THF molecule was refined as disordered over two positions (65:35). Refinement of this disorder was aided by the application of RIGU and SADI restraints. The borohydride ligand and one of the hydride ligands could be located and refined freely.

Compound 2.4 This compound crystallizes with two K-coordinated THF molecules and two free THF molecules in the asymmetric unit. The bridging borohydride and one of the terminal iron hydrides could be refined. The two coordinated THF molecules were modeled as disordered over two positions (70:30 for both). Disorder refinement of K-coordinated THF molecules was aided by a RIGU restraint. One of the free THF molecules was refined as disordered over two positions (72:28). The second THF was refined as disordered over

three positions (50:38:12). Anisotropic refinement of free THF molecules was aided by the application of RIGU, SADI, and SAME restraints.

Compound 2.5 This compound crystallizes in the absence of solvent.

Compound 2.6 This compound crystallizes with a partially occupied Et_2O molecule, which is disordered over a special position. Each of the three phosphine ligands has an independently disordered isopropyl group. Two of the isopropyl groups are disordered over two positions (56:44 and 74:26) while the third is disordered over three positions (37:36:27). Refinement of these disorder components was aided by the application of RIGU restraints. The CH_2OSiMe_3 ligand is disordered over two positions (64:36) and refinement of this disorder is aided by the application of a RIGU restraint and an EADP constraint.

B8. Bond Distances and Angles
Compound 2.2

Bond Distances (Å)		Bond Angles (degrees)	
Fe1			
Fe1-P1 (coord.)	2.171(2)	P1-Fe1-P2	116.32(6)
Fe1-P2 (coord.)	2.206(2)	Fe1-C0AA-O1	174.7(5)
Fe1-P3 (free)	6.183(2)	B1-Fe1-C0AA	128.5(2)
Average Fe-P (coord.)	2.19	P1-Fe1-C0AA	115.0(2)
Fe1-C0AA	1.698(6)	P2-Fe1-C0AA	110.7(2)
Fe1-B1	2.783(5)		
Fe1-H1-B1	1.59(5)		
Fe1-H	1.48(5)		
C0AA-O1	1.235(7)		
Fe2			
Fe2-P4 (coord.)	2.180(2)	P4-Fe2-P5	126.52(6)
Fe2-P5 (coord.)	2.152(1)	Fe2-C38-O2	174.5(5)
Fe2-P6 (free)	4.603(2)	B2-Fe2-C38	116.5(2)
Average Fe-P (coord.)	2.17	P4-Fe2-C38	118.1(2)
Fe2-C38	1.709(5)	P5-Fe2-C38	115.0(2)
Fe2-B2	2.764(6)		
Fe2-HB	1.49(8)		
C38-O2	1.225(6)		
Fe3			
Fe3-P7 (coord.)	2.212(2)	P7-Fe3-P8	117.60(6)
Fe3-P8 (coord.)	2.187(1)	Fe3-C75-O3	175.1(5)
Fe3-P9 (free)	6.189(2)	B3-Fe3-C75	109.8(2)
Average Fe-P (coord.)	2.20	P7-Fe3-C75	127.8(2)
Fe3-C75	1.693(5)	P8-Fe3-C75	114.2(2)
Fe3-B3	2.785(6)		
Fe3-H3A-B3	1.59(6)		
C75-O3	1.239(6)		
Fe4			
Fe4-P10 (coord.)	2.172(2)	P10-Fe4-P11	121.86(7)
Fe4-P11 (coord.)	2.160(2)	Fe4-C111-O4	175.0(5)
Fe4-P12 (free)	4.894(2)	B4-Fe4-C111	116.0(2)
Average Fe-P (coord.)	2.17	P10-Fe4-C111	121.2(2)
Fe4-C111	1.704(5)	P11-Fe4-C111	116.3(2)
Fe4-B4	2.763(6)		
Fe4-HA	1.61(6)		
C111-O4	1.246(6)		

Compound 2.3

Bond Distances (Å)		Bond Angles (degrees)	
Fe1-P1 (coord.)	2.171(3)	P1-Fe1-P2	153.2(1)
Fe1-P2 (coord.)	2.143(2)	P1-Fe1-C1	106.8(2)
Fe1-P3 (free)	4.400(3)	P2-Fe1-C1	100.0(2)
Average Fe-P (coord.)	2.16	Fe1-C1-O1	171.4(6)
Fe1-C1	1.743(7)	B1-Fe1-C1	116.6(3)
Fe1-B1	2.687(6)		
Fe1-H1A-B1	1.802		
Fe1-H	1.54(7)		
C1-O1	1.184(8)		

Compound 2.4

Bond Distances (Å)		Bond Angles (degrees)	
Fe1-P1	2.2166(7)	P1-Fe1-P2	105.57(2)
Fe1-P2	2.1695(6)	P2-Fe1-P3	137.73(2)
Fe1-P3	2.2167(6)	P1-Fe1-P3	109.64(2)
Average Fe-P	2.20	Fe1-C0-O1	177.7(1)
Fe1-C0	1.741(1)	B1-Fe1-C0	178.51(6)
Fe1-B1	2.332(1)	P1-Fe1-C0	102.04(4)
Fe1-H	1.46(3)	P2-Fe1-C0	96.14(4)
C0-O1	1.189(2)	P3-Fe1-C0	98.62(4)

Compound 2.5

Bond Distances (Å)		Bond Angles (degrees)	
Fe1-P1	2.2954(5)	P1-Fe1-P2	115.86(2)
Fe1-P2	2.3444(4)	P2-Fe1-P3	132.81(2)
Fe1-P3	2.2536(4)	P1-Fe1-P3	101.73(2)
Average Fe-P	2.30	Fe1-C1-O1	178.95(9)
Fe1-C1	1.746(1)	B1-Fe1-C1	178.64(4)
Fe1-B1	2.650(1)	P1-Fe1-C1	100.60(4)
Fe1-H1-B	1.53(1)	P2-Fe1-C1	100.47(4)
C1-O1	1.158(1)	P3-Fe1-C1	99.45(4)

Compound 2.6

Bond Distances (Å)		Bond Angles (degrees)	
Fe1-P1	2.425(2)	P1-Fe1-P2	113.63(5)
Fe1-P2	2.395(1)	P2-Fe1-P3	107.59(5)
Fe1-P3	2.348(1)	P1-Fe1-P3	119.09(5)
Average Fe-P	2.39	Fe1-C1A-O1A	113.5(7)
Fe1-C1A	2.07(1)	Fe1-C1B-O1B	104(1)
Fe1-C1B	2.08(2)	B1-Fe1-C1A	173.1(3)
Fe1-B1	2.489(4)	B1-Fe1-C1B	90.7(5)
C1A-O1A	1.46(1)	P1-Fe1-C1A	99.3(3)
C1B-O1B	1.42(2)	P2-Fe1-C1A	108.9(3)
		P3-Fe1-C1A	107.6(3)
		P1-Fe1-C1B	115.1(5)
		P2-Fe1-C1B	108.3(5)
		P3-Fe1-C1B	90.7(5)

B9. Reaction of 2.2 with Stoichiometric R_3SiOTf

A solution of **2.2** (in THF, THF-d_8 or 2-MeTHF) was generated *in situ* and cooled to -78 °C. $^{i}Pr_3SiOTf$ (1 equiv) was added as a dilute solution in Et_2O. The mixture was stirred at -78 °C for 15 min then at room temperature for 15 min slowly turning dark red-orange. A mixture of species is generated, with a single major diamagnetic product **2.7**. We have tentatively assigned this species as the monoanionic product of CO-functionalization in which the silyl electrophile has reacted at the carbonyl O, one hydride equivalent has migrated to the carbonyl C, with the stabilization of this species by a P-C interaction. Reaction impurities and decomposition of the product precluded isolation and crystallization of this species. Similar products were observed with related silyl electrophiles (Me_3SiOTf, $^{t}BuMe_2SiOTf$) but reactions using $^{i}Pr_3SiOTf$ generally proceeded most cleanly.

$^{31}P\{^{1}H\}$ NMR (THF-d_8; 162 MHz): δ 79.1 (dd, J = 140, 13 Hz), 74.3 (dd, J = 140, 9 Hz), 55.6 (dd, J = 13, 9 Hz).

$^{31}P\{^{1}H\}$ NMR (THF-d_8; ^{13}CO-labeled; 162 MHz): δ 79.1 (dd, J = 140, 13 Hz), 74.3 (dd, J = 140, 9 Hz), 55.6 (ddd, J = 66, 13, 9 Hz).

$^{13}C\{^{1}H\}$ NMR (2-MeTHF; ^{13}CO-labeled; 101 MHz): δ 24.1 (br).

^{1}H NMR (THF-d_8; 400 MHz): δ 8.42 (d, J = 7.7 Hz, 1H), 8.28 (d, J = 7.7 Hz, 1H), 8.17 (d, J = 7.4 Hz, 1H), 7.27 (overlapping m, 2H), 7.19 (t, J = 7.5 Hz, 1H), 7.06 (t, J = 7.4 Hz, 1H), 7.00 (t, J = 7.3 Hz, 1H), 6.85 (overlapping m, 2H), 6.77 (t, J = 7.4 Hz, 1H), 6.57 (br m, 1H), 2.7-1.9 (^{i}Pr C-*H*, 7 H), 1.2-0.5 (^{i}Pr CH_3, 42H), -0.55 (dt, J = 13, 9 Hz, 1H), -9.85 (br, Fe-*H*, 1H).

^{1}H NMR (THF-d_8; ^{13}C-labeled; 400 MHz): δ 8.42 (d, J = 7.7 Hz, P-C-*H*, 1H), 8.28 (d, J = 7.7 Hz, 1H), 8.17 (d, J = 7.4 Hz, 1H), 7.27 (overlapping m, 2H), 7.19 (t, J = 7.5 Hz, 1H), 7.06 (t, J = 7.4 Hz, 1H), 7.00 (t, J = 7.3 Hz, 1H), 6.85 (overlapping m, 2H), 6.77 (t, J = 7.4 Hz, 1H), 6.57 (br m, 1H), 2.7-1.9 (^{i}Pr C-*H*, 7 H), 1.2-0.5 (^{i}Pr CH_3, 42H), -0.55 (ddt, J = 127, 13, 9 Hz, 1H), -9.85 (br, Fe-*H*, 1H).

Figure B9.1. ^{1}H NMR (THF-d_8; 400 MHz) spectrum of **2.7**. Note: ^{i}Pr resonances are poorly resolved and overlapping with paramagnetic impurities and added Et_2O.

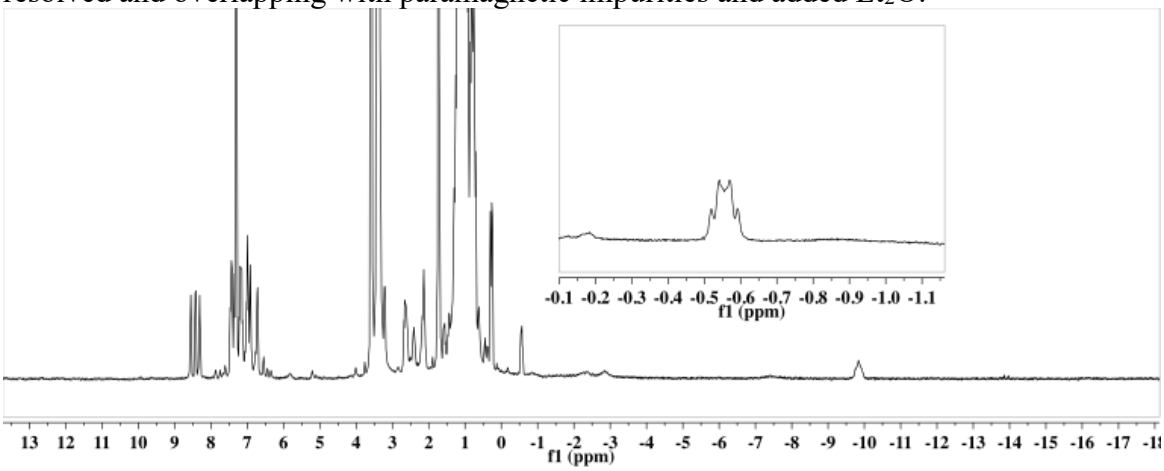

Figure B9.2. ^{1}H NMR (THF-d_8; 400 MHz) spectrum of **2.7-^{13}CO**.

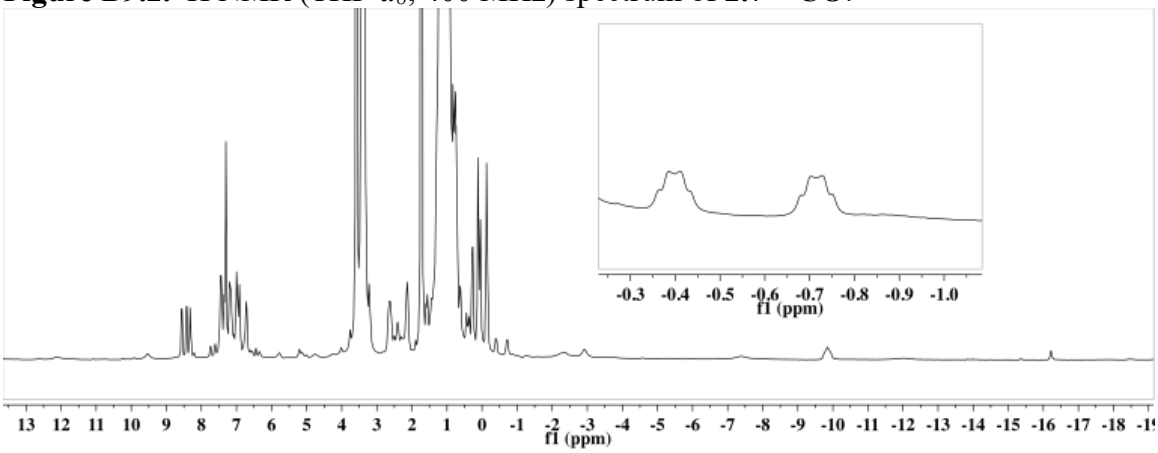

Figure B9.3. ^{1}H NMR (THF-d_8; 400 MHz) spectrum of **2.7-D_2**. Note the observation of the hydridic resonance at -9.85 ppm is consistent with scrambling of ligand protons into this position.

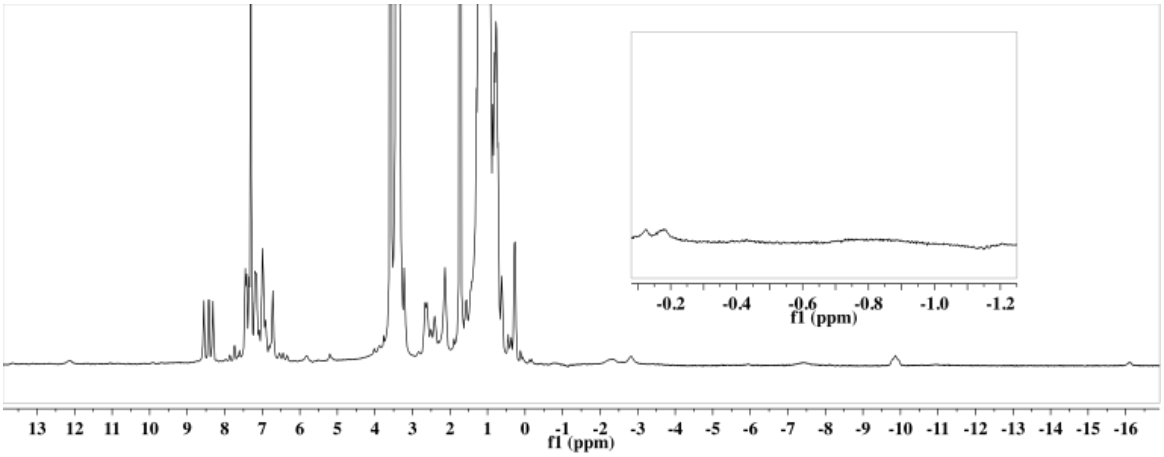

Figure B9.4. $^{31}P\{^{1}H\}$ NMR (THF-d_8; 162 MHz) spectrum of **2.7**.

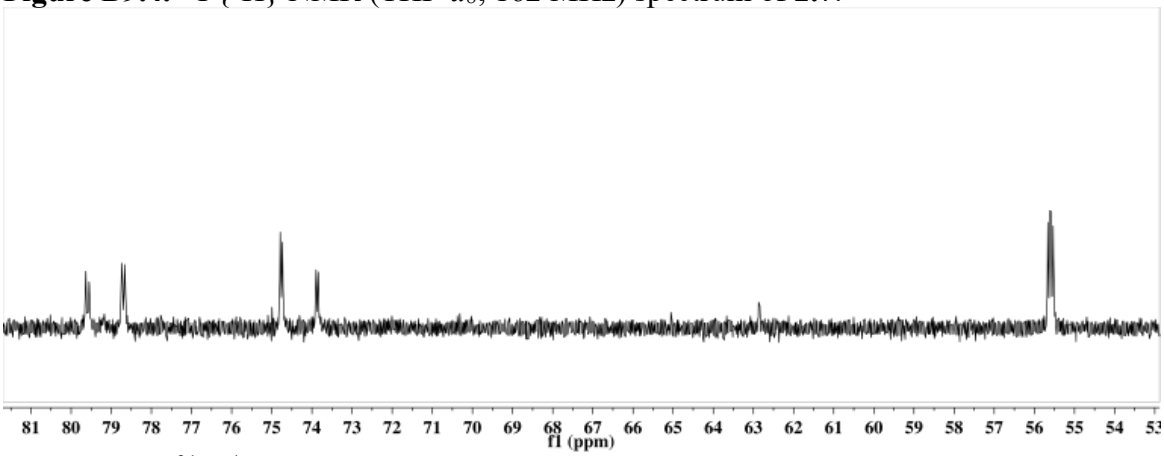

Figure B9.5. $^{31}P\{^{1}H\}$ NMR (THF-d_8; 162 MHz) spectrum of **2.7-^{13}CO**.

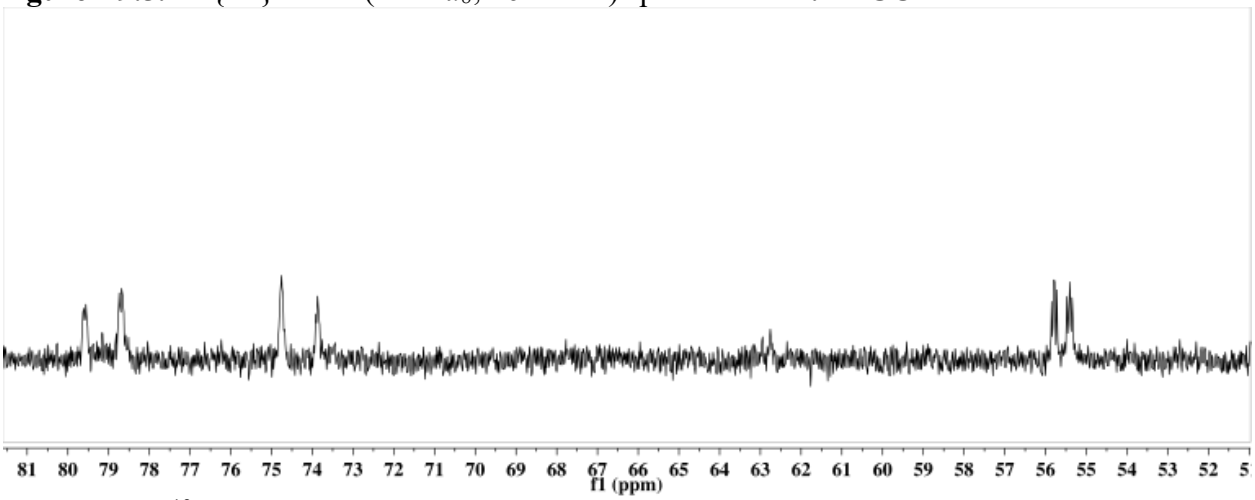

Figure B9.6. ^{13}C NMR (2-MeTHF; 101 MHz) spectrum of **2.7-^{13}CO**. Solvent resonances observable are 2-MeTHF, added C_6D_6, and Et_2O used in the electrophile dilution. In THF, the product resonance directly overlapped with the solvent resonance.

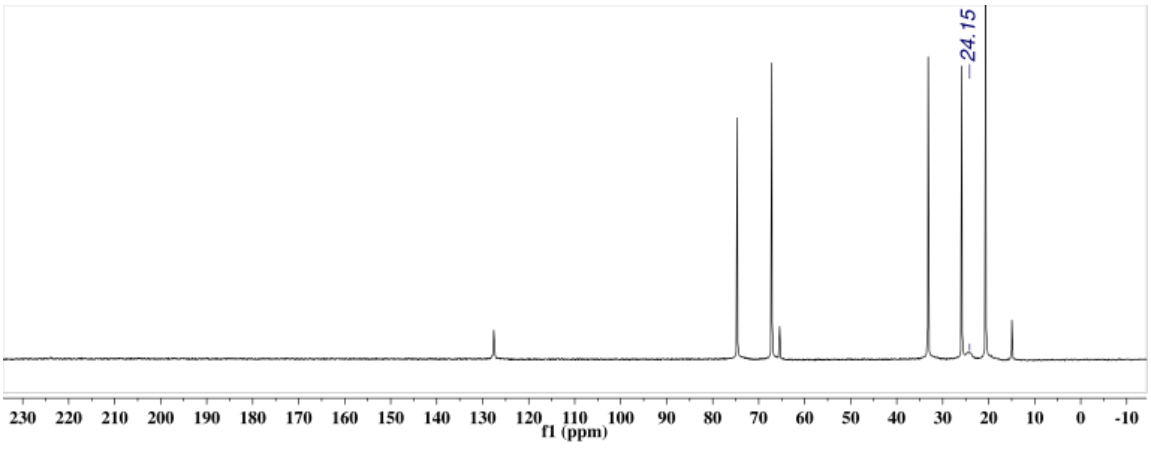

Figure B9.7. ^{13}C-HSQC (THF-d_8) spectrum of **2.7-^{13}CO**.

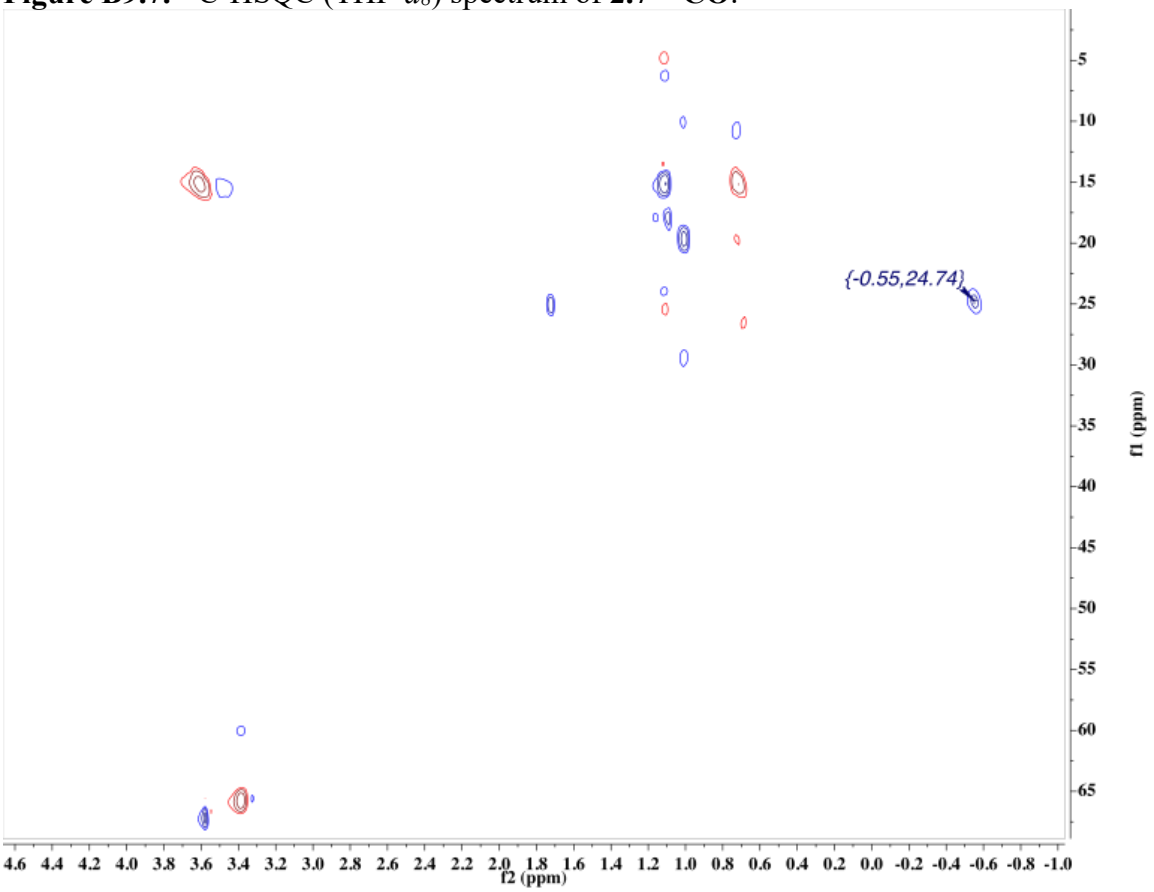

B10. Reaction of 2.6 with H_2/PMe_3 and $PhSiH_3$/PMe_3

Following the reaction of **2.6** with H_2 or $PhSiH_3$, the terminal Fe-containing mixture is intractable in the absence of additives and dependent on the choice of E-H source (H_2 or $PhSiH_3$). In an attempt to identify the Fe-products of these reactions, we explored the addition of coordinating ligands under these conditions. We found that CO and ^{t}BuNC reacted quickly with **2.6**, and no product release was observed in the presence of these additives. When these reactions were carried out with added PMe_3 (5 equiv), similar yields of the free organic products (E-CH_2OSiMe_3) were obtained (H_2: 59%; $PhSiH_3$: 42%; single experiments). Further, the same mixture of Fe-containing products is observed by NMR spectroscopy, with new, paramagnetically shifted resonances (peak picked here) along with an observable amount of **2.1**. This is consistent with the Mössbauer data, which shows a mixture of **2.1**, a new S = 3/2 species, and a residual signal that is likely representative of multiple species.

Figure B10.1: ^{1}H NMR (C_6D_6; 400 MHz) spectrum of the reaction of **2.6** with H_2 (1 atm) and an excess of PMe_3 (5 equiv). Peaks corresponding to a residual amount of **2.6** are observable.

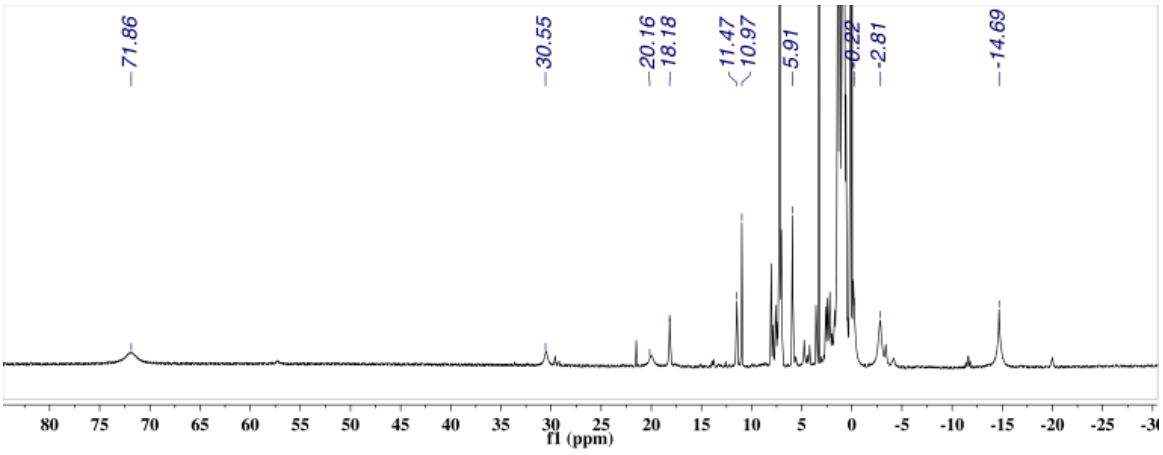

Figure B10.2: ^{1}H NMR (C_6D_6; 400 MHz) spectrum of the reaction of **2.6** with $PhSiH_3$ (5 equiv) and an excess of PMe_3 (5 equiv). Peaks corresponding to diamagnetic **2.1** are also observed.

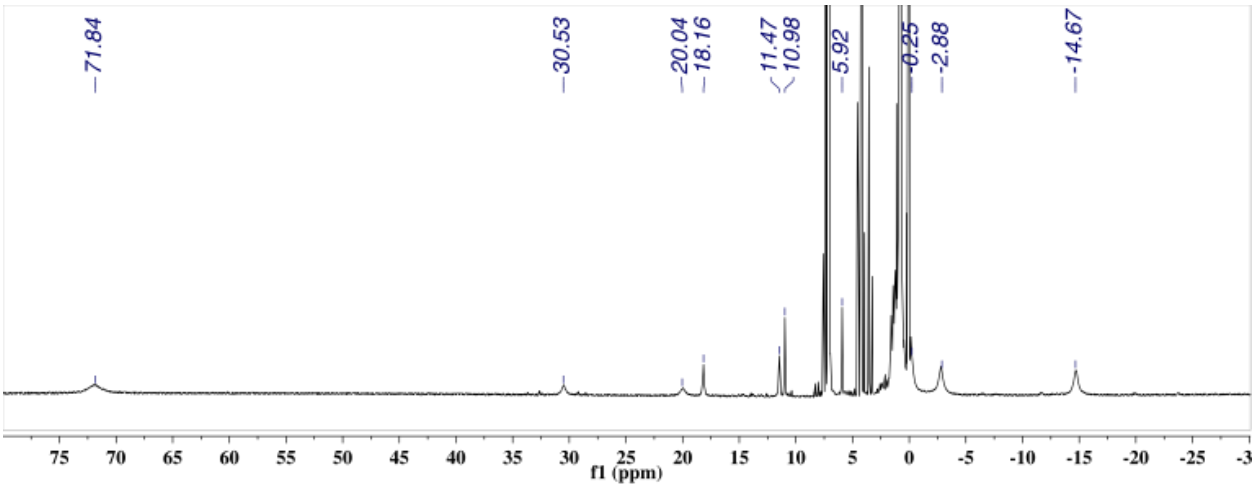

Figure B10.3: Mössbauer spectrum (77 K; benzene; 50 mT) of the reaction of **2.6** with $PhSiH_3$ (5 equiv) and an PMe_3 (5 equiv). The spectrum could be fit as a mixture of three components. In blue, the largest component (δ = 0.52; ΔE_Q = 0.69; 41%) has parameters similar to typical S = 3/2 complexes supported by this scaffold. The species in green (δ = 0.02; ΔE_Q = 1.08; 35%) is **2.1**, which is also observed by ^{1}H NMR. The residual signal in orange (δ = 0.69; ΔE_Q = 1.55; 24%) has an isomer shift consistent with intermediate-to-high spin iron for this system (S = 3/2 or S = 2), but is quite broad and is likely representative of multiple species.

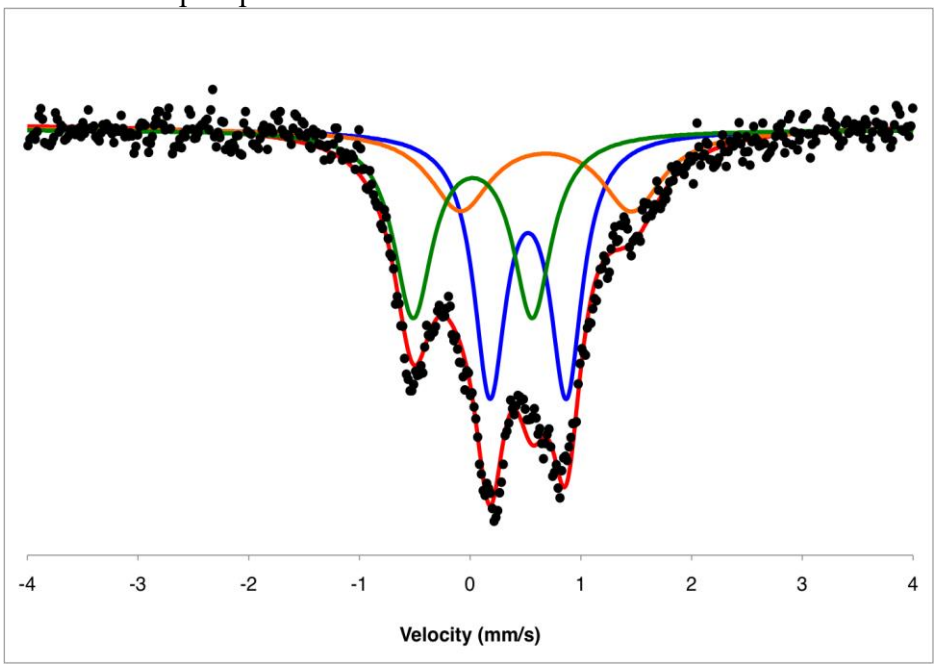

Appendix C

SUPPLEMENTARY DATA FOR CHAPTER 3

C1. NMR Spectra

$[P_3^B(\mu\text{-H})Fe(H)(N_2)][K_2(THF)_n]$ 3.2.

Figure C1.1. ^{1}H NMR spectrum (400 MHz) of **3.2** in THF/THF-d_8.

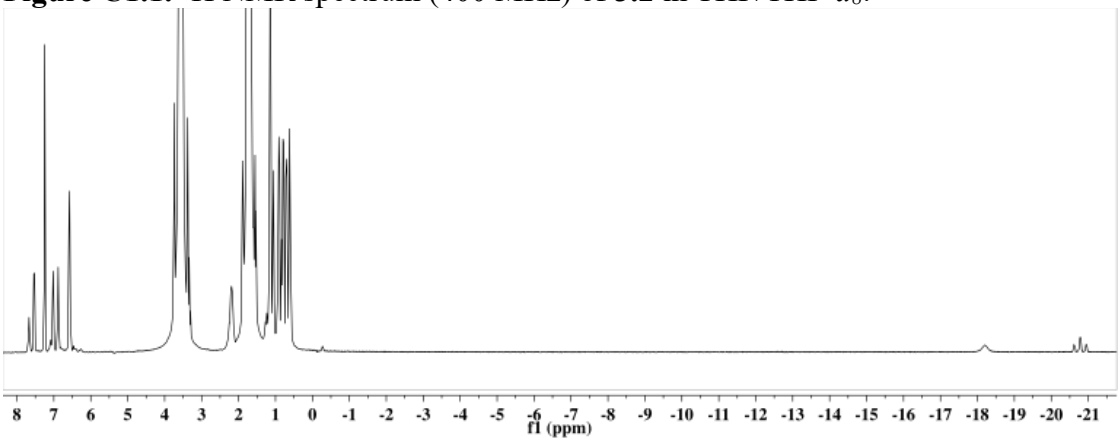

Figure C1.2. ^{31}P NMR spectrum (162 MHz) of **3.2** in THF/THF-d_8.

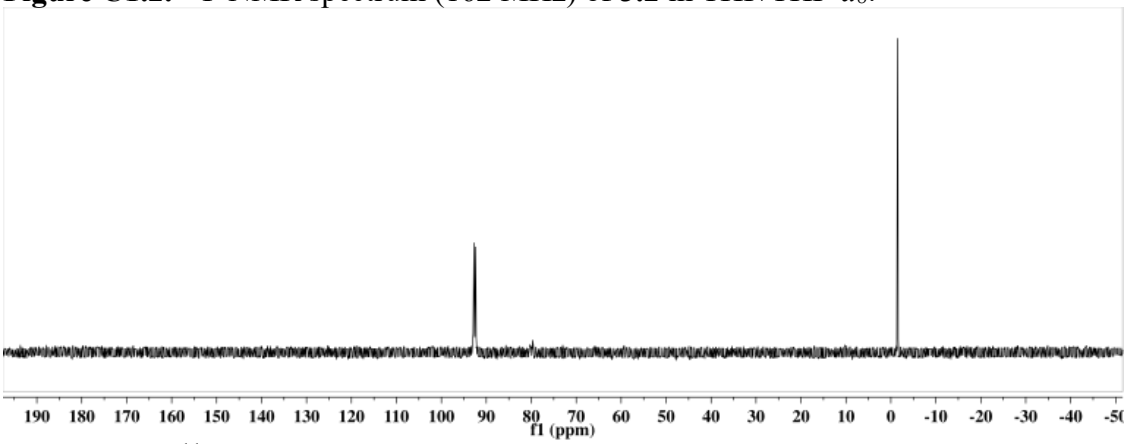

Figure C1.3. ^{11}B NMR spectrum (128 MHz) of **3.2** in THF/THF-d_8.

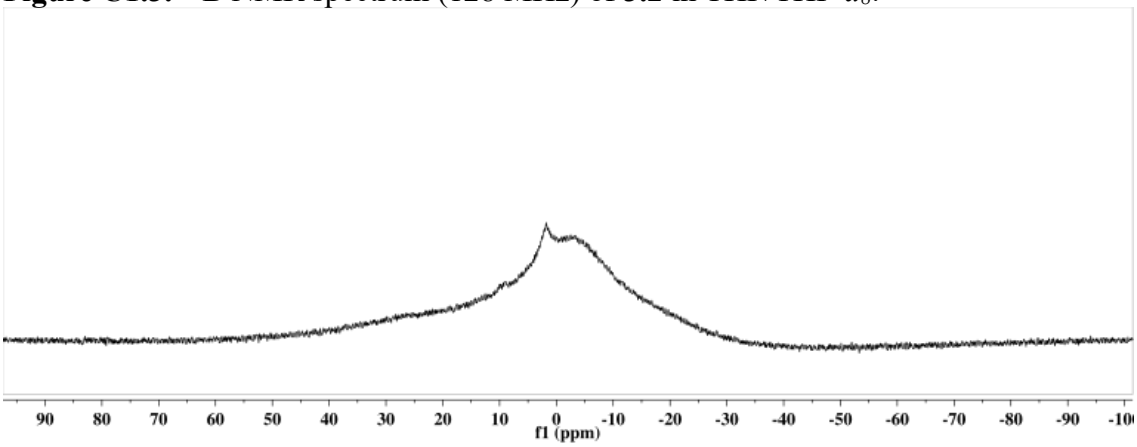

[$P_3^BFe(H)(N_2)$][K(benzo-15-crown-5)$_2$] 3.4.

Figure C1.4. ^{1}H NMR spectrum (400 MHz) of **3.4** in THF-d_8.

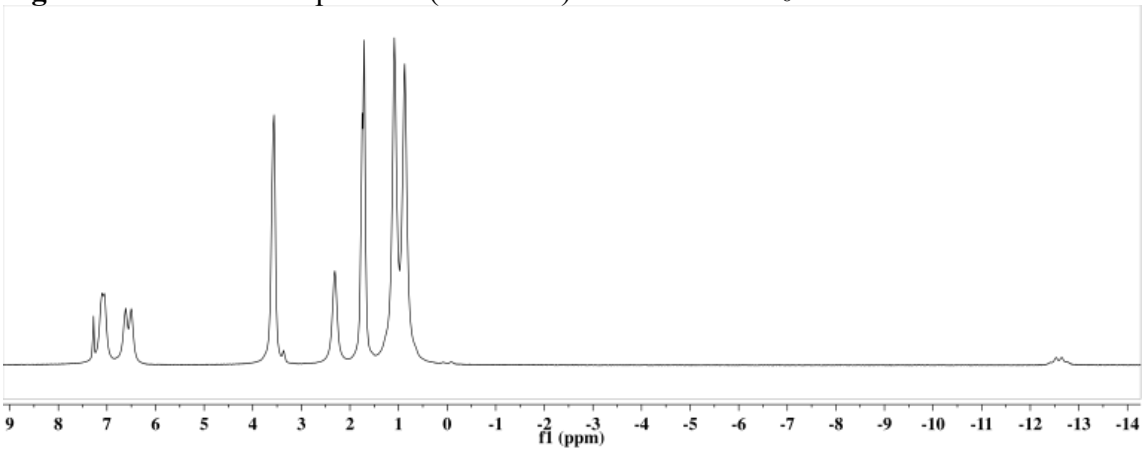

Figure C1.5. ^{31}P NMR spectrum (162 MHz) of **3.4** in THF-d_8.

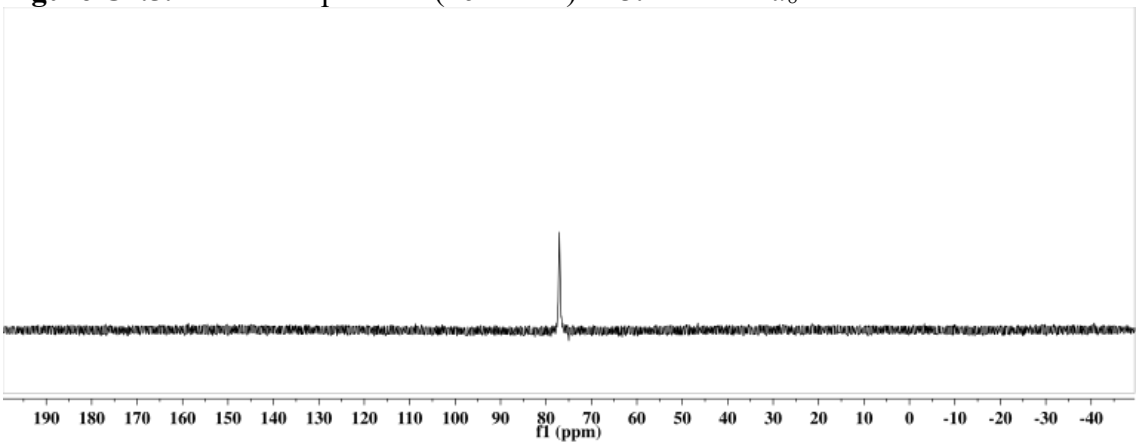

Figure C1.6. ^{31}P NMR spectrum (202 MHz) of **3.4** in THF-d_8 collected at -80 °C.

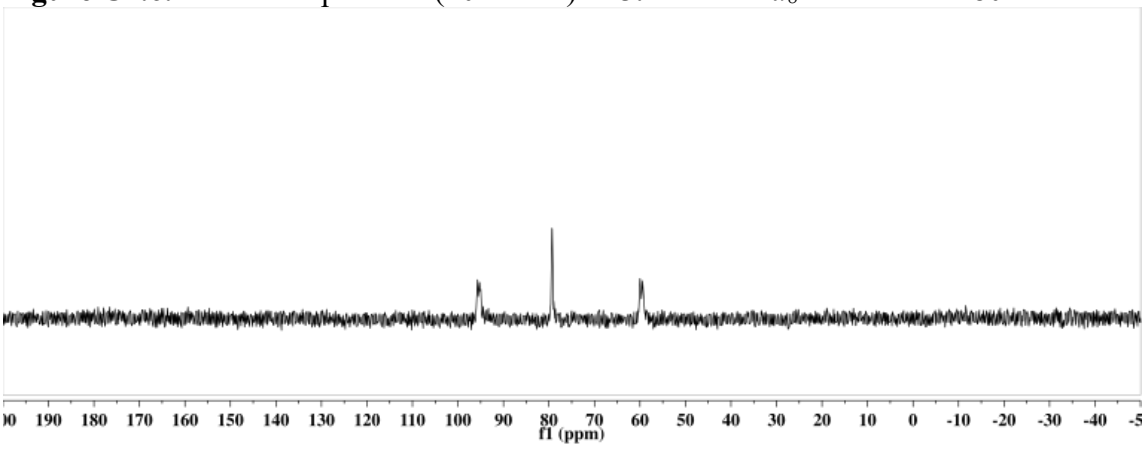

Figure C1.7. ^{11}B NMR spectrum (128 MHz) of **3.4** in THF-d_8.

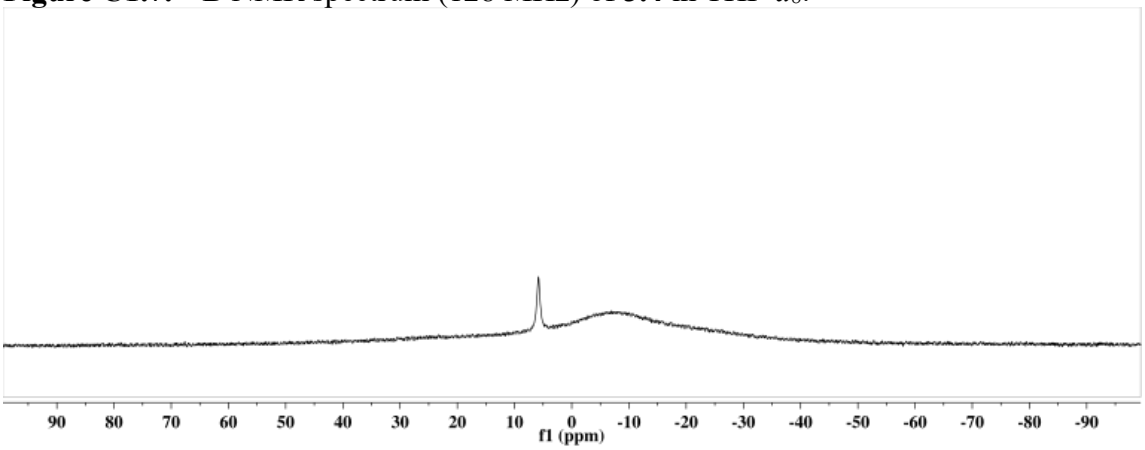

[P$_3^B$(μ-H)Fe(H)(NNSi^{i}Pr$_3$)][K(THF)] 3.7.

Figure C1.8. ^{1}H NMR (400 MHz) spectrum of **3.7** in C_6D_6.

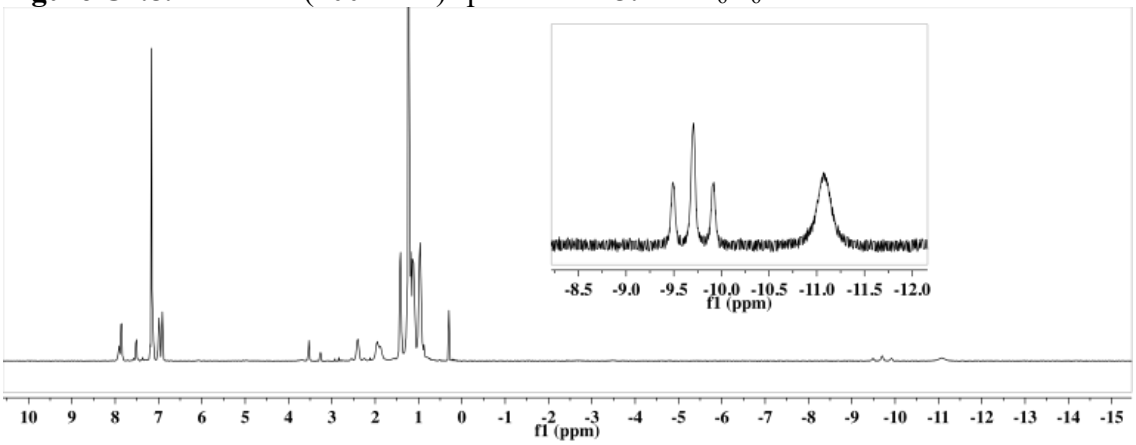

Figure C1.9. ^{31}P NMR spectrum (162 MHz) of **3.7** in C_6D_6.

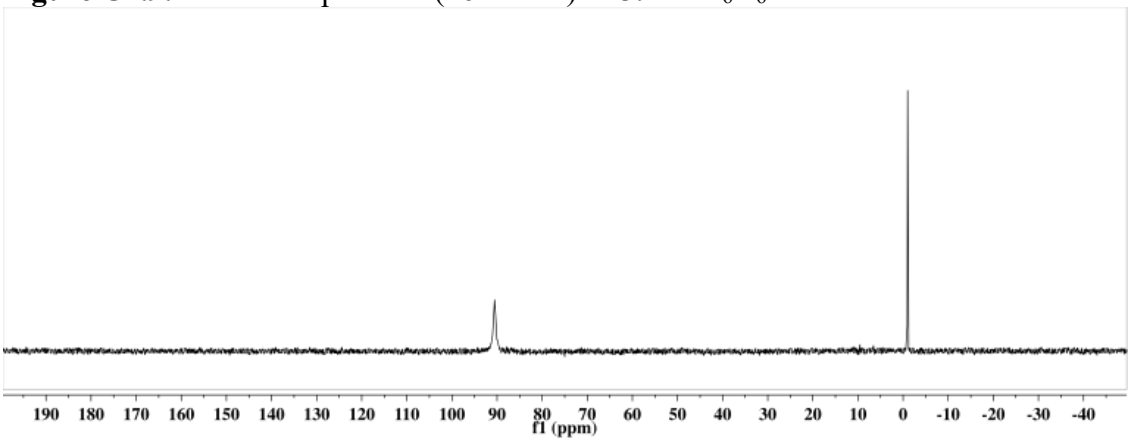

Figure C1.10. ^{11}B NMR spectrum (128 MHz) of **3.7** in C_6D_6.

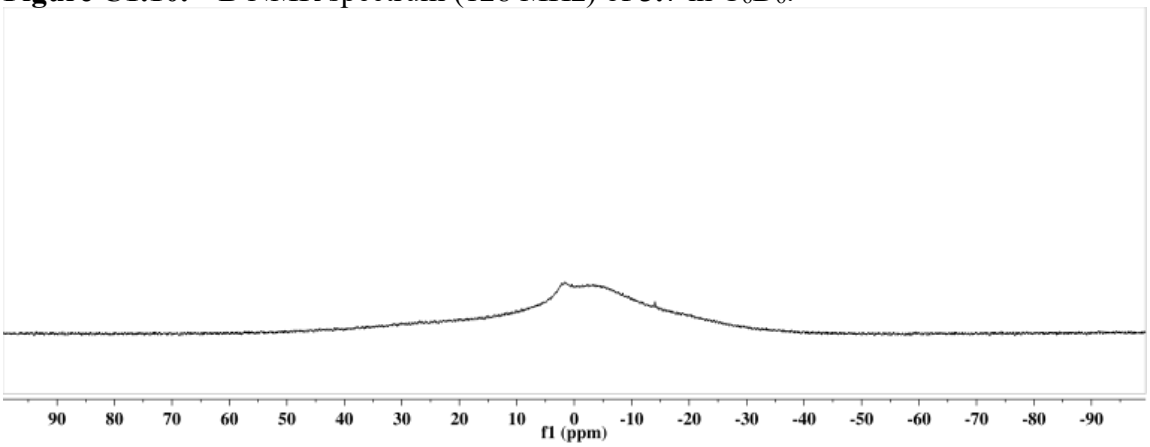

Figure C1.11. ^{29}Si-HMBC spectrum of **3.7** in C_6D_6.

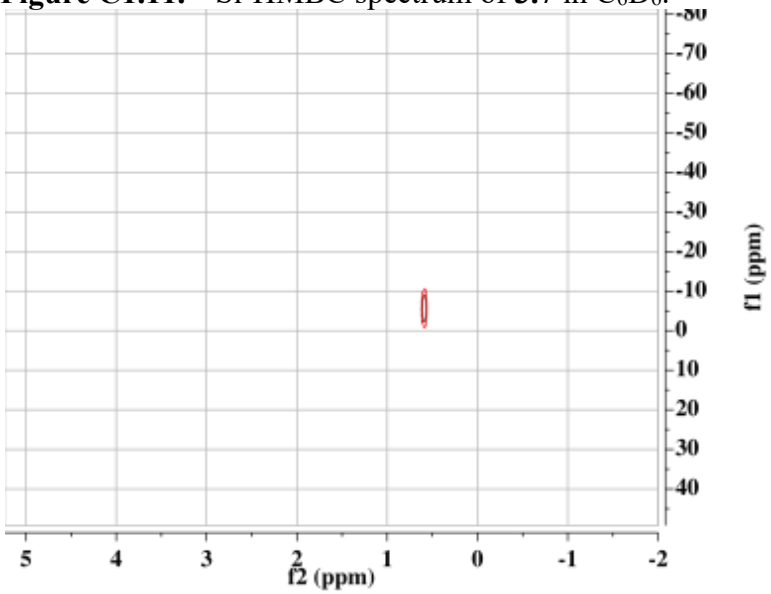

$P_3^B(\mu$-H)Fe(H)(NNSi$_2$) 3.9.

Figure C1.12. Variable temperature ^{1}H NMR data (500 MHz; THF/THF-d_8) for **3.9** collected in 10 degree increments starting at -80 °C (top), increasing to 10 °C (bottom). The paramagnetic product of N-H bond formation is observed in the spectra collected at 0 and 10 °C, with two of the resonances indicated by the # symbol.

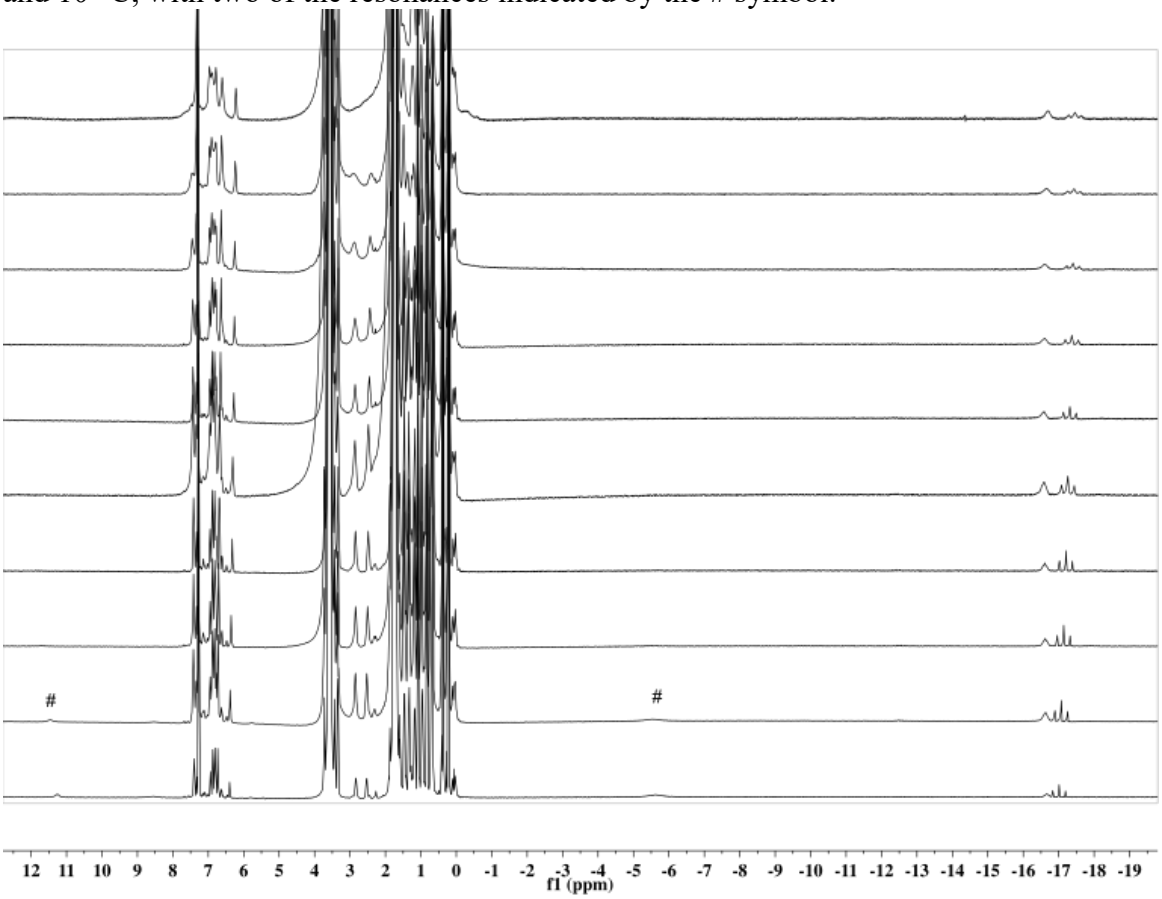

Figure C1.13. Variable temperature ^{31}P NMR (202.4 MHz; THF/THF-d_8) data for **3.9** collected in 10 degree increments starting at -80 °C (top), increasing to 10 °C (bottom).

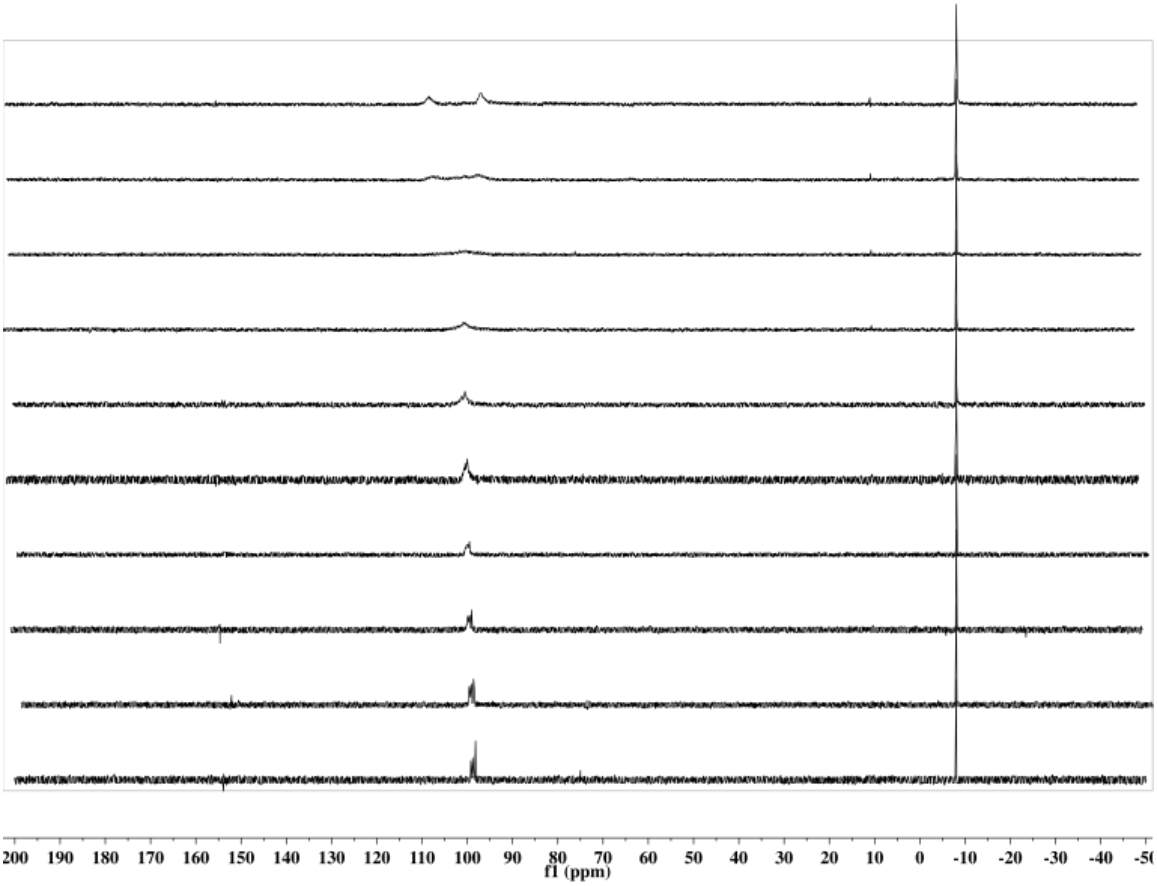

Figure C1.14. ^{1}H NMR spectrum (500 MHz) of **3.9** collected in THF/THF-d_8 at -40 °C.

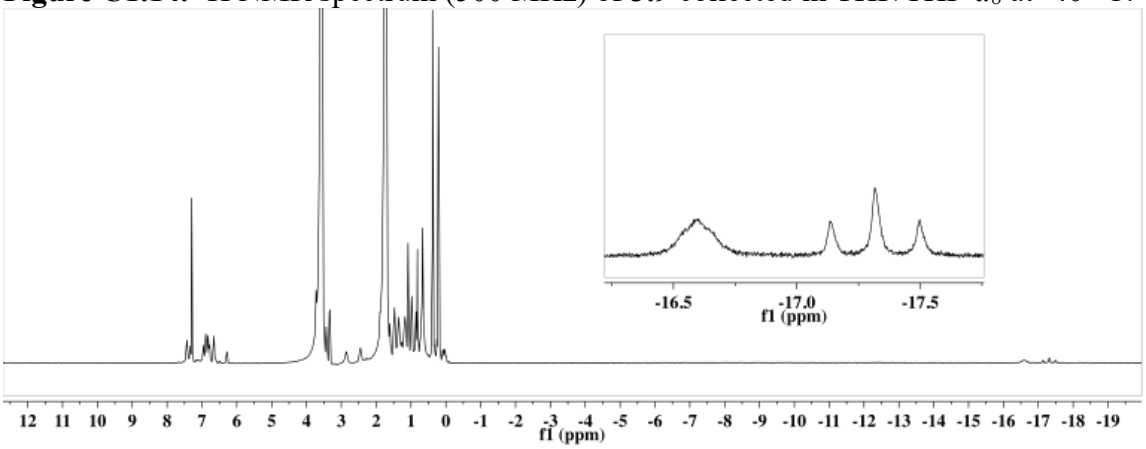

Figure C1.15. ^{31}P NMR spectrum (202 MHz) of **3.9** collected in THF/THF-d_8 at -40 °C.

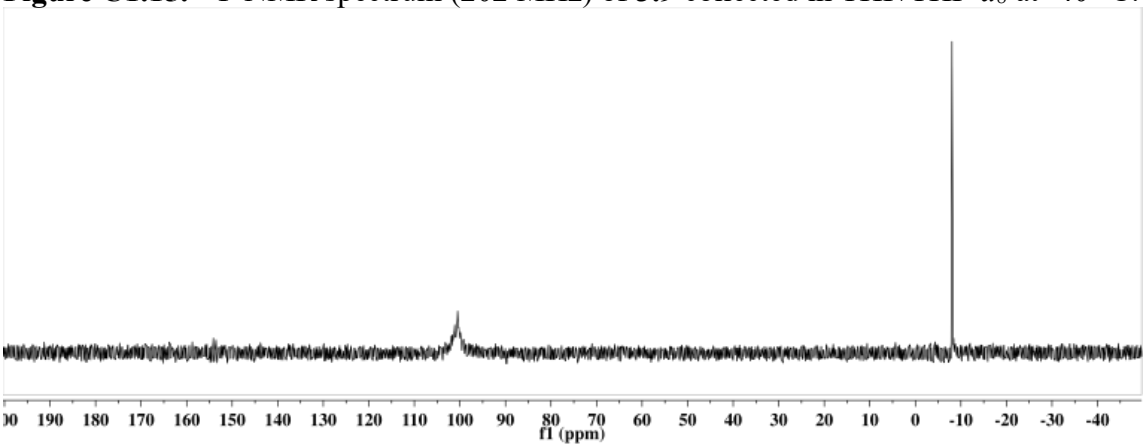

Observation of Decay of 3.9 to $P_3^B(\mu\text{-H})Fe(NHNSi_2)$ 3.10.

Figure C1.16. ^{1}H NMR spectrum (500 MHz) of a mixture containing **3.9** and **3.10** collected in THF/THF-d_8 at -10 °C.

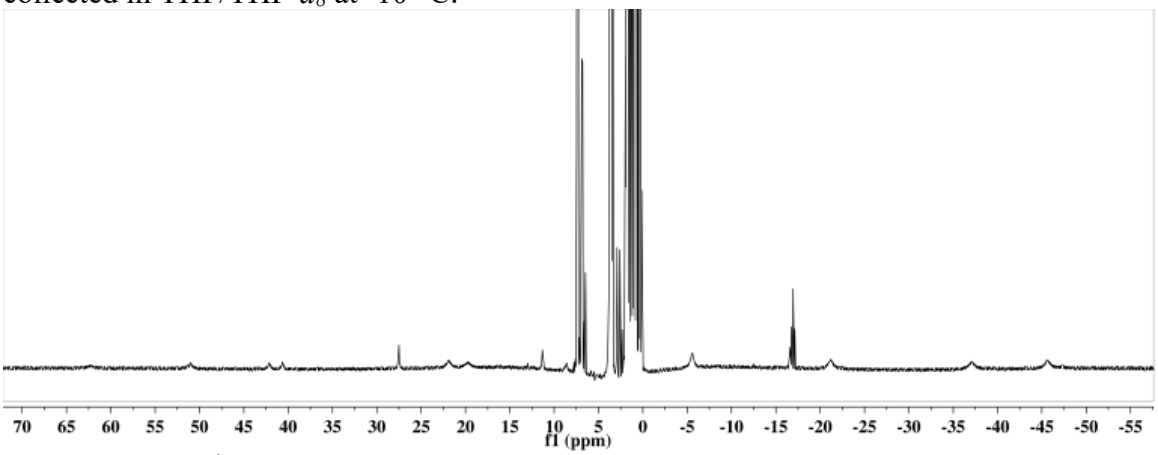

Figure C1.17. ^{1}H NMR spectrum (400 MHz; C_6D_6) containing predominantly **3.10** collected at RT. Minor peaks associated with the precursor **3.9** as well as the initial product of thermal decomposition are also apparent.

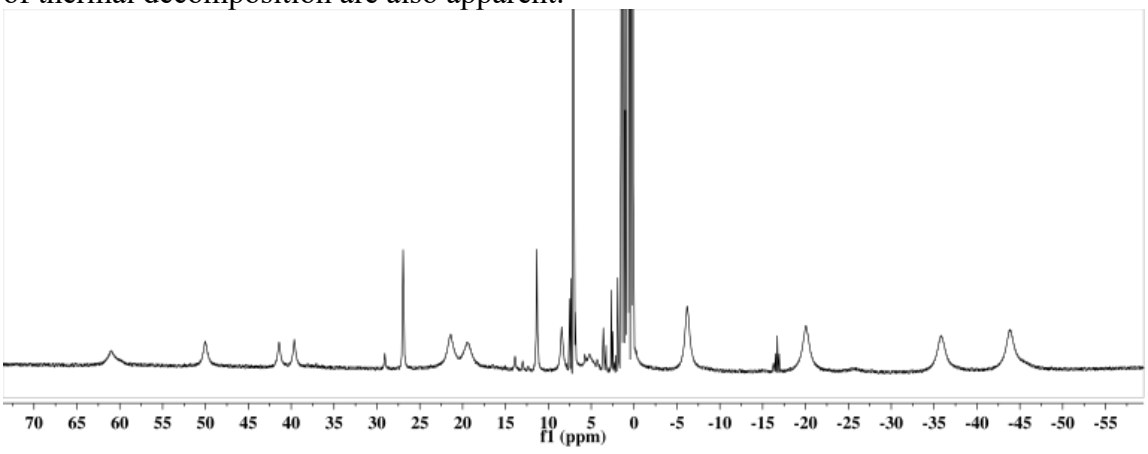

Figure C1.18. ^{1}H NMR spectrum (300 MHz; C_6D_6) showing complete consumption of **3.9** and the further decay of complex **3.10** to its initial decomposition product.

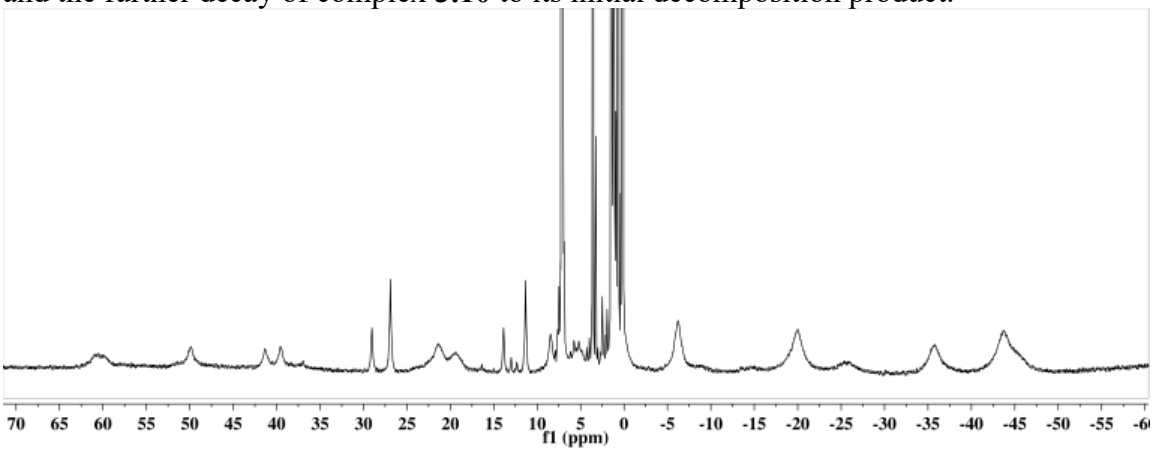

$P_3^B(\mu$-H)Fe(NHNSi$_2$)(CN^{t}Bu) 3.11.

Figure C1.19. ^{1}H NMR spectrum (400 MHz) of **3.11** in C_6D_6.

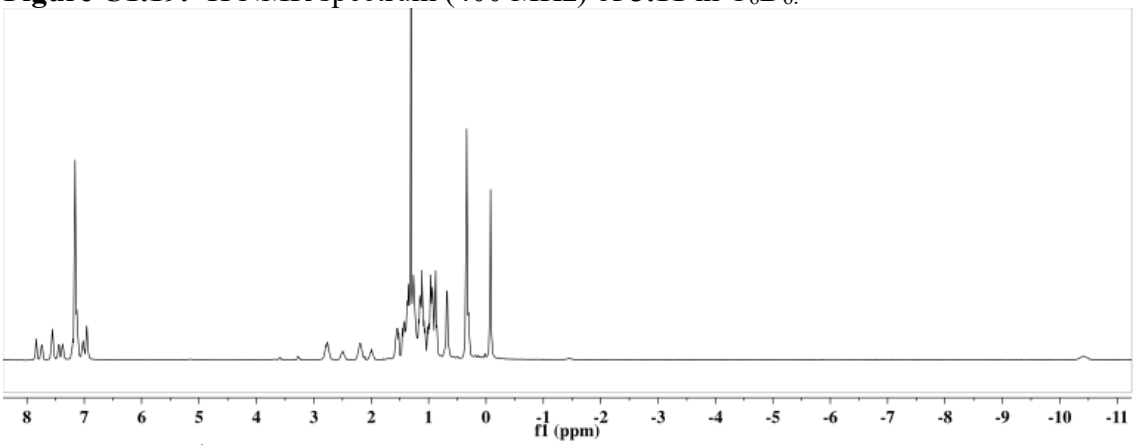

Figure C1.20. ^{1}H NMR spectrum (300 MHz) of **3.11-D$_2$** in C_6D_6 exhibiting the absence of the N-H and B-H-Fe resonances.

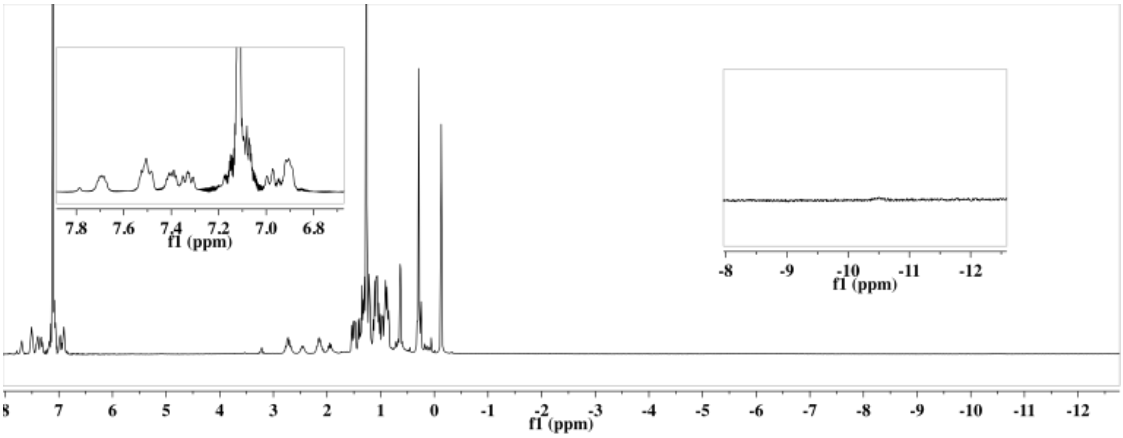

Figure C1.21. ^{31}P NMR spectrum (162 MHz) of **3.11** in C_6D_6.

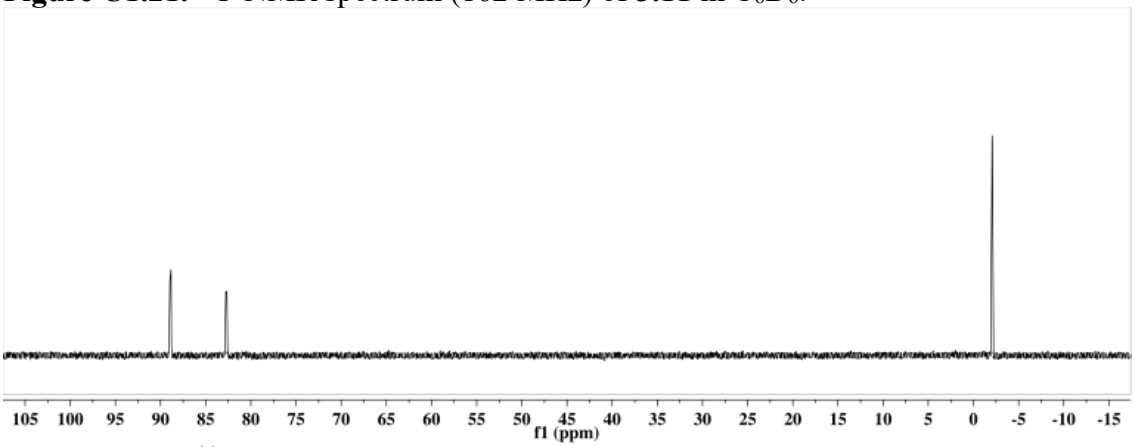

Figure C1.22. ^{11}B NMR spectrum (128 MHz) of **3.11** in C_6D_6.

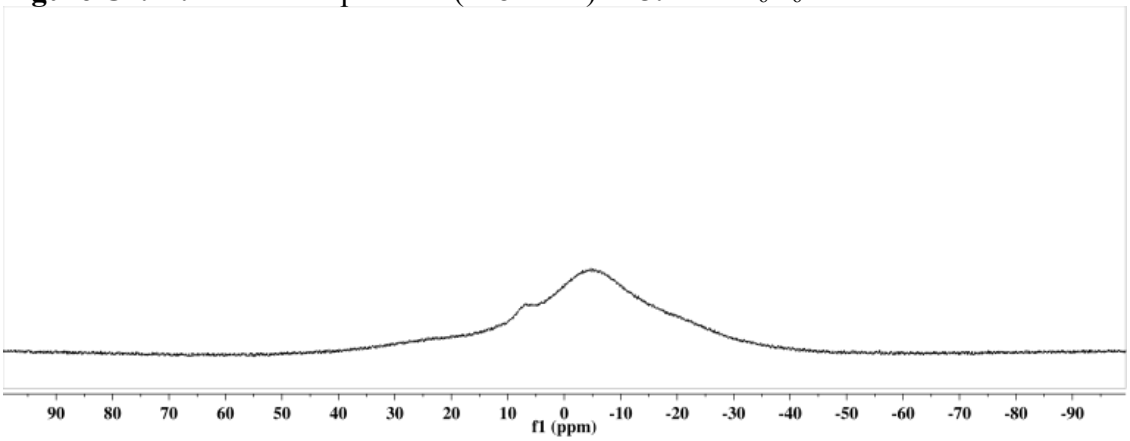

Figure C1.23. ^{29}Si-HMBC spectrum of **3.11** in C_6D_6. Weak coupling is observed to the α-N-H proton (7.84 ppm).

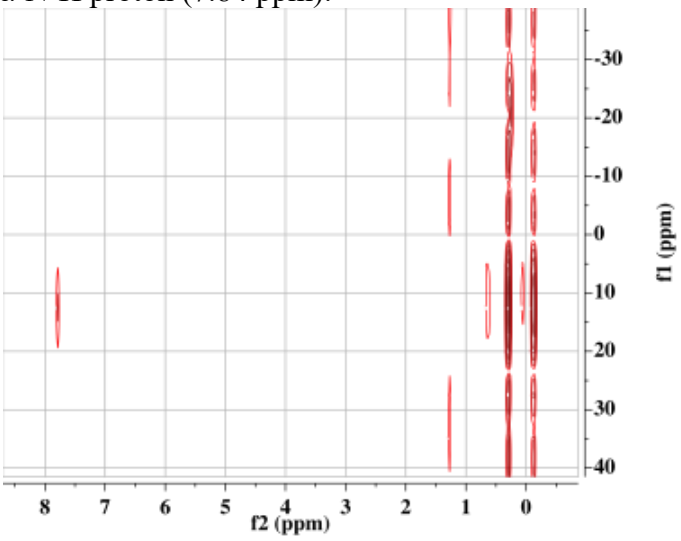

[(P_3^B-H)Fe(CN^{t}Bu)][B($C_8H_3F_6$)$_4$].

Figure C1.24. ^{1}H NMR spectrum (400 MHz) in THF-d_8.

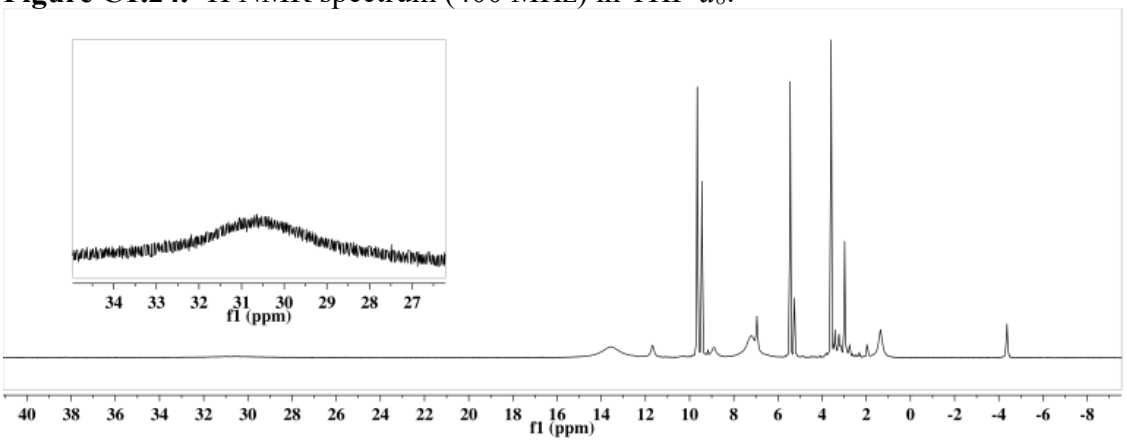

Figure C1.25. ^{19}F NMR spectrum (376 MHz) in THF-d_8.

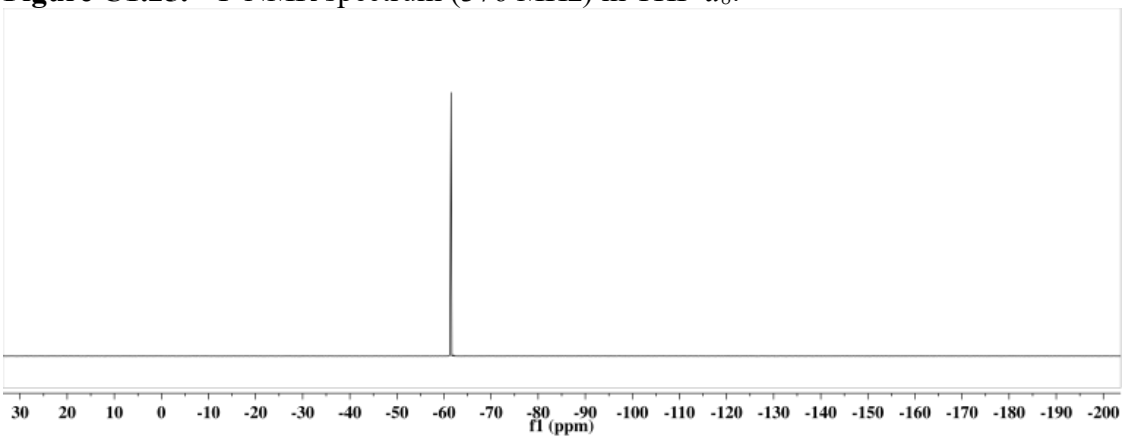

C2. IR Spectra

Figure C2.1. IR spectrum of $[P_3^B(\mu\text{-H})Fe(H)(N_2)][K_2(THF)_n]$ **3.2** (thin film from THF).

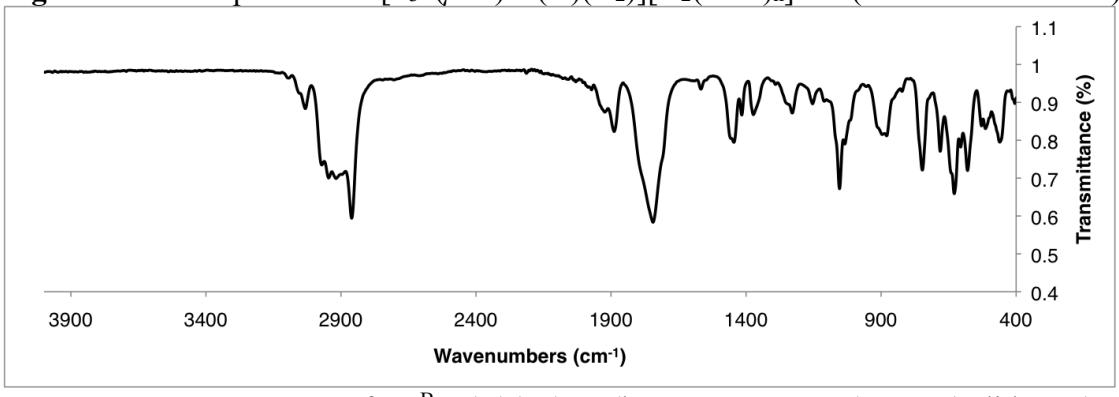

Figure C2.2. IR spectrum of $[P_3^BFe(H)(N_2)][K(benzo\text{-}15\text{-}crown\text{-}5)_2]$ **3.4** (solid state).

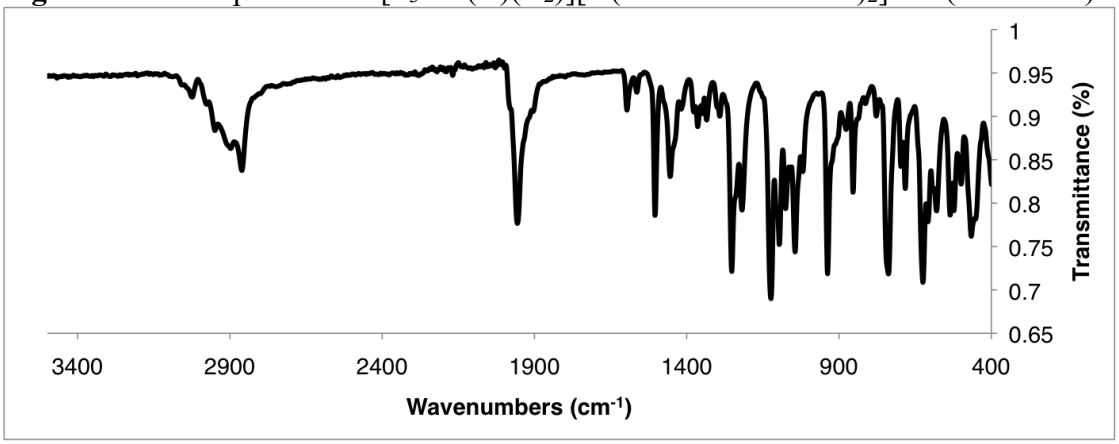

Figure C2.3. IR spectrum of $P_3^B(\mu\text{-H})Fe(H)(NNSi^iPr_3)$ **3.7**.

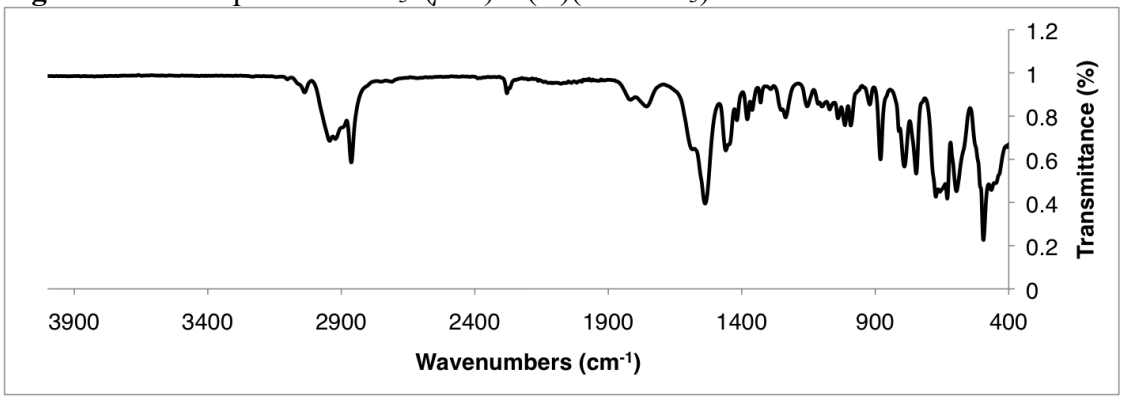

Figure C2.4. IR spectrum of $P_3^B(\mu\text{-H})Fe(NHNSi_2)$ **3.10** (thin film). The proposed N-H stretch is observed at 3263 cm^{-1} and is absent in the spectrum of **3.10-D₂** (Figure S4.5, below). Similarly, the B-H-Fe stretch is found at 1971 cm^{-1}. The presence of a minor N_2 containing impurity from an oxidation side reaction is indicated by #.

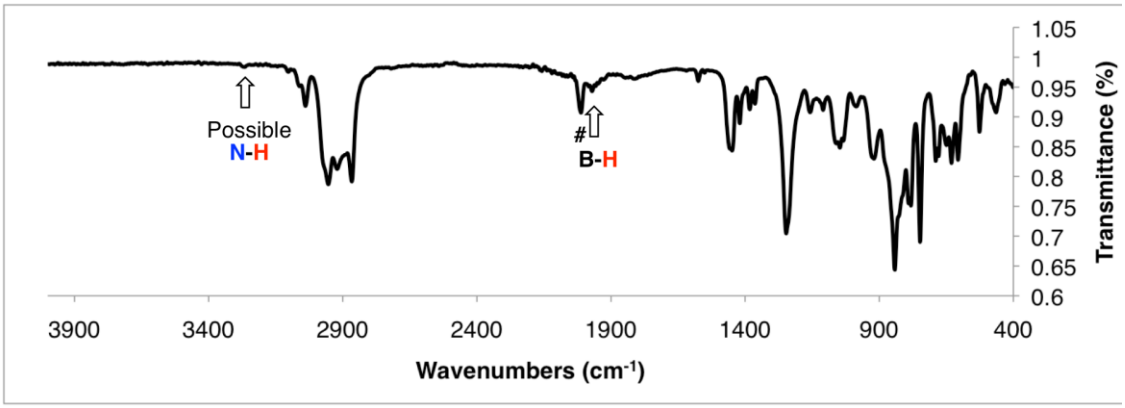

Figure C2.5. IR spectrum of $P_3^B(\mu\text{-D})Fe(NDNSi_2)$ **3.10-D₂** (thin film). The presence of a minor N_2 containing impurity from an oxidation side reaction is indicated by #.

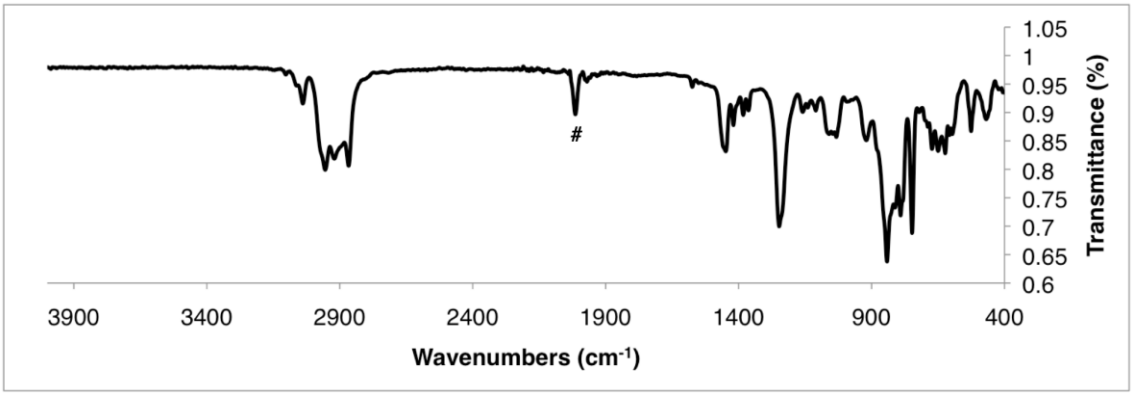

Figure C2.6. IR spectrum of $P_3^B(\mu\text{-H})Fe(NHNSi_2)(CN^tBu)$ **3.11** (thin film from C_6D_6).

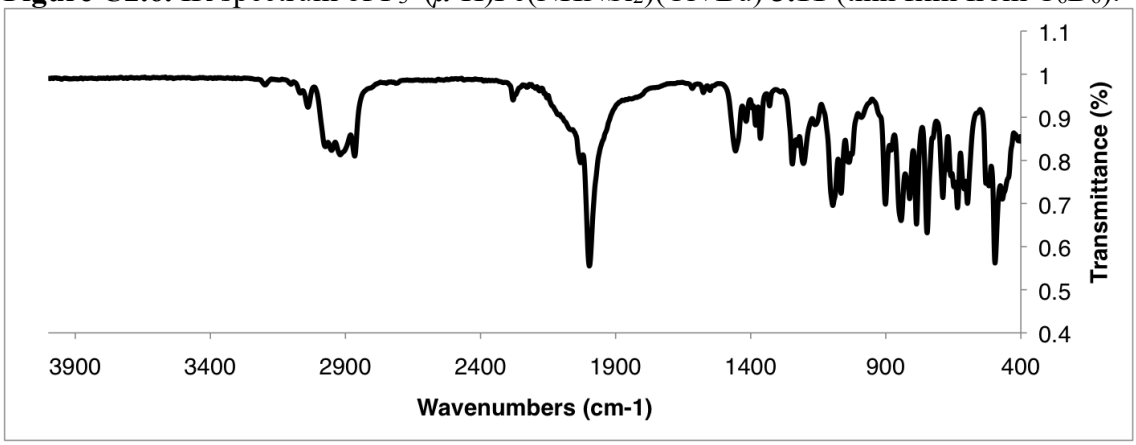

Figure C2.7. IR spectrum of $P_3^B(\mu\text{-D})Fe(NDNSi_2)(CN^tBu)$ **3.11-D2** (thin film from C_6D_6).

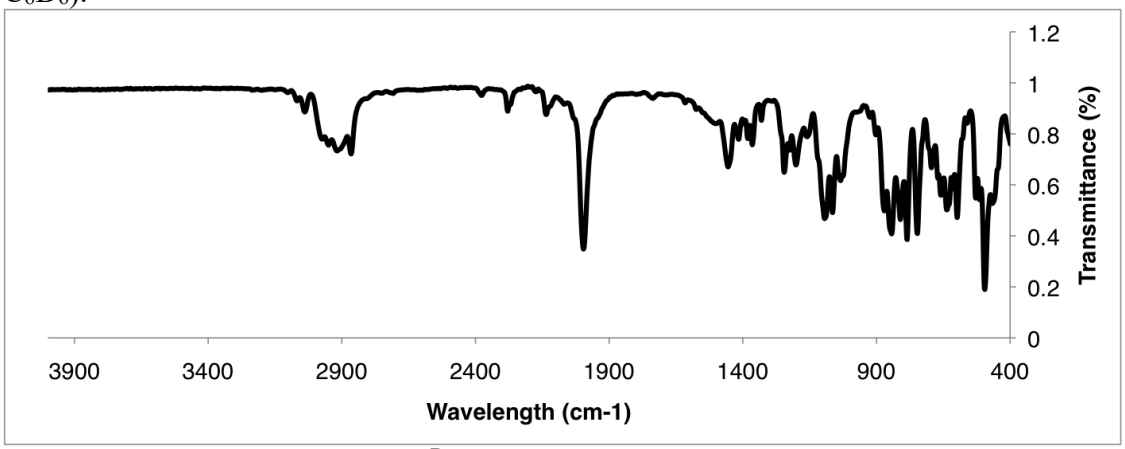

Figure C2.8. IR spectrum of $[(P_3^B\text{-H})Fe(CN^tBu)][B(C_8H_3F_6)_4]$ (thin film from THF-d_8).

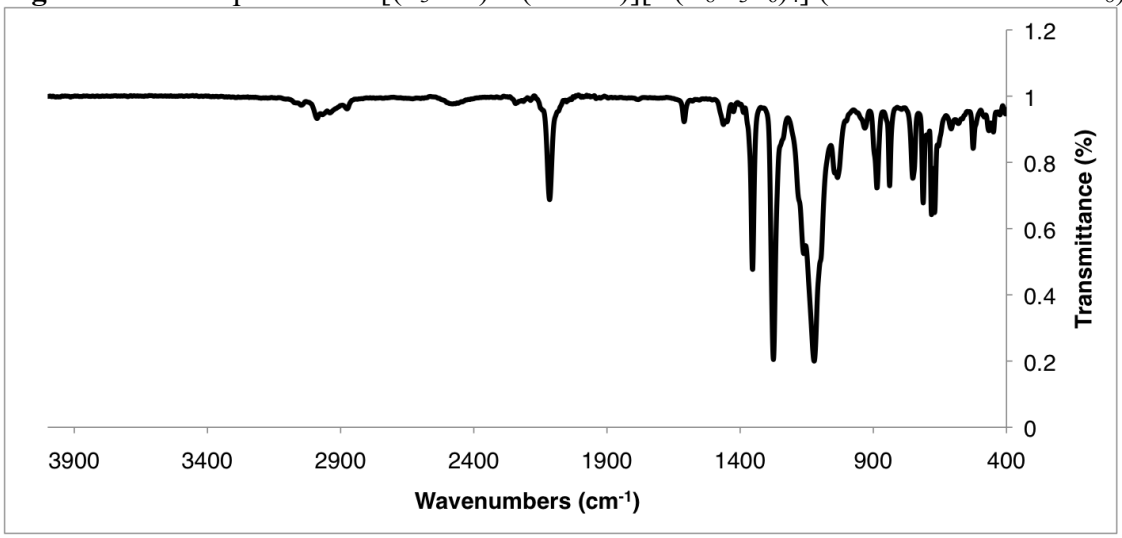

C3. UV-vis Spectra

Figure C3.1. UV-vis spectrum of $[P_3^B(\mu\text{-H})Fe(H)(N_2)][K_2(THF)_n]$ **3.2** (3.2×10^{-4} mM) in THF.

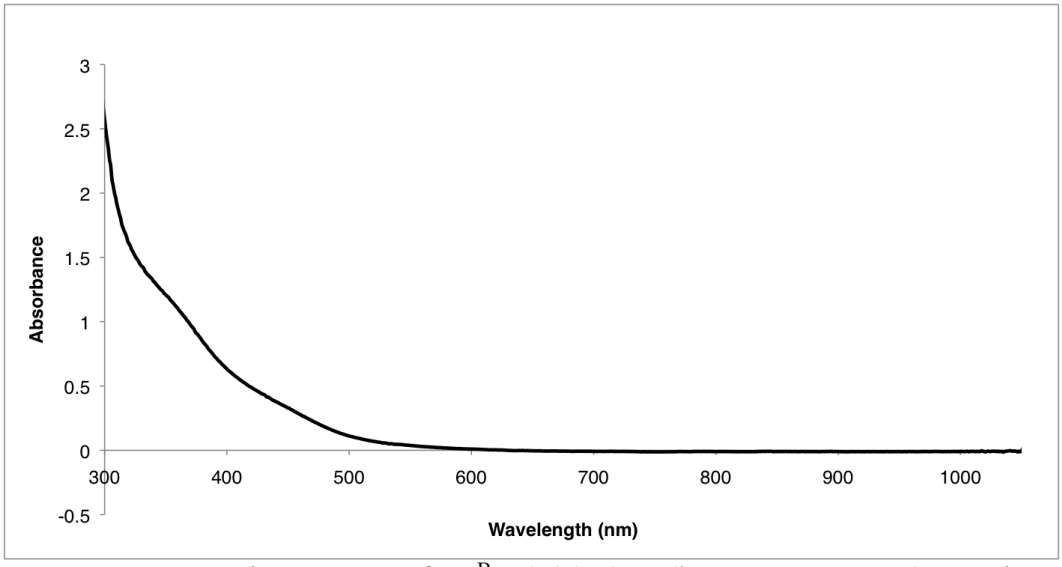

Figure C3.2. UV-vis spectrum of $[P_3^BFe(H)(N_2)][K(benzo\text{-}15\text{-}crown\text{-}5)_2]$ **3.4** in THF.

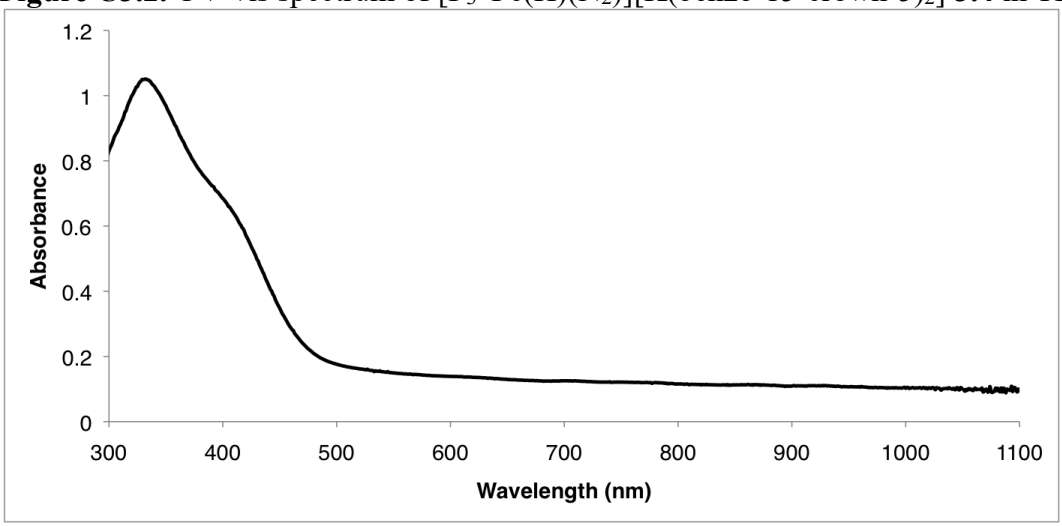

Figure C3.3. UV-vis spectrum of $P_3^B(\mu\text{-H})Fe(H)(NNSi_2)$ **3.9** at -78 °C in THF.

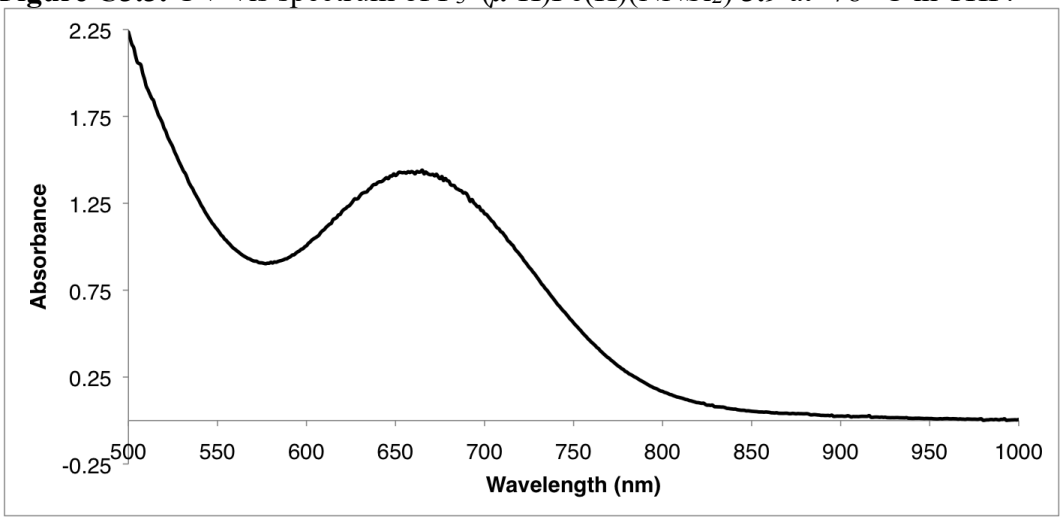

Figure C3.4. UV-vis spectrum of $P_3^B(\mu\text{-H})Fe(NHNSi_2)(CN^tBu)$ **3.11** in THF.

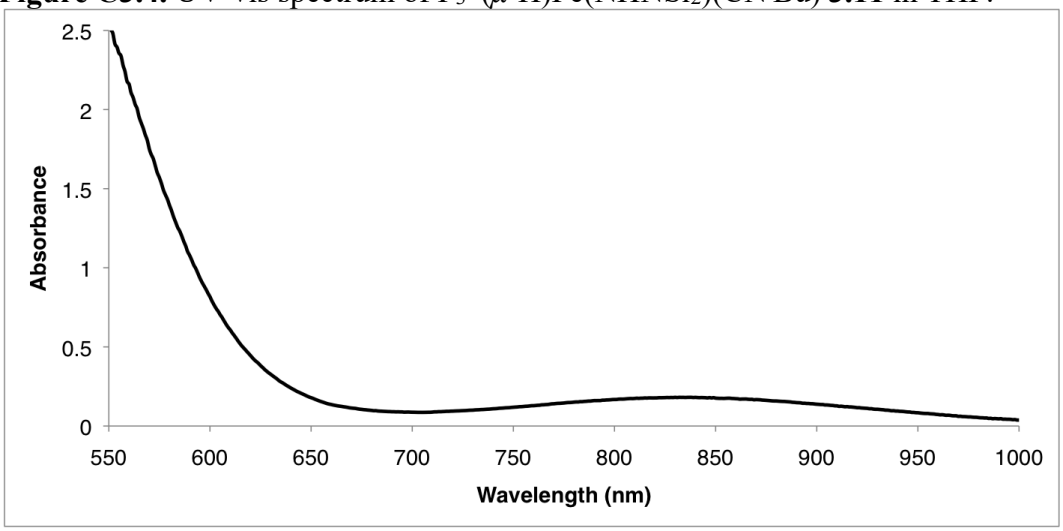

Figure C3.5. UV-vis spectrum of $[(P_3^B\text{-H})Fe(CN^tBu)][BAr^F{}_4]$ in THF.

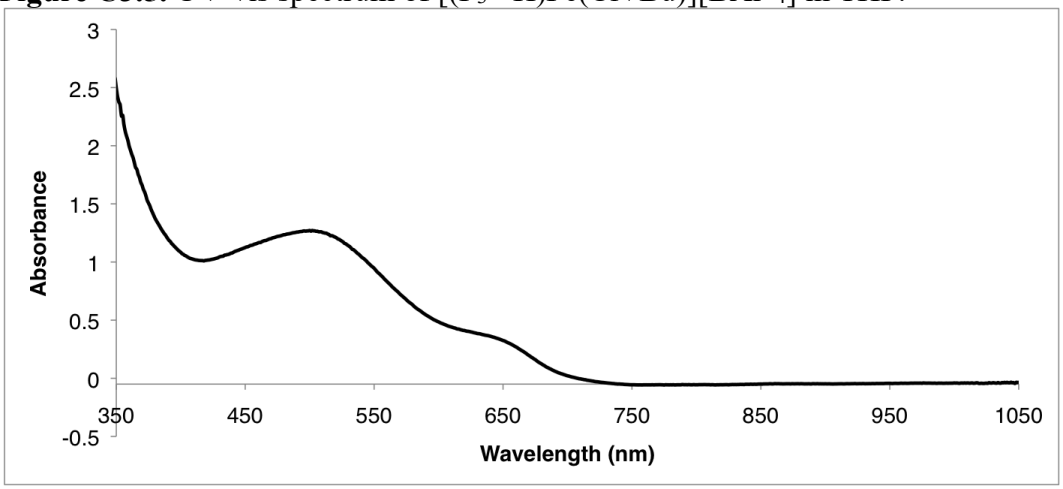

C4. Mössbauer Spectra

Figure C4.1. Mössbauer spectrum of $[P_3^B(\mu\text{-H})Fe(H)(N_2)][K_2(THF)_n]$ **3.2** collected at 80 K in THF ($\delta = 0.25$; $\Delta E_Q = 2.28$). The residual impurity signal ($\delta = 0.30$; $\Delta E_Q = 0.73$) is likely due to oxidation during sample preparation.

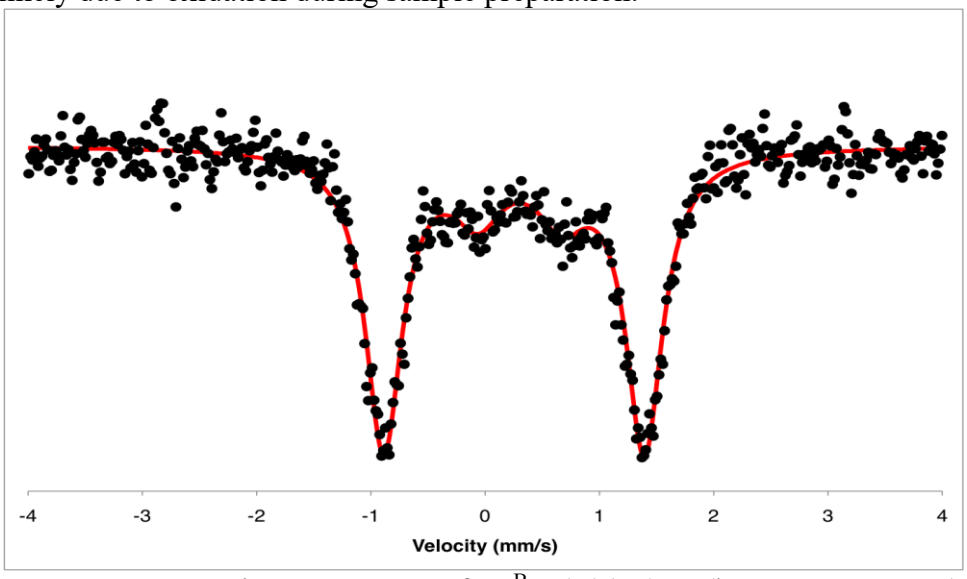

Figure C4.2. Mössbauer spectrum of $[P_3^BFe(H)(N_2)][K(benzo\text{-}15\text{-}crown\text{-}5)_2]$ **3.4** collected at 80 K in THF. ($\delta = 0.20$; $\Delta E_Q = 0.84$)

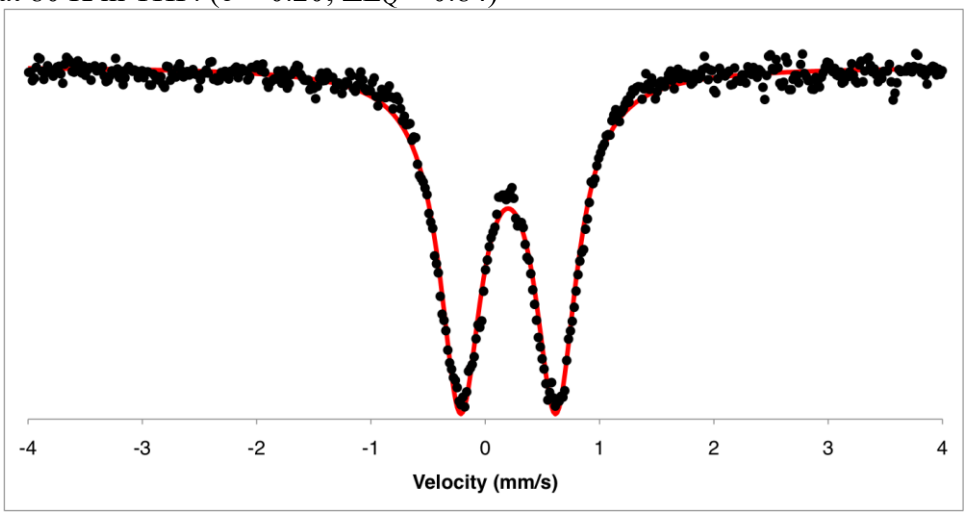

C5. Kinetic Experiments

For kinetic analysis of the N-H bond forming step in the transformation of **3.9** to **3.10**, solutions of **3.9** were prepared *in situ* at -78 °C according to the procedure detailed in chapter 3 and diluted to typical concentrations on the order of 5-9 mM, which allowed for convenient kinetic analysis by following the decay of the absorption at 660 nm ($\varepsilon \approx 240\ M^{-1}cm^{-1}$) in the UV-visible spectrum for the intermediate species **7**, which exhibited clean, isosbestic behavior. Following generation of the species **7** at low temperature, its clean preparation was confirmed by analysis of its UV-visible spectrum at -78 °C. Subsequently, the spectrometer cryostat was warmed to the desired reaction temperature (-15 - 20 °C) and the solutions were equilibrated to the reaction temperature over five minutes prior to initiating data collection. Attempts to obtain meaningful kinetic data at higher reaction temperatures were complicated by the competitive decay of the product **3.10**.

Because of our inability to isolate the starting material and products, extraction of rate constants from raw data was carried out using a method based on the use of difference equations.

For a general 1st order reaction:

a) $A_{\lambda,\infty} - A_{\lambda,t} = (A_{\lambda,\infty} - A_{\lambda,0})e^{-kt}$
b) $A_{\lambda,\infty} - A_{\lambda,t+\Delta t} = (A_{\lambda,\infty} - A_{\lambda,0})e^{-k(t+\Delta t)}$

Taking the difference gives:

$A_{\lambda,t+\Delta t} - A_{\lambda,t} = (A_{\lambda,\infty} - A_{\lambda,0})e^{-kt}(1-e^{-k\Delta t})$

So, with minor manipulation:

$A_{\lambda,t+\Delta t} = A_{\lambda,t}e^{-k\Delta t} + A_{\lambda,\infty}(1-e^{-k\Delta t})$

And a plot of $A_{\lambda,t}$ vs. $A_{\lambda,t+\Delta t}$ is linear with a slope of $e^{-k\Delta t}$: $k = -\ln(m)/(\Delta t)$

The linearity of the data extracted using this analysis confirms the first order nature of this transformation, with significant deviations from linearity expected for higher order reactions.

Figure C5.1. Representative UV-Vis spectrum for transformation of 3.9 to 3.10 (10 °C; Δt = 360).

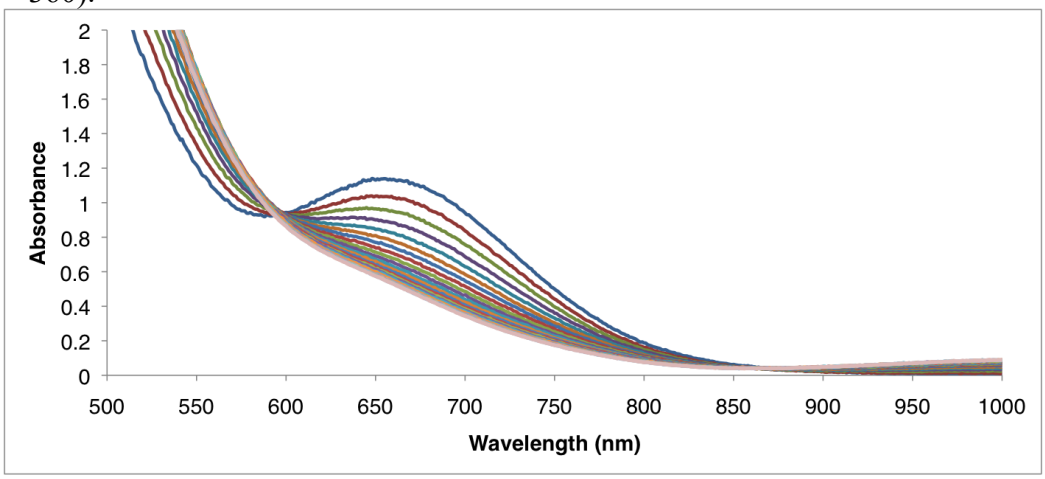

Figure C5.2. Plot of $A_{\lambda,t}$ vs. $A_{\lambda,t+\Delta t}$ at -15 °C (Run 1; 660 nm; Δt = 600 s; k = 2.40 x 10^{-5} s^{-1}).

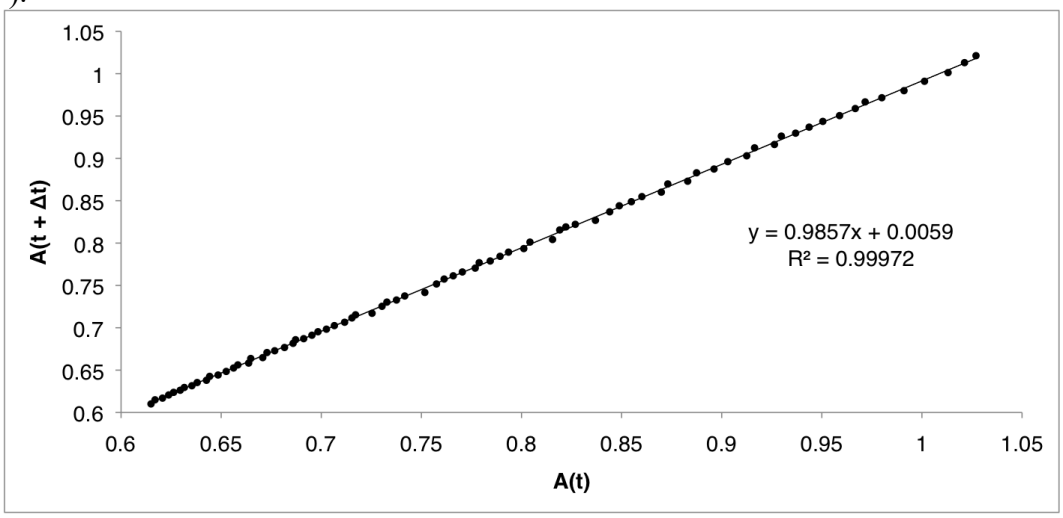

Figure C5.3. Plot of $A_{\lambda,t}$ vs. $A_{\lambda,t+\Delta t}$ at -15 °C (Run 2; 660 nm; Δt = 600 s; k = 2.77 x 10^{-5} s^{-1}).

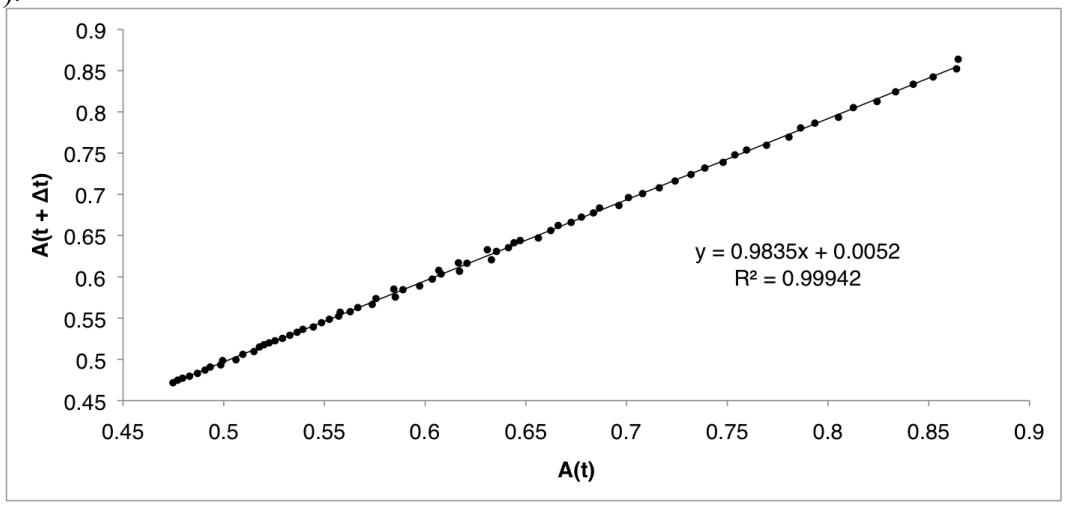

Figure C5.4. Plot of $A_{\lambda,t}$ vs. $A_{\lambda,t+\Delta t}$ at -10 °C (Run 1; 660 nm; Δt = 300 s; k = 4.23 x 10^{-5} s^{-1}).

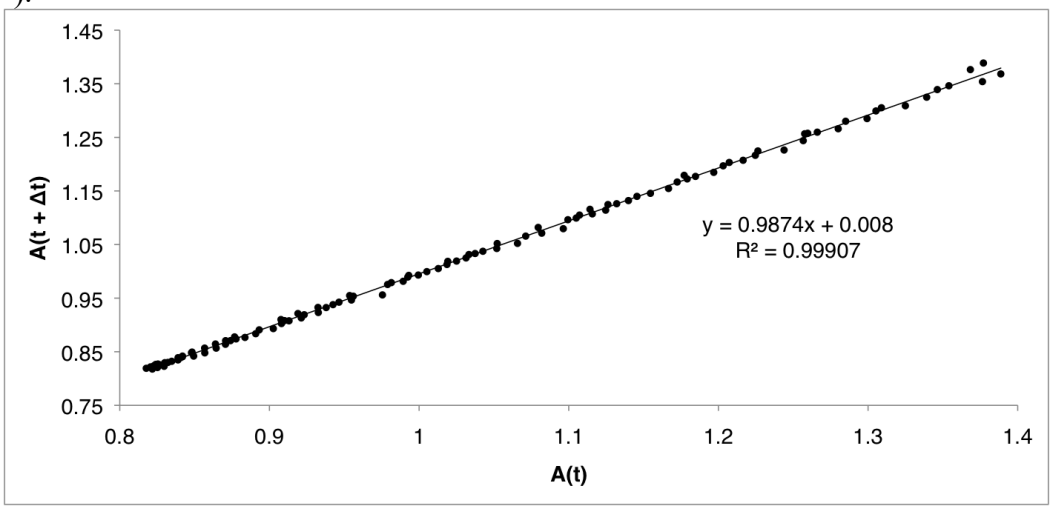

Figure C5.5. Plot of $A_{\lambda,t}$ vs. $A_{\lambda,t+\Delta t}$ at -10 °C (Run 2; 660 nm; Δt = 600 s; k = 4.84 x 10^{-5} s^{-1}).

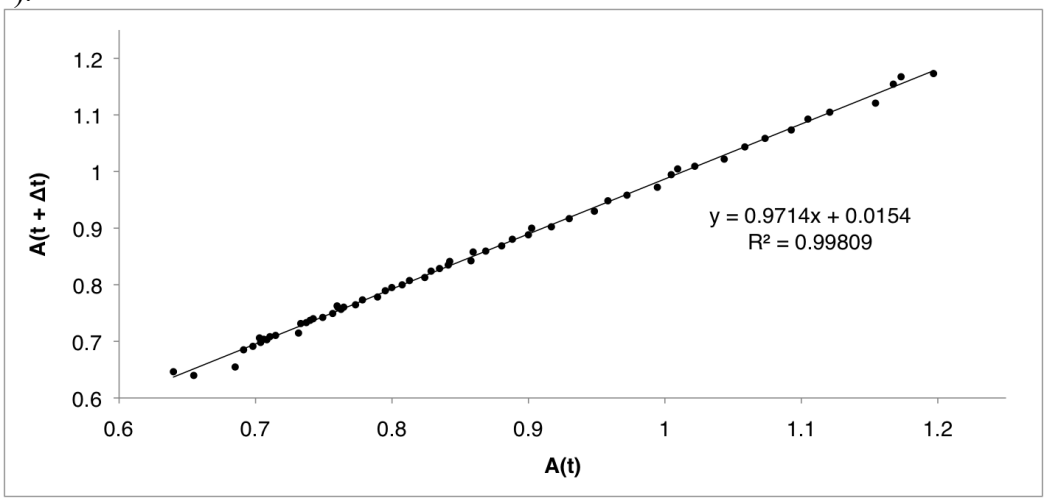

Figure C5.6. Plot of $A_{\lambda,t}$ vs. $A_{\lambda,t+\Delta t}$ at -5 °C (Run 1; 660 nm; Δt = 300 s; k = 1.05 x 10^{-4} s^{-1}).

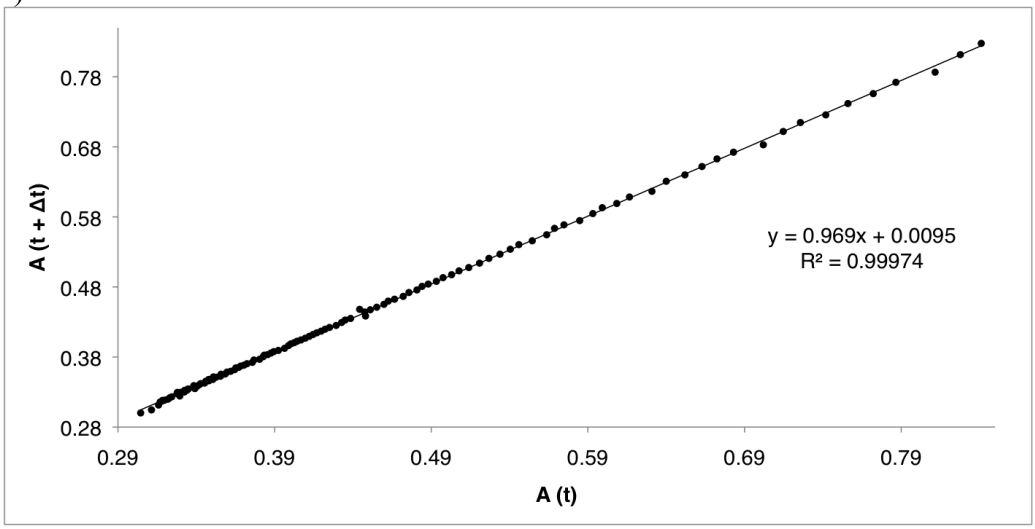

Figure C5.7. Plot of $A_{\lambda,t}$ vs. $A_{\lambda,t+\Delta t}$ at -5 °C (Run 2; 660 nm; Δt = 300 s; k = 8.51 x 10^{-5} s^{-1}).

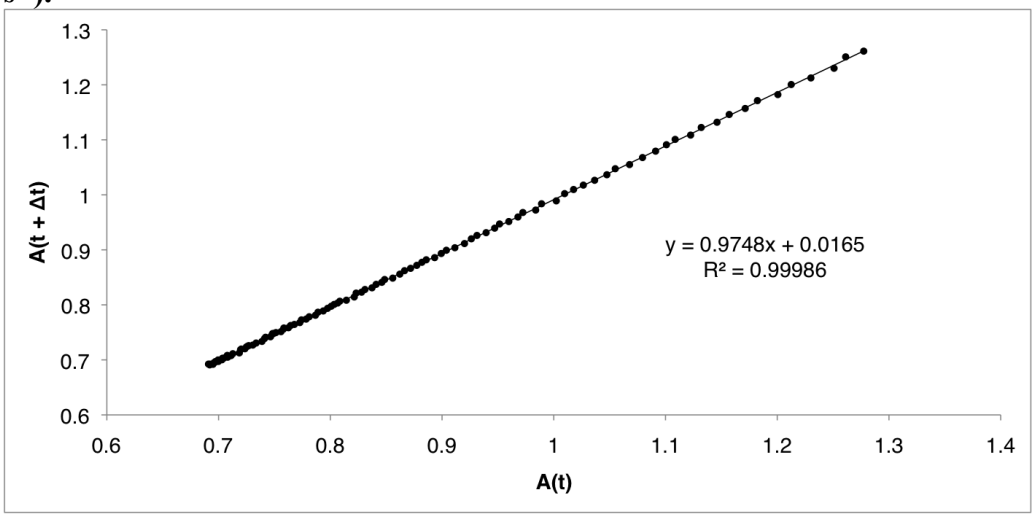

Figure C5.8. Plot of $A_{\lambda,t}$ vs. $A_{\lambda,t+\Delta t}$ at 0 °C (Run 1; 660 nm; Δt = 120 s; k = 1.65 x 10^{-4} s^{-1}).

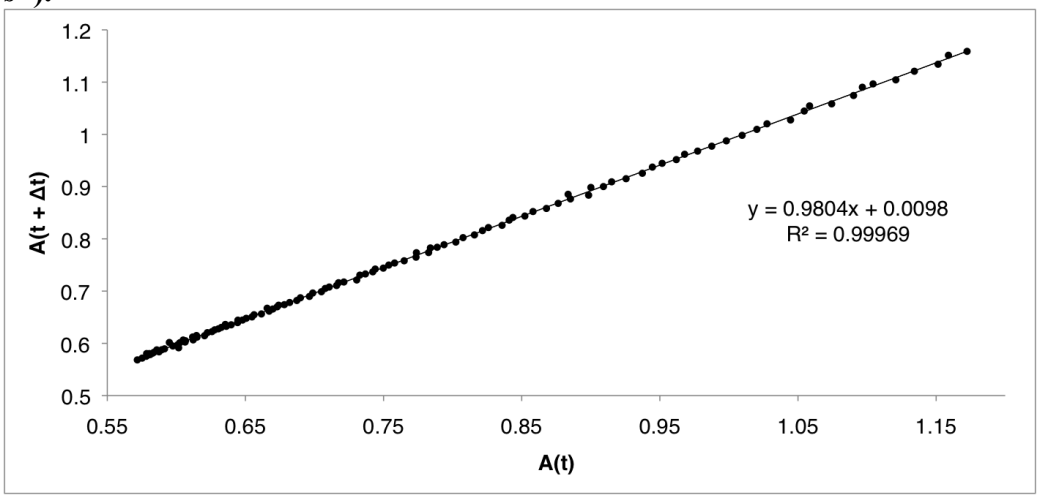

Figure C5.9. Plot of $A_{\lambda,t}$ vs. $A_{\lambda,t+\Delta t}$ at 0 °C (Run 2; 660 nm; Δt = 300 s; k = 1.54 x 10^{-4} s^{-1}).

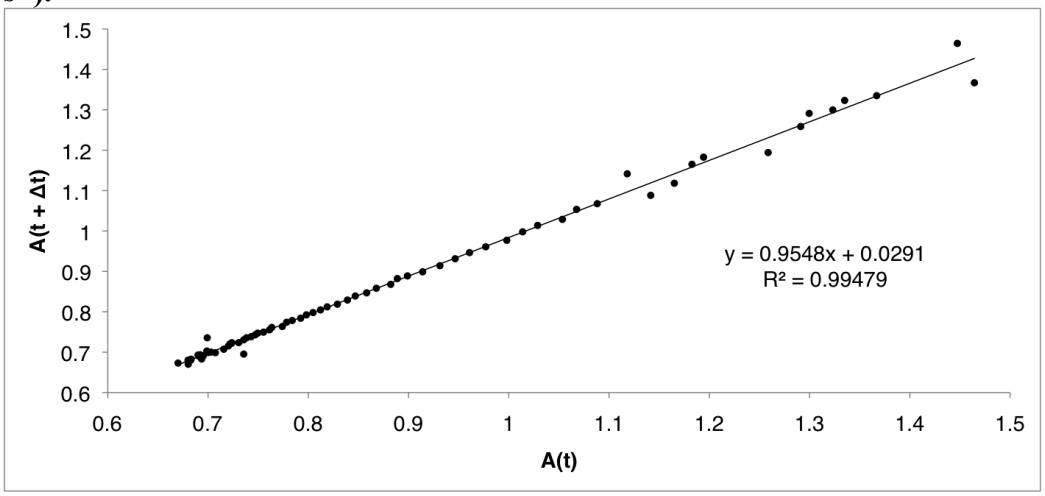

Figure C5.10. Plot of $A_{\lambda,t}$ vs. $A_{\lambda,t+\Delta t}$ at 5 °C (Run 1; 660 nm; Δt = 120 s; k = 3.00 x 10^{-4} s^{-1}).

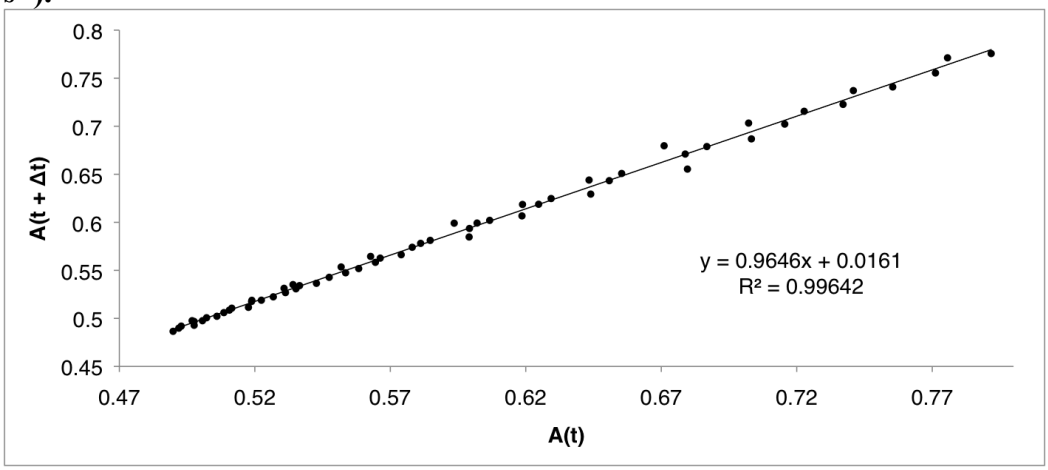

Figure C5.11. Plot of $A_{\lambda,t}$ vs. $A_{\lambda,t+\Delta t}$ at 5 °C (Run 2; 660nm; Δt = 120 s; k = 3.29 x 10^{-4} s^{-1}).

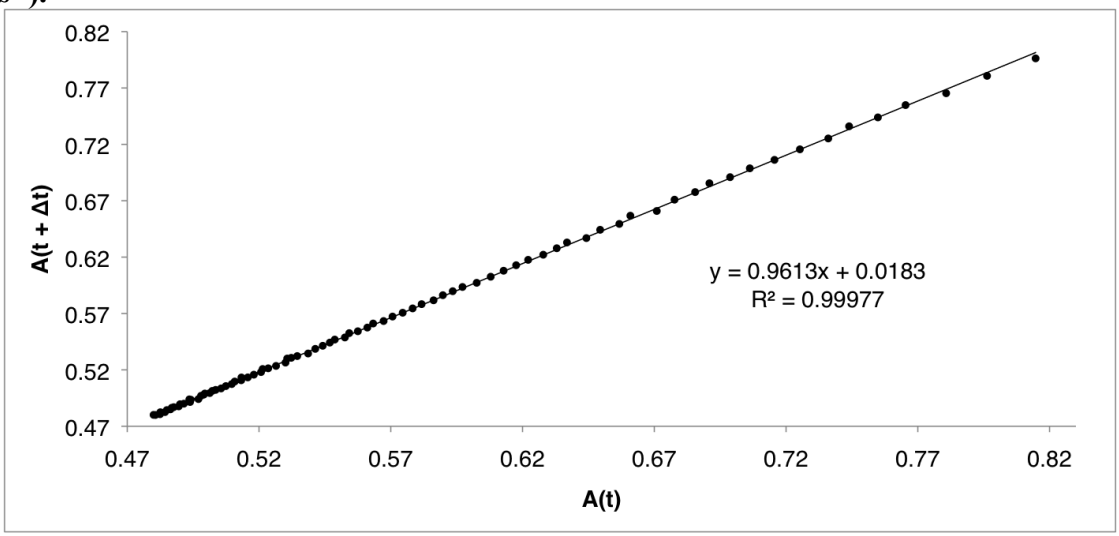

Figure C5.12. Plot of $A_{\lambda,t}$ vs. $A_{\lambda,t+\Delta t}$ at 10 °C (Run 1; 660nm; Δt = 360 s; k = 4.98 x 10^{-4} s^{-1}).

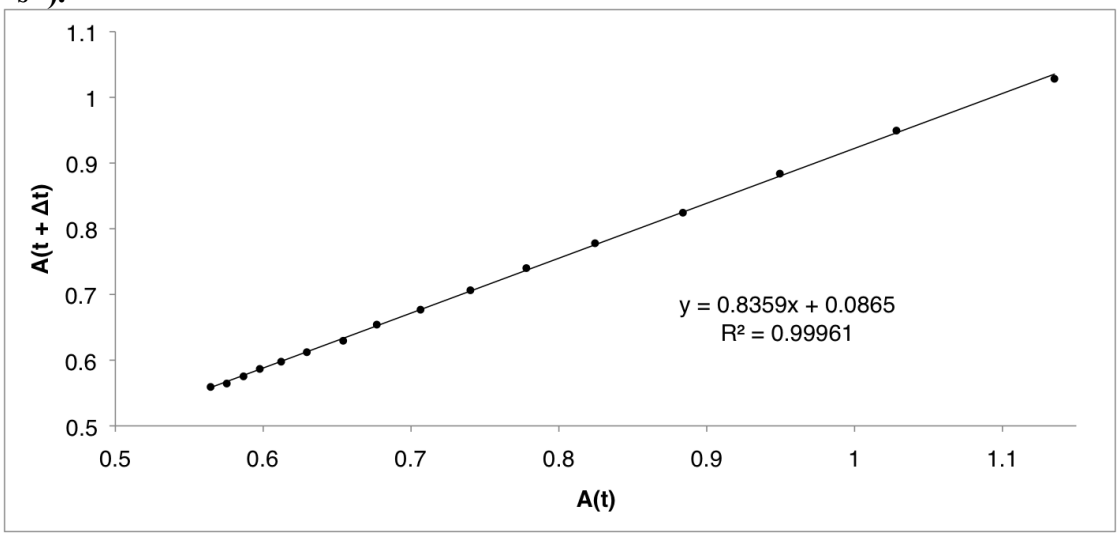

Figure C5.13. Plot of $A_{\lambda,t}$ vs. $A_{\lambda,t+\Delta t}$ at 10 °C (Run 2; 660nm; Δt = 120 s; k = 4.20 x 10^{-4} s^{-1}).

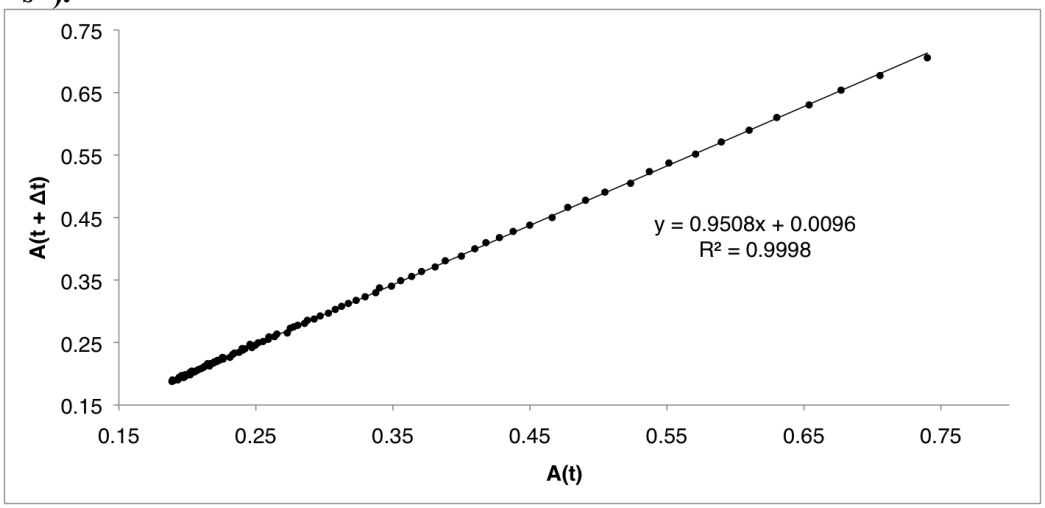

Figure C5.14. Plot of $A_{\lambda,t}$ vs. $A_{\lambda,t+\Delta t}$ at 15 °C (Run 1; 660nm; Δt = 60 s; k = 8.60 x 10^{-4} s^{-1}).

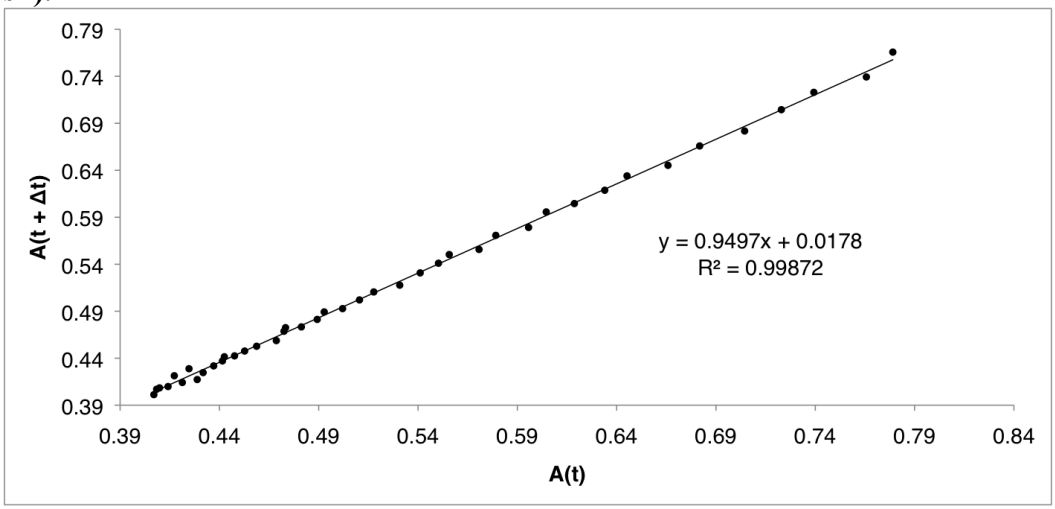

Figure C5.15. Plot of $A_{\lambda,t}$ vs. $A_{\lambda,t+\Delta t}$ at 15 °C (Run 2; 660nm; Δt = 60 s; k = 8.15 x 10^{-4} s^{-1}).

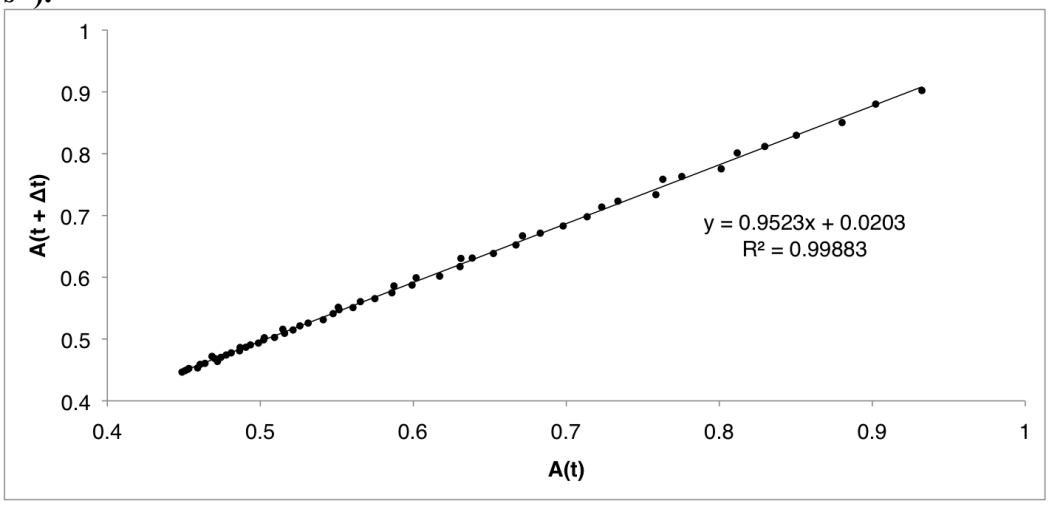

Figure C5.16. Plot of $A_{\lambda,t}$ vs. $A_{\lambda,t+\Delta t}$ at 20 °C (Run 1; 660nm; Δt = 120 s; k = 1.40 x 10^{-3} s^{-1}).

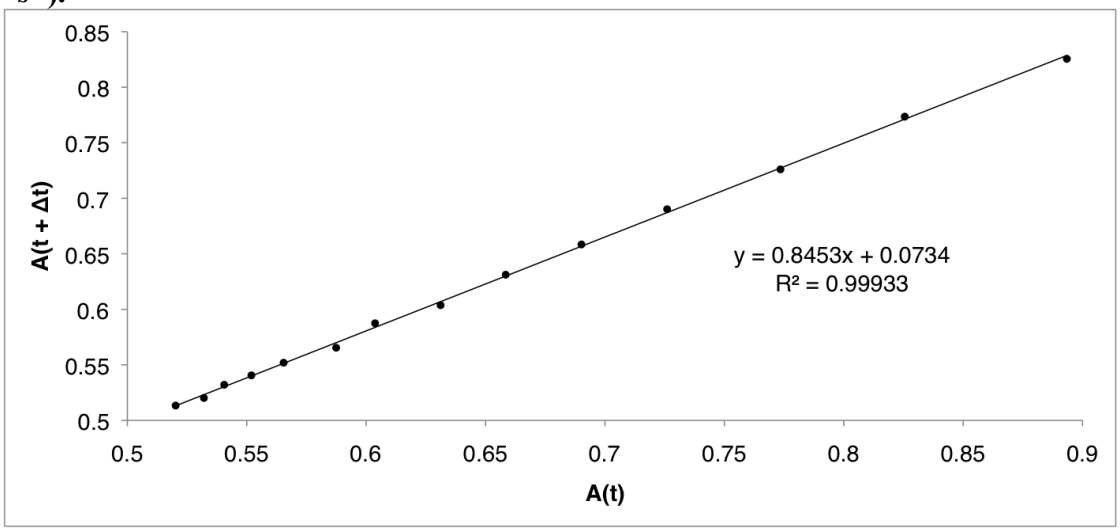

Figure C5.17. Plot of $A_{\lambda,t}$ vs. $A_{\lambda,t+\Delta t}$ at 20 °C (Run 2; 660nm; Δt = 60 s; k = 1.68 x 10^{-3} s^{-1}).

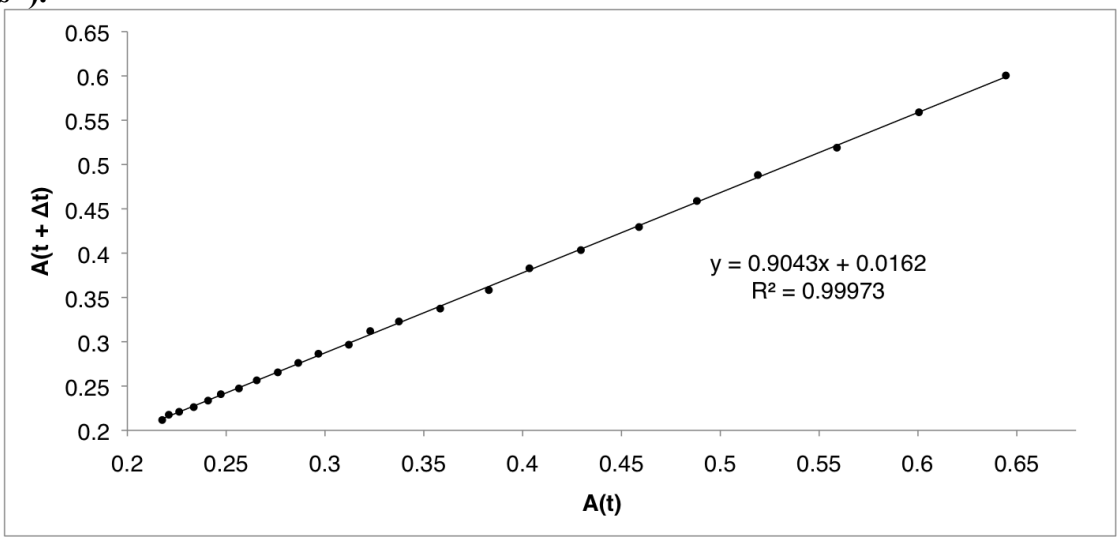

Table C5.1. Rate Constants for the Decay of 3.9 to 3.10

Temperature (K)	Run 1 (s^{-1})	Run 2 (s^{-1})	Average (s^{-1})	Std. Dev. (s^{-1})
258	2.40 x 10^{-5}	2.77 x 10^{-5}	2.59 x 10^{-5}	2.63 x 10^{-6}
263	4.23 x 10^{-5}	4.84 x 10^{-5}	4.54 x 10^{-5}	4.31 x 10^{-6}
268	1.05 x 10^{-4}	8.51 x 10^{-5}	9.50 x 10^{-5}	1.41 x 10^{-5}
273	1.65 x 10^{-4}	1.54 x 10^{-4}	1.60 x 10^{-4}	7.78 x 10^{-6}
278	3.00 x 10^{-4}	3.29 x 10^{-4}	3.15 x 10^{-4}	2.02 x 10^{-5}
283	4.98 x 10^{-4}	4.20 x 10^{-4}	4.59 x 10^{-4}	5.52 x 10^{-5}
288	8.60 x 10^{-4}	8.15 x 10^{-4}	8.37 x 10^{-4}	3.22 x 10^{-5}
293	1.40 x 10^{-3}	1.68 x 10^{-3}	1.54 x 10^{-3}	1.98 x 10^{-4}

Figure C5.18. Eyring Plot for the Decay of 3.9 to 3.10. ($\Delta H^{\ddagger}$ = 16.8; $\Delta S^{\ddagger}$ = -14.0).

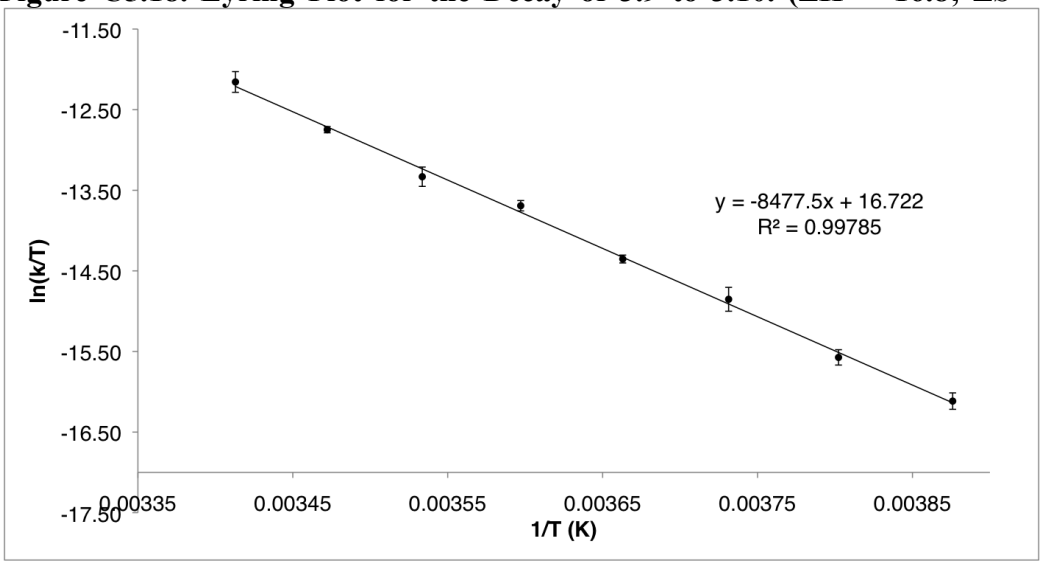

Figure C5.19. Plot of $A_{\lambda,t}$ vs. $A_{\lambda,t+\Delta t}$ at 10 °C (Run 1; 660nm; D_2; Δt = 120 s; k = 3.47 x 10^{-4} s^{-1}).

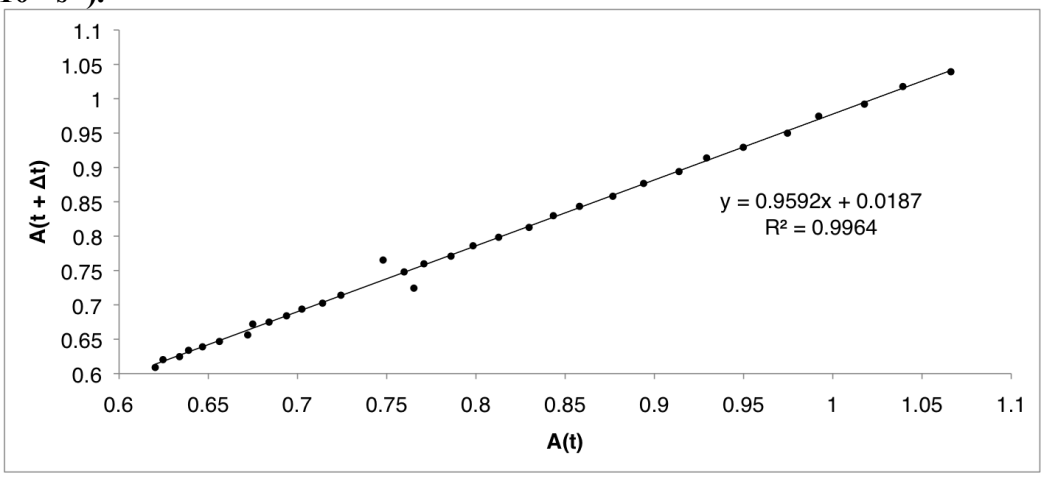

Figure C5.20. Plot of $A_{\lambda,t}$ vs. $A_{\lambda,t+\Delta t}$ at 10 °C (Run 2; 660nm; D_2; Δt = 120 s; k = 3.47 x 10^{-4} s^{-1}).

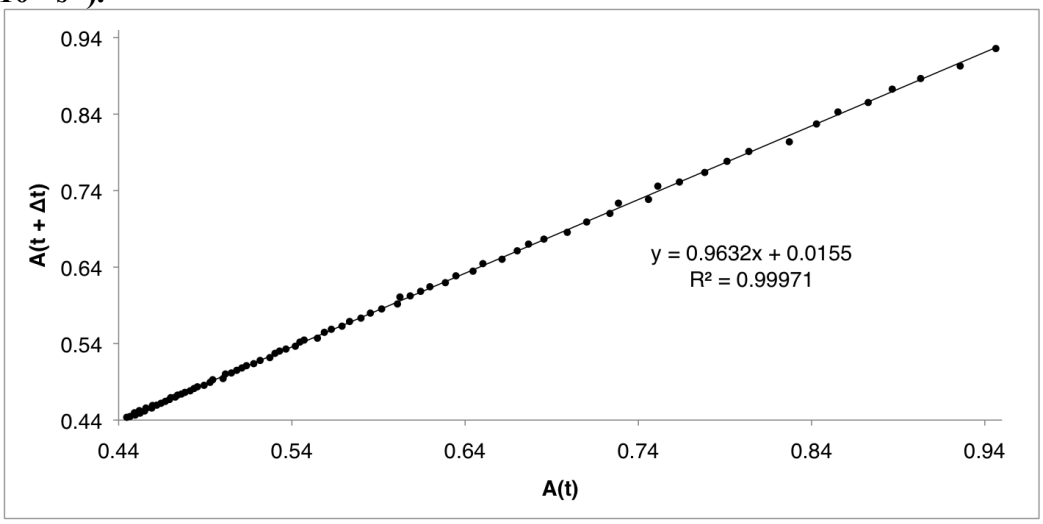

Table C5.2. Rate Constants for the Decay of 7 to 8 for Unlabeled and D_2-Labeled Complexes

	Run 1 (s^{-1})	Run 2 (s^{-1})	Average (s^{-1})
H_2 (Unlabeled)	4.98×10^{-4}	4.20×10^{-4}	4.59×10^{-4}
D_2 (Labeled)	3.47×10^{-4}	3.12×10^{-4}	3.30×10^{-4}
KIE			1.39

C6. Additional Experiments

C6.1. Reactivity of $[P_3^BFe(N_2)(H)][K(benzo\text{-}15\text{-}crown\text{-}5)_2]$ 3.4

Oxidation: Treatment of the anionic hydride complex **3.4** with $[Cp_2Co][PF_6]$ at -78 °C in THF provides access to a new doublet species, which we have tentatively assigned as $(P_3^B\text{-}H)Fe(N_2)$ **3.5**. Attempts to crystallographically characterize either of these neutral complexes have been unsuccessful, with problematic twinning reported in the case of complex **3**[Error! Bookmark not defined.] and the complex generated upon oxidation of **4** observed to decay to $P_3^BFe(N_2)$ in solution over time.

Figure C6.1.1. ^1H NMR (C_6D_6; 300 MHz) spectrum generated from the oxidation of **4** with $[Cp_2Co][PF_6]$.

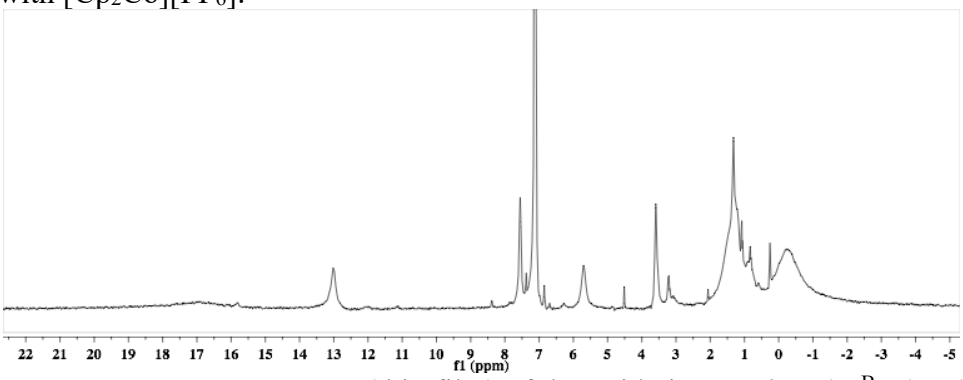

Figure C6.1.2. IR spectrum (thin film) of the oxidation product $(P_3^B\text{-}H)Fe(N_2)$ **3.5**.

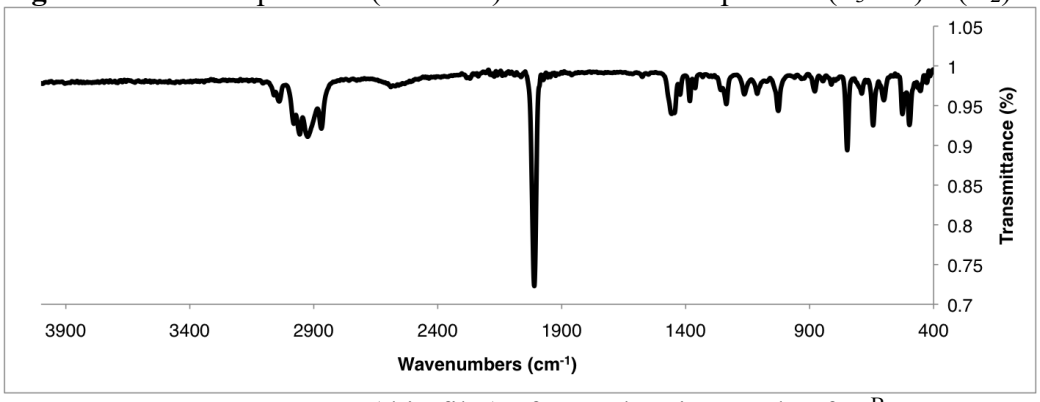

Figure C6.1.3. IR spectrum (thin film) of an authentic sample of $P_3^BFeN_2$ **3.3**.

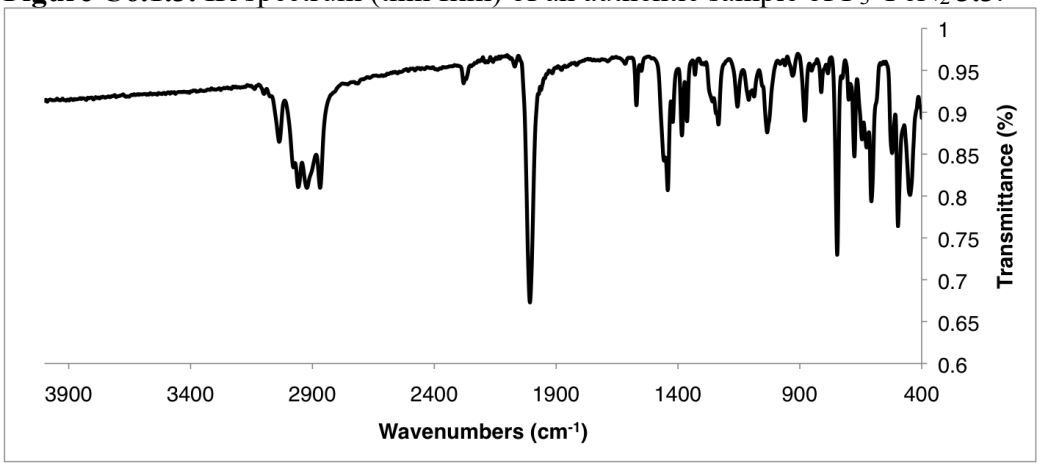

Figure C6.1.4. Mössbauer spectrum of (P_3^B-H)Fe(N_2) **3.5** generated *in situ* ($\delta = 0.42$; $\Delta E_Q = 0.93$).

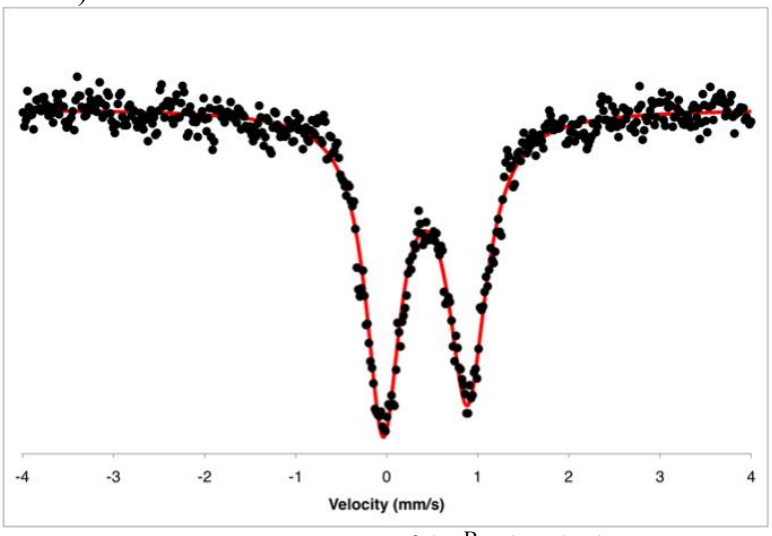

Figure C6.1.5. EPR spectrum of (P_3^B-H)Fe(N_2) **3.5** generated *in situ.*

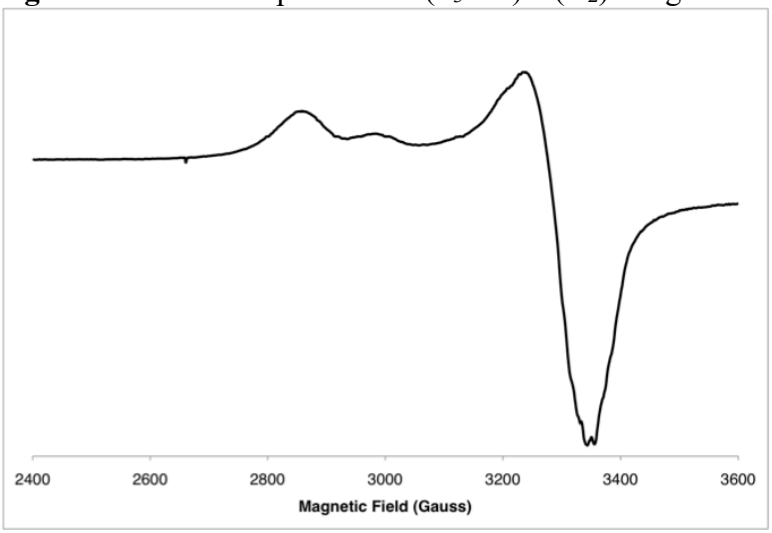

Functionalization: Treatment of the monoanionic complex **4** with a stoichiometric equivalent of trimethylsilyl triflate electrophile leads to the generation of a new species that can be observed at low temperature. By NMR spectroscopy, the product is a diamagnetic species that retains a hydride ligand that we have tentatively assigned as $P_3^BFe(H)(NNSiMe_3)$. This decays to a mixture of species in solution over time.

Figure C6.1.6. ^{1}H NMR spectrum obtained in THF-d_8 at -20 °C of the initial product **3.6** (500 MHz).

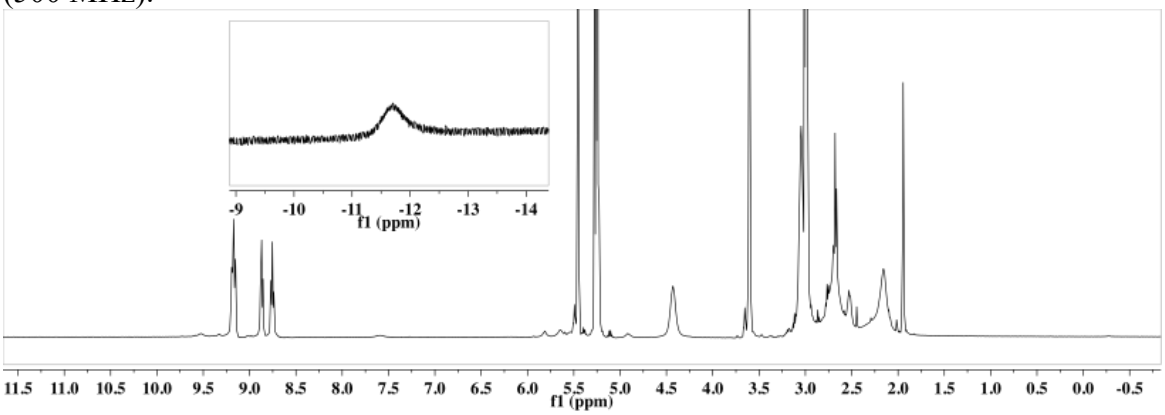

Figure C6.1.7. ^{1}H NMR spectrum (THF-d_8; 500 MHz) showing the mixture of products appearing in the spectrum after warming to room temperature.

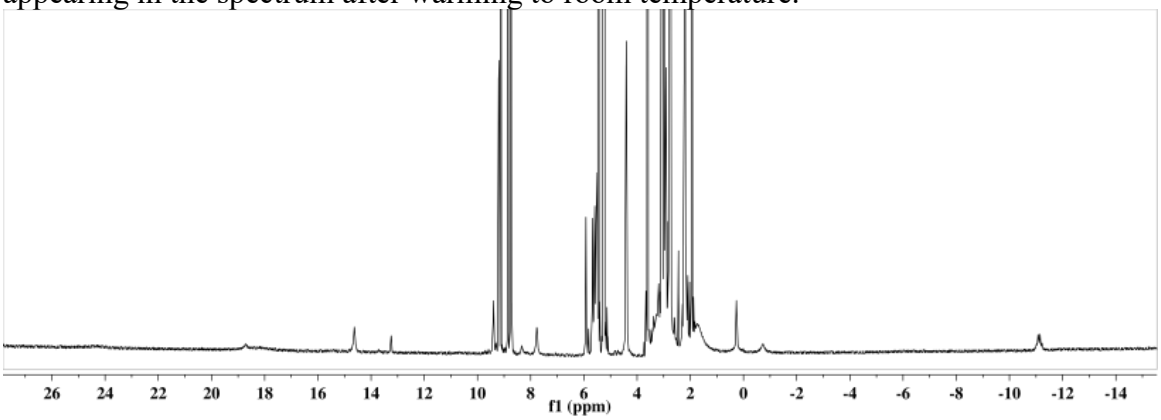

C6.2 Additional Experiments Relevant to N-H Bond Formation

Reaction of **3.12-CN^{t}Bu** with H_2: The complex **3.12-CN^{t}Bu** was prepared according to a previously reported protocol. A solution of this complex was prepared in benzene, degassed by one freeze-pump-thaw cycle, and exposed to an H_2 atmosphere overnight. After mixing for ~12 h, some decay of the starting material **3.12-CN^{t}Bu** was apparent, but the hydrazido(1-) complex **3.11** was not spectroscopically observed.

Figure C6.2.1. $^{31}P\{^{1}H\}$ NMR (C_6D_6; 162 MHz) Spectrum of **3.12-CN^{t}Bu** as prepared prior to exposure to H_2.

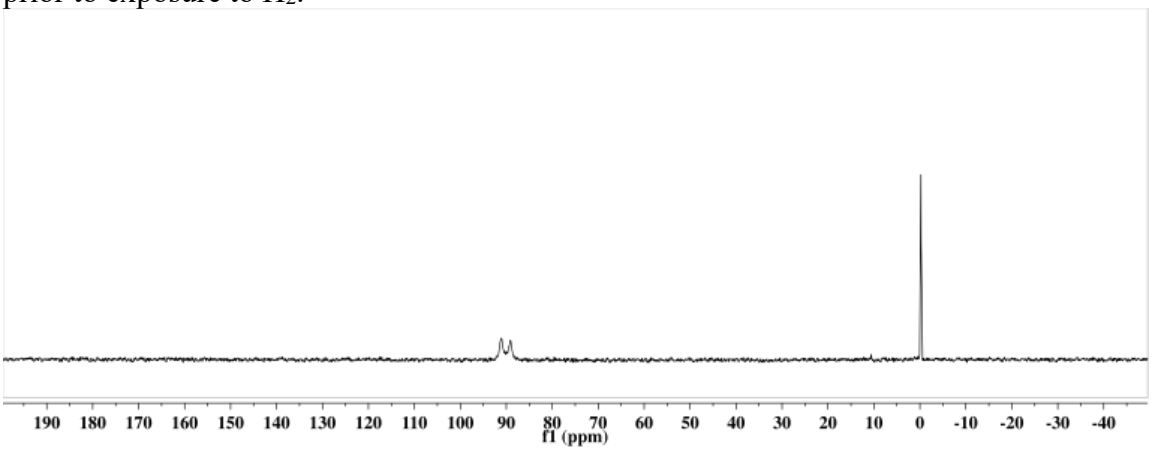

Figure C6.2.2. ^{1}H NMR (C_6D_6; 400 MHz) spectrum of **3.12-CN^{t}Bu** as prepared prior to exposure to H_2 with a minor paramagnetic impurity.

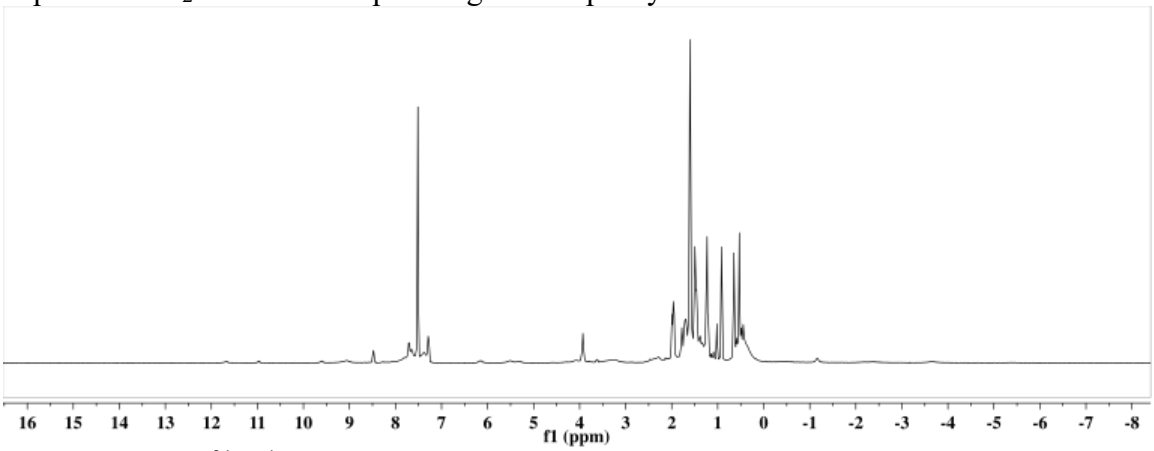

Figure C6.2.3. $^{31}P\{^{1}H\}$ spectrum of **3.12-CN^{t}Bu** after stirring under an H_2 atmosphere overnight. Starting material is observed with a minor amount of a decay product (likely P_3^B(μ-H)Fe(H)(CN^{t}Bu)) and no identifiable **3.11**.

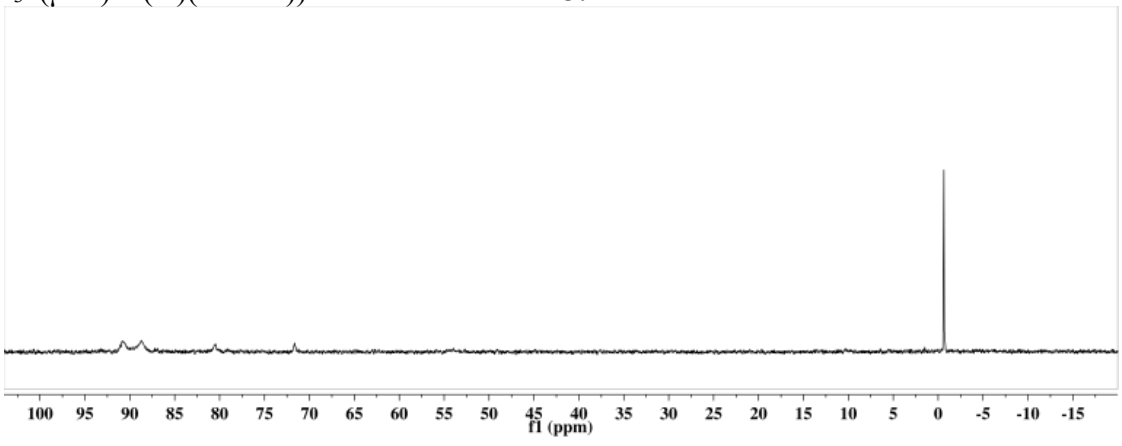

Figure C6.2.4. ^{1}H NMR (C_6D_6; 400 MHz) spectrum of **3.12-CN^{t}Bu** after stirring under an H_2 atmosphere overnight. Starting material is observed along with products of decay including new paramagnetic specie(s) and P_3^B(μ-H)Fe(H)(CN^{t}Bu).

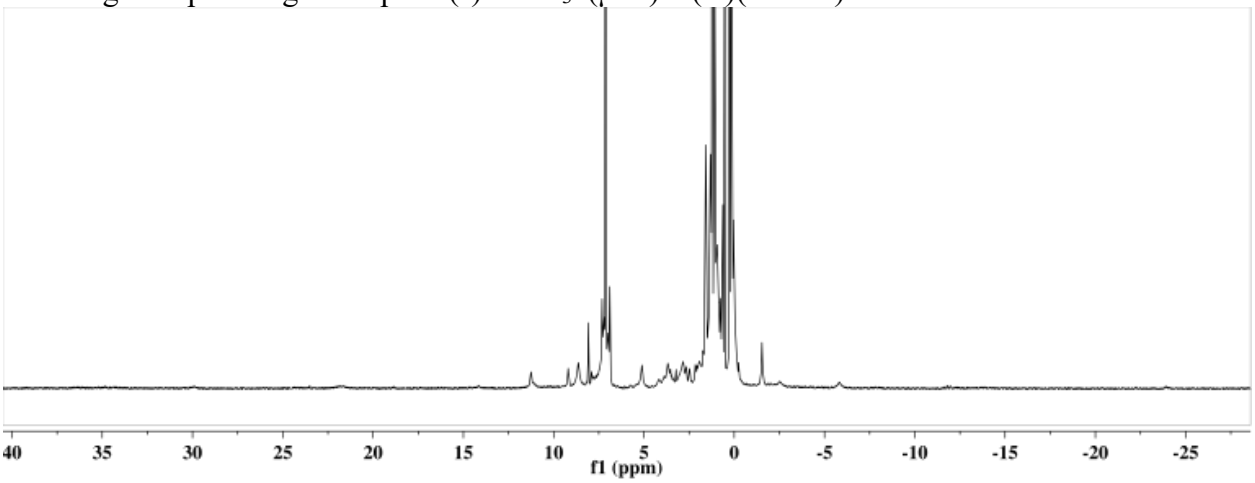

Transformation of **3.9** to **3.11** under a D_2 Atmosphere: Complex **3.9** (0.064 mmol) was prepared in solution at -78 °C under an N_2 atmosphere as above. This solution was transferred to a Schlenk tube with CN^{t}Bu (0.320 mmol, 5 equiv) added. The solution was frozen, the headspace was removed and backfilled with an atmosphere of D_2 and the mixture was thawed and allowed to warm to room temperature. The mixture was degassed by three freeze-pump-thaw cycles and the resulting solution was worked up according to the standard protocol (above). Examination of the product **3.11** showed no incorporation of deuterium by IR or NMR spectroscopy.

Figure C6.2.5. IR spectra comparing authentic samples of unlabeled **3.11** (top), labeled **3.11-D$_2$** (middle), and the product mixture generated from unlabeled **3.9** under a D_2 atmosphere (bottom). Blue arrows highlight the positions of the N-H and B-H-Fe stretches and red arrows highlight the positions of the N-D and B-D-Fe stretches, which are absent in the spectrum of the reaction nmixture.

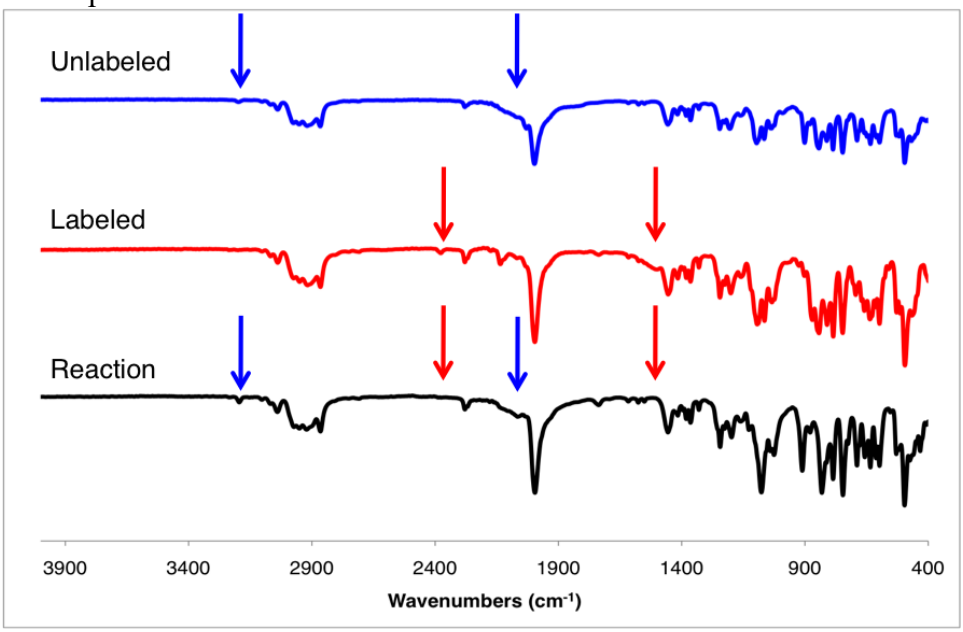

Alternative approaches to the release of N-fixed products:
In all cases, the disilylhydrazido(1-) complex **3.11** was prepared according to the procedure above. Quantification of liberated N-fixed products was done using the protocol described above for colorimetric detection of hydrazine and ammonia. Because the Fe-containing products of these reactions are ill-defined, some of the N-fixed products of these reactions may be derived from the HCl protonolysis step.

Thermolysis: Isolated **3.11** was dissolved in benzene and heated at 60 °C in a sealed Schlenk tube overnight, which resulted in complete consumption of the starting material. Fe containing products from these reactions could not be identified. (Run 1: NH_3 21%, N_2H_4 18%; Run 2: NH_3 23%; N_2H_4 20%)

Figure C6.2.6. Representative ^1H NMR spectrum generated from these reaction mixtures.

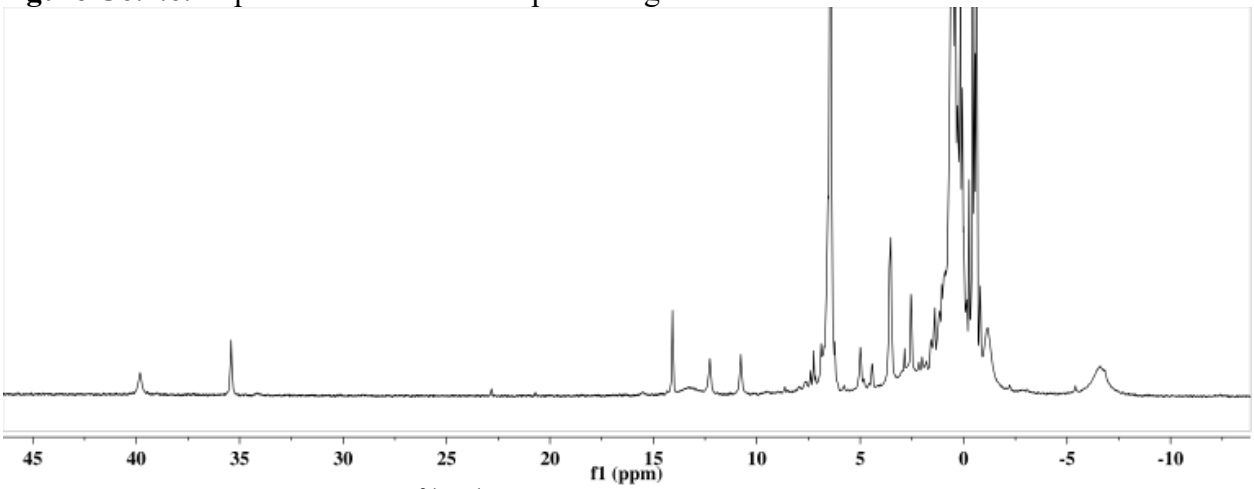

Figure C6.2.7. Corresponding $^{31}P\{^1H\}$ spectrum with resonances consistent with the presence of free phosphine species

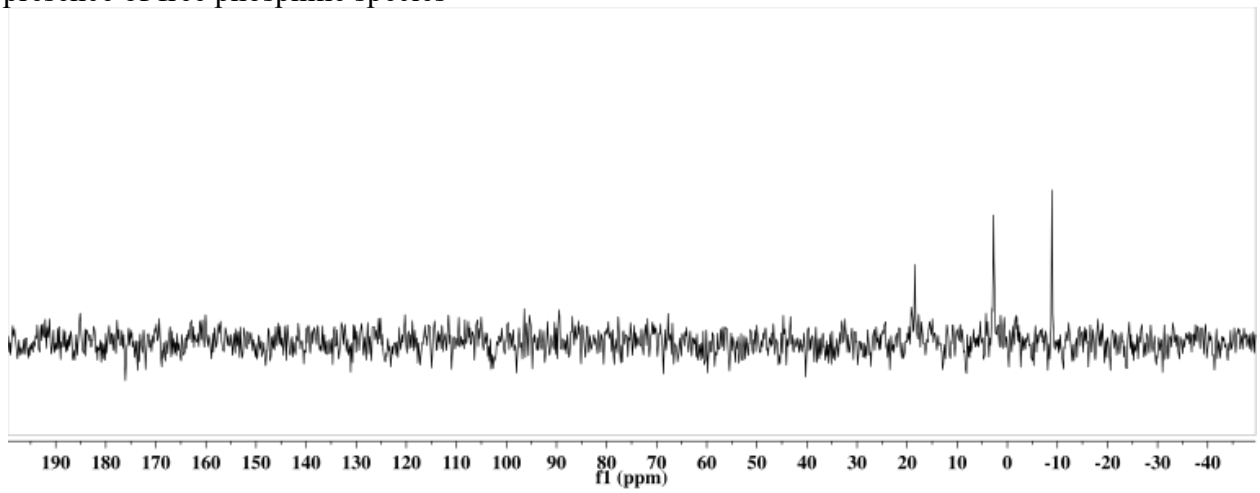

Thermolysis with additives: These reactions were analogous to the thermolysis reactions above, but with additional reagents added to the reaction mixtures. These additives did not appear to substantially perturb the product mixtures that were obtained.

Under an H_2 atmosphere: NH_3 12%, N_2H_4 28%
$PhSiH_3$ (5 equiv) added: NH_3 19%, N_2H_4 26%

Direct reaction of **3.10** with acid: We also explored the reactivity of **3.10** as generated *in situ*, towards exogenous acid. For the second run, crude **3.10** was isolated after stirring at room temperature by removing the solvent and extraction into pentane prior to treatment with acid. (Run 1: NH_3 8%, N_2H_4 42.5%; Run 2: 3.3%, N_2H_4: 47.6%).

Photolysis of **3.11**: Irradiation of a benzene solution of **3.11** with a Hg lamp at room temperature, resulted in the generation of species that were observed as the terminal product(s) of the thermal decay of **3.10**, consistent with the photodissociation of the CN′Bu ligand.

Figure C6.2.7. Terminal product mixture observed by ^{1}H NMR upon thermal decay of complex **3.10**.

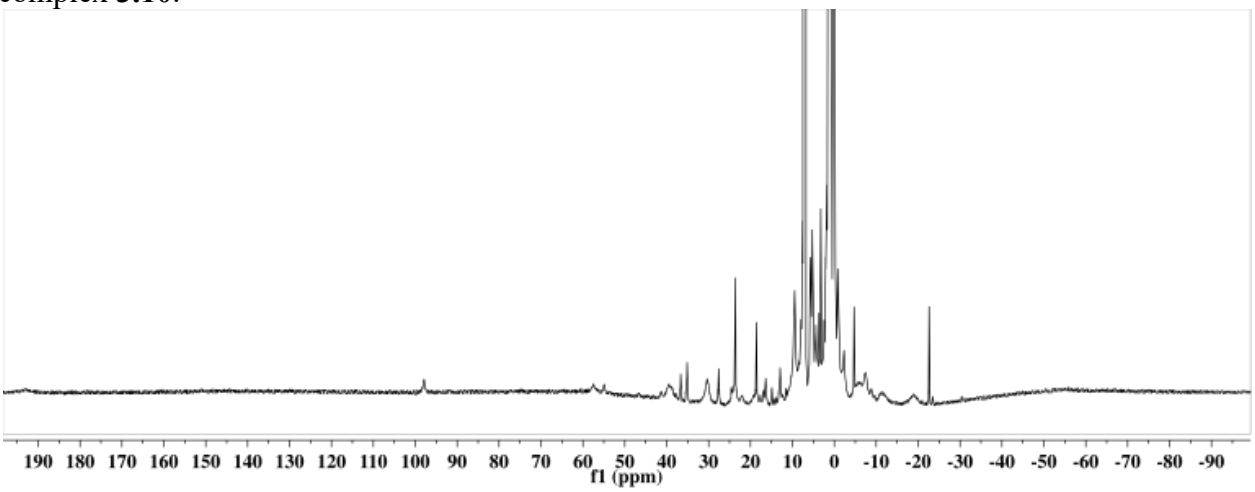

Figure C6.2.8. Product mixture observed by ^{1}H NMR upon Hg lamp irradiation of complex **3.10**.

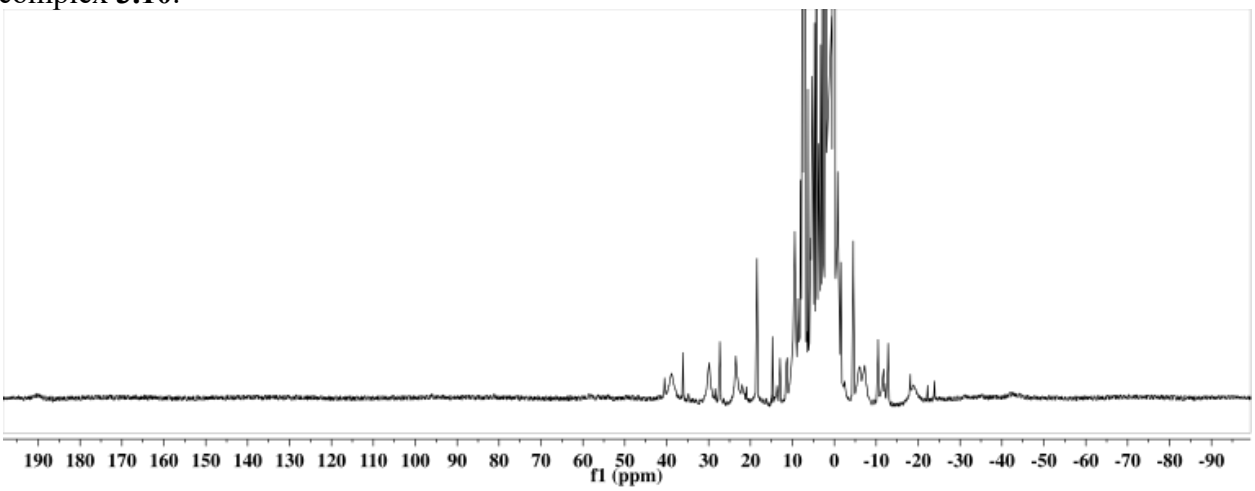

C7. Crystallographic Details

	Dianion 3.2	Monoanion 3.4	Diazenido 3.7	Hydrazido(1-) 3.11	CN^{t}Bu H cation
Crystal system	Monoclinic	Monoclinic	Triclinic	Orthorhombic	Monoclinic
Crystal size (mm)	0.05 x 0.21 x 0.22	0.18 x 0.20 x 0.28	0.11 x 0.20 x 0.27	0.11 x 0.20 x 0.28	0.04 x 0.25 x 0.26
Formula	$C_{48}H_{86}BFeK_2N_2O_6P_3$	$C_{64}H_{95}BFeKN_2O_{10}P_3$	$C_{49}H_{85}BFeKN_2OP_3Si$	$C_{47}H_{81}BFeN_3P_3Si_2$	$C_{79}H_{91}B_2F_{24}FeNP_3$
Formula weight (g/mol)	1024.95	1251.08	944.99	903.90	1680.95
Space group	P n	P 21/c	P -1	P b c a	P 21/c
a (Å)	12.8973(7)	11.3464(4)	12.4653(18)	11.3085(5)	27.577(3)
b (Å)	12.5342(6)	35.5398(14)	13.091(3)	24.2407(12)	15.5573(16)
c (Å)	17.2106(8)	15.8541(6)	21.997(3)	37.5101(18)	38.526(4)
α (deg)	90	90	97.411(10)	90	90
β (deg)	98.668(2)	90.839(1)	95.734(4)	90	100.8630(10)
γ (deg)	90	90	117.826(8)	90	90
Z	2	4	2	8	8
V (Å^3)	2750.4(2)	6392.5(4)	3095.1(10)	10282.5(8)	16232(3)
Indep. Reflections	14778	24375	25264	17889	34202
R(int)	3.84	8.08	5.22	7.14	7.15
R1	3.15	3.89	3.97	5.67	7.48
wR2	6.90	8.72	10.14	12.58	19.84
GOF	1.02	1.04	1.03	1.19	1.12

Remarks on Crystal Structures:

[P_3^B(μ-H)Fe(H)(N_2)][K_2(THF)$_n$] 3.2. This compound crystallizes with two coordinated K countercations stabilized by interactions with the Fe-coordinated N_2 ligand, three total DME solvent molecules, and with an arene ring of the supporting ligand. One of the six phosphine ^{i}Pr groups was modeled as disordered over two positions (59:41). Refinement of this disorder was aided by the application of SIMU and RIGU restraints.

[P_3^BFe(H)(N_2)][K(benzo-15-crown-5)$_2$] 3.4. This compound crystallizes as a monomeric species with a crown encapsulated counter-cation in the absence of solvent. Two of the six total phosphine ^{i}Pr groups were modeled in a related disorder over two positions (64:36). Additionally, one of the K-coordinated crown moieties was modeled as rotationally disordered over two positions (56:44). Application of RIGU restraints aided in the refinement of these disorders.

[P_3^B(μ-H)Fe(H)(NNSi^{i}Pr$_3$)][K(THF)] 3.7. This complex crystallizes with one K-coordinated THF molecule and additional disordered solvent molecules in the asymmetric unit. The residual electron density associated with the disordered solvent was treated using SQUEEZE. The THF molecule was modeled as disordered over two positions (59:41) and this refinement was aided by RIGU restraints. One of the Si ^{i}Pr groups was modeled as disordered over two positions (77:23).

P_3^B(μ-H)Fe(NHN(Si(Me$_2$)CH$_2$CH$_2$SiMe$_2$))(CN^{t}Bu) 3.11. This compound crystallizes in the absence of solvent.

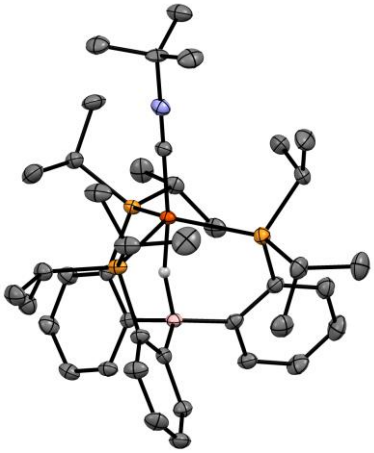

Figure C7.1. Representative structure of $[P_3{}^B(\mu\text{-H})Fe(CN^tBu)][B(C_8H_3F_6)_4]$ with displacement ellipsoids shown at 50% probability, with an additional, similar structure found in the asymmetric unit. C-bound H-atoms, solvent molecules and $B(C_8H_3F_6)_4$ counterions are omitted for clarity.

$[P_3{}^B(\mu\text{-H})Fe(CN^tBu)][B(C_8H_3F_6)_4]$. This compound crystallizes with two molecules in the asymmetric unit and two fully occupied cocrystallized pentane molecules and a third partially occupied pentane moiety (49%). The core iron structures had no disorder, but 7 of the 16 CF_3 groups were modeled as disordered over two positions ($BAr_4{}^F$ 2: 79:21, 91:9, 73:26, 76:24; $BAr_4{}^F$ 1: 75:25, 76:24, 54:46) and one of the pentane molecules was modeled as disordered over two positions (55:45). Refinement of these disorders was aided by the application of SIMU and RIGU restraints.

C8. Bond Distances and Angles

$[P_3^B(\mu\text{-H})Fe(H)(N_2)][K_2(THF)_n]$ 3.2.

Bond Distances (Å)		Bond Angles (degrees)	
Fe1-P1 (coord.)	2.1470(6)	P1-Fe1-P2	122.55(2)
Fe1-P2 (coord.)	2.1505(6)	Fe1-N1-N2	178.4(2)
Fe1-P3 (free)	4.5536(7)	B1-Fe1-N1	111.80(8)
Average Fe-P (coord.)	2.15	P1-Fe1-N1	124.03(7)
Fe1-N1	1.743(2)	P2-Fe1-N1	113.31(7)
Fe1-B1	2.749(3)		
Fe1-H1A-B1	1.69(3)		
Fe1-H	1.37(4)		
N1-N2	1.169(3)		

$[P_3^BFe(H)(N_2)][K(benzo\text{-}15\text{-}crown\text{-}5)_2]$ 3.4.

Bond Distances (Å)		Bond Angles (degrees)	
Fe1-P1	2.1786(4)	P1-Fe1-P2	106.44(2)
Fe1-P2	2.2225(4)	P2-Fe1-P3	104.55(2)
Fe1-P3	2.2151(5)	P1-Fe1-P3	139.95(3)
Average Fe-P	2.21	Fe1-N1-N2	177.0(1)
Fe1-N1	1.800(1)	B1-Fe1-N1	177.79(5)
Fe1-B1	2.289(1)	P1-Fe1-N1	97.84(4)
Fe1-H	1.46(2)	P2-Fe1-N1	100.80(4)
N1-N2	1.132(2)	P3-Fe1-N1	100.63(4)

$[P_3^B(\mu\text{-H})Fe(H)(NNSi^iPr_3)][K(THF)]$ 3.7.

Bond Distances (Å)		Bond Angles (degrees)	
Fe1-P1 (coord.)	2.2202(7)	P1-Fe1-P2	116.59(2)
Fe1-P2 (coord.)	2.21758(7)	Fe1-N1-N2	169.31(9)
Fe1-P3 (free)	4.4191(8)	B1-Fe1-N1	119.31(4)
Average Fe-P (coord.)	2.22	P1-Fe1-N1	125.04(4)
Fe1-N1	1.672(1)	P2-Fe1-N1	117.58(4)
Fe1-B1	2.791(1)	N1-N2-Si1	132.31(9)
Fe1-H1A-B1	1.8245		
Fe1-H	1.45(1)		
N1-N2	1.249(2)		

$P_3^B(\mu\text{-H})Fe(NHN(Si_2))(CN^tBu)$ 3.9.

Bond Distances (Å)		Bond Angles (degrees)	
Fe1-P1 (coord.)	2.227(1)	P1-Fe1-P2	112.84(3)
Fe1-P2 (coord.)	2.2338(7)	Fe1-N1-N2	145.8(1)
Fe1-P3 (free)	5.5746(8)	B1-Fe1-N1	92.39(7)
Average Fe-P (coord.)	2.23	P1-Fe1-N1	125.91(6)
Fe1-N1	1.824(2)	P2-Fe1-N1	115.86(6)
Fe1-B1	2.885(2)	P1-Fe1-C1	89.41(6)
Fe1-H1A-B1	1.9049	P2-Fe1-C1	97.38(6)
N1-H1	0.92(3)	C1-Fe1-N1	106.00(8)
N1-N2	1.404(2)	B1-Fe1-C1	161.47(7)
Fe1-C1	1.811(2)		

$[P_3^B(\mu\text{-H})Fe(CN^tBu)][B(C_8H_3F_6)_4]$.

Bond Distances (Å)		Bond Angles (degrees)	
Fe1-P1	2.390(1)	P1-Fe1-P2	117.24(5)
Fe1-P2	2.406(1)	P2-Fe1-P3	113.68(5)
Fe1-P3	2.392(1)	P1-Fe1-P3	115.03(5)
Fe2-P4	2.406(1)	P4-Fe2-P5	114.14(5)
Fe2-P5	2.398(1)	P5-Fe2-P6	113.84(5)
Fe2-P6	2.378(1)	P4-Fe2-P6	118.24(5)
Average Fe-P	2.395	P1-Fe1-C1	101.5(1)
Fe1-C1	1.869(4)	P2-Fe1-C1	102.2(1)
Fe2-C42	1.869(4)	P3-Fe1-C1	104.4(1)
Fe1-B1	2.763(5)	P4-Fe2-C42	103.8(1)
Fe2-B2	2.769(5)	P5-Fe2-C42	103.1(1)
Fe1-H1-B1	1.39(6)	P6-Fe2-C42	100.8(1)
Fe2-H2-B2	1.49(5)		

Appendix D

SUPPLEMENTARY DATA FOR CHAPTER 4

D1. NMR Spectra

P_2^PCoBr 4.1.

Figure D1.1. ^1H NMR spectrum (400 MHz, C_6D_6) of **4.1**.

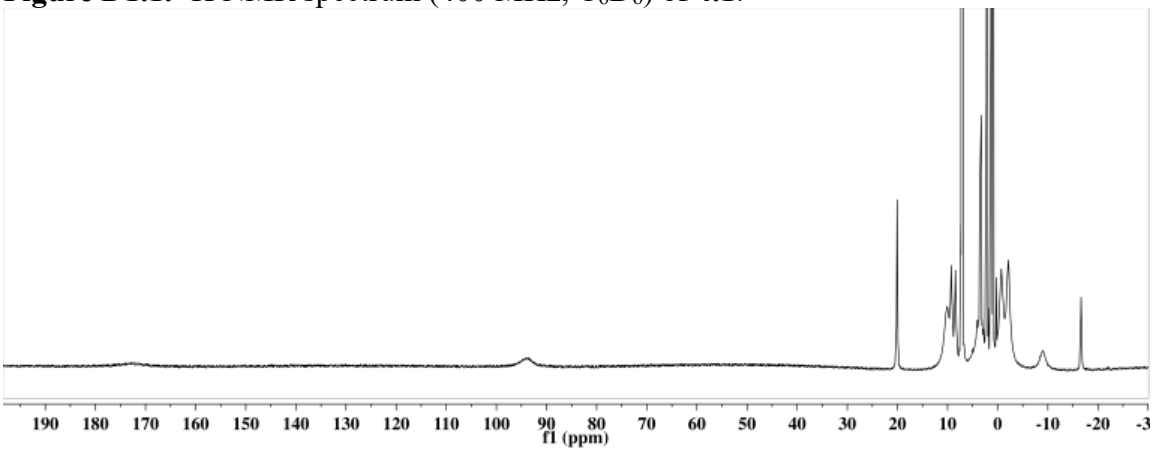

$P_2^PCoBr(CO)$ 4.2.

Figure D1.2. ^1H NMR spectrum (400 MHz, C_6D_6) of **4.2**, a mixture of two isomers.

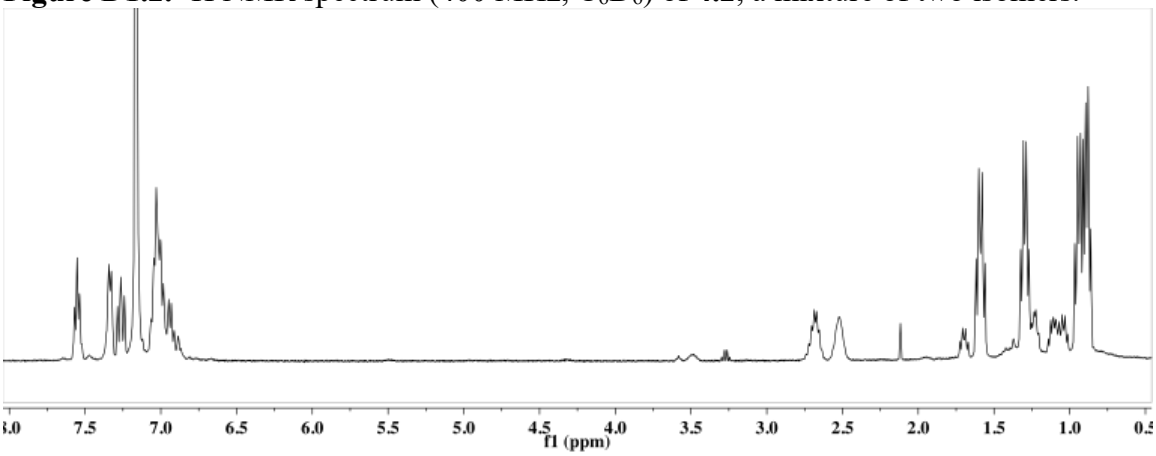

Figure D1.3. $^{31}P\{^{1}H\}$ NMR spectrum (162 MHz, C_6D_6) of **4.2**, a mixture of two isomers.

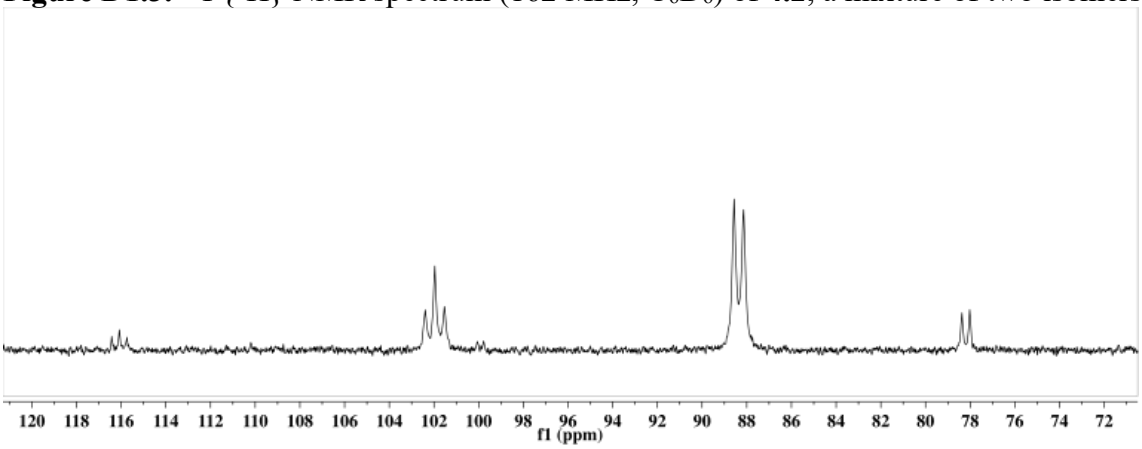

Figure D1.4. $^{31}P\{^{1}H\}$ NMR spectrum (162 MHz, C_6D_6) of **4.2-^{13}CO**, a mixture of two isomers.

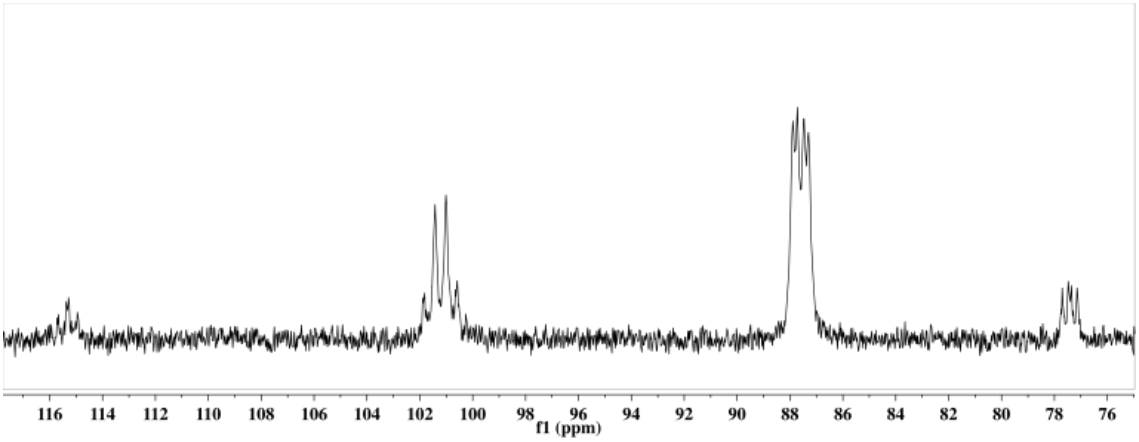

Figure D1.5. $^{13}C\{^{1}H\}$ NMR spectrum (101 MHz, C_6D_6) of **4.2-^{13}CO**, a mixture of two isomers.

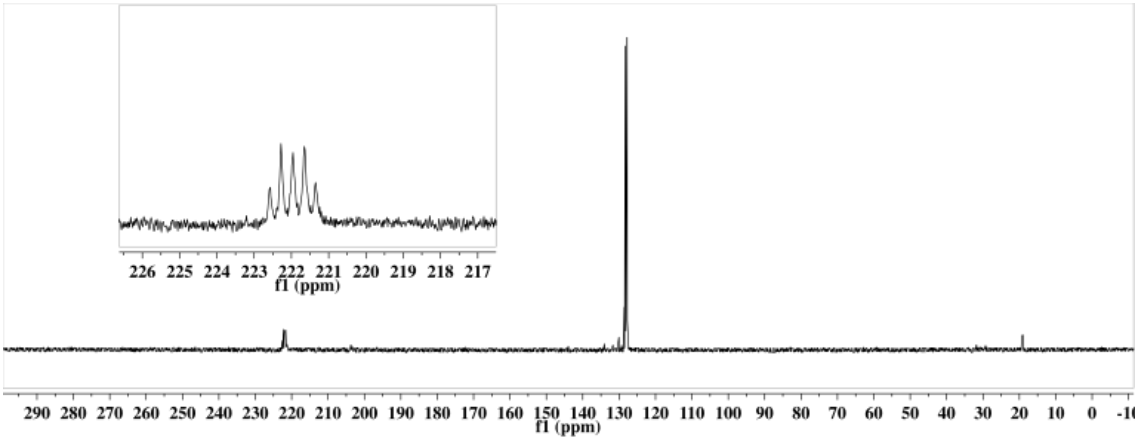

$P_2^PCo(CO)$ 4.3.

Figure D1.6. ^1H NMR spectrum (300 MHz, C_6D_6) of **4.3**.

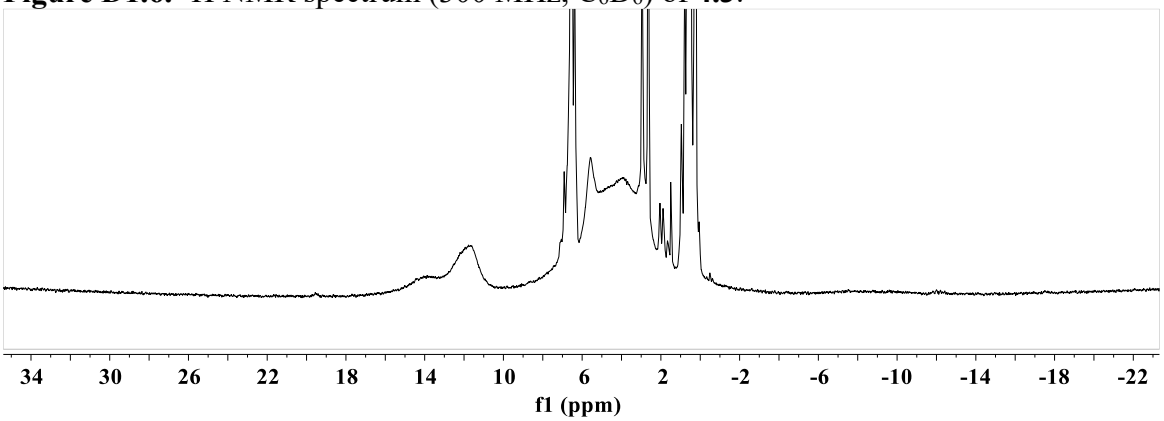

$[P_2^PCo(CO)][Na(THF)_n]$ 4.4.

Figure D1.7. ^1H NMR spectrum (400 MHz, C_6D_6) of **4.4a**. Spectrum obtained of crystalline material with DME, toluene, and pentane observed from the crystallization.

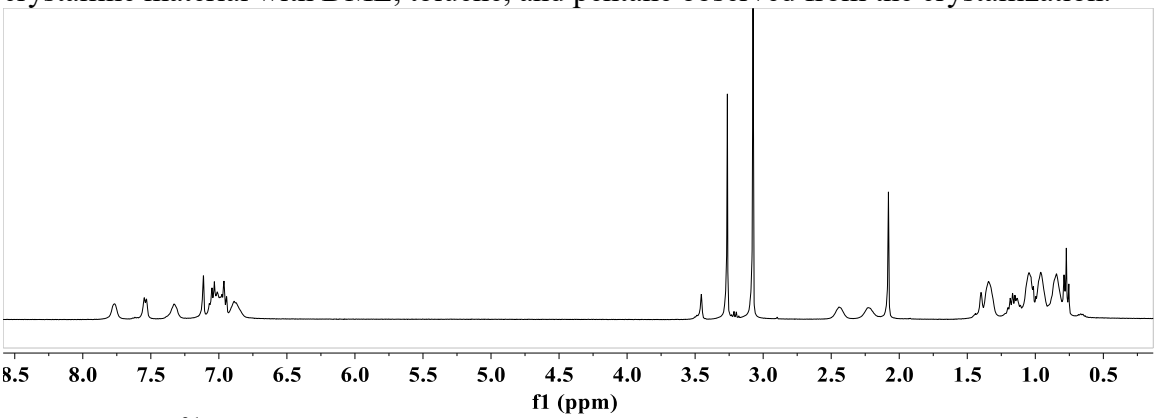

Figure D1.8. ^{31}P NMR spectrum (162 MHz, C_6D_6/THF) of **4.4a**.

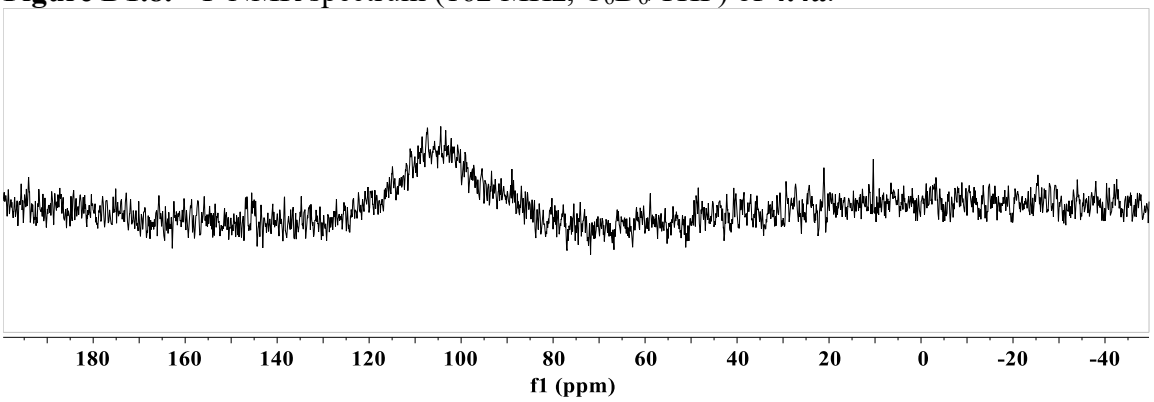

Figure D1.9. ^{13}C NMR spectrum (101 MHz, C_6D_6) of **4.4a-^{13}CO**. The peak at ~210 ppm is attributable to a minor $P_2^PCo(H)$ impurity.

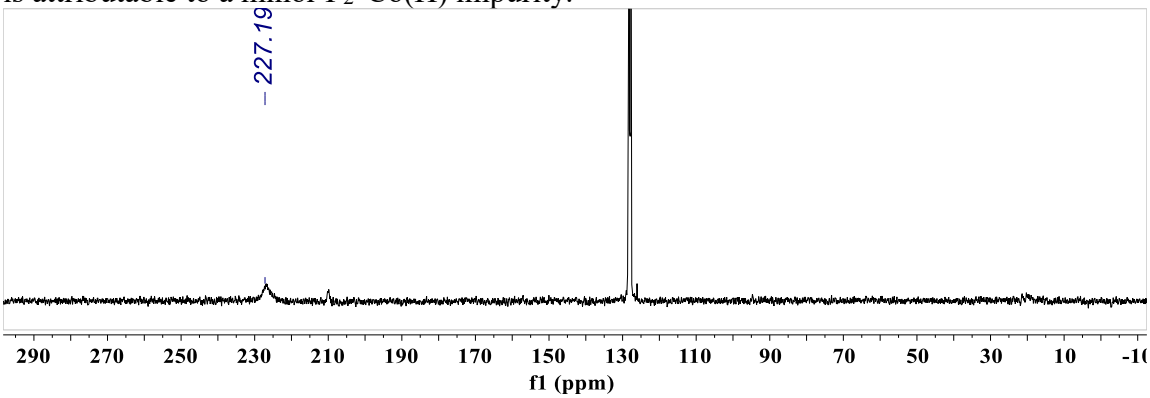

$P_2^PCo(H)(CO)$.

Figure D1.10. ^1H NMR spectrum (400 MHz, C_6D_6) of $P_2^PCo(H)(CO)$.

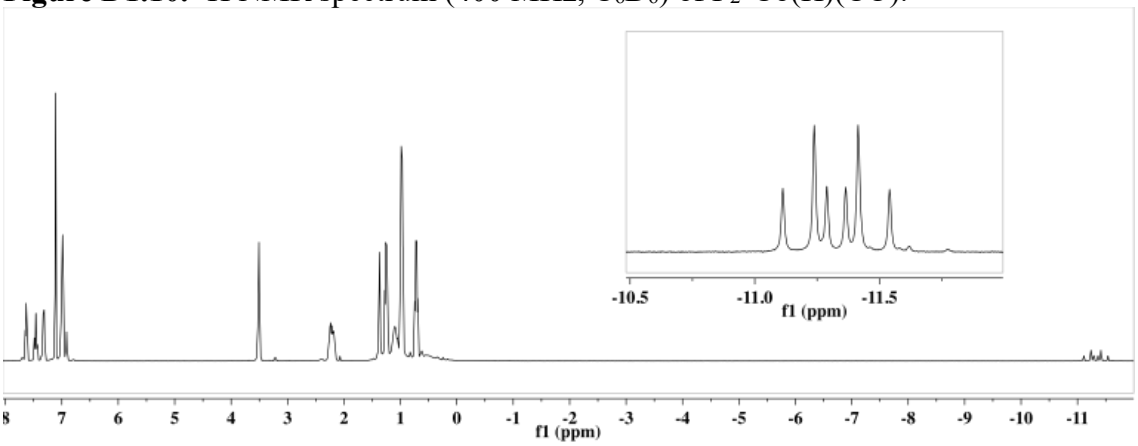

Figure D1.11. ^{31}P NMR spectrum (162 MHz, C_6D_6) of $P_2^PCo(H)(CO)$.

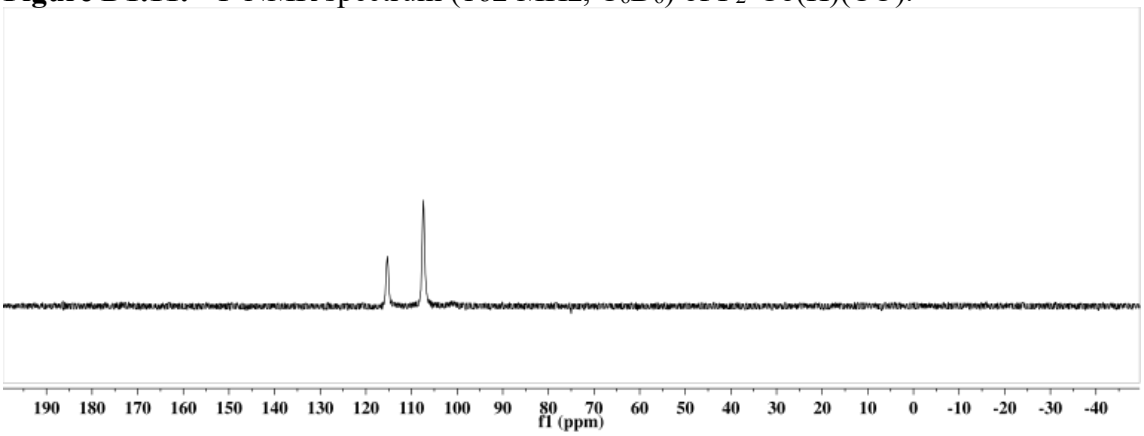

$P_2^PCo(COSi^iPr_3)$ 4.5a.

Figure D1.12. ^1H NMR spectrum (400 MHz, C_6D_6) of **4.5a.**

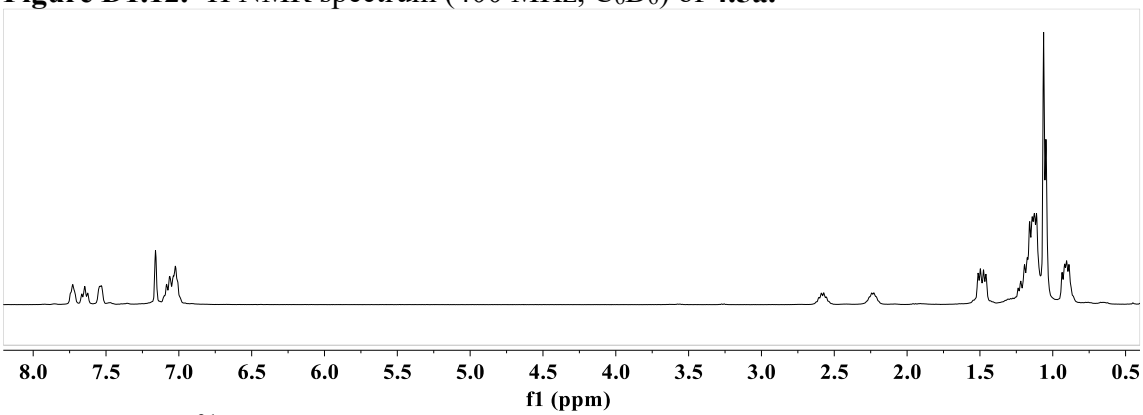

Figure D1.13. ^{31}P NMR spectrum (162 MHz, C_6D_6) of **4.5a.**

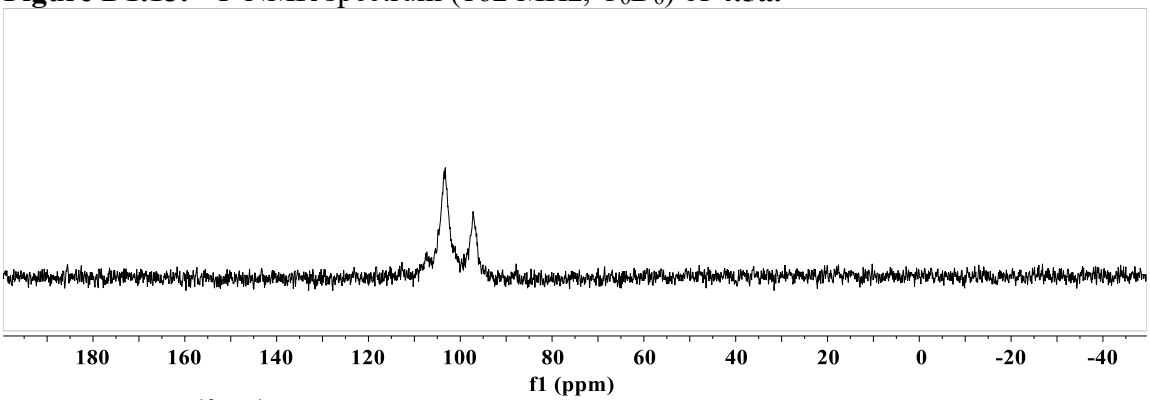

Figure D1.14. $^{13}C\{^1H\}$ NMR spectrum (101 MHz, C_6D_6) of **4.5a-^{13}CO.** The peak at ~210 ppm is attributable to a minor $P_2^PCo(H)$ impurity.

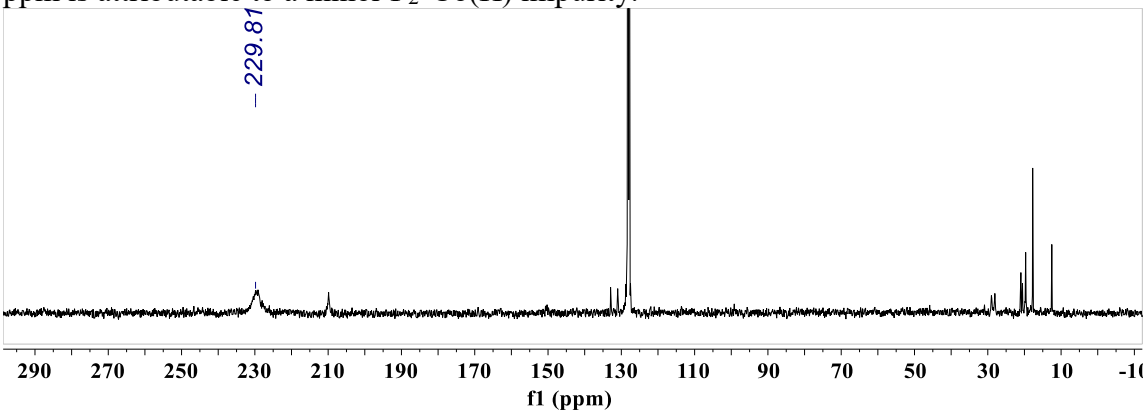

Figure D1.15. $^{13}C\{^{1}H\}$ NMR overlay of **4.4** (grey) and **4.5a** (black) highlighting the shift in the carbonyl resonance.

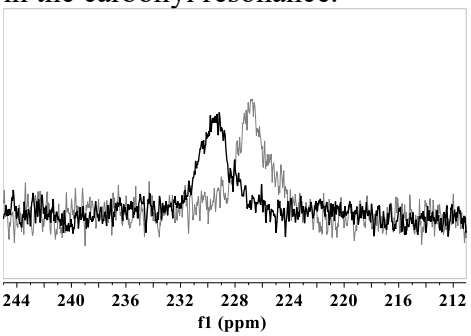

$P_2^PCo(COSi^tBuPh_2)$ 4.5b.

Figure D1.16. ^{1}H NMR spectrum (400 MHz, C_6D_6) of **4.5b.**

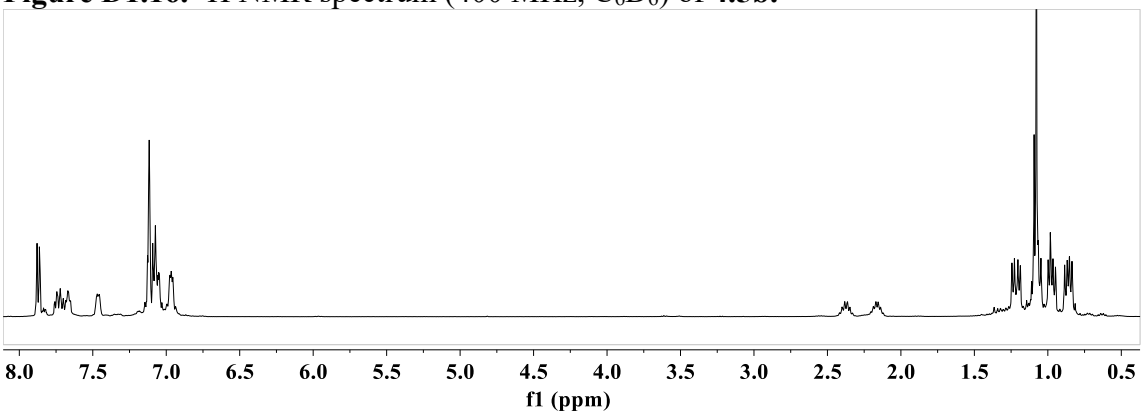

Figure D1.17. ^{31}P NMR spectrum (162 MHz, C_6D_6) of **4.5b.**

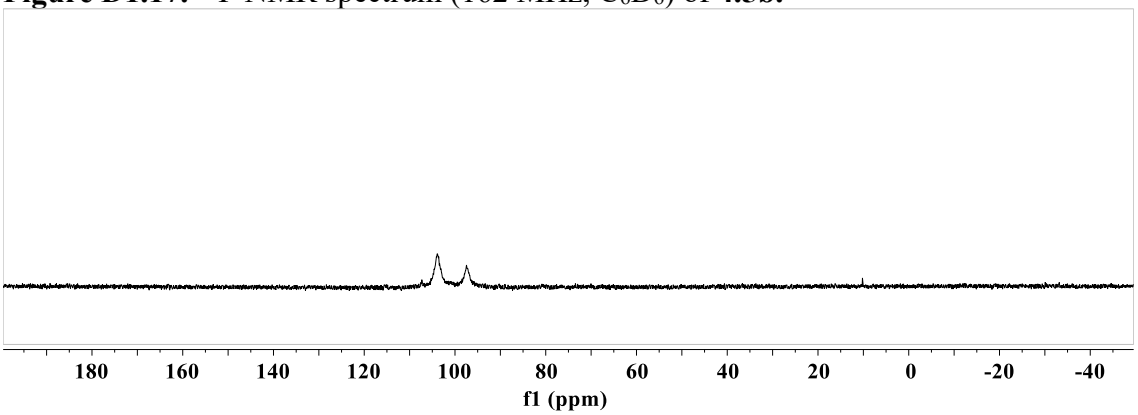

D2. IR Spectra.

$P_2^PCoBr(CO)$ 4.2.

Figure D2.1. Thin film IR spectrum of $P_2^PCoBr(CO)$ **4.2** (ν_{CO} = 1928 cm^{-1}).

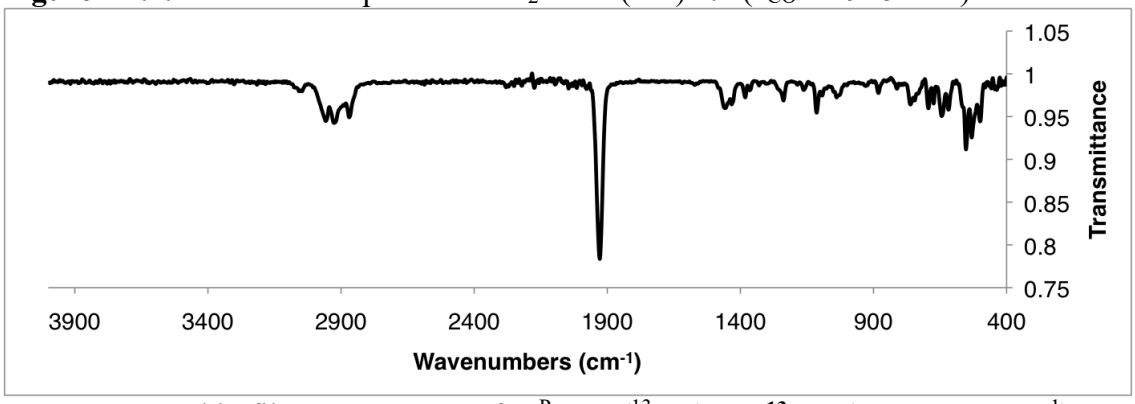

Figure D2.2. Thin film IR spectrum of $P_2^PCoBr(^{13}CO)$ **4.2-^{13}CO** (ν_{CO} = 1884 cm^{-1}).

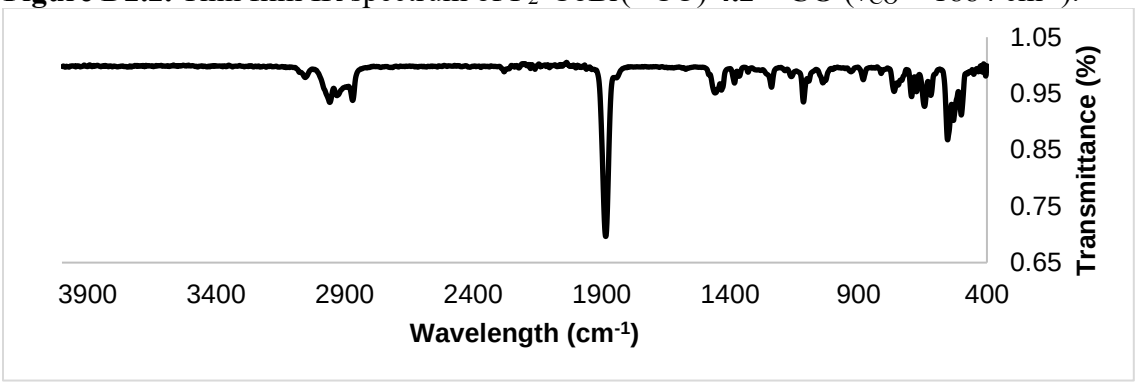

$P_2^PCo(CO)$ 4.3.

Figure D2.3. Thin film IR spectrum of $P_2^PCo(CO)$ **4.3** (ν_{CO} = 1866 cm^{-1}).

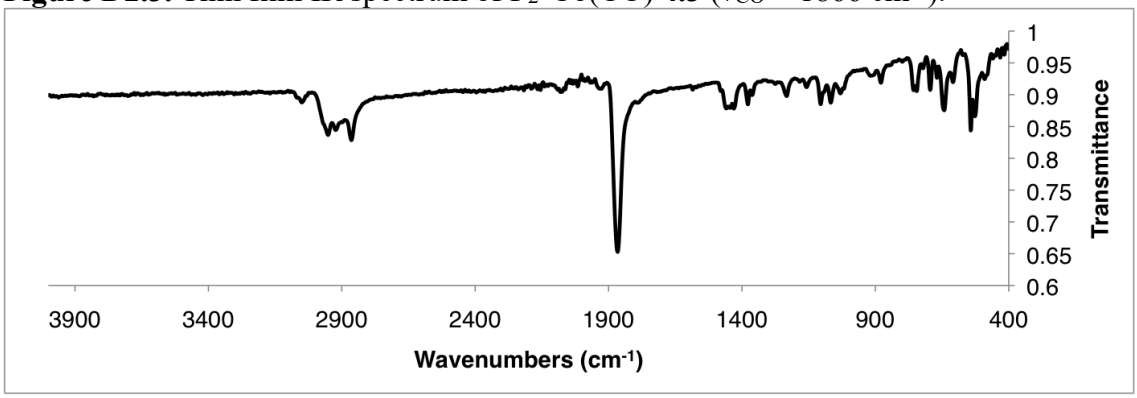

Figure D2.4. Thin film IR spectrum of $P_2^PCo(^{13}CO)$ **4.3-^{13}CO** (ν_{CO} = 1824 cm^{-1}).

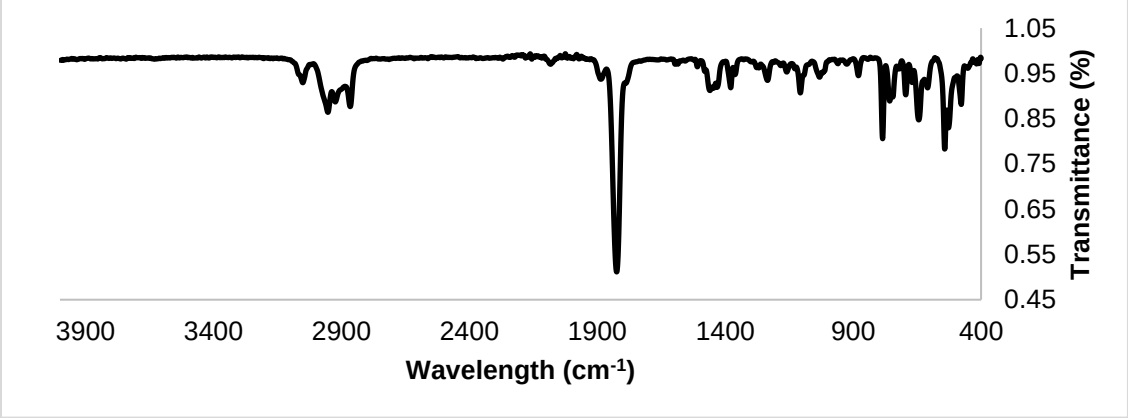

[$P_2^PCo(CO)$][$Na(THF)_n$] 4.4a.

Figure D2.5. Thin film IR spectrum of [$P_2^PCo(CO)$][$Na(THF)_n$] **4.4a** (ν_{CO} = 1731 cm^{-1}).

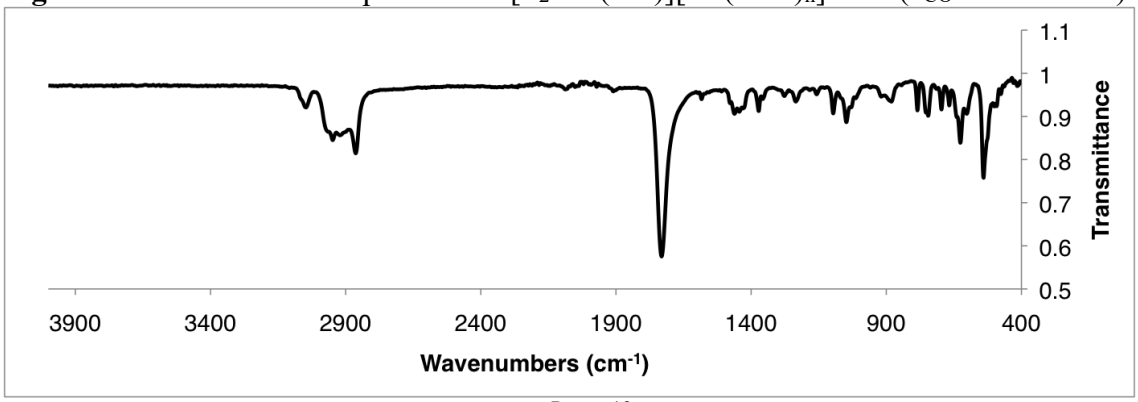

Figure D2.6. Thin film IR spectrum of [$P_2^PCo(^{13}CO)$][$Na(THF)_n$] **4.4a-^{13}CO** (ν_{CO} = 1691 cm^{-1}).

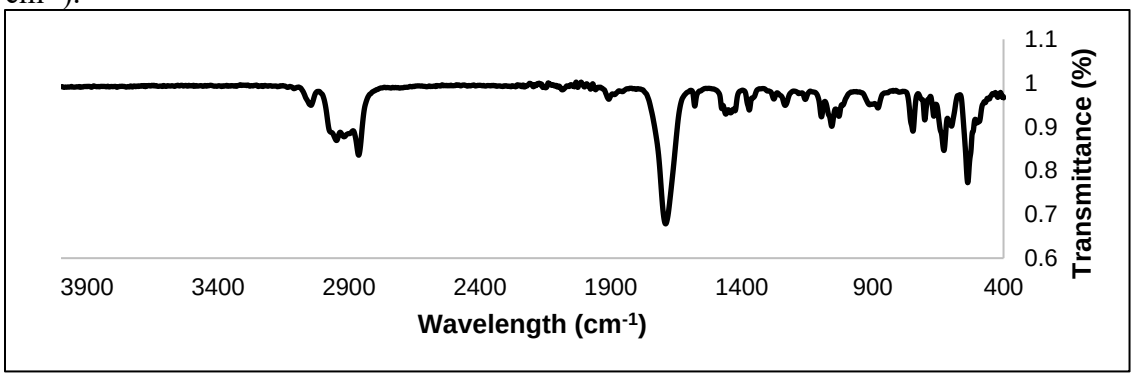

[$P_2^PCo(CO)$][Na(12-crown-4)$_2$] 4.4b.

Figure D2.7. Thin film IR spectrum of [$P_2^PCo(CO)$][Na(12-crown-4)$_2$] **4.4b** (ν_{CO} = 1752 cm^{-1}). A minor amount of oxidized Co(CO) species are present.

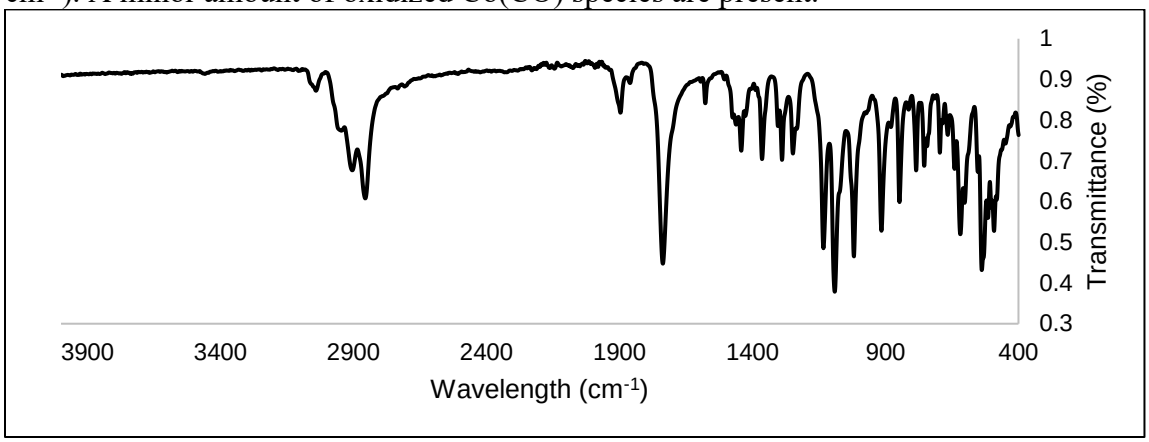

$P_2^PCo(H)(CO)$.

Figure D2.8. Thin film IR spectrum of $P_2^PCo(H)(CO)$ (ν_{CO} = 1901 cm^{-1})

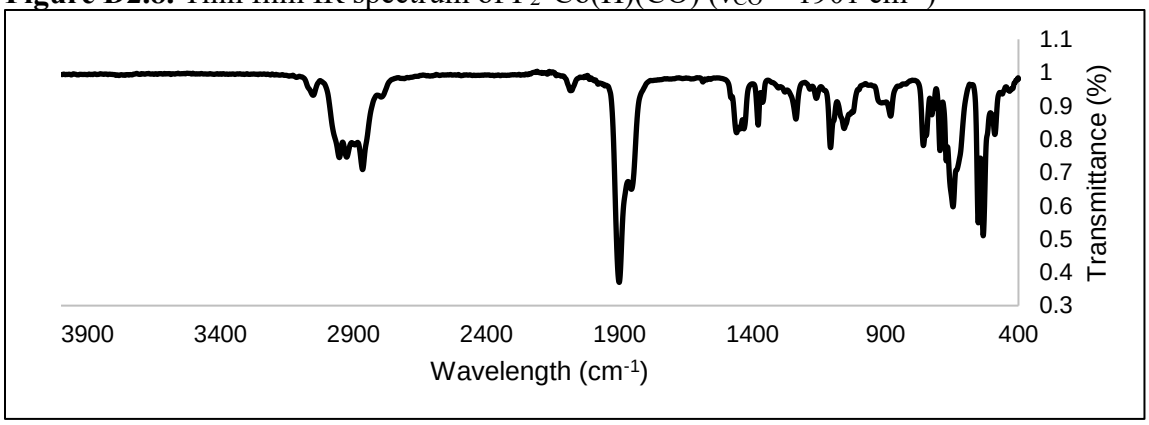

$P_2^PCo(COSi^iPr_3)$ 4.5a.

Figure D2.9. Thin film IR spectrum of $P_2^PCo(COSi^iPr_3)$ **4.5a** (ν_{CO} = 1387 cm^{-1}). A minor amount of oxidized Co(CO) species are observable.

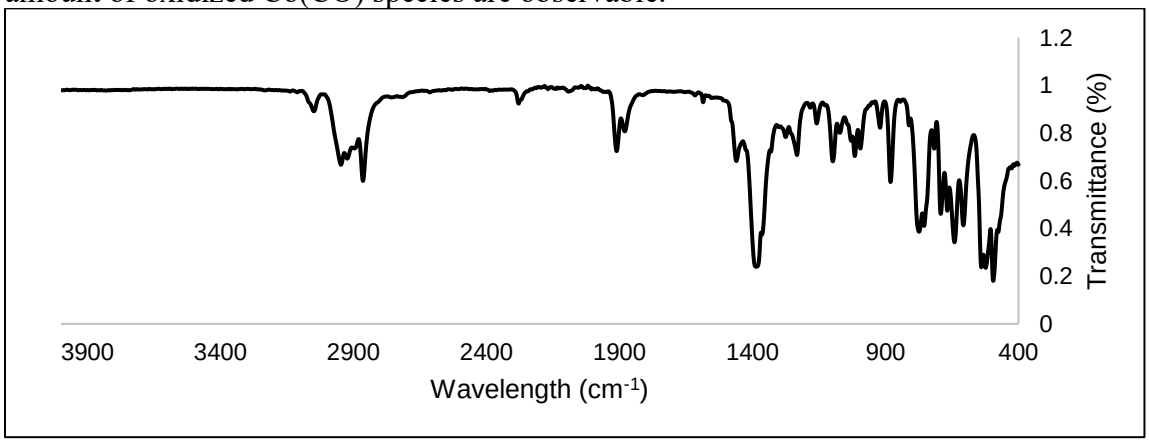

Figure D2.10. Thin film IR spectrum of $P_2^PCo(COSi^iPr_3)$ **4.5a-^{13}CO** (ν_{CO} = 1347 cm^{-1}). A minor amount of oxidized Co(CO) species are observable.

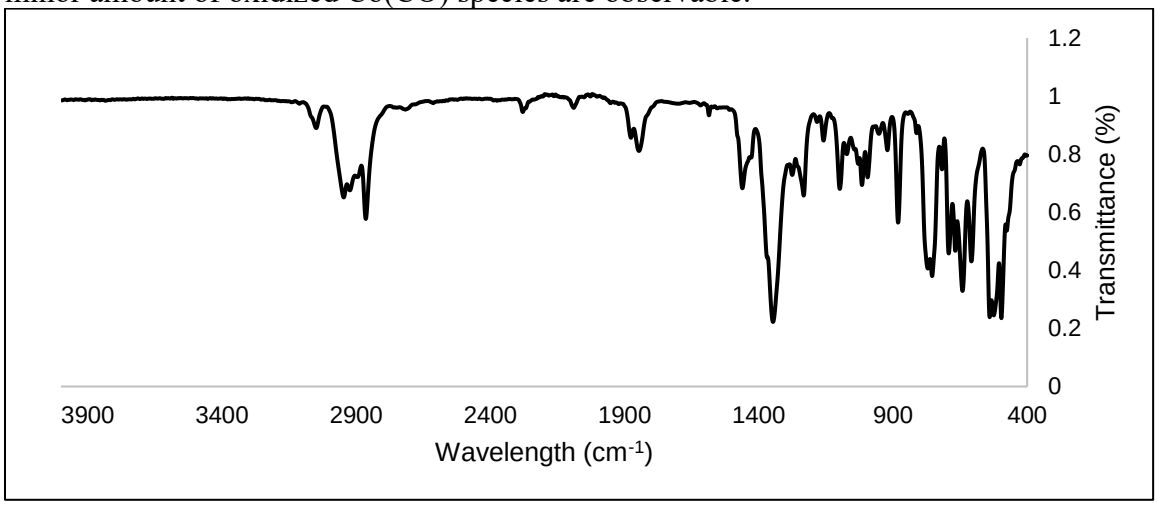

Figure D2.11. Solution IR difference spectrum of **4.5a** – **4.5a-^{13}CO** highlighting the identified CO stretch.

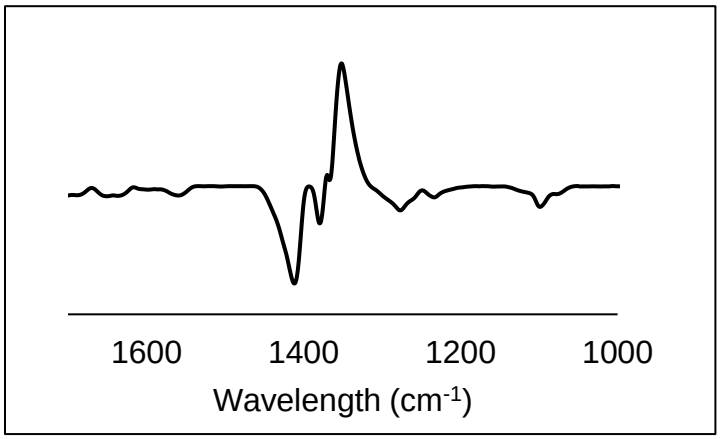

D3. EPR Spectra

Figure D3.1. EPR spectra of $P_2^PCo(CO)$ **4.3** and **4.3-^{13}CO**

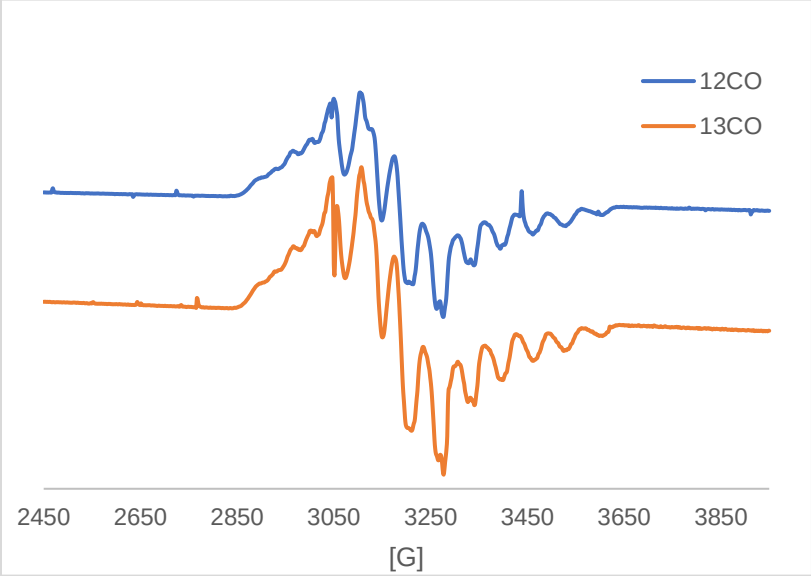

D4. Crystallographic Details

	P_2^PCoBr 4.1	$P_2^PCoBr(CO)$ 4.2	$P_2^PCo(CO)$ 4.3	$[P_2^PCo(CO)][Na(DME)_3]$ 4.4a
Crystal system	Triclinic	Monoclinic	Triclinic	Monoclinic
Formula	$C_{30}H_{41}BrCoP_3$	$C_{41.5}H_{53}BrCoOP_3$	$C_{31}H_{41}CoOP_3$	$C_{43}H_{71}CoNaO_7P_3$
Formula weight (g/mol)	633.37	799.62	581.51	874.88
Space group	P -1	P21/c	P -1	P21/n
a (Å)	9.4625(5)	10.9453(6)	10.843(2)	11.1659(4)
b (Å)	9.5168(5)	14.9644(8)	16.079(3)	16.1007(5)
c (Å)	17.7628(10)	23.9133(15)	17.991(3)	26.6135(8)
α (deg)	100.843(2)	90	109.036(7)	90
β (deg)	96.323(2)	101.797(3)	92.528(7)	97.3840(10)
γ (deg)	102.954(2)	90	90.859(8)	90
Z	2	4	4	4
V (Å³)	1511.54(14)	3834.0(4)	2960.8(9)	4744.9(3)
Indep. Reflections	6696	7232	11895	10157
R(int)	3.12	6.77	6.62	2.09
R1	1.64	3.13	2.48	2.68
wR2	4.26	7.71	6.78	7.59
GOF	1.064	1.069	1.043	1.049

	$[P_2^PCo(CO)][Na(12\text{-}c\text{-}4)_2]$ 4.4b	$P_2^PCo(H)(CO)$	$P_2^PCo(COSi^tBuPh_2)$ 4.5b
Crystal system	Monoclinic	Triclinic	Monoclinic
Formula	$C_{50}H_{76}CoNaO_9P_3$	$C_{31}H_{42}CoOP_3$	$C_{44.5}H_{56.8}CoOP_3Si$
Formula weight (g/mol)	995.99	582.51	787.97
Space group	C2/c	P-1	P21
a (Å)	27.599(3)	9.4357(4)	10.4158(11)
b (Å)	30.400(5)	9.6576(6)	16.6407(12)
c (Å)	18.698(2)	17.4658(8)	12.8005(11)
α (deg)	90	102.756(3)	90
β (deg)	132.65	98.244(2)	95.289(4)
γ (deg)	90	103.517(3)	90
Z	8	2	2
V (Å³)	11538(3)	1477.06(13)	2209.2(3)
Indep. Reflections	16818	6375	9766
R(int)	5.89	4.44	3.89
R1	5.92	2.07	3.21
wR2	15.27	5.38	8.11
GOF	1.073	1.057	1.072

Remarks on Crystal Structures:

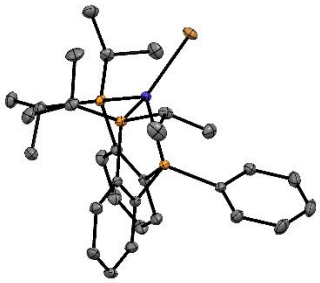

Figure D4.1. Full asymmetric unit of **4.1**. Hydrogen atoms are omitted for clarity.

P_2^PCoBr 4.1. This compound crystallizes in the absence of solvent.

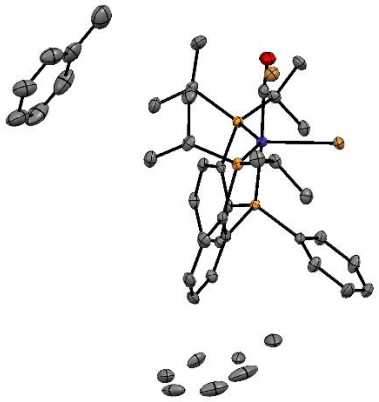

Figure D4.2. Full asymmetric unit of **4.2** showing both toluene molecules and the Br component of the minor product isomer. Hydrogen atoms are omitted for clarity.

P_2^PCoBr(CO) 4.2. This compound crystallizes with two toluene solvent molecules, one of which is modeled as disordered over two symmetry-related positions. The complex appears to co-crystallize with a component of a minor isomer with the Br occupying the axial site (~4%). Omission of this Br component resulted in elongated CO ellipsoids, with the largest residual electron density peak consistent with the presence of this atom. For the minor component, the additional CO co-ligand could not be located, but its presence is consistent with incomplete occupancy of the Br ligand located in the trigonal plane, with approximately 96% occupancy when freely refined.

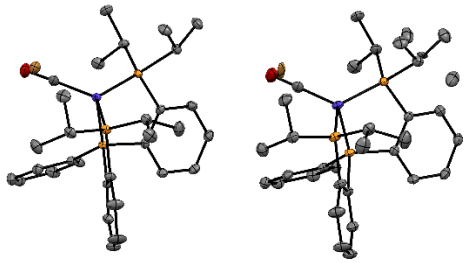

Figure D4.3. Full asymmetric unit of **4.3** showing disordered P^{i}Pr group and minor component of **4.1** for both molecules. Hydrogen atoms are omitted for clarity.

P_2^PCo(CO) 4.3. This compound crystallizes in the absence of solvent with two molecules of the complex in the asymmetric unit. One of the P-^{i}Pr groups on one of the molecules was modeled as disordered over two positions (73:37). For both molecules of the complex, refinement was improved by the inclusion of a very minor component of **4.1**, which was identified by the presence of residual electron density for the Br ligand; these refined to ~1.5% and 2.5% components for the two independent molecules.

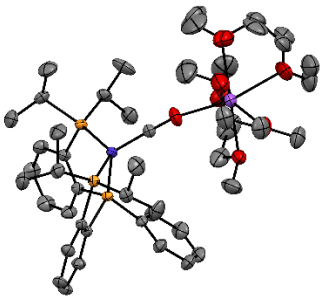

Figure D4.4. Full asymmetric unit of **4.4a**. Hydrogen atoms are omitted for clarity.

[$P_2^PCo(CO)$][$Na(DME)_3$] 4.4a. This compound crystallizes with an O-bound Na counter cation. Three DME molecules are ligated to Na with one of these modeled as disordered over two positions (50:50).

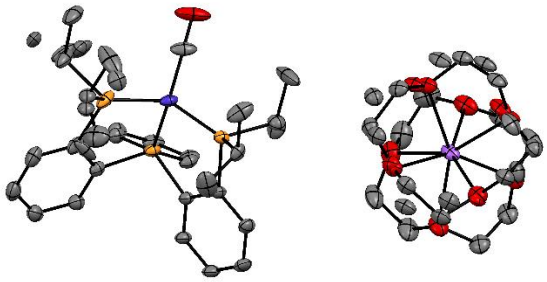

Figure D4.5. Full asymmetric unit of **4.4b**. Hydrogen atoms are omitted for clarity.

[$P_2^PCo(CO)$][$Na(12\text{-crown-}4)_2$] 4.4b. This compound crystallizes with a fully crown-encapsulated Na counter cation and additional residual solvent electron density that could not be fully refined (likely THF and benzene/toluene molecules) that was removed by application of SQUEEZE. Two of the four ligand ^{i}Pr groups were modeled in a crystallographically related disorder over two positions (62:38), with the refinement of this disorder aided by the application of an EADP constraint for one of the methine carbon positions and RIGU restraints. One of the crown ethers was modeled as fully disordered over two positions (67:33), with application of an EADP constraint on one of the oxygen atoms.

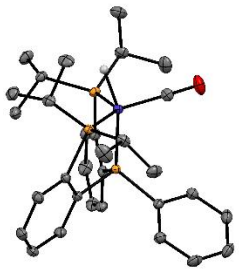

Figure D4.6. Full asymmetric unit of $P_2^PCoH(CO)$. C-bound hydrogen atoms are omitted for clarity.

$P_2^PCoH(CO)$. This compound crystallizes in the absence of solvent.

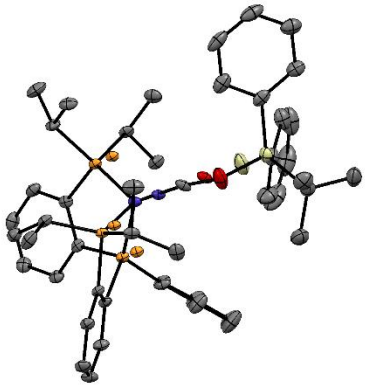

Figure D4.7. Full asymmetric unit of $P_2^PCo(COSi^tBuPh_2)$ **4.5b**. Hydrogen atoms are omitted for clarity.

$P_2^PCo(COSi^tBuPh_2)$ 4.5b. This compound crystallizes in the absence of solvent. A minor component in the crystal lattice (~5%) was present. Within this component the core atoms were modeled best as $P_3Co(OSi)$ with their refinement aided by the application of EADP constraints. The exact identity of the minor component is ambiguous, where the most residual electron density was located at the positions of the Co and Si. Complete disorder of the remaining supporting ligand could not be reliably refined.

D5. Bond Distances and Angles.

P_2^PCoBr 4.1.

Bond Distances (Å)		Bond Angles (degrees)	
Co1-P1	2.1956(5)	P1-Co1-P2	86.70(1)
Co1-P2	2.2484(4)	P1-Co1-P3	87.19(1)
Co1-P3	2.2646(3)	P2-Co1-P3	118.41(2)
Co1-Br1	2.3504(3)	P1-Co1-Br1	130.20(2)
		P2-Co1-Br1	118.80(1)
		P3-Co1-Br1	111.21(1)

$P_2^PCoBr(CO)$ 4.2.

Bond Distances (Å)		Bond Angles (degrees)	
Co1-P1	2.1673(7)	P1-Co1-P2	86.35(2)
Co1-P2	2.1756(6)	P1-Co1-P3	87.24(2)
Co1-P3	2.1835(6)	P2-Co1-P3	137.92(2)
Co1-Br1A	2.4977(4)	P1-Co1-Br1A	95.07(2)
Co1-C1	1.754(4)	P2-Co1-Br1A	109.89(2)
		P3-Co1-Br1	112.09(2)
		P1-Co1-C1	176.0(1)
		P2-Co1-C1	91.2(1)
		P3-Co1-C1	92.6(1)

$P_2^PCo(CO)$ 4.3.

Bond Distances (Å)		Bond Angles (degrees)	
Molecule 1			
Co1-P1	2.1344(6)	P1-Co1-P2	87.36(2)
Co1-P2	2.1769(5)	P1-Co1-P3	87.94(2)
Co1-P3	2.1922(5)	P2-Co1-P3	124.42(2)
Co1-C1	1.752(2)	P1-Co1-C1	109.40(6)
C1-O1	1.161(3)	P2-Co1-C1	117.85(6)
		P3-Co1-C1	115.85(6)
Molecule 2			
Co2-P4	2.1301(6)	P4-Co2-P5	87.94(2)
Co2-P5	2.1740(5)	P4-Co2-P6	87.59(2)
Co2-P6	2.1753(5)	P5-Co2-P6	128.80(2)
Co2-C32	1.747(2)	P4-Co2-C32	111.08(6)
C32-O2	1.162(3)	P5-Co2-C32	115.86(6)
		P6-Co2-C32	113.24(6)

[$P_2^PCo(CO)$][$Na(DME)_3$] 4.4a.

Bond Distances (Å)		Bond Angles (degrees)	
Co1-P1	2.0966(6)	P1-Co1-P2	89.80(2)
Co1-P2	2.1394(4)	P1-Co1-P3	89.23(2)
Co1-P3	2.1409(6)	P2-Co1-P3	126.42(2)
Co1-C1	1.716(1)	P1-Co1-C1	126.19(4)
C1-O1	1.187(1)	P2-Co1-C1	111.27(4)
		P3-Co1-C1	112.00(4)

[$P_2^PCo(CO)$][$Na(12\text{-}c\text{-}4)_2$] 4.4b.

Bond Distances (Å)		Bond Angles (degrees)	
Co1-P1	2.0838(8)	P1-Co1-P2	90.20(3)
Co1-P2	2.1191(8)	P1-Co1-P3	89.97(3)
Co1-P3	2.1304(7)	P2-Co1-P3	128.03(3)
Co1-C1	1.733(3)	P1-Co1-C1	125.9(1)
C1-O1	1.177(4)	P2-Co1-C1	109.1(1)
		P3-Co1-C1	112.3(1)

$P_2^PCoH(CO)$.

Bond Distances (Å)		Bond Angles (degrees)	
Co1-P1	2.1246(5)	P1-Co1-P2	87.25(1)
Co1-P2	2.1387(4)	P1-Co1-P3	87.65(1)
Co1-P3	2.1481(3)	P2-Co1-P3	130.99(2)
Co1-C1	1.748(1)	P1-Co1-C1	111.24(4)
C1-O1	1.156(2)	P2-Co1-C1	117.25(4)
Co1-H	1.46(2)	P3-Co1-C1	109.97(4)
		P1-Co1-H	158.4(8)
		P2-Co1-H	81.6(8)
		P3-Co1-H	85.8(8)
		C1-Co1-H	90.4(8)

$P_2^PCo(COSi^tBuPh_2)$ 4.5b.

Bond Distances (Å)		Bond Angles (degrees)	
Co1-P1	2.120(1)	P1-Co1-P2	89.08(4)
Co1-P2	2.1617(9)	P1-Co1-P3	89.15(4)
Co1-P3	2.154(1)	P2-Co1-P3	116.58(4)
Co1-C1	1.640(4)	P1-Co1-C1	124.5(1)
C1-O1	1.260(5)	P2-Co1-C1	121.3(1)
		P3-Co1-C1	111.1(1)
		Co1-C1-O1	169.8(3)
		C1-O1-Si1	137.7(3)

D6. DFT Calculations

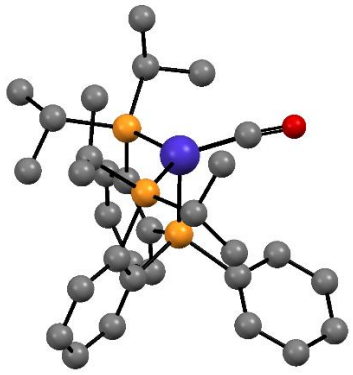

Figure D6.1. DFT optimized structure of P_2^PCoCO **4.3**.

Optimized Coordinates for P_2^PCoCO **4.3**.

Co	-0.00373920	-0.68403331	-1.13110881
P	-1.87398768	-1.29740975	-0.13861284
P	-0.03676809	1.07695207	0.14191298
P	1.94878185	-1.18329652	-0.22032067
O	-0.15144203	0.42470896	-3.84313481
C	-1.56014096	3.51219817	0.00676086
H	-2.23053101	3.10296106	0.76821282
C	-0.44140606	2.77932785	-0.40975202
C	0.39440765	3.32667650	-1.39751807
H	1.25777876	2.75204333	-1.75059220
C	-3.48008828	-0.85564677	-1.00175702
H	-4.31027257	-1.19426742	-0.35454368
C	0.13160535	4.58048467	-1.93718308
H	0.79480533	4.99161772	-2.70197379
C	-2.02331868	1.19571705	3.79240558
H	-2.01389840	1.78644122	4.71156719
C	-2.87196033	0.09683510	3.67355708
H	-3.53163960	-0.17772486	4.50042345
C	2.06214164	-2.54589672	1.07911738
H	1.57955857	-3.40188786	0.57094445
C	-3.55616629	-1.56406300	-2.34495621
H	-2.72944595	-1.24626869	-2.99958276
H	-4.49804559	-1.32423864	-2.86187912
H	-3.50112800	-2.65856426	-2.25840233
C	-2.10968536	-3.09358498	0.38119367
H	-1.61671453	-3.12741100	1.37038101
C	-1.82869539	4.76626423	-0.54480155
H	-2.70603956	5.32633189	-0.21149253
C	-0.98375830	5.30541717	-1.51247816
H	-1.19596055	6.28770625	-1.94119579
C	-1.31891162	-3.99208175	-0.56315747

H	-1.76215067	-4.01445311	-1.57066202
H	-1.29238490	-5.02994813	-0.19656323
H	-0.28085683	-3.64445211	-0.68239284
C	-1.17214040	0.77497158	1.56241859
C	2.55128798	0.29792111	0.70166341
C	3.38568698	-1.56701330	-1.35292128
H	4.29072385	-1.69254644	-0.73152057
C	-3.53798222	-3.59442156	0.53798124
H	-4.14485540	-2.99230063	1.22730559
H	-3.54178431	-4.62549400	0.92454118
H	-4.07249625	-3.61731658	-0.42301612
C	-2.02620674	-0.33932311	1.43786477
C	-2.88133467	-0.65755349	2.49923997
H	-3.55957684	-1.51115617	2.42255209
C	-1.18326174	1.53847712	2.73375752
H	-0.52040556	2.40392156	2.82717876
C	3.45106114	-2.97755182	1.51842265
H	4.08911265	-3.30666771	0.68632378
H	3.38210730	-3.82353269	2.22030132
H	3.97881486	-2.17346988	2.05327583
C	-3.57274070	0.65081904	-1.17921564
H	-3.59876819	1.18695839	-0.21893956
H	-4.48457301	0.92397862	-1.73166635
H	-2.71286500	1.03315742	-1.75478613
C	1.62459331	1.33732193	0.90017804
C	3.61514266	-0.41533321	-2.31816512
H	2.72523731	-0.23564026	-2.94079708
H	4.45674467	-0.63438711	-2.99255734
H	3.84642737	0.52501777	-1.79552016
C	2.01304697	2.50299733	1.57101171
H	1.30361121	3.32895758	1.68417924
C	1.20229291	-2.16700751	2.27542852
H	1.66500159	-1.35519525	2.85944975
H	1.06774625	-3.02194123	2.95550693
H	0.20520374	-1.81561249	1.97056720
C	3.31053089	2.63342610	2.06199940
H	3.60779328	3.54599534	2.58447292
C	3.85902130	0.45131874	1.18066222
H	4.60490918	-0.32787360	1.00009233
C	4.23468222	1.60809749	1.86271842
H	5.25953810	1.71645513	2.22633499
C	3.10131125	-2.86755640	-2.08862046
H	2.99836392	-3.72770900	-1.40961483
H	3.90783916	-3.10703630	-2.79797189
H	2.16678768	-2.78972378	-2.66864491
C	-0.07928258	-0.08910143	-2.79735019

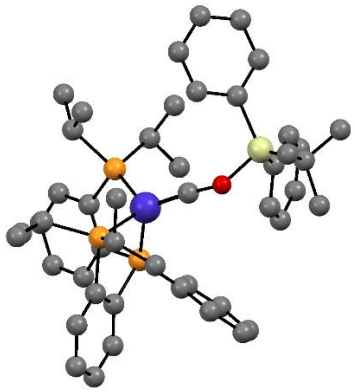

Figure D6.2. DFT optimized structure of $P_2^PCo(COSi^tBuPh_2)$ **4.5**.

Optimized coordinates for $P_2^PCo(COSi^tBuPh_2)$ **4.5**.

Co	-0.45582353	-0.55478023	-0.22567636
P	-1.98357862	0.92316588	-0.02890594
P	-0.70310321	-0.99694976	1.89574102
P	-1.83349838	-1.71910022	-1.42299600
Si	3.61223802	0.33443923	-0.87893290
O	2.11419482	-0.15306411	-1.59390024
C	1.01699847	-0.34261990	-0.93429510
C	-1.81623712	2.75255972	-0.11950474
C	-1.94950883	3.60412380	0.98531803
H	-2.21298569	3.19010182	1.96268118
C	-1.76737175	4.98161492	0.84910490
H	-1.88362968	5.63056912	1.72102350
C	-1.44995947	5.53028448	-0.39175656
H	-1.31871620	6.60968187	-0.49946671
C	-1.29392319	4.68888661	-1.49666945
H	-1.03679952	5.10867856	-2.47264631
C	-1.46604274	3.31505149	-1.35909167
H	-1.33655929	2.65911902	-2.22743672
C	-2.89728378	0.65774722	1.55750011
C	-4.12801616	1.24916230	1.85476155
H	-4.57144753	1.96274248	1.15315186
C	-4.80127653	0.92778016	3.03185169
H	-5.77020291	1.38276758	3.25202088
C	-4.23359278	0.01826301	3.92302176
H	-4.75702253	-0.24189980	4.84666705
C	-2.99729238	-0.56353520	3.64009216
H	-2.57181896	-1.26920617	4.35723372
C	-2.31774340	-0.26348229	2.45260686
C	0.47847336	-0.14979874	3.08556288
H	0.15938218	-0.43891607	4.10428087

C	1.90501923	-0.61061182	2.84476455
H	2.04537772	-1.69484683	2.96650219
H	2.60425923	-0.10747392	3.53184813
H	2.21313131	-0.35607313	1.81826549
C	0.37835817	1.35942746	2.94475300
H	0.62791475	1.67110351	1.91660778
H	1.08759612	1.86063348	3.62172307
H	-0.62673181	1.74076405	3.17964889
C	-0.74519687	-2.77838605	2.52576033
H	-1.79248673	-3.07849014	2.33211780
C	0.16143364	-3.63904163	1.65322811
H	0.02960349	-3.41379968	0.58337656
H	-0.02635673	-4.71151292	1.82112923
H	1.22309419	-3.45452885	1.88078238
C	-0.43441812	-3.01516730	3.99694039
H	0.61500609	-2.78168175	4.23061165
H	-0.58303303	-4.07591031	4.25432426
H	-1.05560115	-2.43024934	4.68755889
C	-3.29432715	0.63494307	-1.30893921
C	-4.28631777	1.55446579	-1.66989107
H	-4.33588899	2.52839530	-1.17169265
C	-5.19151109	1.25226094	-2.68579817
H	-5.95645436	1.97919276	-2.97020796
C	-5.10714088	0.02881469	-3.35030898
H	-5.80326956	-0.20383515	-4.16010896
C	-4.12152139	-0.89150568	-2.99421697
H	-4.04873391	-1.83309847	-3.54642352
C	-3.20993832	-0.60259879	-1.97108366
C	-2.79677954	-3.20759035	-0.76124782
H	-2.02029485	-3.77400178	-0.21461980
C	-3.43248564	-4.14480657	-1.77454839
H	-4.20369638	-3.64035449	-2.37600932
H	-3.93852666	-4.97477751	-1.25584382
H	-2.70804145	-4.59873834	-2.46456461
C	-3.82625046	-2.72656394	0.24996740
H	-4.23240441	-3.56669666	0.83441645
H	-4.67617899	-2.23212445	-0.24713791
H	-3.40384695	-2.00044927	0.95899008
C	-1.17762029	-2.34459196	-3.06046603
H	-2.01986133	-2.84003428	-3.57693811
C	-0.07551636	-3.36205550	-2.81356358
H	0.77472231	-2.88332322	-2.30160039
H	0.29711901	-3.78213916	-3.76054346
H	-0.40341409	-4.20416004	-2.18471194
C	-0.68540406	-1.19938444	-3.92930430
H	-1.47901930	-0.47157673	-4.15406842

H	-0.30312840	-1.57898205	-4.88958659
H	0.13234844	-0.65494926	-3.43421884
C	3.20854642	1.83647134	0.16363962
C	3.93204319	2.18847598	1.31412860
H	4.75069073	1.55106238	1.66459594
C	3.61303979	3.33391220	2.04317408
H	4.18747064	3.58807423	2.93771599
C	2.55642879	4.14659755	1.63486021
H	2.29878946	5.04065431	2.20879951
C	1.81902953	3.81070706	0.49955994
H	0.97856578	4.43381370	0.18343704
C	2.14248546	2.66695535	-0.22730215
H	1.53759985	2.40605802	-1.10226450
C	4.24059216	-1.14397040	0.08589095
C	5.40917422	-1.09108229	0.86624510
H	5.99827920	-0.16885721	0.91631024
C	5.84680317	-2.20081245	1.58827547
H	6.75458758	-2.13442525	2.19299610
C	5.12801643	-3.39449184	1.53505556
H	5.47022847	-4.26547128	2.09950729
C	3.97338059	-3.47145823	0.75795189
H	3.40560225	-4.40447949	0.71059736
C	3.53206293	-2.35801702	0.04493789
H	2.60494543	-2.42988103	-0.53309647
C	4.68460093	0.73981046	-2.38940051
C	6.08710986	1.12973140	-1.92027441
H	6.07417079	1.98928759	-1.23024864
H	6.71739960	1.41797604	-2.77833227
H	6.60147062	0.29802085	-1.41367668
C	4.75824287	-0.49559730	-3.28804357
H	5.20832488	-1.35737662	-2.77111796
H	5.37600602	-0.29074255	-4.17866744
H	3.76341494	-0.80465490	-3.64325368
C	4.04841713	1.90324251	-3.15062274
H	3.02648901	1.66653569	-3.48424433
H	4.63815041	2.14698268	-4.05041028
H	3.99397665	2.81747558	-2.53958877

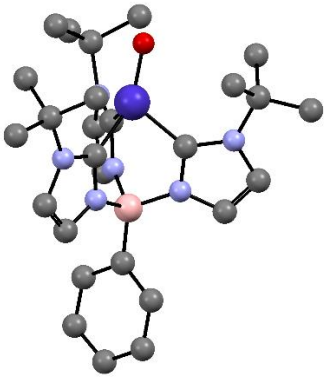

Figure D6.3. DFT optimized structure of Co(O).

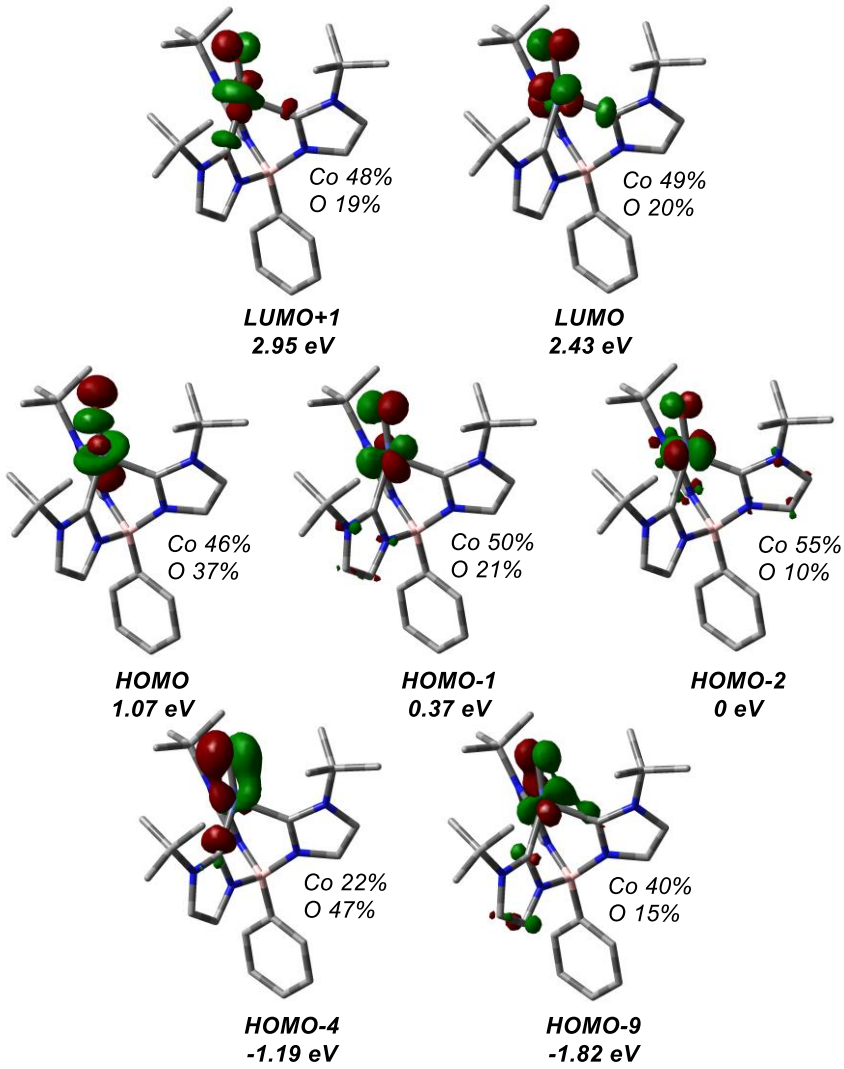

Figure D6.4. Depiction of MOs of the Co(O) relevant to Figure 4.5. Orbital energies are listed relative to the HOMO-2 in eV. Calculated contribution of Co d-orbitals and O p-orbitals for each MO are noted. Lobal representations are shown with 0.07 isocontours.

Optimized coordinates for Co(O).

C	-0.32852371	1.43037743	-0.58181757
N	-0.74902062	2.58448943	-1.18762547
C	0.31451266	3.15626727	-1.86704040
C	1.39802044	2.36276548	-1.65777511
N	1.00106934	1.33043307	-0.84293059
B	1.77225880	0.06266385	-0.34265467
N	1.42395196	-0.06696068	1.17054149
C	0.12697408	-0.10216129	1.53852943
N	0.12252777	-0.23164917	2.89780186
C	1.43027487	-0.27873990	3.36204643
C	2.24012920	-0.17430535	2.27283867
N	1.00466586	-1.10748934	-1.05346077
C	-0.32672417	-1.26883237	-0.82944757
N	-0.71710406	-2.32466845	-1.61168590
C	0.36775948	-2.76879706	-2.35062713
C	1.43266470	-1.99835089	-2.00663704
Co	-1.29922923	-0.00758968	0.23568676
O	-2.95315902	-0.08691461	0.02812560
C	-2.13408902	3.15711828	-1.17686977
C	-2.08735866	4.57586325	-1.73306464
C	-3.03388924	2.29394492	-2.05396721
C	-2.63622674	3.20819981	0.26095914
C	-1.10762400	-0.33754181	3.73236215
C	-0.71659990	-0.41224040	5.20119081
C	-1.97072458	0.89546785	3.48862450
C	-1.85691811	-1.60229729	3.32601531
C	-2.08580332	-2.93111623	-1.71987745
C	-2.59865507	-3.25643963	-0.32208342
C	-3.00445324	-1.95467992	-2.44482701
C	-1.99271509	-4.22722850	-2.51816341
H	-3.09044573	5.01536844	-1.65788669
H	-1.40044398	5.22286533	-1.16836366
H	-2.63537002	2.23092247	-3.07735716
H	-4.03735851	2.73972481	-2.10879021
H	-3.13654207	1.28332204	-1.63636401
H	-1.95403914	3.79089430	0.89740368
H	-2.74741614	2.19976837	0.67682482
H	-3.62400921	3.68871714	0.28943505
H	-0.16233575	0.47950780	5.52743750
H	-0.11204811	-1.30211718	5.42710285
H	-1.62653127	-0.47401510	5.81212693
H	-1.41634701	1.81989196	3.70533123
H	-2.86076419	0.86837303	4.13265594
H	-1.22661534	-2.49448102	3.45135419

H	-2.75715151	-1.72633432	3.94399893
H	-2.17840961	-1.54309095	2.27587866
H	-3.56867818	-3.76725503	-0.39726249
H	-1.90203691	-3.92399395	0.20680579
H	-3.98777840	-2.42051432	-2.60245231
H	-3.15358467	-1.04574082	-1.84650689
H	-1.29097835	-4.94669994	-2.07185622
H	-1.70945265	-4.06124134	-3.56709054
H	-2.98353744	-4.69937648	-2.52834956
H	-1.80507716	4.60390072	-2.79486742
H	-2.59243659	-1.69233000	-3.43069462
H	-2.31955452	0.92858855	2.44575757
C	3.36540779	0.06641450	-0.50251334
C	4.12133569	1.24844268	-0.41072555
C	5.51645766	1.23741963	-0.39878454
C	6.20764199	0.02918338	-0.46004305
C	5.48691210	-1.16296116	-0.50472276
C	4.09265112	-1.13779432	-0.51738151
H	3.61232422	2.21104081	-0.30771276
H	6.06657688	2.17961936	-0.32852731
H	7.30031856	0.01554148	-0.45254648
H	6.01397206	-2.12073083	-0.51893224
H	3.55663270	-2.09176522	-0.50425046
H	0.22650535	4.07480998	-2.43399839
H	2.40789996	2.45564592	-2.04379117
H	1.68115165	-0.37548347	4.41186748
H	3.32468008	-0.16635503	2.20162818
H	0.30520313	-3.58982850	-3.05364889
H	2.45078662	-2.01283018	-2.38209113
H	-2.74919476	-2.34435392	0.26678564

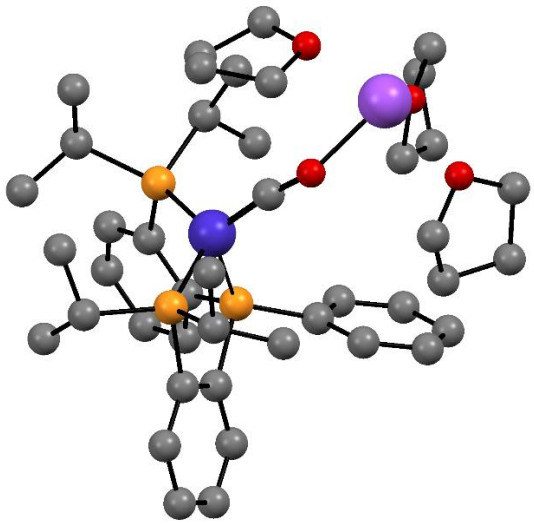

Figure D6.5. DFT optimized structure of the anionic Co(CO) complex **4.4a**.

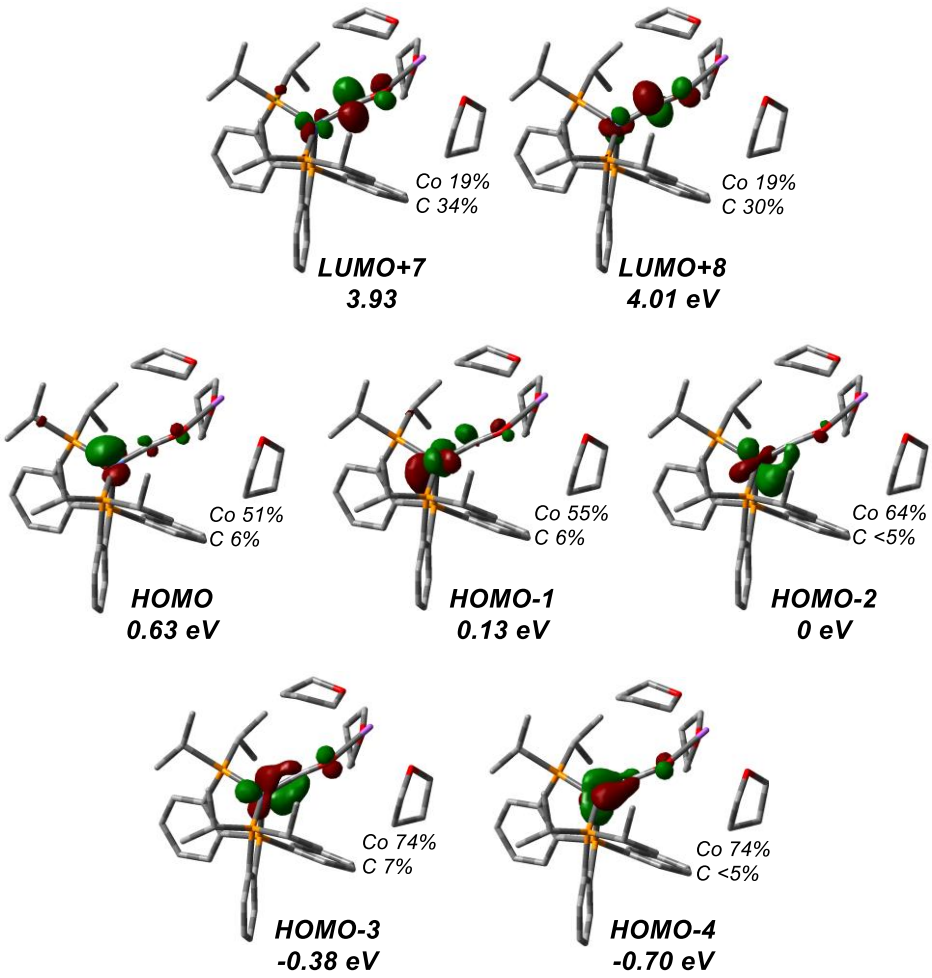

Figure D6.6. Depiction of MOs of the [Co(CO)][Na(THF)$_3$] relevant to Figure 4.5. Orbital energies are listed relative to the HOMO in eV. Calculated contributions of Co d-orbitals and C p-orbitals for each MO are noted. Lobal representations are shown with 0.07 isocontours.

Optimized coordinates for [$P_2^PCo(CO)$][Na(THF)$_3$] **4.4a**.

Co	-0.62536986	0.69858865	0.06613693
P	-1.57773157	1.18801862	1.92307923
P	-1.61617366	-1.16276482	0.07736372
P	-1.53240179	1.10860177	-1.85969381
Na	4.34187214	0.81480924	-0.02433994
O	2.23326925	0.85548486	0.55729858
O	4.92133365	-0.64310596	1.63315916
C	-0.78948460	-2.80784669	-0.03067047
O	3.85667330	-0.76285179	-1.59090831
C	-2.58512749	-1.38904434	1.64467275
O	4.19665841	3.08947297	-0.15650994
C	-2.60530306	-0.26060130	2.47889327
C	1.05679951	0.83754237	0.28372391

C	-2.90436338	-1.24052673	-1.25216313
C	-3.30904332	-0.31390549	3.68761532
H	-3.33313610	0.56211094	4.34566283
C	-2.88509075	-0.14451688	-2.13475467
C	-0.46812403	1.28849696	3.45678471
H	-1.13709031	1.40615624	4.33035884
C	-3.81869482	-0.09445182	-3.17635715
H	-3.80660305	0.73863283	-3.88605387
C	-3.23974194	-2.56152682	2.04239156
H	-3.18967452	-3.45692206	1.41417082
C	0.02745883	-3.17847967	1.05412072
H	0.05087194	-2.53687621	1.94287261
C	-0.79627027	-3.63767873	-1.16295046
H	-1.42393003	-3.37794997	-2.02095872
C	-0.44714070	0.66959147	-3.37565157
H	-0.94240741	1.11785944	-4.25790327
C	-2.36278611	2.65091742	-2.59499594
H	-2.61737783	2.40094495	-3.64172344
C	-3.97710342	-1.47655752	4.06989515
H	-4.52459043	-1.50766461	5.01588830
C	-3.85488614	-2.25403956	-1.42098276
H	-3.86323048	-3.11395940	-0.74404709
C	-4.79173703	-2.18311046	-2.45235335
H	-5.53690771	-2.97403765	-2.57090208
C	-2.78081450	2.61361475	2.24789540
H	-2.86959938	2.74781337	3.34309736
C	-3.93464548	-2.60568089	3.25012831
H	-4.44361817	-3.52372725	3.55571661
C	0.80159720	-4.33290153	1.01267388
H	1.41454506	-4.60691244	1.87694075
C	0.79095796	-5.14697802	-0.12487409
H	1.39665027	-6.05618675	-0.15954589
C	0.31543203	-0.00432383	3.60909761
H	-0.33943909	-0.88071983	3.73293290
H	0.98126694	0.03860171	4.48739540
H	0.93725951	-0.17673108	2.71642868
C	-3.64158155	3.02612462	-1.86753951
H	-4.35091602	2.18924865	-1.79125792
H	-4.15708430	3.84882646	-2.38843159
H	-3.43550978	3.37354738	-0.84578146
C	-4.77268248	-1.10012376	-3.33038907
H	-5.50330570	-1.03980090	-4.14158366
C	-0.01273639	-4.79309440	-1.20790154
H	-0.03682710	-5.42688885	-2.09914227
C	-0.35385230	-0.83398229	-3.57516100
H	-0.01026073	-1.32224425	-2.64516107

H	0.36590689	-1.08296757	-4.37261047
H	-1.31315857	-1.29441612	-3.84975071
C	-1.39294177	3.82223879	-2.61479794
H	-0.94046956	3.97649897	-1.62077287
H	-1.90672670	4.75588096	-2.89469874
H	-0.57312997	3.68134466	-3.33319553
C	0.47832918	2.47580880	3.39094417
H	1.02672317	2.47510298	2.43421514
H	1.22190322	2.43390771	4.20428252
H	-0.04026661	3.44037741	3.48099529
C	-2.23016226	3.89329808	1.63442549
H	-1.32268917	4.25192615	2.13919124
H	-2.97204257	4.70710914	1.67134033
H	-1.95222041	3.72634652	0.58091800
C	-4.14678983	2.26556197	1.67178444
H	-4.05158427	1.83543656	0.66101702
H	-4.78734928	3.15797956	1.58812467
H	-4.68308541	1.52641216	2.28166490
C	0.94927823	1.25387285	-3.23657165
H	0.94699890	2.33580391	-3.04373963
H	1.54550697	1.07829462	-4.14920183
H	1.47316651	0.78560527	-2.38648652
C	4.03052077	-0.66927608	2.75270661
H	4.61107133	-0.70137460	3.69489056
C	5.28505806	-1.98968658	1.31298652
H	5.27214733	-2.08375967	0.21446944
H	6.31783643	-2.18657618	1.64884009
C	2.76319796	-1.66937474	-1.31237276
H	2.90914978	-2.08775942	-0.30538961
C	4.35110027	-0.98787096	-2.91198074
H	4.48650409	-0.01542762	-3.41383104
H	5.34387941	-1.47460370	-2.85386320
C	3.38001122	3.36447365	-1.30467216
C	3.65421416	3.75233630	0.99661992
H	4.47941599	4.24062714	1.53702995
H	1.80995847	-1.10704209	-1.29366351
H	3.20062276	2.99680920	1.66379731
H	3.93958340	4.03079001	-1.98681366
H	3.18983940	2.41847333	-1.84210547
H	3.43701845	0.25625716	2.73641194
C	4.26692603	-2.89784848	2.00870901
C	3.21858796	-1.92544178	2.54217091
H	3.84125360	-3.64906761	1.32776134
H	4.74255379	-3.45038872	2.83301794
H	2.43497661	-1.73084330	1.79209056
H	2.71601684	-2.28008622	3.45270218

C	2.11325554	4.00660520	-0.77936905
C	2.61172076	4.71795826	0.46923083
H	3.07599968	5.68445413	0.21423131
H	1.81626850	4.91718339	1.20040338
H	1.65216502	4.68404479	-1.51098555
H	1.36392670	3.23664380	-0.52180556
C	2.80826659	-2.69910378	-2.41915678
C	3.33226216	-1.87997481	-3.58760420
H	3.76046851	-2.48013465	-4.40145010
H	2.52025857	-1.26977152	-4.01269915
H	3.50867959	-3.51462159	-2.17014481
H	1.82613350	-3.15518033	-2.60187365

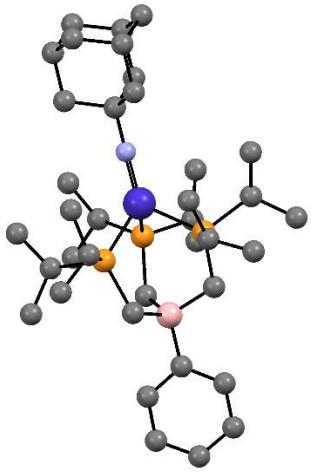

Figure D6.7. DFT optimized structure of [BP_3]Co(NAd).

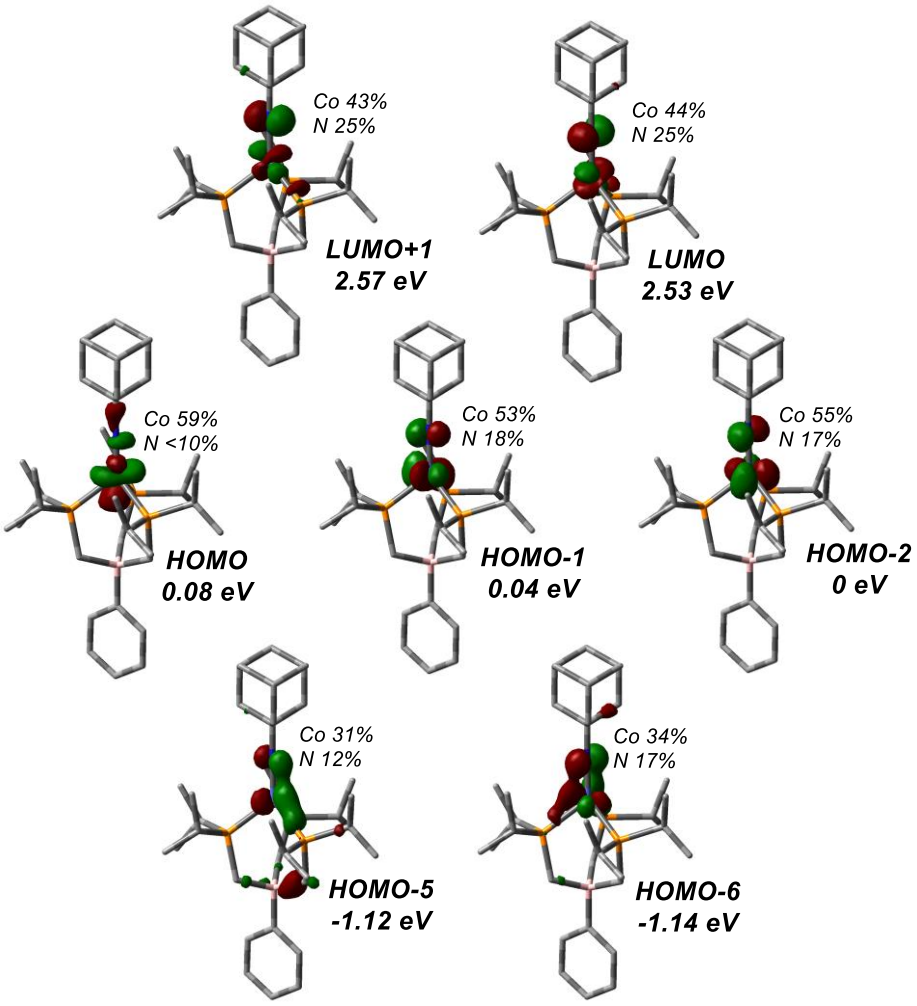

Figure D6.8. Depiction of MOs of [BP_3]Co(NAd) relevant to Figure 4.5. Orbital energies are listed relative to the HOMO in eV. Calculated contributions of Co d-orbitals and N p-orbitals for each MO are noted. Lobal representations are shown with 0.07 isocontours.

Optimized coordinates for [BP_3]Co(NAd).

P	-0.69223535	1.79102954	-0.54345551
P	-0.86732128	-0.32694887	1.77760176
P	-0.79233515	-1.30378049	-1.21333122
N	2.12089638	-0.03340685	0.06087001
B	-3.07584892	0.13246391	-0.10795458
C	-4.70351951	0.13410295	-0.11899981
C	-5.40877824	-1.08475128	-0.08980846
H	-4.84465736	-2.02667586	-0.08286566
C	-6.79978334	-1.15096182	-0.06435939
H	-7.30213422	-2.12284767	-0.04247927
C	-7.55429379	0.02343772	-0.06648503
H	-8.64652246	-0.01848719	-0.04897436
C	-6.89253081	1.24878709	-0.09013014

H	-7.46860047	2.17916698	-0.09006516
C	-5.49620980	1.29439074	-0.11412046
H	-5.01267905	2.27785978	-0.12820555
C	-2.48373729	1.67597262	-0.22582951
H	-2.70614671	2.23675865	0.69906109
H	-3.00147682	2.22769957	-1.03073701
C	-2.60888917	-0.59612209	1.32172520
H	-2.77656870	-1.68372082	1.23073437
H	-3.25184321	-0.27871241	2.15983018
C	-2.52912419	-0.78197414	-1.38343664
H	-2.60765227	-0.20721509	-2.32384728
H	-3.16149407	-1.66994380	-1.54101894
C	0.81554514	1.84493666	-2.95365439
H	0.77623771	1.70485291	-4.04562272
H	1.28832265	0.95670863	-2.50924251
H	1.49054029	2.69258992	-2.76605415
C	-0.57647729	2.09182885	-2.39069506
H	-1.23976664	1.28761619	-2.75725399
C	-1.15241120	3.40954869	-2.88494734
H	-0.48352132	4.25325391	-2.66045180
H	-2.13976797	3.63663539	-2.45880440
H	-1.26954226	3.38535859	-3.97928347
C	1.34524372	3.70223108	-0.13483175
H	1.37257496	4.15223148	-1.13894731
H	1.99381433	2.81216141	-0.14233817
H	1.78988997	4.43702981	0.55382630
C	-0.07009856	3.35207654	0.29252534
H	-0.01003784	3.03375859	1.34453695
C	-1.00308413	4.55520523	0.24806241
H	-0.64892928	5.32763108	0.94822562
H	-2.03359502	4.30525811	0.53673735
H	-1.04412117	5.02381963	-0.74361529
C	0.50231792	1.53246251	3.34859583
H	0.51116358	2.49784570	3.87801910
H	1.17828543	1.60664398	2.48165410
H	0.94462583	0.79253762	4.03520302
C	-0.91097496	1.14016308	2.94342655
H	-1.34331099	1.94373173	2.32341425
C	-1.81748584	0.96815429	4.15212239
H	-1.46777647	0.17519910	4.83101121
H	-2.85571158	0.73812134	3.87765794
H	-1.84030222	1.89617620	4.74383199
C	1.05089769	-2.26572382	2.64530592
H	1.41175719	-2.91301443	3.45991615
H	1.80293324	-1.48483545	2.46565011
H	1.01387399	-2.87842837	1.73277477

C	-0.30022092	-1.66814178	2.99859151
H	-0.15781253	-1.09819015	3.93254530
C	-1.35485172	-2.72403378	3.28948011
H	-1.57022595	-3.36496603	2.42016675
H	-2.30988325	-2.28605290	3.61179847
H	-1.01105038	-3.39264458	4.09403138
C	0.49198807	-3.75431457	-0.70251693
H	0.58964158	-4.60544654	-0.01057944
H	1.36319532	-3.09743499	-0.54781742
H	0.55394050	-4.16748852	-1.72013992
C	-0.82125701	-3.02337337	-0.46465563
H	-0.86063280	-2.79070961	0.61129602
C	-2.03042670	-3.89256405	-0.77315923
H	-2.15664286	-4.08869160	-1.84718980
H	-2.96833951	-3.45165921	-0.40767200
H	-1.92343345	-4.87048933	-0.27740697
C	1.31888060	-1.69930161	-3.12975643
H	1.61183866	-2.75269359	-3.01897208
H	1.88719763	-1.11970091	-2.38619213
H	1.65038819	-1.38187343	-4.13062342
C	-0.18195906	-1.49836775	-2.97640322
H	-0.41724911	-0.49581429	-3.37552945
C	-0.97936804	-2.50645223	-3.79175892
H	-0.72916181	-2.41957929	-4.86045385
H	-2.06545118	-2.36368432	-3.69809271
H	-0.74894326	-3.54212591	-3.50006868
C	3.53491059	-0.04750503	0.07507787
C	4.10553589	0.76033783	-1.11218939
H	3.73415771	0.32269670	-2.05457328
H	3.71437112	1.79060329	-1.06804718
C	4.07393843	-1.49275201	-0.02307745
H	3.65970881	-2.08643315	0.80933960
H	3.69838402	-1.94925164	-0.95484317
C	4.05831319	0.57956311	1.38630711
H	3.67031051	1.60931804	1.46855729
H	3.64527899	0.01703095	2.24085684
C	5.63377477	0.75524153	-1.07909845
H	6.01622355	1.33994005	-1.93296410
C	6.12005945	1.37860907	0.23053965
H	5.78046779	2.42584040	0.30283268
H	7.22260094	1.40384316	0.25294980
C	5.58591498	0.56846108	1.41336806
H	5.93471914	1.01892019	2.35821077
C	6.08914894	-0.87293536	1.31542555
H	5.72684917	-1.46149338	2.17537524
H	7.19099884	-0.89521870	1.36157680

C	5.60285008	-1.49743162	0.00612483
H	5.96303341	-2.53778826	-0.06525000
C	6.13848794	-0.68560142	-1.17546023
H	7.24138874	-0.70368253	-1.18060110
H	5.81227742	-1.13902084	-2.12679716
Co	0.47745868	0.01351792	0.03650482

Appendix E

SUPPLEMENTARY DATA FOR CHAPTER 5

E1. NMR Spectra

Figure E1.1. ^{1}H NMR spectrum (MHz) of **5.2-H$_2$** in THF-d_8.

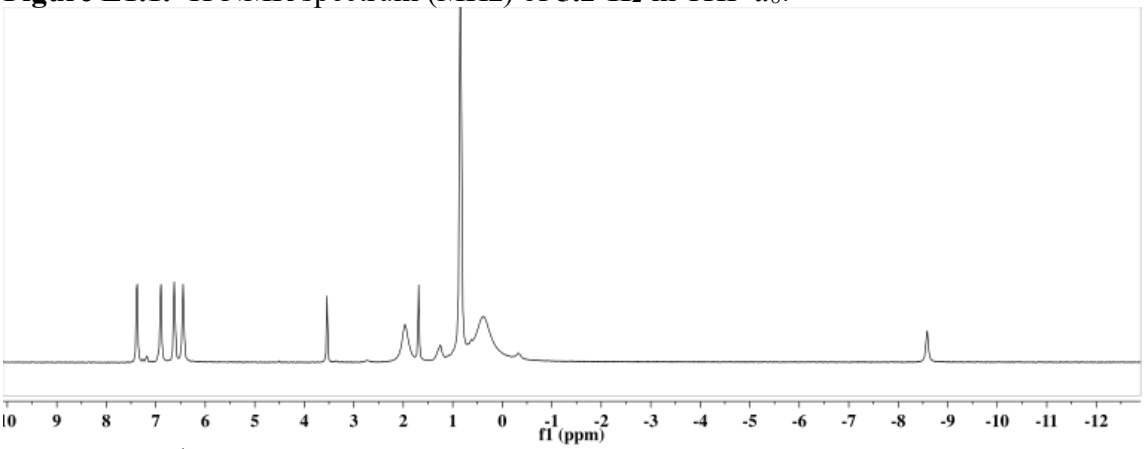

Figure E1.2. ^{1}H NMR spectrum (400 MHz) of **5.2** in THF-d_8 with a 1:1 mixture of H_2 and D_2: J_{HD} = 29.5 Hz.

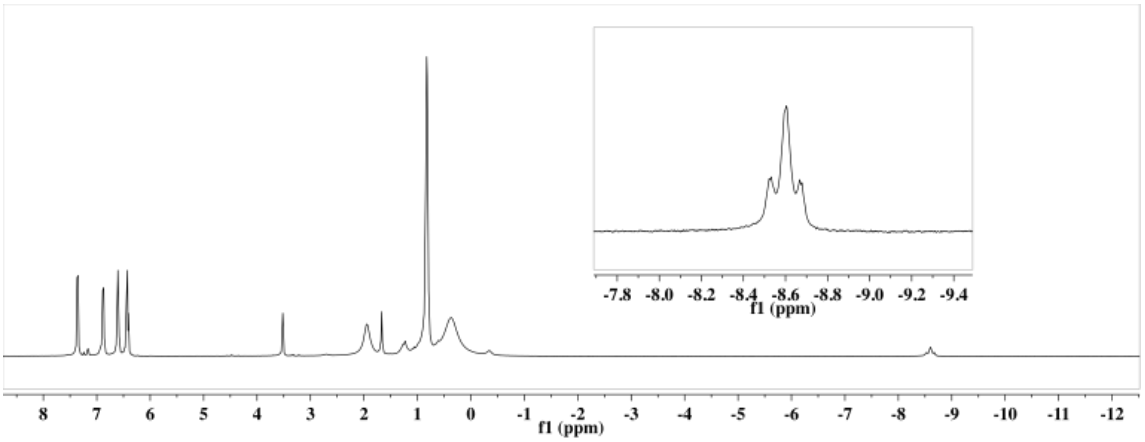

Figure E1.3. ^{31}P NMR spectrum (MHz) of **5.2-H$_2$** in THF-d_8.

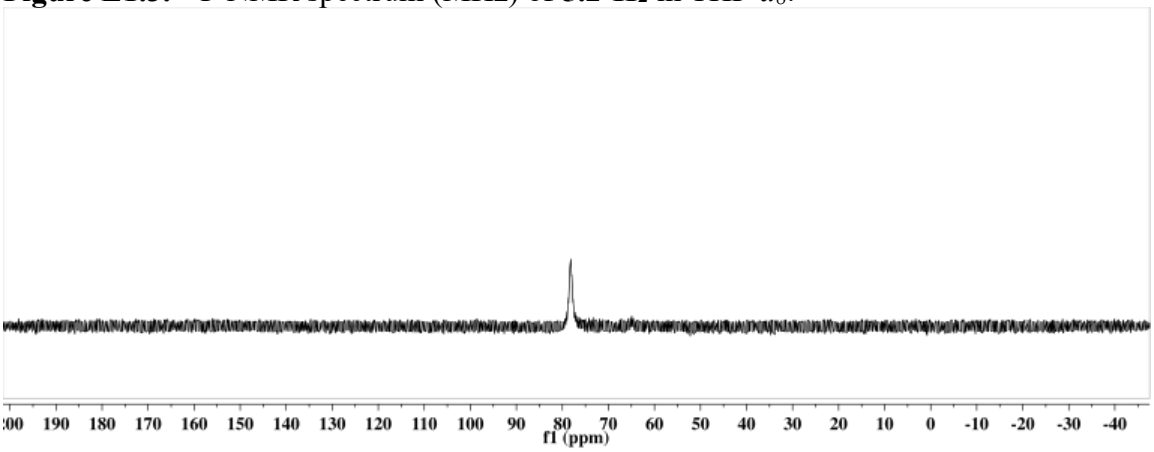

Figure E1.4. ^{11}B NMR spectrum (128 MHz) of **5.2-H$_2$** in THF-*d$_8$*.

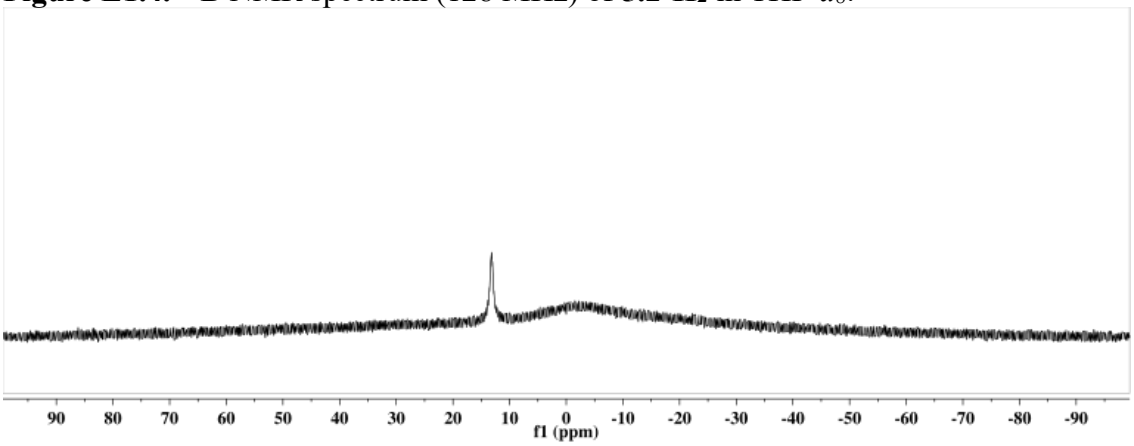

P$_3^B$Co(H) 5.3:

Figure E1.5. ^{1}H NMR spectrum (500 MHz) of **5.3** in toluene-*d$_8$* under an N_2 atmosphere.

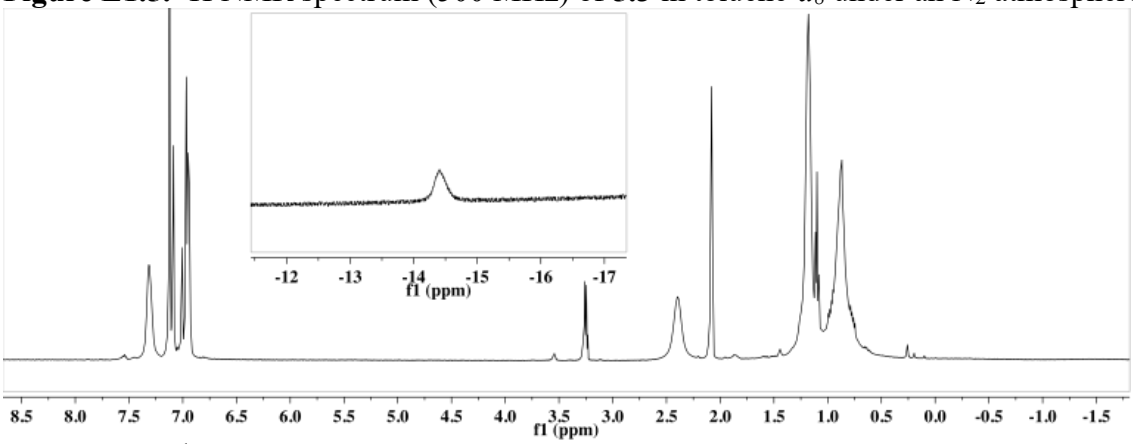

Figure E1.6. ^{1}H NMR spectrum (500 MHz) of **5.3** in toluene-*d$_8$* under an H_2 atmosphere at 10 °C.

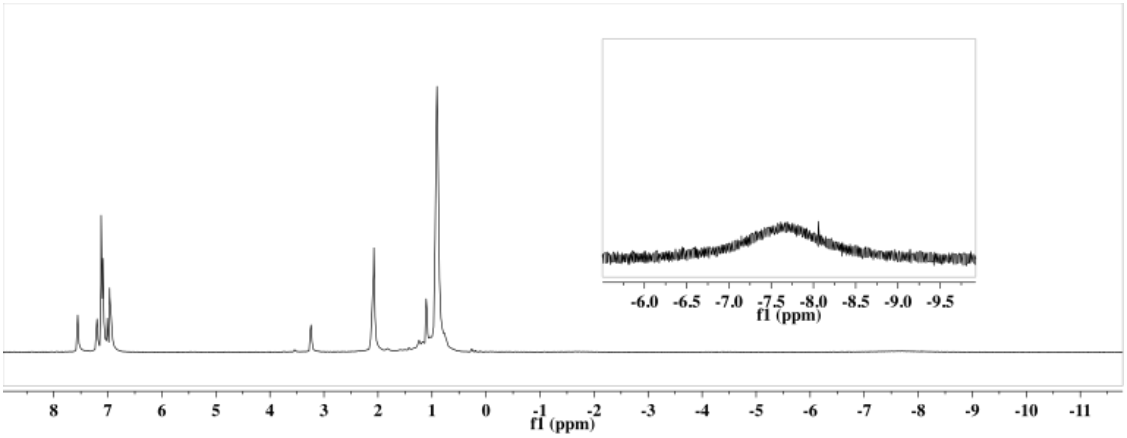

Figure E1.7. ^{1}H NMR spectrum (500 MHz) of **5.3** in toluene-d_8 under vacuum.

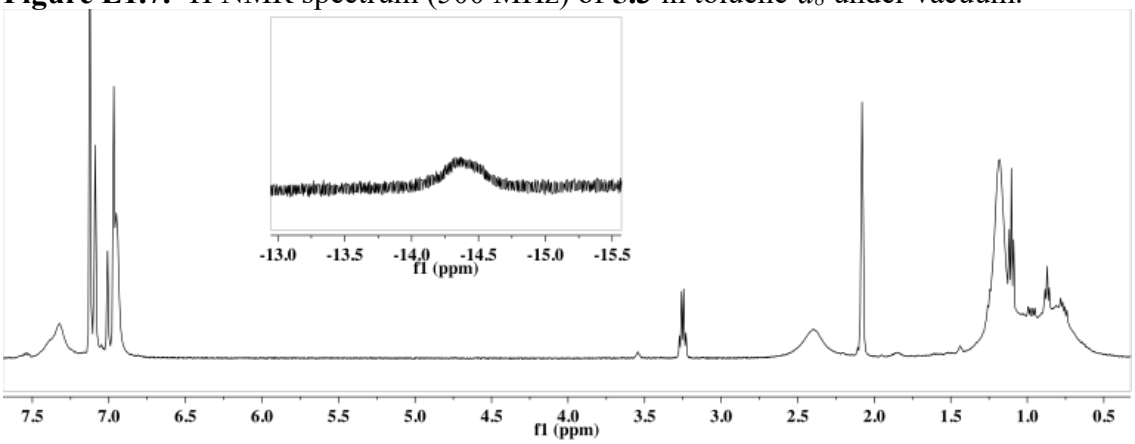

Figure E1.8. ^{31}P NMR spectrum (202 MHz) of **5.3** in toluene-d_8 under an N_2 atmosphere at 10 °C.

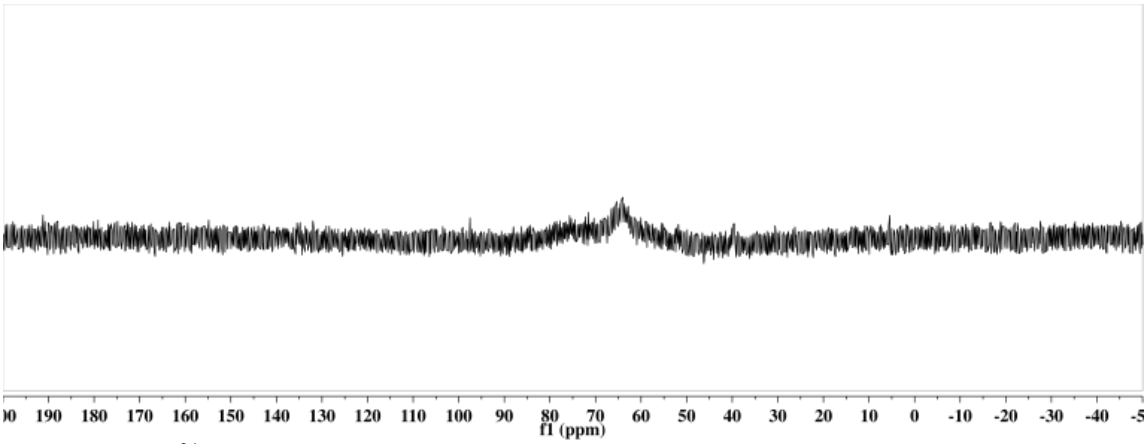

Figure E1.9. ^{31}P NMR spectrum (202 MHz) of **5.3** in toluene-d_8 under an H_2 atmosphere.

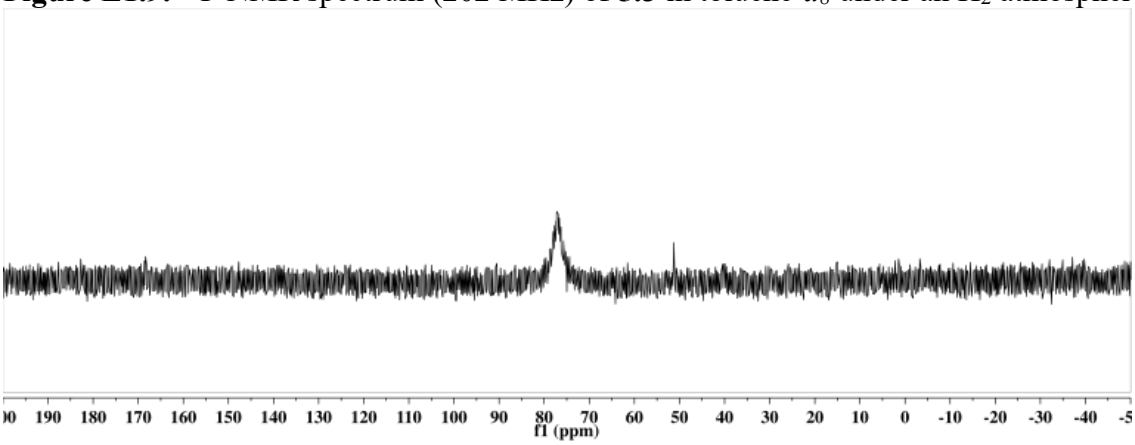

Figure E1.10. ^{31}P NMR spectrum (202 MHz) of **5.3** in toluene-d_8 under vacuum at 20 °C.

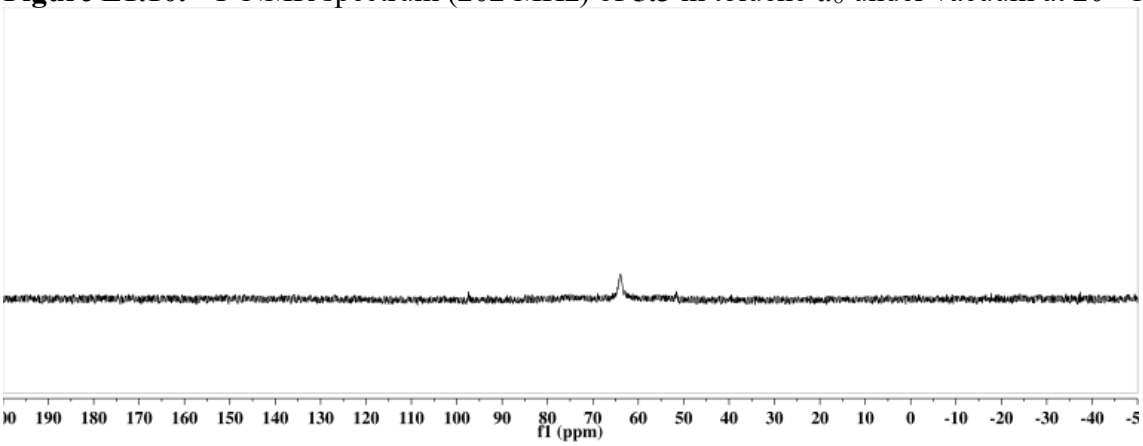

Figure E1.11. ^{11}B NMR spectrum (128 MHz) of **5.3** in C_6D_6 under an N_2 atmosphere.

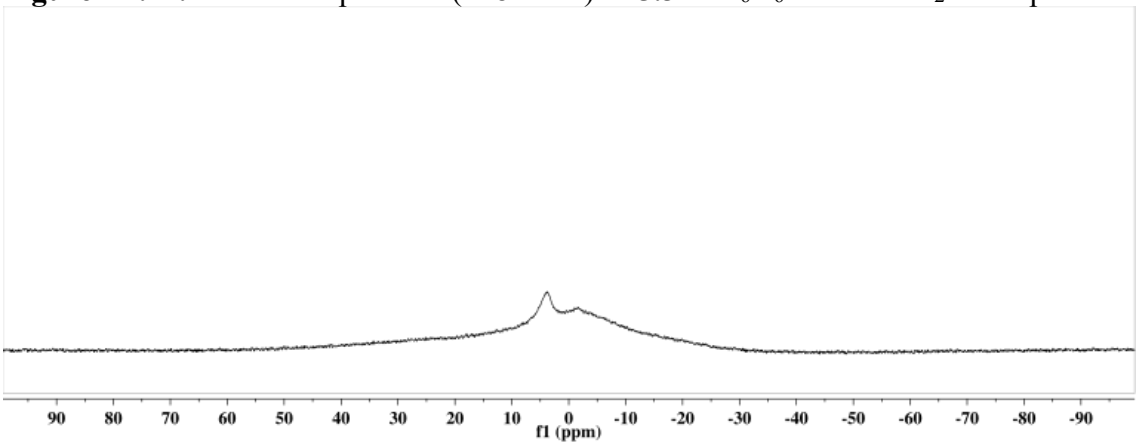

Figure E1.12. Variable temperature ^{31}P NMR spectra (202 MHz) of **5.3** in toluene-d_8 under vacuum from -80 °C (top) to 50 °C (bottom).

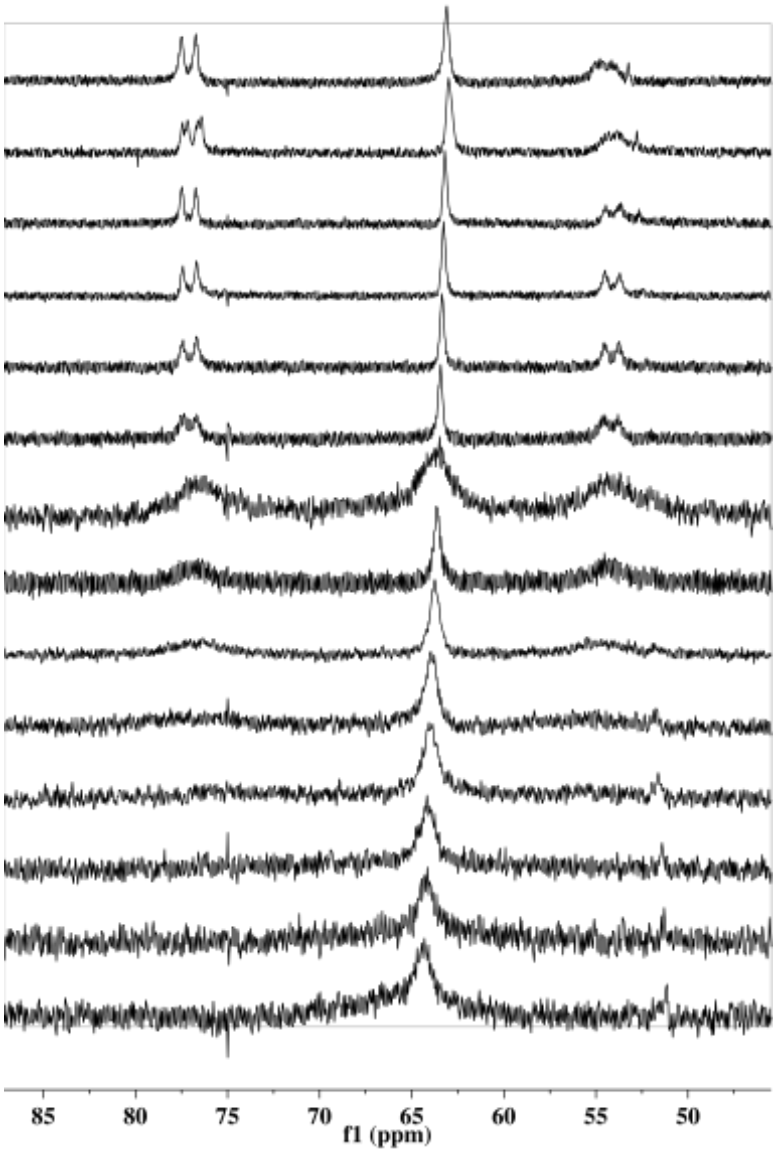

Figure E1.13. Variable temperature ^{1}H NMR (500 MHz) spectra highlighting the hydridic resonance of **5.3** in toluene-d_8 under vacuum from -80 °C (top) to 60 °C (bottom).

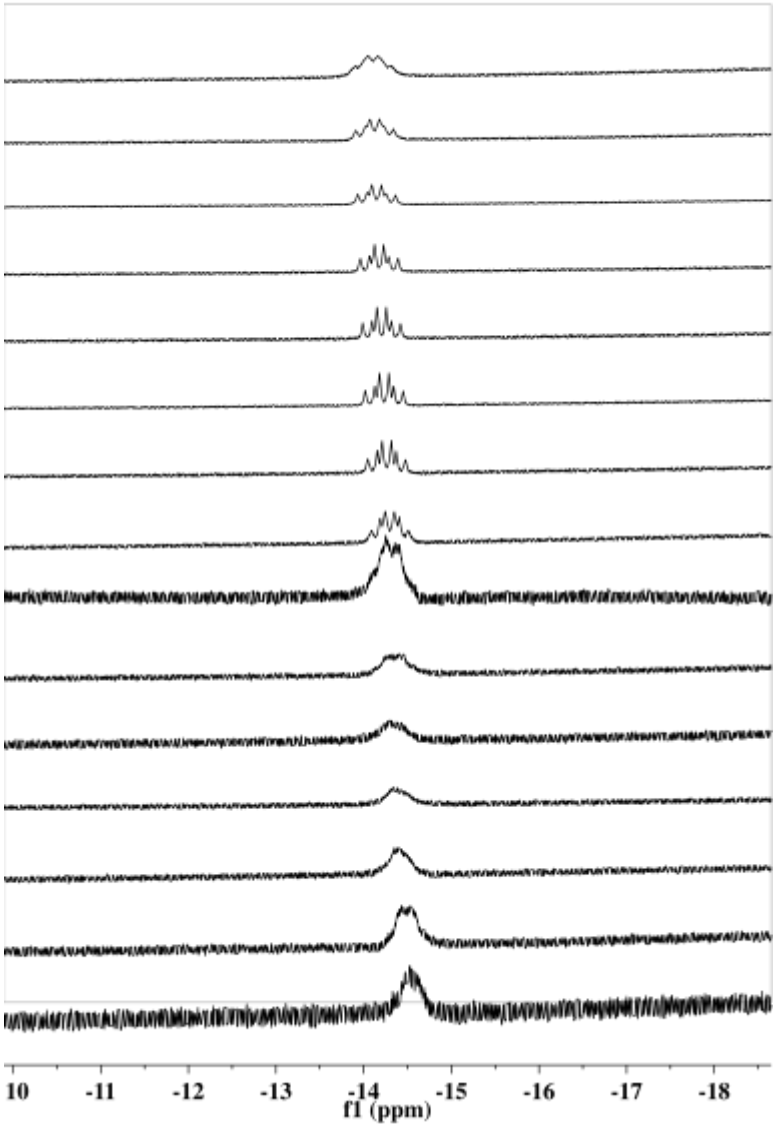

Figure E1.14. Variable temperature ^{31}P NMR (202 MHz) spectra highlighting the hydridic resonance(s) of **5.3** in toluene-d_8 under an H_2 atmosphere from 25 °C (top) to -80 °C (bottom).

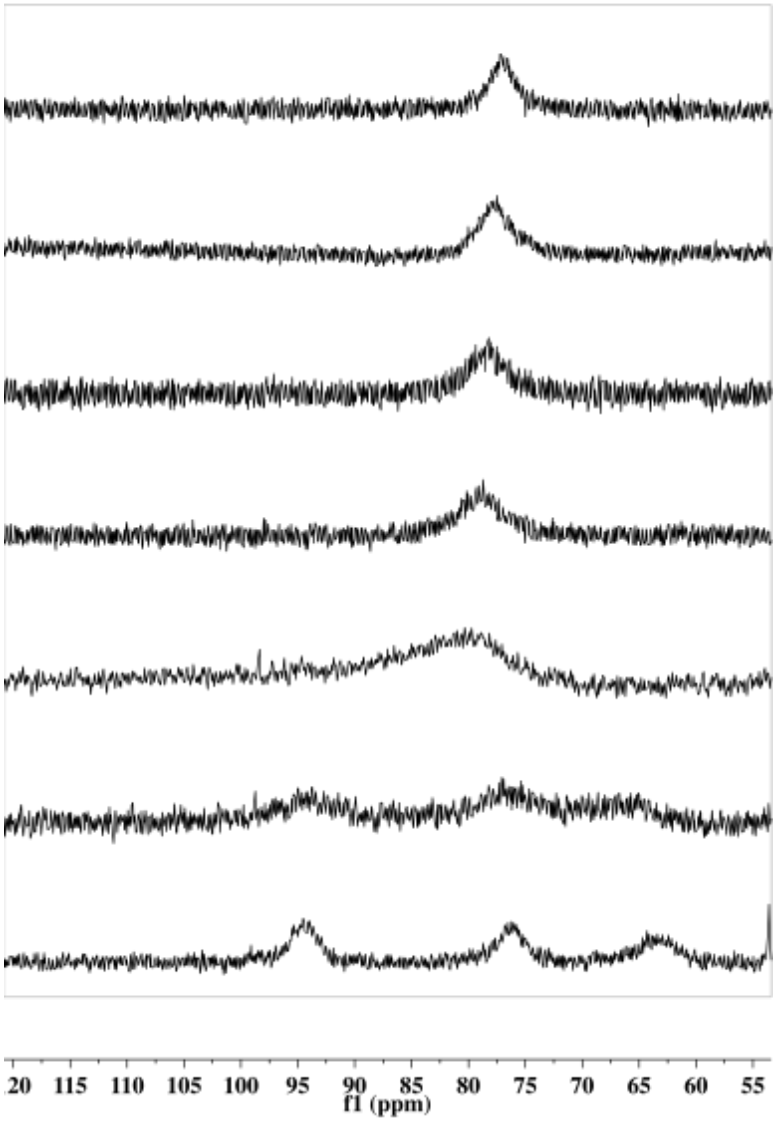

Figure E1.15. Variable temperature ^{1}H NMR (500 MHz) spectra highlighting the hydridic resonance(s) of **5.3** in toluene-d_8 under an H_2 atmosphere from -80 °C (bottom) to 10 °C (top).

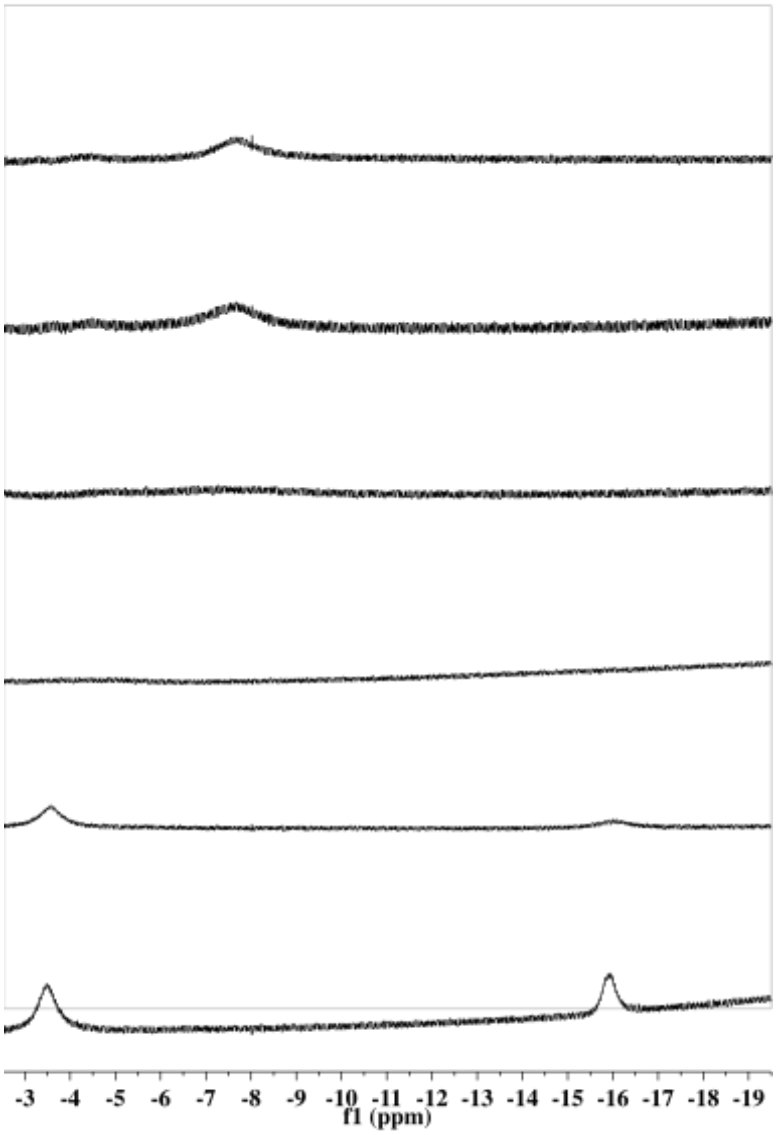

Figure E1.16. Variable temperature ^{31}P NMR spectra (202 MHz) of **5.3** in toluene-d_8 under an N_2 atmosphere from 10 °C (top) to -80 °C (bottom).

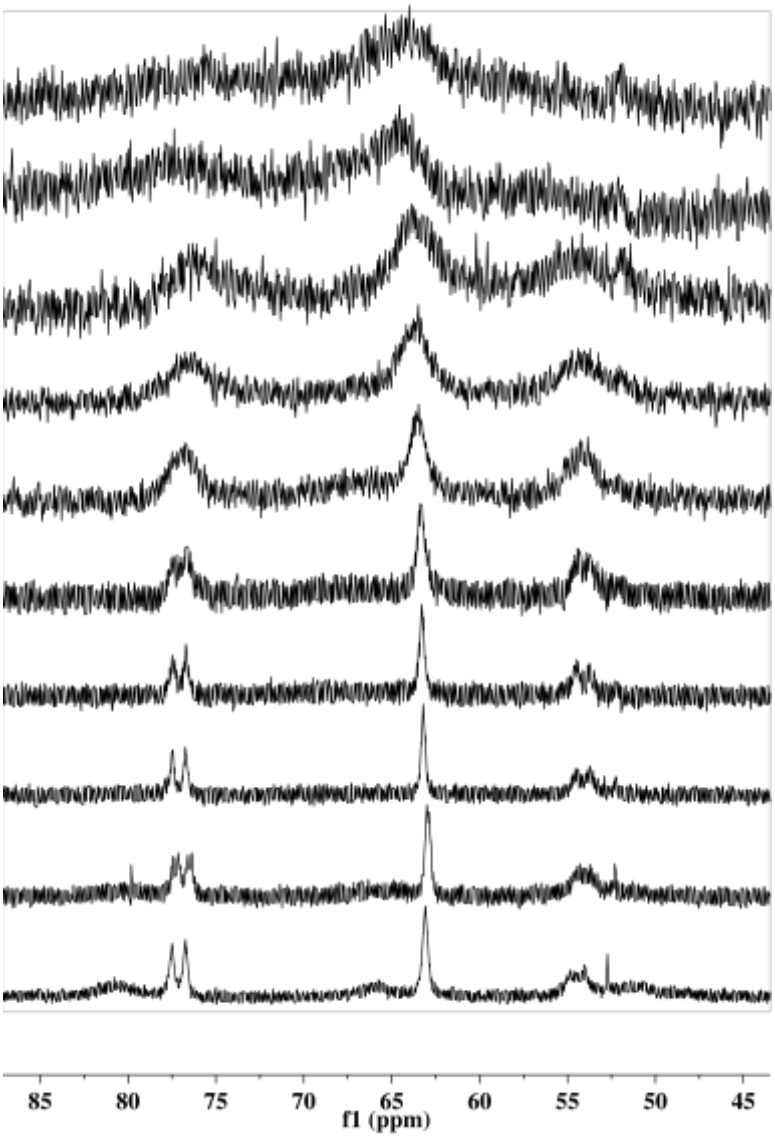

Figure E1.17. Variable temperature ^{1}H NMR (500 MHz) spectra highlighting the hydridic resonance of **5.3** in toluene-d_8 under an N_2 atmosphere from -80 °C (bottom) to 25 °C (top).

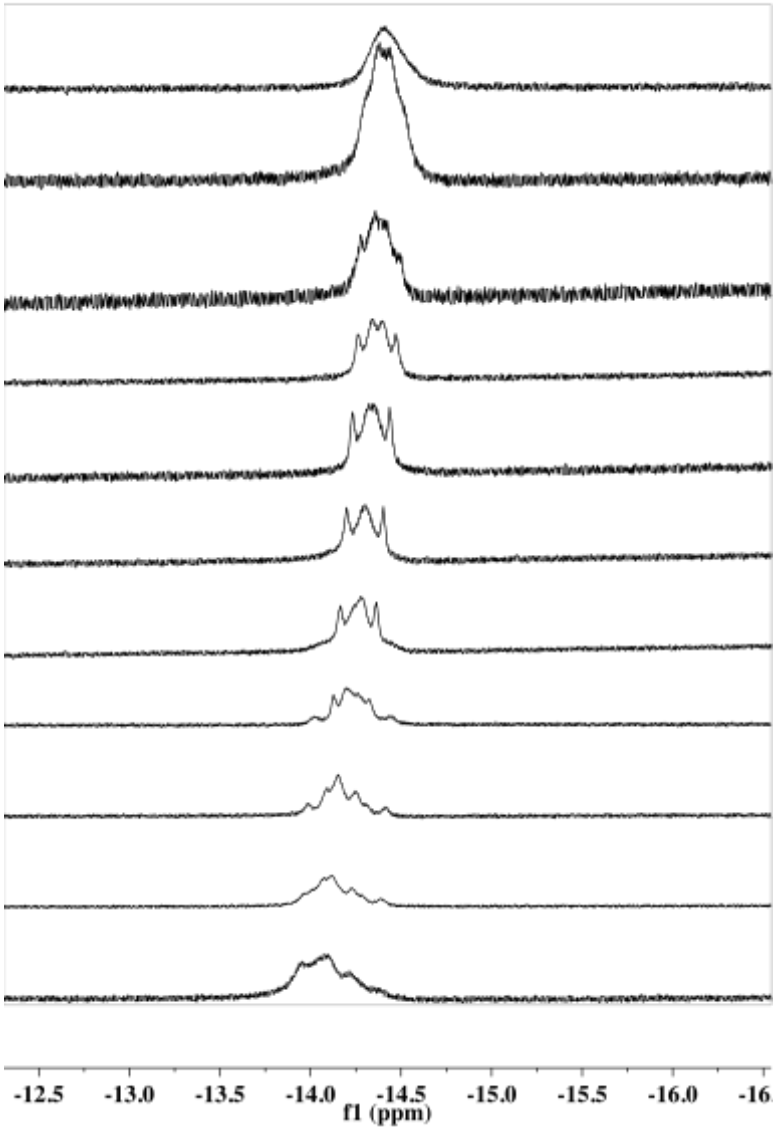

E2. Calculation of d_{HH} from J_{HD} and T_1(min).
Empirical correlations between J_{HD} and d_{HH} have been described by Morris[1] and Heinekey[2]:

$$d_{HH} = 1.42 - 0.0167(J_{HD})$$
$$d_{HH} = 1.44 - 0.0168(J_{HD})$$

Using these correlations to predict d_{HH} from J_{HD} = 29.5(6) Hz for the anionic H_2 adduct **5.2-H2** gives a predicted distance of 0.93(1) Å and 0.94(1) Å, respectively, consistent with its formulation as a non-classical H_2 adduct. As Heinekey's equation is derived from a more rigorous data set, we cite that value in the main text.

Similarly, predicted values of d_{HH} can be derived from a corrected value of T_1(min_corr) that corrects for dipolar interactions with the H_2-ligated Co center and the supporting ligand (L).[3]

Figure S.4.1. Plot of T_1 relaxation time vs. temperature as measured on a 500 MHz spectrometer in THF-d_8. A T_1(min) value of 26(1) ms was obtained at 258 K.

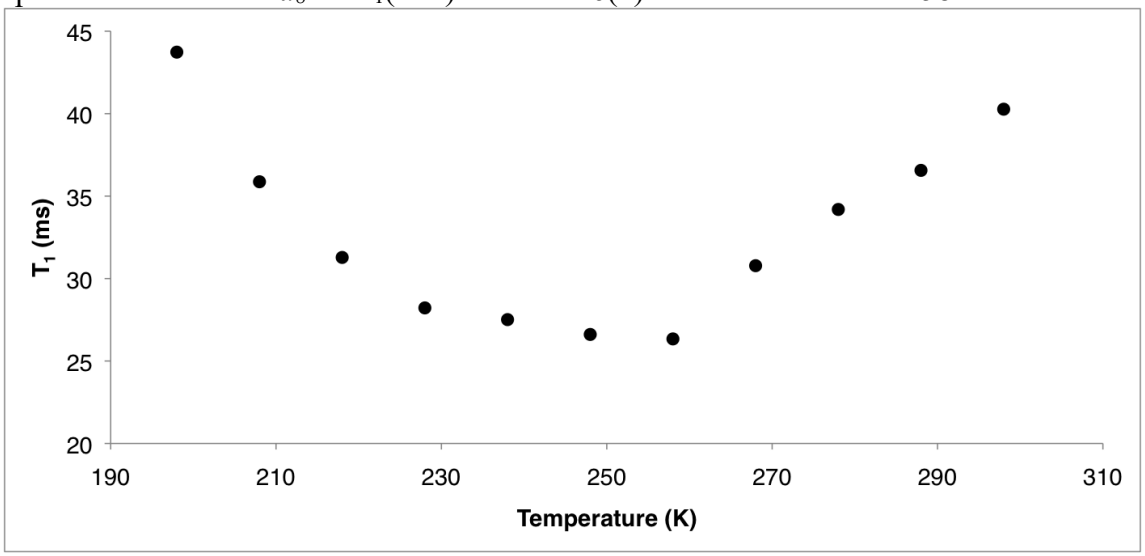

(1) Maltby, P. A.; Schlaf, M.; Steinbeck, M.; Lough, A. J.; Morris, R. H.; Klooster, W. T.; Koetzle, T. F.; Srivastava, R. C. *J. Am. Chem. Soc.* **1996**, *118*, 5396.
(2) Luther, T. A.; Heinekey, D. M. *Inorg. Chem.* **1998**, *37*, 127.
(3) (a) Desrosiers, P. J.; Cai, L.; Lin, Z.; Richards, R.; Halpern, J. *J. Am. Chem. Soc.* **1991**, *113*, 4173-4184; (b) Bautista, M. T.; Earl, K. A.; Maltby, P. A.; Morris, R. H.; Schweitzer, C. T.; Sella, A., *J. Am. Chem. Soc.* **1998**, *110*, 7031-7036. (c) Vollmer, M. V.; Xie, J.; Lu, C. C. *J. Am. Chem. Soc.* **2017**, *139*, 6570.

A corrected value of T_1(min), T_1(min(corr)) can be determined from the following equation, where the dipolar interactions from the ligand and Co center can be derived from the DFT optimized structure of **5.2-H$_2$**.

$$1/T_1(\text{min\_corr}) = 1/T_1(\text{min}) - 1/T_1(\text{L}) - 1/T_1(\text{M})$$

To obtain these values for the supporting ligand and metal center, the following general equation can be considered,

$$1/T_1(\text{E}) = R_\text{E} = K_\text{X}/\ d^6_\text{EH}$$

where the parametrized corrections depend on the constant K_x, determined based on the elements gyromagnetic ratio and nuclear spin, and the distance between the nuclei of interest. Thus, for Co:

$$1/T_1(\text{Co}) = R_\text{Co} = 88.80\ \text{Å}^6\ \text{s}^{-1}/(1.62)^6 = 4.9\ \text{s}^{-1}$$

Similarly, for all of the protons of the supporting ligand:

$$1/T_1(\text{L}) = R_\text{L} = \Sigma\ 77.51\ \text{Å}^6\text{s}^{-1}/\ (d_\text{HH})^6 = 3.9\ \text{s}^{-1}$$

A corrected T_1(min_corr) can then be obtained:

$$1/T_1(\text{min\_corr}) = 1/0.026\ \text{s} - 4.9\ \text{s}^{-1} - 3.9\ \text{s}^{-1} = 29.7\ \text{s}^{-1} = 33.7\ \text{ms}$$

From this corrected value, d_HH can be extracted, considering both fast and slow H_2 rotation, which has been discussed by Morris.[4]

For *slow* H_2 rotation:

$$= 1.172\ \text{Å}$$

For *fast* H_2 rotation:

$$= 0.930\ \text{Å}$$

The value derived by considering the fast rotation regime (d_HH = 0.93(1)) is far more similar to the value obtained from the empirical relationship between J_HD and d_HH (d_HH = 0.94(1)), consistent with the rapid rotation of H_2 observed in trigonal symmetry.

As shown in Table 1 of the main text, the difference between the corrected and uncorrected values of $T_{1\ \text{min}}$ is smaller for our complex than for those reported by Lu and coworkers. This is to obtained values normalized for instrument, with their spectra collected on a 400 MHz instrument corrected to match convention. Our spectra were obtained using a 500 MHz instrument, thus this correction was not needed.

---

(4) Morris, R. H. *Can. J. Chem.* **1996**, *74*, 1907.

E3. IR Spectra.

Figure E3.1. IR spectrum of $P_3{}^BCo(H)$ collected as a thin film under an N_2 atmosphere ($\nu_{Co\text{-}H}$ = 1943 cm^{-1}). The weak sharp stretch at 2092 cm^{-1} is reproducibly observed and may be attributable to the equilibrium N_2 ligation observed by alternative spectroscopies (UV-Vis, NMR). Alternatively, this may be due to the presence of $P_3{}^BCo(N_2)$, with a reported N_2 stretch at 2089 cm^{-1} within the error of the instrument.